FINAL REPORT: AHTD TRC-0406

LOW VOLUME FLEXBILE PAVEMENT ROADS REINFORCED WITH GEOSYNTHETICS

Submitted by:

Kevin D. Hall, Ph.D., P.E.
Department Head, Civil Engineering
University of Arkansas
4190 Bell Engineering
Fayetteville, Arkansas 72701

Authors:

Kimberly A. Warren, Ph.D.
Assistant Professor, Civil Engineering
UNC Charlotte
9201 University City Boulevard, Cameron 120
Charlotte, North Carolina 28223

Isaac L. Howard, Ph.D.
Assistant Professor, Civil Engineering
Mississippi State
P.O. Box 9546
Mississippi State, Mississippi 39762

TABLE OF CONTENTS

LIST OF TABLES

LIST OF FIGURES

1. INTRODUCTION

1.1 General and Background Information

In general, low-volume, flexible pavement roadways typically consist of some combination of a natural soil subgrade, granular base course, and asphalt concrete surface. Weak subgrade soils commonly pose a problem for the transportation engineering community since the subgrade serves as a foundation to the pavement structure. Conventionally, poor quality materials are excavated and replaced or alternative soil stabilization techniques are used. However, these methods can be labor and cost intensive especially if adequate replacement material is not available in the area. Geotextiles and geogrids offer alternative solutions to these conventional solutions.

Geosynthetic materials are commonly used to improve Civil Engineering design for various transportation, geotechnical, hydraulic, and environmental applications. Fabric reinforcement dates as far back as 1926 when the South Carolina Department of Transportation used natural cotton fibers to reinforce a roadway. Until the cotton fibers deteriorated, the roads remained in good condition, and roadway cracking, raveling, and localized failures were reduced (Koerner, 1986; Kaswell, 1963).

The properties and performance of synthetic fibers has improved significantly over the last 30 years and the increasing popularity of these materials can be attributed to their high strength, chemical resistance, and relatively low cost (Koerner, 1986). Both geotextiles and geogrid materials provide additional tensile reinforcement and confinement to the pavement system, ultimately reducing deformation and stress transfer from the surface to the subgrade. Geotextiles that are installed at the subgrade-base course interface also provide filtration and separation between dissimilar materials. Vehicular loads imposed on poor quality, saturated soils tend to increase existing pore pressures, decrease soil strength, reduce the bearing capacity, and promote the migration of subgrade fines into the base course layer. As a result, the initial design thickness and the drainability of the pavement structure is sacrificed.

The pumping of fines into the aggregate will eventually result in surface roughness, rutting, cracking, and eventual loss of load carrying capacity (Al-Qadi et al., 1996; Perkins and Ismeik 1997).

According to FHWA (1990), FHWA (2001), and Huang (1993), approximately 94% - 97% of the 2.5 million miles of paved US roads are surfaced with asphalt. Additional field testing is needed to further investigate the effects of each performance mechanism (separation versus reinforcement), demonstrate the performance of these materials under a variety of conditions, and collect stress-strain data for calibration of the upcoming mechanistic-empirical design approach.

As a result, the Arkansas Highway and Transportation Department (AHTD) initiated the construction of a full-scale test site consisting of thirteen test sections in July of 2003. Prior to construction, MIRAFI Construction Products expressed an interest in adding an additional four test sections to the test site. After some construction delays, seventeen test sections were constructed in the summer of 2005.

1.2 Research Objectives

In order to develop a better understanding of geosynthetic-reinforced flexible pavements and conduct high quality research in a field environment, the following objectives were systematically executed. Each objective/task is described in more detail within the chapters highlighted at the end of each objective.

1. ***Conduct a Literature Review:*** A review of the literature pertaining to all field experimentation, laboratory testing, and modeling efforts for the current application was performed in 2003 to establish the current state of practice at the time the project was initiated (Chapter 2).
2. ***Develop an Instrumentation and Plan:*** A detailed instrumentation plan was developed to establish the type, quantity, location, and installation method for all gages utilized in this study (Chapter 4).

3. ***Calibrate and Prepare the Instrumentation:*** All sensors were properly calibrated (or checked) and all foil strain gages were installed on the geosynthetic materials, prior to field installation (Chapter 4).
4. ***Install the Test Sections:*** An installation plan was developed to detail the special precautions used during for each phase of the construction process to maximize gage survivability in the presence of harsh construction conditions (Chapter 5).
5. ***Develop a Data Acquisition System and Develop the Software Code:*** A data acquisition system was developed and extensive programming was required to seamlessly acquire data from each axle and test section using independent, section-specific trigger sensors. Additionally, the software was programmed to calculate the critical statistics and organize the data files in an attempt to soften the post processing effort (Chapter 6).
6. ***Monitor, Collect, and Reduce the Data:*** Data was collected during three test phases over the course of four weeks, and a significant post-processing effort was performed to organize the data into a manageable database, prior to any data analysis (Chapter 7).
7. ***Analyze the Field Data:*** An empirical data analysis was conducted using Asphalt Institute transfer functions coupled with Miner's Concept (Chapter 8).
8. ***Establish the Governing Geosynthetic Performance Mechanisms:*** The choice and configuration of the geosynthetic materials was developed to assess the governing performance mechanism under full-scale loading conditions.
9. ***Develop a Finite Element Model:*** PLAXIS was utilized to develop a finite element model to predict critical structural responses of the geosynthetic-reinforced flexible pavement test sections (Chapter 9).

2. LITERATURE REVIEW

2.1 Introduction

Geosynthetic materials are manufactured from polymers (hydrocarbons) including polyester (PE), polypropylene (PP), polyethylene (PE), polyamide (PA), and polyvinyl chloride (PVC). The properties of these materials are monitored and tested during the manufacturing process to ensure quality control of each product. Unlike natural site materials, the properties of geosynthetics are well defined by the manufacturer. While there are a variety of innovative geosynthetic materials, the four most common classifications are geotextiles, geogrids, geomembranes, and geocomposites, and the five primary geosynthetic functions include reinforcement, separation, filtration, drainage, and containment. The use of geotextiles and geogrids will be highlighted in this project.

Geotextiles were originally developed as an alternative to granular soil filters (originating the term "filter fabrics"), allowing water to pass through the fabric while retaining soil particles. Similarly, some geotextiles can be used as a drainage product capable of dissipating excess pore pressures if the thickness and transmissivity of the material is adequate. They are also commonly placed between dissimilar materials to act as a separator. For example, a geotextile placed between a subgrade and base course layer prevents the migration of fine-grained particles into a coarse-grained aggregate layer, which would compromise the integrity of the pavement structure. In general, soils possess little to no tensile strength. The addition of a geosynthetic material provides additional reinforcement to the Civil Engineering system.

In general, geogrids are used for reinforcement and confinement. As discussed previously, soils and unbound aggregate have very little (if any) tensile strength without the inclusion of additional reinforcement. In addition to the direct tensile strength and confinement capability provided by a geogrid, the apertures "lock" the aggregate in place and create additional passive resistance. While there has been significant research advances in the area of geosynthetics, additional field testing is always necessary to demonstrate the capabilities of synthetic materials. Geosynthetics

can improve the design of many Civil Engineering applications and they are gaining popularity in both the private and the public sector, but there is still hesitations (especially in the public sector) to use these materials. The incorporation of geosynthetics into our roadways is not a simple problem due to the wide range of parameters that affect the performance of the material and the pavement structure. According to Perkins and Ismeik (1997), the geosynthetic type, manufacturing process, mechanical properties, material placement and layering, base course thickness and quality, asphalt thickness, subgrade type, strength, and stiffness, and vehicular load magnitude and frequency are all contributing factors. A survey of published field tests and laboratory experiments related to geosynthetic-reinforced flexible pavements conducted at the initiation of this project is presented in the following sections of this chapter. *A literature review of existing numerical analysis was also performed and is available upon request.*

2.2 Field Testing for Geosynthetic-Reinforced Paved Roads

2.2.1 Field Test 1

An eight year field study was initiated in 1994 by Virginia Tech on a secondary road in Bedford County, Virginia (Al-Qadi and Appea(2003), Al-Qadi and Bhutta(1999), Brandon et al.(1996)). The study consisted of nine 15 m (50 ft) long test sections with limestone base course material (VDOT 21-B). Each base course thickness (100 mm (4 in), 150 mm (6 in), and 200 mm (8in)) contained three configurations that included a geogrid, a geotextile, and a control test section. In all cases, the geosynthetic material was placed at the subgrade/base interface, the average hot mix asphalt (HMA) thickness was 95 mm (3.75 in), the average California Bearing Ratio (CBR) value was 7, and the average annual daily traffic (AADT) was approximately 550 (5% trucks).

Kulite 0234 and Carlson TP-101 earth pressure cells (0 to 690 kPa (0-100 lb/in^2) operating stress level) were used (50% and 76% survivability rate, respectively). Carlson JO-1 horizontal strain gages were used in the soil at the surface of the subgrade layers in the control sections (83% survivability rate). Kyowa KM

horizontal strain gages were used at the bottom of the HMA wearing surface (74% survivability rate). Vishay Micro-Measurement N2A 06 40 CBY 120 foil strain gages were attached to the bottom of the geotextiles (6% survivability rate) and Texas Measurements FLK-6-1L foil strain gages were attached to the bottom of the geogrid (28% survivability rate). T-Type thermocouples (88% survivability rate) were used to measure temperature and Gypsum block moisture sensors measured water content (100% survivability rate). AMP Sensors Inc. Roadtrax® Series P traffic sensors were used to monitor and trigger traffic for the data acquisition system, which was a Keithley 500. The Quick Basic® software handled a 200 Hz sampling rate.

In general, test sections with a 100 mm (4 in) base experienced significant improvement from the geogrids and geotextile inclusions while there was less of an affect on pavements with a thicker base course. Using a 20 mm (0.79 in) rut depth as a failure criterion for the 100 mm (4 in) base sections, it was determined that the geotextile and geogrid sections carried 195% and 187% more traffic than the control, respectively. However, the inclusion of geosynthetic materials did not prevent excessive deformation during the first few months, which is typical in comparison to the same time interval at another stage of pavement life.

Using the Falling Weight Deflectometer (FWD) data, the Base Damage Index (BDI) for the geotextile sections was approximately half the value calculated for control test sections. The BDI directly relates the pumping of fines into the base course from the subgrade, which is a strength reduction mechanism. Furthermore, it was concluded that improvements to the pavements as a result of the geosynthetics increased as the study progressed in comparison to control test sections.

2.2.2 Field Test 2

A field study along a 1.4 km section of Wisconsin State Highway 60 was initiated in the fall of 2000 (Edil et al. (2002)). Twelve test sections were constructed including three control, four industrial bi-product, and five geosynthetic test sections (a geocell, non-woven geotextile, woven geotextile, drainage geocomposite, and a geogrid). All test sections were designed with approximately the same structural

number as the control ($\approx$4.2) in an attempt to determine if the various reinforcement schemes would enhance the performance. The subgrade was a lean silt (ML) or lean clay (CL) with water contents near the plastic limit. The unconfined compressive strength varied from 100-250 kPa (14.5-36.25 psi). Each control test section had a 840 mm (33 in) rock sub-base, 140 mm (5.5 in) salvaged asphalt base, 115 mm (4.5 in) crushed aggregate base, and a 125 mm (5 in) HMA layer. The geosynthetics were located at the subgrade-base interface and were covered with a 300 mm (12 in) thick layer of excavated rock (less than the control sections).

Falling weight deflectometer (FWD) data was obtained taken on three different occasions to cover the seasonal variations. There was little difference in the performance between the geotextiles and geogrids versus the control test section. Overall, the study showed that test sections reinforced with geosynthetics provided equivalent support with respect to the control with much thinner base courses. To date, the test sections have provided adequate support to the construction equipment necessary to complete the pavement structure.

2.2.3 Field Test 3

A roadway with an AADT of 17,065 (3% trucks) was constructed in Delaware County, Pennsylvania along Route 30 (Al-Qadi and Hughes (2000)). The test sections consisted of an 88 mm (3.5 in) HMA, 200 mm (8 in) bituminous concrete base course (BCBC), 150 mm (6 in) subbase, and a subgrade layer, and the structure had an average CBR equal to 4. The study focused on the use of geocells in combination with geogrids and geotextiles. After three years of service, the roadway showed no signs of pavement distress (rutting, cracking, or base failure). Quantification of the benefits associated with the use of geocells in conjunction with geosynthetics was not achieved due to the variety of combinations used. However, it was concluded that using a geocell in conjunction with a Class 4 geotextile has the potential to effectively reinforce a highly traveled roadway over a weak subgrade.

2.2.4 Field Test 4

The Montana Highway Department constructed a roadway using geotextiles and geogrids over a soft subgrade in Bozeman, Montana (Yarger et al. (1991)). The natural subgrade was predominately an AASHTO A-4 and A-2-4. Due to the poor subgrade soils, three design alternatives were formulated by the DOT. In the first alternative, 0.9 m (36 in) of subgrade soil would be excavated and replaced with AASHTO A-1-b granular fill material. In the second alternative, 0.75 m (30 in) of subgrade would be excavated and replace with AASHTO A-1-b granular fill material in addition to the placement of a geogrid on top of a geotextile at the subgrade-base course interface. In the third alternative, a geotextile was considered for reinforcement and drainage, but it was decided that significant deformations would be necessary before any tension reinforcement benefit was mobilized. Option 2 was selected and based on the results from the study (no experimental data was provided), the DOT estimated a cost savings equal to \$40,000 for the 41,800 m^2 (50,000 yd^2) project using \$11.75/m^3 (\$9/yd^3) for the A-1-b material, \$6.5/m^3 (\$5/yd^3) for excavation of subgrade, and \$1.80/m^2 (\$1.50/yd^2) for the geosynthetic (installed).

2.2.5 Field Test 5

A 2.5 km (8100 ft) test section was constructed in Greenville County, South Carolina to evaluate the performance of geotextiles (Sprague and Cicoff (1993)). The subgrade material was deemed insufficient by the necessity to resurface two times in the 18 months prior to construction of the test sections. The experimental sections included the following configurations: (a) a 25 mm (1 in) triple treatment surface coarse over a 75 mm (3 in) stone base, (b) a 38 mm (1.5 in) asphalt concrete over 75 mm (3 in) compacted stone base, and (c) a 63 mm (2.5 in) full depth asphalt concrete binder course. A 4 and 6 oz. non-woven, needle punch and a 4 oz. woven, slit film geotextile were utilized, and in all three cases, they were placed at the subgrade interface.

In an attempt to assess geotextile damage during construction, 99 samples were extracted from the roadway, and most of the samples had minor puncture damage. It

was determined that the 4 oz. geotextiles were not able to resist localized punctures when used in conjunction with thin base courses. To assess deterioration of the pavement over time, the American Public Works Association Micro Paver was used to establish the pavement condition indice (PCI) on a scale from 0-100. Failure was equated to a PCI value of 50 or less. Using a Greenville-County based deterioration curve and data obtained during the first four years, the pavement life of each section was projected. It was estimated that the service life of the section with a full depth asphalt concrete binder course (option 3) would be increased by 1.1 years using the 4 oz. non-woven fabric, but the service life of the test section with the woven, slit film material would decrease by 4.6 years. The asphalt concrete over stone base (option 2) had a projected service life increase of less than one year for both 4 ounce fabrics. Without any geosynthetic, the triple treatment surface course over the stone base (option 1) would only have a six year service life (the worst of the three pavement configurations); the 4 oz. slit film fabric would increase the service life by 6 months while the 4 oz. non-woven fabric would reduce the life by approximately 9 months.

Overall, the 75 mm (3 in) stone base with 38 mm (1.5 in) asphalt overlay performed the best. The equivalent uniform annual cost (EUAC) of the roadway was increased only slightly as a result of inclusion of the geotextile. Therefore, even small increases in the service life can justify the material. In summary, short-term results were promising but inconclusive based on the findings of the study.

2.2.6 Field Test 6

A 300 m (980 ft) long test section was constructed on the Takeo-Fukudomi route in Japan consisting of soft clays with a CBR ranging between 4 and 6 and a PI equal to 37 (Miura et al. (1990)). The field test was initiated as a result of a laboratory study and subsequent finite element analysis that determined polymer geogrids could be useful as reinforcement. In the study, four sections consisting of a 5 cm (2 in) asphalt concrete surface, 15 cm base (5.9 in), 20 cm (7.9 in) sub base, and a clay subgrade were reinforced with geogrid. The control section contained 5 cm (2 in) of an asphalt concrete surface, a 20 cm (7.9 in) base, a 25 cm (9.8 in) sub base, and a clay

subgrade. The bi-axial geogrid was placed at the bottom of the base in two of the sections and at the bottom of the subbase in the other two sections. The construction costs for these sections were approximately the same.

Six months after construction was complete, rut measurements varied between 4-6 mm (0.16-.24 in) for sections with geogrids at the bottom of the subgrade, depths of 6-8 mm (0.24-0.32 in) for sections with geogrids at the bottom of the sub base, and 8 mm (0.32 in) for the control test sections. The control section did out perform the reinforced sections in terms of crack percentage and overall deflection as determined by the Benkelman beam test. Geogrids located at the surface of the subgrade out performed geogrids located at the surface of the sub base in terms of settlement. In summary, one layer of bi-axial geogrid was comparable to 10 cm (4 in) of base course material.

2.2.7 Field Test 7

A geotextile overlay study was performed between 1989 and 1992 on a regional highway in China (Li et al. (1992)) using two different non-woven products. The AADT for the test section was 3500 and it was constructed using an 80 mm (3.2 in) asphalt concrete surface, a 120 mm (4.8 in) of asphalt stabilized crushed stone base course, and a 350 mm (14 in) granular sub base. As a result of this study, they predicted that the asphalt concrete overlay would extend the pavement life and reduce cracking as well as rutting.

2.2.8 Field Test 8

A 3 km (1.9 mile) stretch of US Route 1A between Frankfort and Winterport, Maine was examined to determine the benefits of geosynthetics in cold climates for flexible pavements with a thick base course (Fetten and Humphrey (1998)). The subgrade was an AASHTO A-6 and the CBR value was approximately 3. The aggregate base was approximately 580-640 mm (23-25 in) thick, and the asphalt surface was 180 mm (7 in) thick. A geogrid, high strength geotextile, non-woven geotextile, and a geocomposite were utilized for this study but the location of each

geosynthetic varied with test section. The roadway was designed to carry 1.5 million equivalent single axle loads. A control section was incorporated into the test program, but it failed prematurely.

Minimal tension developed in the geogrid and high strength geotextile. In some instances, less than 5% of the ultimate strength of the geogrid was mobilized. The majority occurred during the placement of the first base course layer. Furthermore, Falling Weight Deflectometer (FWD) data proved to be inconclusive in evaluating the geosynthetic contribution to the roadway. Placement of a geosynthetic beyond 250 mm (10 in) had minimal effects. In summary, there were few reinforcement benefits as a result of the base course thickness.

2.2.9 Field Test 9

In order to assess the performance of geotextiles under a variety of climate conditions, the Geosynthetic Research Institute coordinated test sites in the states of New York, Pennsylvania, Minnesota, Washington, South Carolina, and Virginia (Suits and Koerner (2001)). The site located in the state of New York is a two lane rural road with an AADT just over 100 with (9% trucks and an FHWA 1-A climate). Two types of subgrade soils (SC and SM) were encountered. The sandy clay (AASHTO A-2-6) has a PI equal to 21 and an average CBR equal to 9. The sandy silt (AASHTO A-2-4) has a PI equal to 12 and an average CBR less than 1.

Five geotextile and one control test section was constructed. The geotextiles were located at the surface of the subgrade, and the pavement structure consisted of a 300 mm (12 in) sub-base, a 70 mm (2.8 in) asphaltic base, and a 45 mm (1.8 in) asphaltic wearing surface. Visual inspection during construction did not reveal signs of distress. FWD testing performed during the service life has shown decreasing subgrade resilient modulus values with time. The intent is to monitor these test sites for approximately 15-20 years post construction.

2.3 Laboratory Studies

2.3.1 Laboratory Investigation 1

Laboratory test sections were performed in a concrete box and loaded with cyclic 40 KN (9,000 lb) applications using a stationary plate (Perkins (1999)). Of the 19 different test sections constructed, ten contained soft clay and nine had silty-sand subgrades. The clay material was highly plastic, had a liquid limit equal to 100, a plastic limit equal to 40, and a CBR value of approximately 1.5 when compacted at 45% moisture. The silty sand contained 40% non plastic fines, had a liquid limit equal to 18, and a CBR value of approximately 15 when compacted at 14% moisture. The HMA had a 6% asphalt content for all clay subgrade and four of the silty sand subgrades. The remaining sections contained cold mix asphalt due to the unavailability of HMA during the winter. The asphalt concrete layer was 75 mm (3 in) thick for all test sections. No comparisons were made between HMA and cold mix sections. The crushed stone base course (USCS GW or AASHTO A-1) varied in thickness from 200-375 mm (8-15 in), and the specific gravity and maximum dry unit weight of this material was 2.63 and 21.5 KN/m^3 (137 pcf), respectively. Tensar BX-1100 geogrid, Tensar BX-1200 geogrid, and Amoco 2006 woven geotextiles were placed at three different locations: the base-subgrade interface, 40 mm (1.6 in) above this interface, and 100 mm (4 in) above this interface. All sections were heavily instrumented to measure the applied pavement load, surface deflection, and stress, strain, temperature, and moisture content in various pavement layers.

Significant improvement was observed due to inclusion of geosynthetic materials as defined by surface rutting criteria. Geosynthetic reinforcement permitted a 20% reduction in base course thickness for the 300 mm (12 in) and 375 mm (15 in) thick base course sections. Improvement was substantial for the clay subgrade, but minimal improvement was observed for the silty sand sections. No mixing of the subgrade and base was observed in any of the test sections indicating that the primary function of the geosynthetics was reinforcement. The geogrid sections out performed the geotextiles. The stiffer geogrid (Tensar BX-1200) outperformed the BX-1100. Less of a benefit was observed when a BX-1100 geogrid was installed at the subgrade-

base interface in comparison to the same material placed 100 mm (4 in) above the interface. Additionally, a BX-1100 geogrid installed at the subgrade-base interface of a 375 mm (15 in) thick base section did not perform as well as the 300 mm (12 in) section under the same conditions. These observations indicate that the depth location has an affect on material performance.

2.3.2 Laboratory Investigation 1

Virginia Tech created seven test sections using a 122 cm (48 in) thick silty sand subgrade, a 10.9 cm – 19.6 cm (4.3-7.7 in) thick granite base course (21-A VDOT), a 6.1 cm - 7.9 cm (2.4-3.1 in) thick HMA, two polypropylene geotextiles, and a polypropylene geogrid to determine the benefits of incorporating geosynthetics at the bottom of the base course (Valentine et al. (1993), Al-Qadi et al. (1996), Al-Qadi et al. (1994)). The CBR ranged from 1.7 - 4.6, and the sections were loaded with a dual tire load simulating an 80-KN (18-kip) axle load with a tire pressure of 550-kPa (80 psi). Deformation of 2.54 cm (1.0 in) under this load was considered to be failure.

It was shown that a pavement section containing a 7.1 cm (2.8 in) thick HMA layer, a 15.2 cm (6 in) thick aggregate base layer, and a subgrade CBR of 4 could maintain a service life of approximately 20 years for one sixth of the cost. Without the geotextile, an 8.9 cm (3.5 in) overlay would be required to achieve the same 20 year service life (based on an AADT of 200, which was converted to 3750 ESALs per year). While both geotextiles and geogrids showed improvement, the geogrids were not as effective for subgrades that had a CBR of 4 or less. It was also observed that the reinforcement (both geotextile and geogrid) provided almost immediate benefits to the pavement system and it took the reinforced sections approximately eight times the number of load cycles to reach 1.25 cm (0.5 in) failure displacement. This observation differed from the results of the field studies (Al-Qadi and Appea (2003), Al-Qadi and Bhutta (1999), Brandon et al. (1996)) where the benefits of geosynthetic reinforcement were not as pronounced during the early stages of loading.

2.3.3 Laboratory Investigation 3

Geogrids were placed at the base-subgrade interface of test sections that had a soft clay subgrade (average CBR equal to 1.9), a base course thickness ranging from 180 mm - 290 mm (7.2 - 11.6 in), and a 50 mm (2 in) thick HMA layer (Collin et al. (1996)). Results indicated that the control section with a 180 mm (7.2 in) thick base course had a 47 mm (1.88 in) rut at 1014 cycles of a 20 kN (4500 lb) load while the geogrid reinforced sections experienced less than 34 mm (1.36 in) ruts for the same pavement structure. Similar findings were observed for other base course thicknesses. It was estimated that geogrids will increase pavement life by two to four times in comparison to unreinforced sections.

2.3.4 Laboratory Investigation 4

A laboratory study was conducted at the University of Waterloo in Canada to determine the effectiveness of geogrid at various locations within the roadway structure (Carroll et al. (1987)). The asphalt thickness of the geogrid reinforced (TENSAR SS1) test sections ranged from 75 mm - 100 mm (3-4 in), and included a well graded gravel aggregate base course and a poorly graded sand subgrade. Layers were constructed inside a rectangular box that was 4.5 m (14.75 ft) by 1.8 m (5.9 ft) by 0.9 m (2.95 ft) deep. A 40 kN (9000 lb) load was applied through a 300 mm (12 in) diameter steel plate. A series of dynamic loads were applied at a frequency of 8 Hz followed by a single static load.

The testing program consisted of six loops to isolate certain parameters necessary to determine the benefits of geogrid reinforcement with respect to a control section. Loop 1 was constructed to examine geogrid performance in conjunction with a 200 mm (8 inch) base and a relatively firm subgrade (CBR of 8) with a 20 mm (0.8 in) rut depth failure criteria. Testing showed that the optimum location of the geogrid was in the lower half of the base.

The second loop (subgrade CBR of 4) was designed to determine if there would be a possible reduction in the base course thickness with a geogrid placed at the bottom of the base. For base course thickness of 100 mm - 200 mm (4-8 in), the base

thickness could be reduced by as much as 50% to achieve the same result with the inclusion of the geogrid.

The third loop was similar to the second, but the base course thicknesses ranged between 250 mm and 300 mm (10-12 in). The bottom of the base course was the optimum location for bases that were less than 250 mm (10 in) and the midpoint was the optimum location for thicker bases that were greater than 250 mm (10 in).

The remaining loops had a subgrade CBR of 1 and used a 38 mm (1.5 in) rut failure criteria. During loop 4, the geogrid reinforcement provided a threefold improvement to the pavement service life. During loop 5, the geogrid was pretensioned, and no additional benefits were observed. Finally, an additional layer of geogrid was placed at the center of the base course during loop 6, and this configuration carried 15,000 cycles, which was more than a threefold improvement with respect to the control section.

As a result of this testing, an empirical flexible pavement design procedure complete with a design chart was proposed. After calculating a structural number for the pavement system, corrections are applied for both laboratory scale effects and the inclusion of the geosynthetic.

2.3.5 Laboratory Investigation 5

A test loop was constructed at the Ministry of Defense in Sandleheath over a weak soil subgrade (ranging from 1-4) (Halliday and Potter (1984)). The quality of the test sections was questioned due to flooding conditions that existed during construction. The test section had a nominal asphalt thickness equal to 160 mm (6.4 in). According to the paper, variations in the asphalt thickness from section to section were accounted for while assessing the performance of the woven multifilament polyester fabrics used in the study. The base was constructed using 300 mm (12 in) granite. The sections were instrumented to measure vertical subgrade stress, vertical subgrade strain, transverse subgrade strain, and longitudinal-transverse strain at the bottom of the base. Thermocouples were also installed to monitor temperature. The traffic consisted of a 2 axle Leyland lorry with dual rear axle wheels. The tire pressure

was 760 kPa (110 psi), and the vehicle speed was 5-8 km/h (3.1-5.0 mph). The test section was loaded with approximately 74,000 standard axle loads.

Subgrade transient stress and strain were recorded and did not vary with fabric inclusion. Vertical compressive stress was recorded between approximately 15-50 kPa (2.17-7.25 psi), vertical compressive strain between 1,000-3,500 μm/m, and transverse tensile strain in the 200-1,100 μm/m range. Deflection measurements were also taken (90-350 mm x 10^{-2}) and were not influenced by fabric. Permanent vertical subgrade strains ranged from 0.06-0.40%, and permanent transverse subgrade strains were less than 0.01%. Deformation in the wheel path was also unaffected by the fabric; values ranged from approximately 1-25 mm (0.04-1 in) at 74,000 standard axles.

After loading the test section, 0.6 m (2 ft) wide areas were excavated to determine the condition of the fabric and control sections. The fabric did not suffer from any puncture damage and the base course aggregate penetrated approximately 70 mm (2.8 in) into the subgrade. It was concluded that the roadway was not affected by the presence of the fabric between the base and subgrade.

2.3.6 Laboratory Investigation 6

A comprehensive laboratory and computer modeling study was performed to determine the benefits of geogrid and geotextile inclusions placed at various locations within the flexible pavement structure (Barksdale et al. (1989)). A 25-38 mm (1.0-1.5 in) asphalt, 150 mm or 200 mm (6 in or 8 in) aggregate base, and a silty clay subgrade (CBR of approximately 2.5) layer was utilized for large-scale pavement testing. Geosynthetics were mainly located at the bottom and middle location of each base course layer. The loading was performed with a 7 kN (1.5 kip) wheel moving at 4.8 km/hr (3 mph). As many as 70,000 repetitions were applied at constant temperature.

The permanent vertical surface deformations were used to evaluate the test sections during the study. Inclusion of a stiff geotextile at the bottom of a weak base reduced rutting 44% in comparison to the control section (a 13% rut reduction was observed a higher quality base course layer). When the geotextile was relocated to the

middle of the stronger base, rut reduction increased from 13% to 28%. Furthermore, it was concluded that the inclusion of geosynthetics in the middle thin aggregate base layers was desired to reduce total permanent deformation. For weak subgrades the optimal location was found to be at or near the bottom of the base. Additionally, a geogrid with a modulus that was 2.5 times less outperformed a geotextile when placed at the middle of the base course layer. The superior performance of the geogrid was attributed to the ability of the geogrid apertures to interlock with the base and prevent lateral spreading. It was also shown that the geotextile required significantly higher deformations to generate equivalent reinforcement potential.

3. TEST SITE AND MATERIAL PROPERTIES

3.1 Site Location

The project test site runs parallel to US Highway 63 in eastern Arkansas and intersects Arkansas Highway 75 in Marked Tree, approximately halfway between Jonesboro, Arkansas (33 miles away) and Memphis, Tennessee (38 miles away). Marked Tree is located in the Gulf Coastal Plains area of northeast Arkansas. Crowley's Ridge lies to the west of the site and consists of rolling hills. Table 3.1 displays typical climate information for the area (obtained from the chamber of commerce in Trumann, which is approximately 15 miles from the site). Marked Tree is a relatively small town located in an agricultural area with a population of approximately 3,100.

This site was selected for this research project since it contained weak subgrade soils (due to the proximity of the Mississippi Delta). The location of the test site within the state of Arkansas is displayed in Figure 3.1 (inside District 10), and Figure 3.2 displays an illustration of the site prior to construction. A tractor trailer is traveling on the southbound lane of US Hwy 63 on the left side of the photograph, and the AR Hwy 75 overpass is just barely visible in the background of this photograph.

Prior to the construction of this frontage road, traffic entered Highway 63 directly from local businesses adjacent to this highway. Currently, traffic is forced to access US Hwy 63 at a controlled access point via AR Hwy 75 (Exit 14 on US Hwy 63). The frontage road dead ends and will, therefore, remain a low volume road. It was a small component of a larger Federal Aid Project HPP-1018(2) and was used for this Arkansas Highway and Transportation Department research project (TRC-0406). The research project originally consisted of thirteen test sections located between STA. 137+50 and STA. 144+00 (which was later modified due to the inclusion of additional Mirafi geosynthetic products). Each test section was 15.2 m (50 ft) in length, and a description of the test configuration and instrumentation is included in the following sections of this chapter.

Figure 3.1 – Test Site Location in Arkansas (District 10)

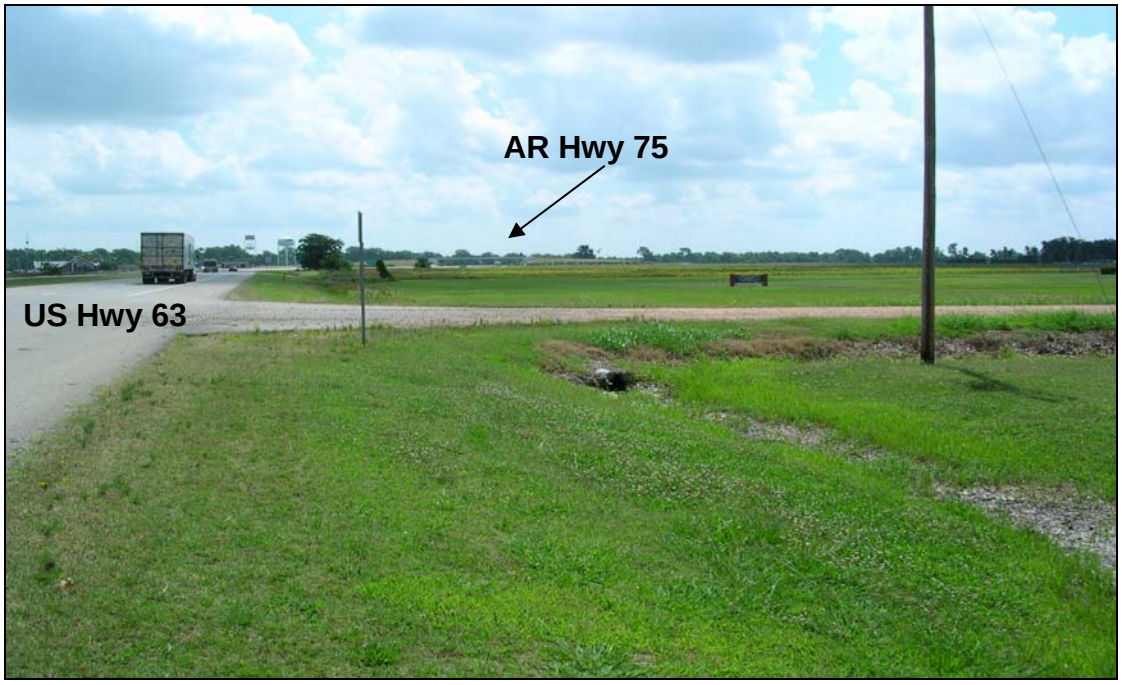

Figure 3.2 – Test Site Prior to Construction

Table 3.1 – Local Climate Information

Mean Daily Maximum Temperature	22 ^{0}C (72 ^{0}F)
Mean Daily Minimum Temperature	11^{0}C (52 ^{0}F)
Normal Annual Precipitation	1.25 m (50 in)
Normal Mean Daily Humidity (Noon)	57%
Normal Mean Daily Humidity (Midnight)	79%
Days with 0.25 mm (0.01 in) or More Precipitation	112
Days With Maximum Temperature 32 °C (90 °F) or More	53
Days With Minimum Temperature Under 10 °C (50 °F)	45

3.2 Soil Characterization

A subsurface exploration was conducted by the Arkansas Highway and Transportation Department (AHTD) in September of 2003 (the year before construction was anticipated) to obtain split spoon, Shelby tube, and bulk samples for laboratory index testing. Drilling was terminated 3 m (10 ft) below the existing ground surface and all borings were performed along the centerline of the road in the center of each of the 13 original test sections (with the exception of Section 7 since it was a transition section). Table 3.2 summarizes the standard Atterberg limit, specific gravity, select grain size, and USCS soil classification information from the auger bulk samples. Therefore, these values are considered to be an average for the entire depth of each boring. All tests were performed in accordance with ASTM specifications. In general, the soil had a plasticity index range from 35 to 54, was classified as a fat clay (CH), and was reasonably uniform across the site.

After the subgrade was brought to grade and properly compacted, an additional series of borings were performed in October of 2004. Shelby tube samples were obtained for the first 1.5 m (5 ft), but split spoon and bulk samples were retrieved for the entire 3 m (10 ft) depth. Both the on-site material and the material that was transported from a nearby borrow site were highly plastic with a fair amount of organic material and localized sandy pockets.

Table 3.3 summarizes the results of the Atterberg limit, specific gravity, standard Proctor, and CBR tests performed on a limited number of split spoon and Shelby tube samples obtained from the compacted subgrade in the fall of 2004. While the Atterberg limit and specific gravity data were similar to the previous data, the

slight variations in these values were attributed to the difference in sample type (bulk versus depth-specific). Similar to previous results, the percentage of fines (percent passing the No. 200 sieve) also ranged from approximately 75% to 88% for the only three sections tested (Sections 2, 6, and 12).

Table 3.2 –Laboratory Test Results from Bulk Samples

Section	*LL*	*PL*	*PI*	G_S	*% Sand*	*#200*	*ASTM Classification*
1	67	20	47	2.72	10.6	89.4	Fat Clay (CH)
2	63	21	41	2.69	12.3	87.7	Fat Clay (CH)
3	66	23	43	2.69	9.8	90.2	Fat Clay (CH)
4	66	20	47	2.68	14.7	85.3	Fat Clay (CH)
5	61	19	42	2.69	16.1	83.9	Fat Clay w/ Sand (CH)
6	63	17	46	2.69	17.0	83.0	Fat Clay w/ Sand (CH)
8	49	14	35	2.71	32.7	67.3	Sandy lean Clay (CL)
9	55	17	38	2.68	23.2	76.8	Fat Clay w/ Sand (CH)
10	60	17	43	2.67	16.4	83.6	Fat Clay w/ Sand (CH)
11	61	18	43	2.71	14.3	85.7	Fat Clay (CH)
12	62	17	45	2.71	12.2	87.8	Fat Clay (CH)
13	73	20	54	2.71	11.0	89.0	Fat Clay (CH)
2	49	19	30	2.71	15.9	84.1	Lean Clay w/ Sand (CL)
6	50	18	32	2.72	22.5	77.5	Fat Clay w/ Sand (CH)
12	57	21	36	2.73	11.6	88.4	Fat Clay (CH)

Additionally, Standard Proctor tests were performed by an independent testing agency associated with the roadway contractor using bulk samples obtained from the

borrow pit used to build the compacted subgrade. The maximum dry unit weight measured 16.89 kN/m^3 (107.4 pcf) and 16.20 kN/m^3 (103.0 pcf) and the corresponding optimum moisture content values were 16.8% and 20.4%, respectively. The majority of the testing that was performed from this point forward was performed on samples obtained from Section 13 since this section was relatively homogeneous with depth. Therefore, the maximum dry unit weight reported in Table 3.3 for Section 13 (16.67 kN/m^3) was used to obtain the CBR values reported in the same table. This value also corresponded well with the values measured independently by the contractor. CBR values equal to 1.66 and 1.38 were interpolated from a test plot that displayed soaked CBR as a function of dry density so the representative soaked CBR range was approximately 1-2. All tests were performed in accordance with ASTM specifications with the exception of the CBR test, which was performed using AASHTO T193-99.

Table 3.3 – Laboratory Test Results from Split Spoon and Shelby Tube Samples

Section	*Depth (cm)*	*LL*	*PL*	*PI*	*SG*	γ_{dry} *(kN/m^3)*	*OMC*	*Soaked CBR*
1	15-60	49.3	19.1	30.2	-	16.10	19.5%	1.66
1	76-122	76.1	24.5	51.6	-			
7	15-60	50.3	18.5	31.9	-	-	-	-
7	76-122	-	-	NP	-	-	-	-
13	15-60	56.7	20.5	36.2	-	16.67	16.8 %	1.38
13	76-122	42.6	16.5	26.1	-			
2	15-60	-	-	-	2.71	-	-	-
6	15-60	-	-	-	2.72	-	-	-
12	15-60	-	-	-	2.73	-	-	-

Table 3.4 displays the nuclear gauge results (obtained by the AHTD) for the compacted subgrade in the fall of 2004 and summer of 2005. AHTD took a measurement at three locations around the point of interest in each test section and the values in Table 3.4 represent the average of those three values. Note that the field conditions in 2004 were slightly different than the 2005 field conditions due to construction problems experienced in 2004. The contractor was unable to complete

construction of the frontage road before the end of the 2004 construction season so the previously installed earth pressure cells and environmental instrumentation had to be removed from the subgrade and the subgrade had to be re-worked in the summer of 2005. Based on all available information, the June 2005 values were deemed unreliable and not used in any further analysis.

Triaxial and resilient modulus tests were performed using Shelby tube samples obtained from three different depths in each of the control sections (Sections 1 and 13) during both subsurface explorations (a total of six different sampling locations). However, all material had to be remolded due to the length of time between sampling and testing, and the need to re-work the subgrade in the summer of 2005. Figure 3.3 displays the depths of the six testing zones with respect to final grade. For future reference, zones 1 and 2 were considered to be compacted subgrade, zones 3 and 4 were considered to be upper natural ground, and zones 5 and 6 were considered to be lower natural ground. All samples were prepared in a 69.6 mm x 142.4 mm (2.74 in x 5.6 in) split mold using three layers, and the compaction energy was adjusted depending upon the desired unit weight and moisture content. The samples were stored in plastic and foil in a chilled environment (to allow hydration) prior to testing.

Table 3.4 – Subgrade Nuclear Gauge Readings

Station	*Section*	*October 2004*		*June 2005*	
		γ_d *kN/m³ (pcf)*	*w%*	γ_d *kN/m³ (pcf)*	*w%*
137+75	1	16.40 (104.3)	11.8	18.68 (118.8)	10.6
138+25	2	16.42 (104.4)	11.4	18.25 (116.1)	10.5
138+75	3	15.91 (101.2)	15.4	18.02 (114.6)	11.7
139+25	4	15.93 (101.3)	18.3	17.53 (111.5)	12.3
139+75	5	15.06 (95.8)	19.3	17.28 (109.9)	11.5
140+25	6	15.39 (97.9)	19.3	17.44 (110.9)	12.2
140+75	7	15.33	12.8	16.87	12.4

		(97.5)		(107.3)	
141+25	8	16.04	12.5	17.44	12.6
		(102.0)		(110.9)	
141+75	9	15.68	12.1	18.10	12.3
		(99.7)		(115.1)	
142+25	10	15.75	15.1	17.67	12.2
		(100.2)		(112.4)	
142+75	11	15.36	16.0	17.14	13.4
		(97.7)		(109.0)	
143+25	12	15.31	14.2	17.00	13.7
		(97.4)		(108.1)	
143+75	13	15.86	12.3	17.00	15.7
		(100.9)		(108.1)	

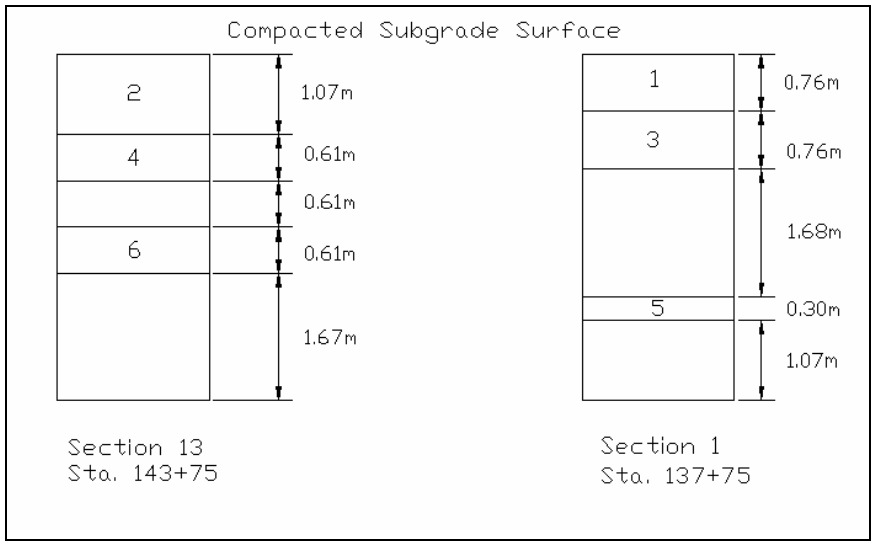

Figure 3.3 – Soil Sample Locations for Strength Testing

The dry unit weights associated with the upper natural ground (13.4 kN/m^3) and lower natural ground (14.9 kN/m^3) were measured from undisturbed samples that were trimmed in a consolidation ring. As stated previously, the maximum dry unit weight measured in Section 13 was 16.67 kN/m^3 (Table 3.3). Therefore, the dry unit weight and optimum moisture content associated with the compacted zone in Figure 3.3 (15.84 kN/m^3 and 16.8, respectively) was determined using a 95% relative compaction (as specified by AHTD).

Advanced soil testing of the compacted subgrade was performed at moisture contents ranging from optimum to 120% of optimum (105-120% of optimum is

typical in the field). Testing of the upper natural ground was performed at moisture contents ranging from optimum to 150% of optimum, and the lower natural ground value was a constant 30% (based on field sampling results).

3.3 UU Triaxial Testing

Unconsolidated Undrained (UU) triaxial testing was performed (according to AASHTO T307) at a rate of 1% per minute until the test reached 15% strain with the exception of the sample from Zone 3 (Figure 3.3), which terminated at 6.6% strain. The confining pressures were 20.7 kPa (3 psi) for the compacted subgrade, 27.6 kPa (4 psi) for the upper natural ground, and 34.5 kPa (5 psi) for the lower natural ground. A total of 11 UU triaxial tests were performed on soil obtained from Section 13, and a total of 6 tests were performed on soil obtained from Section 1. The previously described unit weight and moisture content values for each soil zone (Figure 3.3) were used to re-mold the test specimens.

Figure 3.4 illustrates an example of the stress-strain plot generated from a UU triaxial test conducted on soil from Zone 2 in Figure 3.3. Table 3.5 summarizes the results of all UU triaxial testing performed. Initial tangent stiffness values and secant stiffness values (at 2%, 3%, and 5% strain) were also calculated for each test (available upon request). After a visual examination of the tested samples, it was determined that samples with a higher unit weight tended to experience classic shear failures at lower moisture contents. As the moisture content increased, the shear planes became less apparent, resulting in more of a bulge. Samples compacted at lower unit weights did not have a defined shear failure plane.

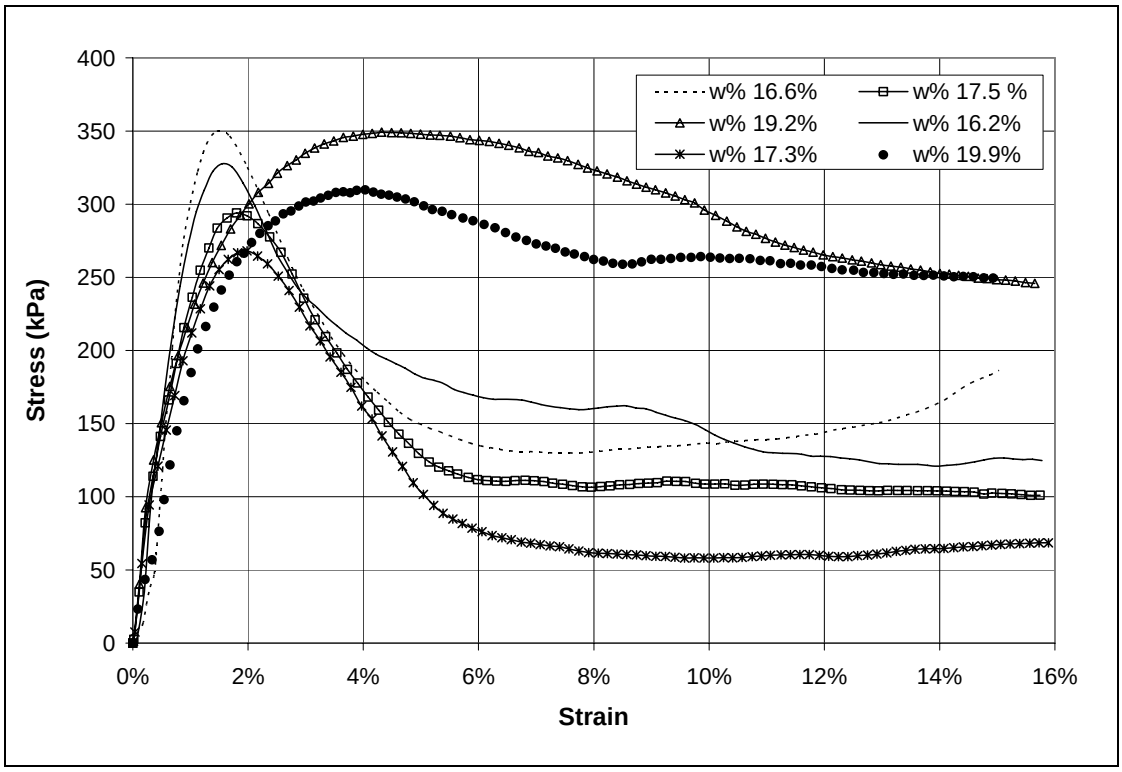

Figure 3.4 – UU Triaxial Results for a Soil Obtained from Zone 2

3.4 CU Triaxial Testing

Three specimens from Zone 2 (Figure 3.3) were consolidated using 172.4 kPa (25 psi), 103.4 kPa (15 psi), and 68.9 kPa (10 psi) confining pressures. Consolidated Undrained (CU) triaxial tests were subsequently performed on back pressure saturated specimens while measuring the deviator stress, confining pressure, and pore water pressure to develop a Mohr-Coulomb failure envelope using effective stress properties. Figure 3.5 displays an example of the results from the CU triaxial tests. None of the samples displayed distinct failure planes (only a bulge was visible). The angle of internal friction was determined to be 7° for this relatively weak clay in Zone 2, which fits well with the 3-20° clay range reported by Bowles (1996). The soil also had a 12.8 kPa (1.85 psi) cohesion value.

Table 3.5 –Unconsolidated Undrained Testing Results

Zone	*w%*	*Stress Value kPa (psi)*			
		2% Strain	*3% Strain*	*5% Strain*	*Maximum*
1	15.5	196.5	172.4	115.8	197.2 (28.6) at

		(28.5)	(25.0)	(16.8)	1.7%
1	16.5	227.5 (33.0)	184.1 (26.7)	143.4 (20.8)	229.6 (33.3) at 1.8%
1	18.4	198.5 (28.8)	209.6 (30.4)	215.1 (31.2)	215.1 (31.2) at 5.0%
1	19.9	152.4 (22.1)	164.1 (23.8)	176.5 (25.6)	191.7 (27.8) at 11.8%
2	16.2	308.2 (44.7)	236.5 (34.3)	182.7 (26.5)	327.5 (47.5) at 1.5%
2	16.6	325.4 (47.2)	238.5 (34.6)	149.6 (21.7)	350.2 (50.8) at 1.5%
2	17.3	267.5 (38.8)	222.7 (32.3)	103.4 (15.0)	268.2 (38.9) at 1.9%
2	17.5	292.3 (42.4)	233.7 (33.9)	128.9 (18.7)	293.7 (42.6) at 1.8%
2	19.2	299.2 (43.4)	335.0 (48.6)	348.1 (50.5)	348.8 (50.6) at 4.5%
2	19.9	270.2 (39.2)	301.3 (43.7)	301.3 (43.7)	309.5 (44.9) at 4.0%
3	27.0	117.2 (17.0)	122.7 (17.8)	121.3 (17.6)	123.4 (17.9) at 4.0%
4	16.6	144.8 (21.0)	145.5 (21.1)	142.0 (20.6)	146.2 (21.2) at 2.5%
4	19.0	95.8 (13.9)	77.9 (11.3)	61.4 (8.9)	104.1 (15.1) at 1.3%
4	20.7	87.6 (12.7)	93.1 (13.5)	101.3 (14.7)	112.4 (16.3) at 7.8%
4	25.6	71.7 (10.4)	74.5 (10.8)	77.9 (11.3)	87.6 (12.7) at 12.3%
5	29.0	33.8 (4.9)	36.5 (5.3)	40.7 (5.9)	50.3 (7.3) at 15.0%
6	28.1	242.7 (35.2)	261.3 (37.9)	275.8 (40.0)	282.7 (41.0) at 7.5%

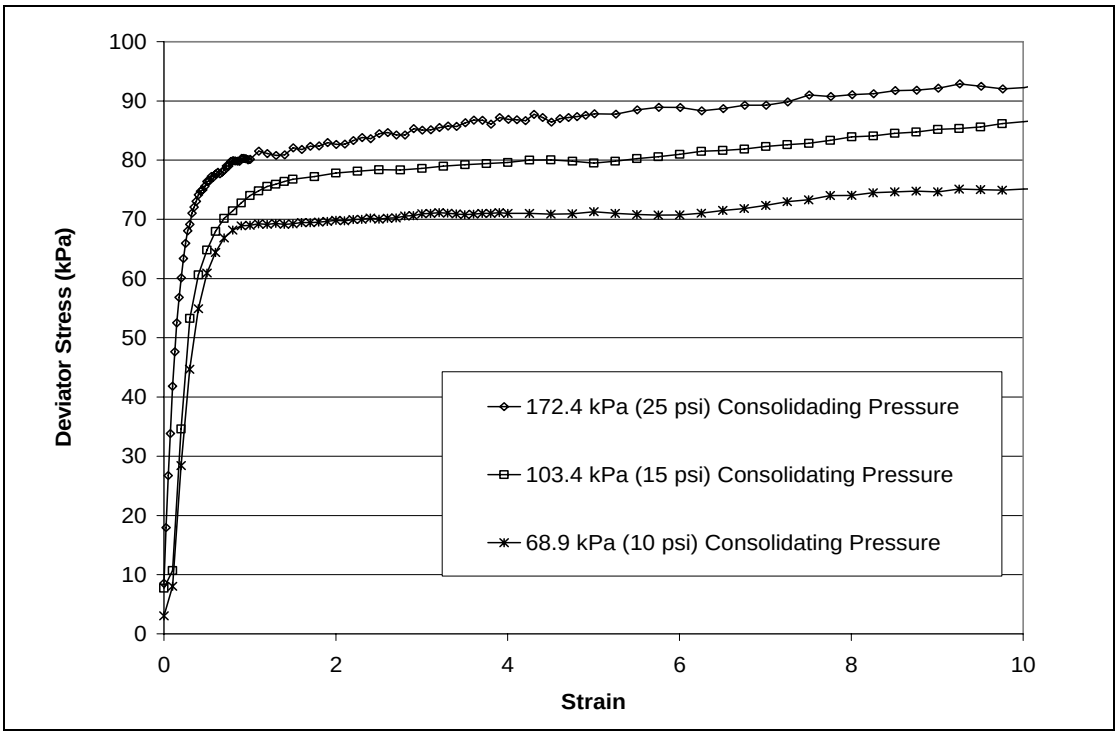

Figure 3.5 – CU Triaxial Results for Soil Obtained in Zone 2

3.5 Resilient Modulus

A total of 10 resilient modulus tests were performed on samples obtained from Section 13 and five tests were performed on samples from Section 1 (according to AASHTO T307). Testing was performed in all soil zones (Figure 3.3) with the exception of Zone 5. An example resilient modulus test plot for Zone 4 is displayed in Figure 3.6 (each curve represents a different confining pressure), and a summary of the results are displayed in Tables 3.6 – 3.8. The data did appear to be somewhat variable, especially at a deviator stress of 12.4 kPa (1.8 psi). Five data points were not retrieved at this level of stress and select data were considered questionable based on engineering judgment. There appeared to be more of a variability in the compacted subgrade than there was in the lower zones. A stress softening behavior was observed and the magnitudes of the readings appeared to be reasonable. Note that the stiffness values provided by the resilient modulus tests were always greater than the stiffness values measured during triaxial testing at any given moisture content.

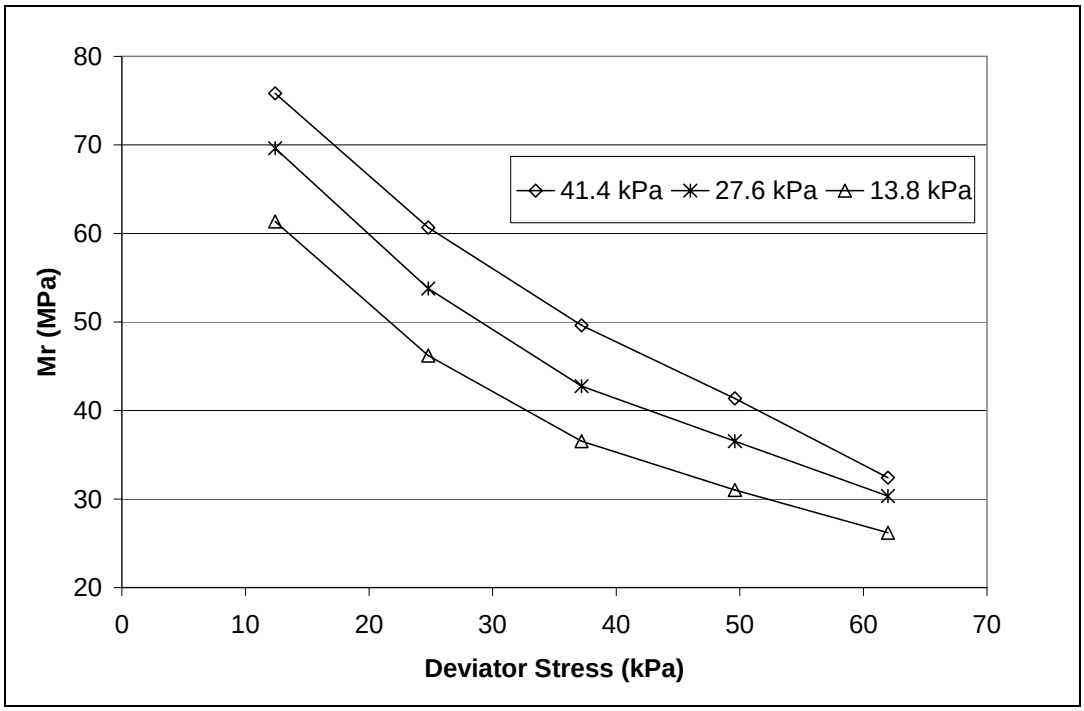

Figure 3.6 – Resilient Modulus Test Results for Zone 4 (20.7% Water Content)

Table 3.6 – Resilient Modulus Test Results for Section 1

Deviator Stress kPa (psi)	*Confining Pressure kPa (psi)*	*Zone 1 w% 15.5% Mr MPa (ksi)*	*Zone 1 w% 16.5% Mr MPa (ksi)*	*Zone 1 w% 18.4% Mr MPa (ksi)*	*Zone 1 w% 19.9% Mr MPa (ksi)*	*Zone 3 w% 27.0% Mr MPa (ksi)*
12.4 (1.8)	41.4 (6.0)	113.1 (16.4)	154.4 (22.4)	164.8 (23.9)	126.2 (18.3)	88.9 (12.9)
24.8 (3.6)	41.4 (6.0)	100.7 (14.6)	142.7 (20.7)	140.6 (20.4)	115.8 (16.8)	71.0 (10.3)
37.2 (5.4)	41.4 (6.0)	88.9 (12.9)	132.4 (19.2)	131.7 (19.1)	102.7 (14.9)	60.7 (8.8)
49.6 (7.2)	41.4 (6.0)	81.4 (12.2)	119.3 (17.3)	116.5 (16.9)	91.7 (13.3)	53.1 (7.7)
62.0 (9.0)	41.4 (6.0)	78.6 (11.4)	101.3 (14.7)	105.5 (15.3)	81.3 (11.8)	46.2 (6.7)
12.4 (1.8)	27.6 (4.0)	108.2 (15.7)	108.9 (15.8)	151.7 (22.0)	123.4 (17.9)	86.9 (12.6)
24.8 (3.6)	27.6 (4.0)	97.9 (14.2)	91.0 (13.2)	130.3 (18.9)	100.7 (14.6)	66.2 (9.6)
37.2 (5.4)	27.6 (4.0)	85.5 (12.4)	78.6 (11.4)	113.8 (16.5)	89.6 (13.0)	56.5 (8.2)
49.6 (7.2)	27.6 (4.0)	82.7 (12.0)	76.5 (11.1)	102.7 (14.9)	80.0 (11.6)	49.6 (7.2)

62.0 (9.0)	27.6 (4.0)	80.0 (11.6)	75.8 (11.0)	97.2 (14.1)	74.5 (10.8)	42.7 (6.2)
12.4 (1.8)	13.8 (2.0)	97.9 (14.2)	91.0 (13.2)	130.3 (18.9)	109.6 (15.9)	No Data
24.8 (3.6)	13.8 (2.0)	95.8 (13.9)	75.8 (11.0)	108.9 (15.8)	86.2 (12.5)	57.9 (8.4)
37.2 (5.4)	13.8 (2.0)	88.9 (12.9)	73.8 (10.7)	95.1 (13.8)	74.5 (10.8)	48.9 (7.1)
49.6 (7.2)	13.8 (2.0)	83.4 (12.1)	72.4 (10.5)	88.9 (12.9)	68.3 (9.9)	42.7 (6.2)
62.0 (9.0)	13.8 (2.0)	80.7 (11.7)	73.8 (10.7)	78.6 (11.4)	62.7 (9.1)	37.2 (5.4)

Table 3.7 – Resilient Modulus Test Results for Section 13 (Compacted Subgrade)

Deviator Stress kPa (psi)	*Confining Pressure kPa (psi)*	*Zone 2 w% 16.2% Mr MPa (ksi)*	*Zone 2 w% 16.6% Mr MPa (ksi)*	*Zone 2 w% 17.3% Mr MPa (ksi)*	*Zone 2 w% 17.5% Mr MPa (ksi)*	*Zone 2 w% 19.2% Mr MPa (ksi)*
12.4 (1.8)	41.4 (6.0)	128.9 (18.7)	No Data	86.2 (12.5)	87.6 (12.7)	158.6 (23.(
24.8 (3.6)	41.4 (6.0)	117.9 (17.1)	152.4 (22.1)	72.4 (10.5)	70.3 (10.2)	144.1 (20.9)
37.2 (5.4)	41.4 (6.0)	109.6 (15.9)	168.2 (24.4)	69.6 (10.1)	69.6 (10.1)	133.1 (19.3)
49.6 (7.2)	41.4 (6.0)	97.2 (14.1)	164.8 (23.9)	69.6 (10.1)	69.6 (10.1)	125.5 (18.2)
62.0 (9.0)	41.4 (6.0)	92.4 (13.4)	166.1 (24.1)	67.6 (9.8)	69.6 (10.1)	120.0 (17.4)
12.4 (1.8)	27.6 (4.0)	80.7 (11.7)	191.0 (27.7)	86.2 (12.5)	92.4 (13.4)	157.2 (22.8)
24.8 (3.6)	27.6 (4.0)	69.6 (10.1)	168.2 (24.4)	74.5 (10.8)	77.9 (11.3)	137.9 (20.0)
37.2 (5.4)	27.6 (4.0)	71.7 (10.4)	159.3 (23.1)	68.3 (9.9)	70.3 (10.2)	124.8 (18.1)
49.6 (7.2)	27.6 (4.0)	74.5 (10.8)	156.5 (22.7)	66.9 (9.7)	70.3 (10.2)	114.4 (16.6)
62.0 (9.0)	27.6 (4.0)	81.3 (11.8)	151.0 (21.9)	68.3 (9.9)	71.0 (10.3)	109.6 (15.9)
12.4 (1.8)	13.8 (2.0)	80.0 (11.6)	124.1 (18.0)	86.9 (12.6)	82.0 (11.9)	131.0 (19.0)
24.8 (3.6)	13.8 (2.0)	68.3 (9.9)	96.5 (14.0)	75.1 (10.9)	77.2 (11.2)	111.7 (16.2)
37.2 (5.4)	13.8 (2.0)	69.6 (10.1)	94.4 (13.7)	68.3 (9.9)	68.9 (10.0)	104.8 (15.2)
49.6 (7.2)	13.8 (2.0)	75.1 (10.9)	100.0 (14.5)	67.6 (9.8)	70.3 (10.2)	101.3 (14.7)
62.0 (9.0)	13.8 (2.0)	80.0 (11.6)	104.1	68.9	71.7	91.0

(15.1) (10.0) (10.4) (13.2)

Table 3.8 - Resilient Modulus Test Results for Section 13 (Natural Subgrade)

Deviator Stress kPa (psi)	*Confining Pressure kPa (psi)*	*Zone 4 w% 16.6% Mr MPa (ksi)*	*Zone 4 w% 19.0% Mr MPa (ksi)*	*Zone 4 w% 20.7% Mr MPa (ksi)*	*Zone 4 w% 25.6% Mr MPa (ksi)*	*Zone 6 w% 28.1% Mr MPa (ksi)*
12.4 (1.8)	41.4 (6.0)	126.2 (18.3)	97.2 (14.1)	75.8 (11.0)	65.5 (9.5)	126.2 (18.3)
24.8 (3.6)	41.4 (6.0)	106.9 (15.5)	80.0 (11.6)	60.7 (8.8)	38.6 (5.6)	89.6 (13.0)
37.2 (5.4)	41.4 (6.0)	97.9 (14.2)	72.4 (10.5)	49.6 (7.2)	27.6 (4.0)	77.2 (11.2)
49.6 (7.2)	41.4 (6.0)	86.9 (12.6)	55.8 (8.1)	41.4 (6.0)	18.6 (2.7)	73.8 (10.7)
62.0 (9.0)	41.4 (6.0)	77.2 (11.2)	50.3 (7.3)	32.4 (4.7)	18.6 (2.7)	77.9 (11.3)
12.4 (1.8)	27.6 (4.0)	122.7 (17.8)	No Data	69.6 (10.1)	49.6 (7.2)	90.3 (13.1)
24.8 (3.6)	27.6 (4.0)	104.1 (15.1)	73.1 (10.6)	53.8 (7.8)	29.6 (4.3)	76.5 (11.1)
37.2 (5.4)	27.6 (4.0)	90.3 (13.1)	62.7 (9.1)	42.7 (6.2)	20.7 (3.0)	70.3 (10.2)
49.6 (7.2)	27.6 (4.0)	80.0 (11.6)	53.8 (7.8)	36.5 (5.3)	15.2 (2.2)	68.3 (9.9)
62.0 (9.0)	27.6 (4.0)	67.6 (9.8)	46.9 (6.8)	30.3 (4.4)	16.5 (2.4)	64.1 (9.3)
12.4 (1.8)	13.8 (2.0)	106.9 (15.5)	No Data	61.4 (8.9)	No Data	108.9 (15.8)
24.8 (3.6)	13.8 (2.0)	88.2 (12.8)	64.8 (9.4)	46.2 (6.7)	24.8 (3.6)	78.6 (11.4)
37.2 (5.4)	13.8 (2.0)	76.5 (11.1)	55.8 (8.1)	36.5 (5.3)	16.5 (2.4)	75.8 (11.0)
49.6 (7.2)	13.8 (2.0)	72.4 (10.5)	46.2 (6.7)	31.0 (4.5)	15.9 (2.3)	73.1 (10.6)
62.0 (9.0)	13.8 (2.0)	60.7 (8.8)	42.7 (6.2)	26.2 (3.8)	15.2 (2.2)	68.3 (9.9)

3.6 FWD Testing

Loading scheme, climate, and pavement variability affects the results of non-destructive FWD deflection testing (Huang, 1993; Bhutta, 1998). Pavement response to load is typically non-linear so there is a need for precise knowledge of the load amplitude and frequency. Temperature effects (if accounted for) are typically addressed using procedures reported by Kim et al. (1995) or Park et al. (2002). Numerous procedures are currently available to back-calculate pavement layer and subgrade moduli (MODULUS, WESDEF, BOUSDEF, and ELMOD are just a few). Most programs use a convergence or optimization technique using either closed form solutions or numerical solutions based on static elastic layer theory. Nishizawa et al. (1994) discussed the use of a numerical solution based on static elastic layer theory and determine that this type of static analysis was adequate to characterize the dynamic FWD load-pulse for the purpose of material property determination. According to Suits and Koerner (2001), FWD data used to back-calculate stiffness moduli can vary as much as $\pm$ 6,900 kPa (1,000 psi) assuming operator consistency.

In this study, ROADHOG (Hall and Elliott, 1992) was used to determine the resilient modulus of the subgrade using ILLI-PAVE, which is a finite element analysis program. The procedure does not directly account for pavement temperature, thickness, or the finite depth of the subgrade. However, the use of a finite element based algorithm to produce primarily finite element input data appeared to be more sound than other approaches that incorporate the drawbacks of elastic layer theory. Table 3.9 summarizes the subgrade resilient modulus values back-calculated for all four field testing phases using this method.

The moduli reported in Table 3.9 for Sections 8-13 were generally higher than those values reported for Sections 1-6. This observation qualitatively compares well with previously discussed results obtained from soil testing in Sections 1 and 13. Namely, Section 13 had a higher cohesion (by approximately 33%), a slightly higher dry unit weight, and a lower optimum moisture content (16.8% versus 19.5%) in comparison to Section 1 values.

Field calculated resilient modulus averages (Table 3.9) also compare well with laboratory measured resilient modulus averages (Tables 3.6 and 3.7) representative of

the same conditions (higher deviator stresses and lower laboratory confining pressures). For a deviator stress equal to 62.0 kPa and a confining pressure equal to 13.8 kPa in Table 3.6 (the values most representative of field conditions), the average resilient modulus value for all water contents in Zone 1 of Section 1 was approximately 74.0 MPa (10.7 ksi). For the same stress state, the average resilient modulus value for all water contents in Zone 2 of Section 13 was approximately 83.1 kPa (12.1 ksi). Similarly, the average back-calculated field values displayed in Table 3.9 were 65.0 MPa (9.4 ksi) for Section 1 and 81.6 MPa (11.8 ksi) for Section 13.

Table 3.9 – Subgrade Resilient Modulus Values Back-Calculated from FWD Data

Test Phase		*September 2005*	*December 2005*	*December 2005*	*February 2006*
Section	*Target Load KN (kips)*	*Mr MPa (ksi)*	*Mr MPa (ksi)*	*Mr MPa (ksi)*	*Mr MPa (ksi)*
13	26.7 (6)	85.6 (12.4)	81.3 (11.8)	81.9(11.9)	81.2 (11.8)
	40.0 (9)	81.3 (11.8)	84.3 (12.2)	81.9(11.9)	81.2 (11.8)
	53.4 (12)	78.9 (11.4)	81.3 (11.8)	79.5 (11.5)	81.2 (11.8)
12	26.7 (6)	74.8 (10.9)	68.0 (9.9)	81.9 (11.9)	88.7 (12.9)
	40.0 (9)	74.2 (10.8)	72.5 (10.5)	79.5 (11.5)	92.5 (13.4)
	53.4 (12)	72.5 (10.5)	68.0 (9.9)	75.9 (11.0)	89.9 (13.1)
11	26.7 (6)	82.5 (12.0)	73.6 (10.7)	74.8 (10.8)	84.9 (12.3)
	40.0 (9)	81.9 (11.9)	78.3 (11.4)	74.8 (10.8)	85.5 (12.4)
	53.4 (12)	80.1 (11.6)	73.6 (10.7)	71.3 (10.3)	84.3 (12.2)
10	26.7 (6)	63.7 (9.2)	71.3 (10.3)	77.1 (11.2)	86.2

					(12.5)
	40.0 (9)	64.2 (9.3)	71.3 (10.3)	77.7 (11.3)	89.9 (13.1)
	53.4 (12)	63.2 (9.2)	71.3 (10.3)	75.9 (11.0)	89.9 (13.1)
	26.7 (6)	90.2 (13.1)	88.1 (12.8)	83.1 (12.1)	85.5 (12.4)
9	40.0 (9)	86.8 (12.6)	88.8 (12.9)	83.1 (12.1)	88.7 (12.9)
	53.4 (12)	84.9 (12.3)	88.1 (12.8)	83.1 (12.1)	89.3 (13.0)
	26.7 (6)	88.2 (12.8)	88.1 (12.8)	83.1 (12.1)	81.8 (11.9)
8	40.0 (9)	88.1 (12.8)	90.6 (13.1)	83.1 (12.1)	83.1 (12.1)
	53.4 (12)	87.4 (12.7)	88.1 (12.8)	83.1 (12.1)	85.5 (12.4)
	26.7 (6)	66.9 (9.7)	66.9 (9.7)	66.4 (9.6)	70.8 (10.3)
6	40.0 (9)	64.7 (9.4)	69.1 (10.0)	64.8 (9.4)	70.2 (10.2)
	53.4 (12)	62.1 (9.0)	66.9 (9.7)	63.7 (9.2)	68.0 (9.9)
	26.7 (6)	61.1 (8.9)	63.2 (9.2)	63.7 (9.2)	64.8 (9.4)
5	40.0 (9)	62.1 (9.0)	67.6 (9.8)	60.6 (8.8)	61.1 (8.9)
	53.4 (12)	61.6 (8.9)	63.2 (9.2)	57.5 (8.3)	55.0 (8.0)
	26.7 (6)	62.1 (9.0)	65.8 (9.5)	72.5 (10.5)	75.4 (10.9)
4	40.0 (9)	59.6 (8.6)	63.7 (9.2)	69.1 (10.0)	74.2 (10.8)
	53.4 (12)	56.5 (8.2)	65.8 (9.5)	65.3 (9.5)	69.6 (10.1)
	26.7 (6)	68.5 (9.9)	65.3 (9.5)	70.8 (10.3)	79.4 (11.5)
3	40.0 (9)	66.4 (9.6)	70.2 (10.2)	68.6 (10.0)	76.5 (11.1)
	53.4 (12)	63.7 (9.2)	65.3 (9.5)	65.9 (9.6)	71.9 (10.4)
	26.7 (6)	69.1 (10.0)	70.2 (10.2)	79.5 (11.5)	81.3 (11.8)
2	40.0 (9)	68.5 (9.9)	74.2 (10.8)	77.1 (11.2)	78.2 (11.4)
	53.4 (12)	66.4 (9.6)	70.2 (10.2)	73.0 (10.6)	77.1 (11.2)
	26.7 (6)	59.6 (8.6)	59.0 (8.6)	69.1 (10.0)	74.9 (10.9)
1	40.0 (9)	58.0 (8.4)	63.8 (9.3)	68.6 (9.9)	74.3 (10.8)
	53.4 (12)	55.1 (8.0)	59.0 (8.6)	65.8 (9.5)	72.5 (10.5)

3.7Crushed Stone (Base Course)

Table 3.10 contains some of the relevant properties of the crushed stone (AHTD Class 7 aggregate) used in the base course. Most of the property data were either obtained from the quarry that was used, from strength testing that was performed on material of the same class designation and quarry by Welcher (2004), or from additional references (Bowles, 1996; Gonzalez, 1994).

Additionally, George and Shah (1974) studied crushed limestone that had a gradation commonly used in flexible pavements for the purpose of observing the dilatency of the material in drained triaxial shear (a necessary parameter for numerical analysis of this problem). The angle of dilatency for this project was estimated using this source in conjunction with Figure 3.21(b) of the Plaxis Reference Manual (Brinkgreve et al., 2002), which is not displayed herein. Additional details regarding the properties listed in Table 3.10 are available upon request.

Finally, the base course resilient modulus was determined in accordance with AASHTO T307 by colleagues at the University of Arkansas and can be described by Equation 3.1 ($R^2 = 0.8966$).

$$M_r = 2.5983(\theta)^{0.7081} \quad (3.1)$$

Where,

M_r = Resilient Modulus (ksi)

θ = Bulk Stress (psi)

Table 3.10 - Crushed Stone Properties

Property	*Value*
Dry Unit Weight (Modified Proctor)	22.39-22.64 kN/m^3 (142.4-144.0 pcf)
Dry Unit Weight (Nuclear Density)	23.35-23.63 kN/m^3 (148.5-150.3 pcf)
Percent Passing 38 mm (1.5 in) Sieve	100%
Specific Gravity	2.80 – 2.81
Friction Angle	43°
Geology	Dolomite
Cohesion	41.4 kPa (6 psi)
Plasticity	Non-plastic
Fines	9.3%

Angle of Dilatency	7°
Optimum Moisture	6.5% - 8.2%

3.8 Asphalt Concrete Properties

Table 3.11 contains all pertinent asphalt concrete properties. Many of the properties were necessary to characterize the dynamic asphalt stiffness modulus (E^*), which was necessary for the numerical analysis portion of this project. The dynamic modulus (E^*) incorporates the asphalt temperature, loading rate, age, and mix design characteristics into a Master Curve based on Witczak's Equation and the procedures of NCHRP 1-37a. Many of the properties in Table 3.11 were obtained directly from the mix design (VMA, All Gradations, P_b, G_{mm}, and Binder Grade). However, both VMA and P_b were also measured from loose material obtained at the asphalt manufacturing plant prior to paving. It should be noted that the measured values did not vary enough from the mix design values to warrant property adjustments. However, the design air void content (4.5%) varied significantly from the cores obtained from the field and tested by the research team.

Table 3.11 – Asphalt Concrete Material Properties

Input	*Units*	*Value Used*
Loading Frequency (f)	Hz	Variable
Asphalt Mat Temperature (T_R)	°C (°F)	Variable
In Place Air Void Content (V_a)*	%	9.3
Voids in Mineral Aggregate (VMA)	%	14.9
Effective Bitumen Content (V_{beff} = VMA-V_a)	%	5.6
Cumulative % Retained on 19 mm (3/4 in) Sieve ($P_{3/4}$)	%	0
Cumulative % Retained on 9.5 mm (3/8 in) Sieve ($P_{3/8}$)	%	16
Cumulative % Retained on No. 4 Sieve (P_{No4})	%	42
Percent Passing No. 200 Sieve (P_{No200})	%	4.9
Asphalt Content (P_b)	%	5.4
Asphalt Volume (V_b)	%	11.5
Maximum Theoretical Specific Gravity (G_{mm})	-	2.405
CORELOCK™ Bulk Specific Gravity (G_{mb})*	-	2.182
Regression Intercept**	-	10.98
Regression Slope**	-	-3.68

* *Average value determined by testing two cores taken from a test section*

*** Related to Binder Grade (PG 64-22)*

3.9 Test Configuration

The original test configuration consisted of thirteen sections and each test section was 15.2 m (50 ft) in length. The geosynthetic configuration for the first six sections was a mirror image of the configuration in the last six test sections, which were separated by a transition section in the middle. The purpose of the middle test section was to transition a 25.4 cm (10 in) thick base course layer to a 15.2 cm (6 in) thick base course layer. The test sections were constructed with a 5.1 cm (2 in) thick asphalt concrete hot-mix (ACHM) mat, and either 15.2 cm (6 in) or 25.4 cm (10 in) of AHTD Class 7 aggregate base course.

Prior to construction, two MIRAFI Construction Products were added to the study. A MIRAFI geotextile and geogrid were both placed at each end of the test section to evaluate performance for each base course thickness. These test sections were identified as Sections 1a, 1b, 13a, and 13b. Therefore, the final test configuration consisted of seventeen test sections in the southbound lane of the frontage road (displayed in Figure 3.7) and the geosynthetics included: 1) MIRAFI HP 5270 woven geotextiles, 2) Propex 2044 woven geotextiles, 3) Propex 2006 woven geotextiles, 4) Propex 4553 nonwoven geotextiles, 5) MIRAFI BasXGrid 11 geogrids, and 6) Tensar BX 1200 biaxial geogrids. These materials were selected to encompass a wide range of geosynthetic properties to aid in establishment of the governing performance mechanism.

A profile view of the test configuration is displayed in Figure 3.8, which displays the symmetry of the test configuration about the transition section (Section 7). Details regarding the instrumentation will be discussed in the following chapter. Figure 3.7 also displays the general configuration of the permanent cable protection system and the location of the two data acquisition enclosures, which was adjacent to test section 7. Standard sewer and drain pipe (10.2 cm (4 in) in diameter) was used to house and protect the instrumentation cable.

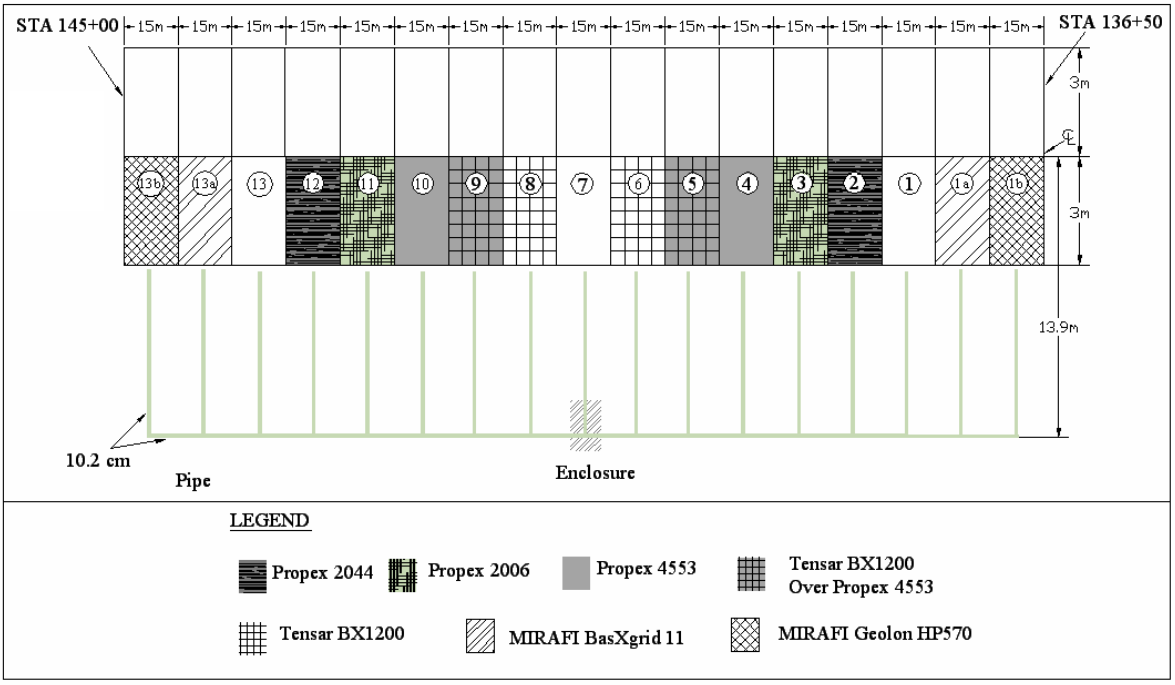

Figure 3.7 – Plan View of the Test Configuration

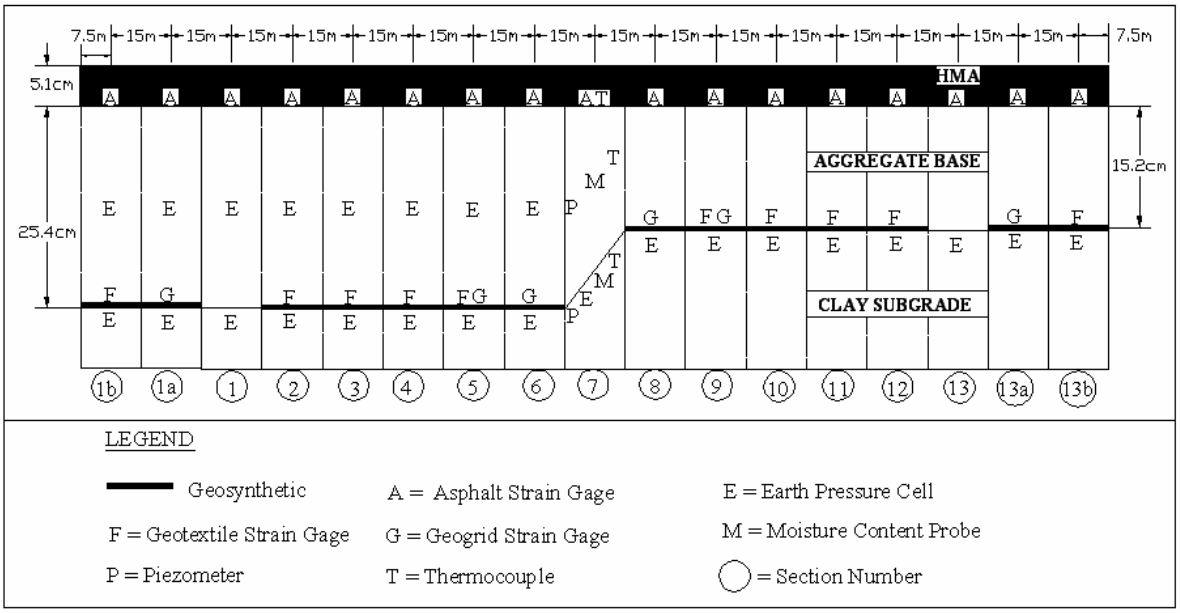

Figure 3.8 – Profile View of the Test Configuration

4. INSTRUMENTATION

4.1 Introduction

The frontage road was heavily instrumented with structural and environmental gages to collect data and monitor the performance of each test section for this project. The structural sensors (earth pressure cells, asphalt strain gages, and foil strain gages) measured a dynamic response from the traffic load, and each response had multiple data points (unlike the environmental gages described below). The foil strain gages were attached to the geosynthetic materials while the remaining sensors were installed within the layers of the pavement. All structural sensors were positioned in the outside wheel path of the travel lane, which was approximately 2.49 m ± 13 mm (98 in ± 0.5 in) from the centerline. The location of the outside wheel path was determined by physically measuring rut locations on similar types of roads in Marked Tree, and comparing this measurement to referenced work by Brandon, et al. (1996) and Trimm et al. (2004).

Each environmental sensor (T-type thermocouple, moisture content probe, piezometer, and tipping bucket) was located in Section 7 and measured a single-point static response for each vehicle pass. Additional geosynthetic foil strain gages were installed in Section 7 in locations that were unaffected by the pavement load to serve as temperature compensation and drift measurement devices. Additionally, a tipping bucket and a Weigh-In-Motion system were utilized. The details of each gage are outlined in the following sections.

All gages were either calibrated in a controlled laboratory setting or the calibration curves provided by the manufacturer were checked, prior to construction. Information from the literature review was used in conjunction with manufacturer instructions to develop an installation procedure for each type of gage. With the exception of the earth pressure cells, back-up gages were installed to ensure that data was acquired in every test section despite anticipated failures during construction. Table 4.1 lists vendor and model information for each gage utilized in this study and Figure 4.1 displays the depth location and type of instrumentation in each test section

(this figure is also included in Chapter 3). These figures should be referenced throughout the discussion in this chapter. Additional details can be obtained from Howard (2006). Note that a total of 129 gages were installed during construction, and of those gages, 85 gages were being actively monitored during the testing sequence.

Table 4.1 – Research Instrumentation

Vender	*Model*	*Function*	*Installed (Active)*
Structural Gages (Located in the Outer Wheel Path)			
Geokon	3500-2	Total Vertical Pressure	26 (25)
Construction Technology Labs	ASG-152	Asphalt Strain	34 (17)
Vishay Micro-Measurement	EP-08-19CDZ-350	Geotextile Strain	32 (17)
Vishay Micro-Measurement	EP-08230DS-120	Geogrid Strain	16 (8)
MSI	MSI Roadtrax BL-CLS1	Vehicle Data	2(2)
Environmental Sensors (Located in the Transition Section)			
Omega T-Type	CPSS-14G-12-NHX	Asphalt Temperature	3 (3)
Omega T-Type	TMQSS-125G-6	Other Temperatures	8(8)
Geokon	3400-S-2	Pore Water Pressure	2(2)
Decagon	EC-20	Moisture Content	5(2)
Texas Electronics	TR-525M	Rainfall	1(1)
		Total Count	**129 (85)**

4.2 Gage Identification

Due to the number of gages and more importantly, the number and length of the cables associated with this research, a specific identification scheme (1_2_3/4-5/6) was created. The components of this identification tag are defined in Table 4.1 using "EPC_B1_16/3-MOD2/ai7" as an example. Each identification tag was printed on a label that adhered to each end of the cable and was covered with clear heat shrink tubing for long term protection.

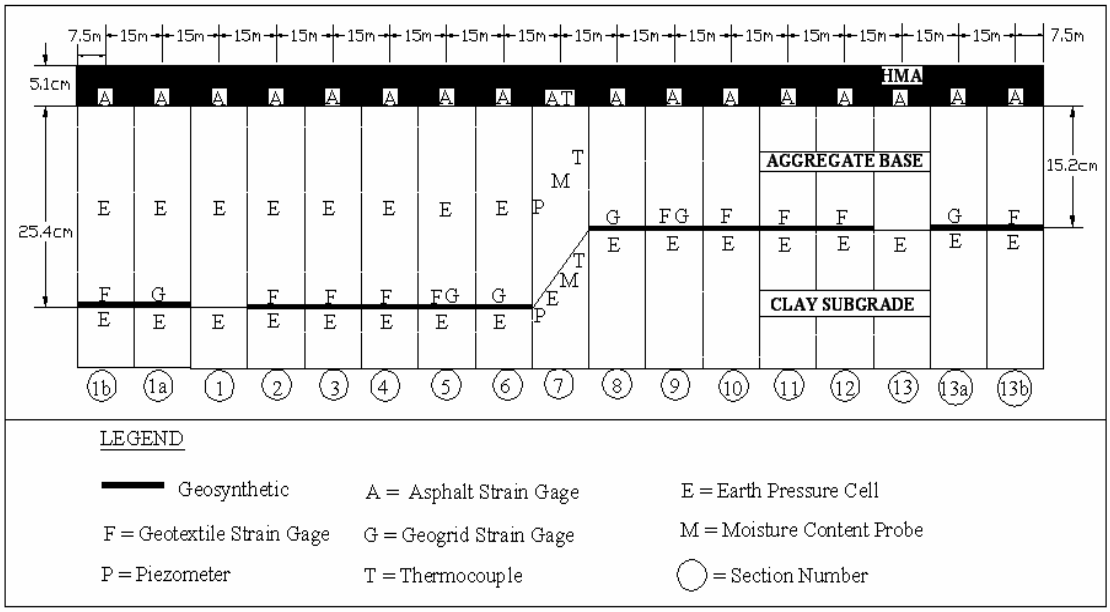

Figure 4.1 – Profile View of the Test Configuration with Instrumentation

Table 4.2 – Gage and Cable Identification Scheme

Identification Number	*Meaning*
1	Type of Instrumentation (Example: EPC - Earth Pressure Cell)
2	Depth Location and Tracking Information (Example: B1 - the first Earth Pressure Cell in the Base Course)
3	Section Number (Example: 16 - the gage is located in Section 16)
4	Data Acquisition Chassis Number (Example: 3 - Chassis 3)
5	Module and Terminal Block (Example: MOD2 - the second module in Chassis 3)
6	Channel Number (Example: ai7 - Channel 7 on Module 2 in Chassis 3)

4.3 Earth Pressure Cell

Geokon earth pressure cells (model 3500-2) measured total vertical pressure in the subgrade and base course of each test section (Figure 4.2). The cell was purchased at a cost of $662 for the sensor and $2.95/m ($0.9/ft) for the appropriate cable. Of the 26 earth pressure cells installed, 16 active cells were installed in the subgrade (1.9 cm - 2.2 cm from the subgrade surface) in all 16 structural test sections, two cells were

installed in the transition section to monitor gage drift, and eight cells were installed mid-depth (12.5 cm from the aggregate surface) within the base course in Sections 1b through 6 (Figure 4.1).

A properly designed pressure cell should be able to: 1) measure stresses in the free-field condition without changing the state of stress in the soil, and 2) be placed in the soil without significant disturbance to the existing state of stress (Sebaaly et al. 1989). This type of earth pressure cell consists of two stainless steel plates welded together at the perimeter. The cavity between the plates is filled with de-aired hydraulic fluid, and a pressure transducer is attached to the instrument to measure the change in hydraulic fluid pressure that results from externally applied loads. The cell is approximately 230 mm (9 in) in diameter and 13 mm (0.5 in) thick, and the aspect ratio is approximately 0.06. Each earth pressure cell was calibrated in a laboratory environment using an MTS load frame, prior to field installation. Table 4.3 provides the technical specifications supplied by the manufacturer and Figure 4.2 provides an illustration of the cell. A survey rod is displayed in Figure 4.2 so each major increment is one tenth of a foot.

Table 4.3 – Geokon Model 3500-2 Product Specifications

Transducer Type	Semi-conductor
Output	0-5 VDC
Pressure Range	0-0.42 MPa (0-60 psi)
Resolution	Infinite
Accuracy	$\pm$ 0.5% F.S.
Linearity	< 0.5% F.S.
Thermal Effect on Zero	< 0.05% F.S.
Excitation Voltage	10v maximum
Temperature Range	-20°C to +80°C [-4 to 176 °F]

During the subgrade installation phase, each earth pressure cell was positioned in the outside wheel path (laterally) and in the center of each test section (longitudinally) using the surveyed center line stakes as a reference. After the installation of each subgrade earth pressure cell, the coordinates of each location were carefully surveyed so that each location could be relocated for all subsequent

installation phases (geosynthetic, base course, and asphalt) to ensure that the gages were aligned vertically, thereafter.

Figure 4.2 - Earth Pressure Cell

An outline of the cell was spray painted on the subgrade surface (oriented longitudinally with traffic) using a wooden template of the cell. Subsequently, the subgrade material inside the spray-painted outline was excavated using hand tools to a depth sufficient for a thin sand cushion, the earth pressure cell, and the backfill material (which was sand in the subgrade and a mixture of sand and aggregate in the base course layer) without over-excavating. The inside of the hole, the sand cushion, and the earth pressure cell were carefully leveled and compacted during the process. A trench was also excavated to a depth that would protect the cables and in a pattern that would provide sufficient strain relief.

Figure 4.3 displays an earth pressure cell that was installed in the subgrade before it was covered up with sand, which was manually compacted with a steel tamper. The cable was positioned inside of a 7.5 cm (3 in) deep trench and landscaping pins were used to prevent the cable from moving.

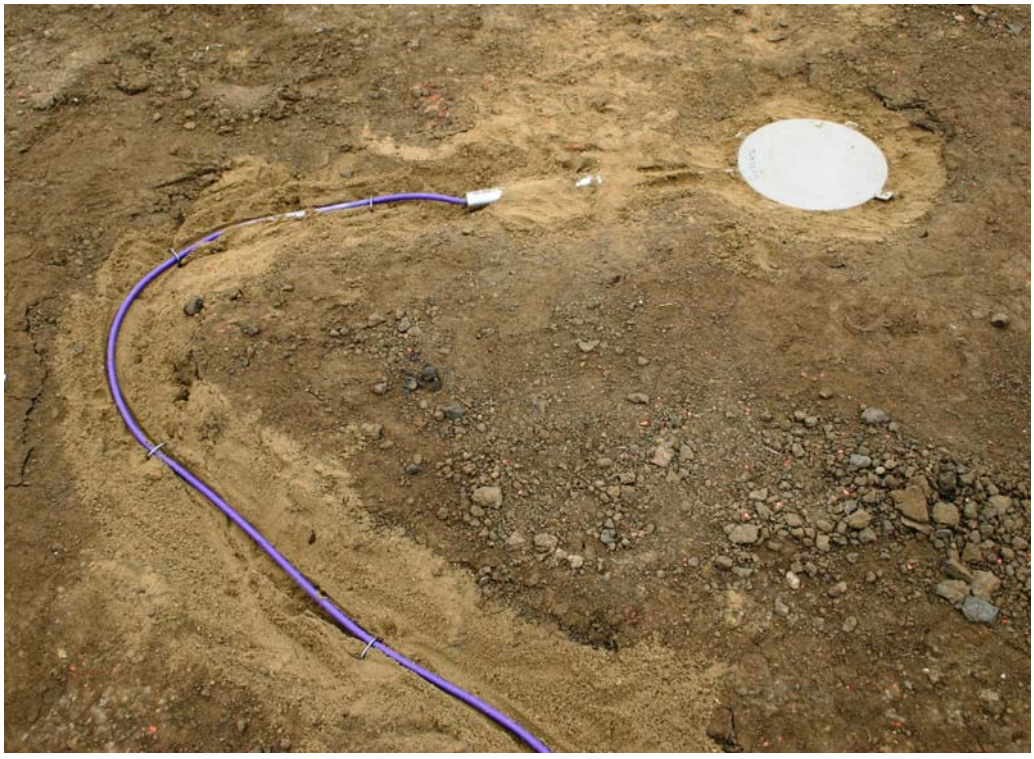

Figure 4.3 – Installed Subgrade Earth Pressure Cell

In order to install the earth pressure cell in the base course without requiring a survey crew to stand guard during the tedious installation process, the original coordinates were surveyed, and a nail was driven in at this location. Two string lines were then used to generate the diagonals of an imaginary square with the intersection of the diagonals crossing at the sensor location. Nails were then driven into the four corners of the imaginary box and used repetitively to relocate the exact location (using the string line) and precisely position the gage in the base course. Figure 4.4 displays this technique. A plumb bob was necessary since the gages were embedded at mid-depth within the base course. Figure 4.5 displays an earth pressure cell installed mid-

depth in the base course, and Figure 4.6 displays the tamper that was used to re-compact the material on top of each gage.

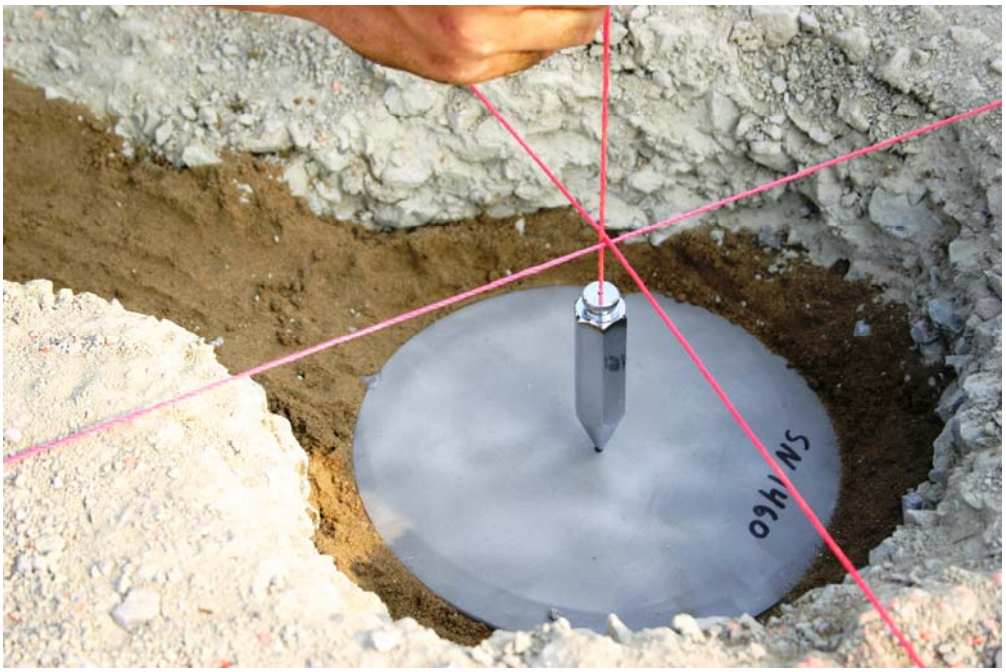

Figure 4.4 – Re-Location Technique Used in the Base Course

Figure 4.5 – Installed Base Course Earth Pressure Cell

Figure 4.6 – Tamper

4.4 Asphalt Strain Gage

Asphalt strain gages were purchased from Construction Technologies Laboratory (model ASG-152) at a cost of $500 per gage and $3.25/m ($1/ft) for the cable that was spliced to the 9.1 m (30 ft) long, heat resistant leads. They were full bridge, electrical resistance strain gages embedded in a two-part polysulfide liquid polymer, which was encapsulated in silicone with a butyl rubber outer core. This configuration results in a relatively low stiffness coupled with high flexibility and strength, which is significant since the measured value will only be true strain if the gage stiffness is less than or equal the asphalt stiffness (Tabatabee and Sebaaly, 1990). The actual strain gage is located on an axial bar (oriented longitudinally with traffic), which is connected to two threaded aluminum end bars with a locking nut (considered to be an "H-Type" gage for this reason). The end bars screw onto the axial bar so the nut serves as an extra safety factor. Table 4.4 summarizes the specification provided by the manufacture and Figure 4.7 displays the asphalt strain gage used in this study. A survey rod is displayed in Figure 4.7 so each major increment is one tenth of a foot.

Table 4.4 – Asphalt Strain Gage Specifications

Bridge Completion	Full bridge, none required
Gage Resistance	350 Ω
Excitation	Up to 10 Volts
Temperature Range	-34 °C to 204 °C [-29 to 400 °F]
Output	≈2mV/V @ 1500 μs
Grid Area	0.133 cm^2 (0.0206 in^2)
Gage Area	1.22 cm^2 (0.189 in^2) overall
Modulus	≈2.34GPa (340,000 psi)
Fatigue Life	$<10^5$ repetitions @ $\pm$ 1500 μs
Cell Material	Black 6/6 nylon

Figure 4.7 – Asphalt Strain Gage

The calibration factors provided by the manufacturer were verified in the laboratory, prior to field installation. Two gages were installed at the bottom of the asphalt layer in each structural test section (a total of 32 strain gages), and two gages

were installed in the transition section to monitor gage drift. All gages had a back-up in case of failure during the installation.

The location of each gage was determined using the previously surveyed coordinates and marked with a nail. Unlike the earth pressure cells (buried at a designated depth within the subgrade and base course layers), they were positioned on the surface of the base course and protected until the asphalt construction phase was initiated. While the sensors remained on the surface prior to paving, the cables were buried in a trench from the sensor to the edge of the road while leaving just enough lead length exposed at the sensor to permit movement of the gages off and on the measurement location prior to paving (the reason will become clear as the installation procedure is discussed).

Figure 4.8 displays two asphalt strain gages that have been loosely installed on the surface of the base course prior to paving. The survey nail is located under the center of the right most gage. Both gages can be moved on and off this nail since the lead cables (shown towards the top of the picture) were left unburied near the sensor. The actual strain gage is located at the center point of the axial bar. Note that a portion of the lead cable nearest to the strain gage (shown on the top half of each gage in Figure 4.8) is secured to both the axial bar and the end bar using zip-ties to prevent pullout of the electronics near the full-bridge strain gage.

Just prior to paving, a protective asphalt cushion was placed around each gage (top and bottom) to minimize damage. A minus No. 4 Superpave asphalt batch was pre-mixed at the University of Arkansas to avoid on-site sieving of the asphalt material and facilitate the paving train process. Two metal pans of the minus No. 4 Superpave mix were prepared for each test section (one for the bottom cushion and one for the top), and the pans were heated on site for approximately three hours using ovens that were powered by gas generators. The timing of this operation was critical in order to keep the asphalt as hot as possible and minimize cold joints between this protective cushion and the actual HMA layer. The method used to place the pre-mixed material is described in the following paragraphs.

Figure 4.8 – Asphalt Strain Gage Pair Prior to Paving

Immediately before paving, the alignment nail was partially pulled up, the pre-mix was transferred from the first pan to the surface of the base course to generate a 30.5 cm (12 in) square layer of material around the nail, and a rubber mallet was used to compact the material. When the nail was removed, the remaining void was utilized to position the active and back-up gages, and both gages were visually aligned so they were parallel to the road. Figure 4.9 shows the bottom asphalt cushion with the protruding nail and Figure 4.10 shows the two gages positioned on the asphalt cushion just before applying the top cushion.

Figure 4.9 – Bottom Asphalt Cushion and Alignment Nail

Figure 4.10 – Strain Gage Installation In Progress

The gages were then covered with the mix from the second pan and this material was compacted by standing on a square metal plate and subsequently using a mallet. Figure 4.10 also displays the metal plate and the pans. Any remaining hot mix material was positioned behind the sensors to buffer any movement during paving. It

was also important to position the lead wire closest to the gage so that it rolled towards the gage during paving (rather than being pulled). Full vibration was permitted over the gages after one initial static pass.

4.5 Foil Strain Gages

Quarter-bridge foil strain gages were purchased from Vishay Micro-Measurements and attached to all geosynthetic materials. The cost of these gages ranged from $7 to $20 and cable was purchased at a cost of $1.05/m ($0.32/ft). The backing material was manufactured using polyimide to enable superior elongation capabilities, and the measurement grid was manufactured using a fully annealed constantan alloy (a ductile material) that can sustain strains up to 20%.

The gage patterns for the geotextiles and the geogrids were selected to maximize the length of the gage on each material to obtain the best statistical average. The longest possible gage was selected for the geotextiles and the geogrid gages were selected based on the rib size of each material. A 350 Ω gage was needed for the geotextiles and for the MIRAFI geogrid (due to their position within the test configuration) to offset the long lead lengths so model EP-08-19CDZ-350 (48.3 mm (1.9 in) in length) was selected for the geotextiles and model EP-08-500GC-350 (12.7 mm (0.5 in) in length) fit the polyester ribs of the MIRAFI BasXgrid11 geogrid. Model EP-08-230DS-120 (5.8 mm (0.23 in) in length) was used on the Tensar BX1200 due to the limited surface area of the polypropylene rib. An example of a geotextile and a geogrid foil strain gage is displayed in Figure 4.11. All foil strain gages were calibrated using an MTS testing apparatus in conjunction with digital photography analysis techniques (Warren et al, 2006).

At least two foil strain gages were attached to each geosynthetic in a controlled laboratory setting, and the details of the attachment procedure that was developed during this research project (involving special adhesives and waterproofing materials) are described by Warren et al. (2006). Of the seven geosynthetic configurations on each side of the transition section, each suite of geosynthetics included a combination geotextile-geogrid section, four different types of geotextiles, and two different types of geogrid. Additionally, two foil strain gages were installed on each of five smaller

geosynthetic samples for temperature compensation, two additional strain gages were rotated 90 degrees and attached to the geotextile in Section 11, and four additional strain gages were attached on both sides of the active gage in Section 10 (two gages on each side) to assess vehicle wander.

Figure 4.11 – Foil Strain Gages

Figure 4.12 and Figure 4.13 displays waterproofed foil strain gages attached to one of the geogrids and one of the geotextiles, respectively. Subsequent to placement of the geosynthetics, the gages were checked for functionality, and then additional protection was added to each gage to ensure they survived the base course installation phase of construction. A small piece of strip drain was used to protect the geogrid gages and a neoprene cover was utilized for the geotextile. The following chapter will outline the procedures used to position the geosynthetics on the surface of the subgrade.

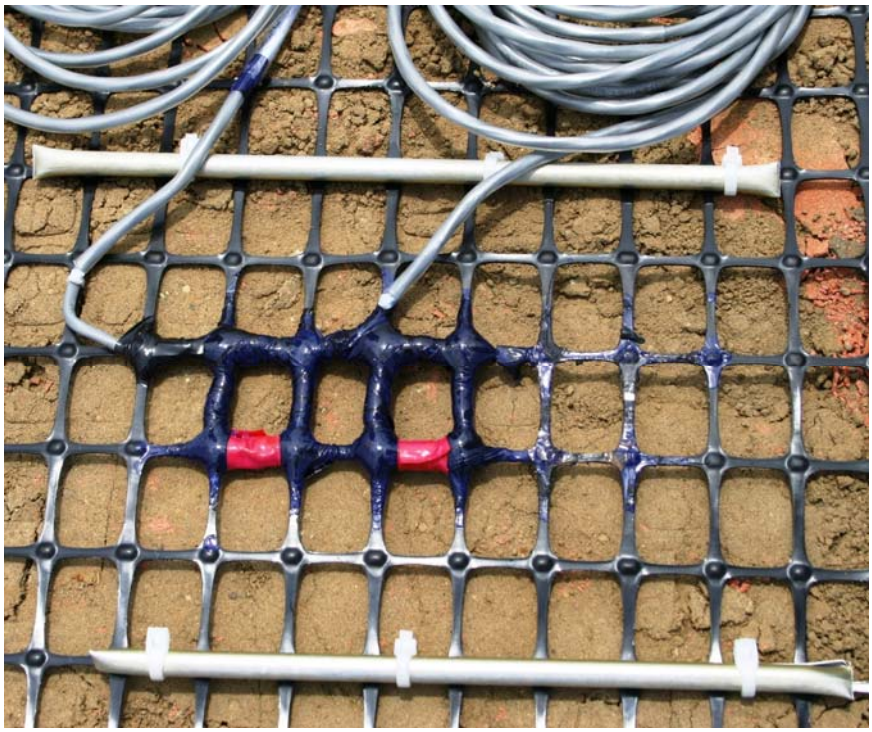

Figure 4.12 – Geogrid Strain Gage in the Field

Figure 4.13 – Geotextile Strain Gage in the Field

4.6 Thermocouples

Two types of thermocouples were purchased from Omega (ranging in price from $24 to $40) and the cable was purchased for $1.21/m ($0.37/ft). T-type thermocouples consist of two dissimilar metals (copper and constantan) joined together at an "exposed measurement" junction, and the presence of the two different metals induces a voltage that is a function of temperature. A total of 11 thermocouples were installed. Of those 11, three high temperature thermocouples (model CPSS-14G-12-NHX) were placed at the bottom of the asphalt layer, and Omega model TMQSS-125G-6 was utilized for all remaining thermocouples. Two were positioned approximately 1.22 m (4 ft) from the surface of the subgrade, two were positioned 0.16 m (0.5 ft) from the surface of the subgrade, two were positioned mid-depth within the base course, one gage was placed inside the data acquisition box, and one gage was attached to a nearby utility pole. Figure 4.14 displays both thermocouples in addition to the lead wire and the rubber boots that were used to weatherproof the junction. A survey rod is displayed in Figure 4.14 so each major increment is one tenth of a foot.

The measurement junction of each probe was water proofed by wrapping the rubber boots displayed in Figure 4.14 (provided by the manufacturer) with Aqua Seal (a bituminous material), coating the Aqua Seal with Gagekote 7 (a Vishay Micro-Measurements product), and then wrapping it with electrical tape. The calibration information supplied by the manufacturer was also verified prior to field installation.

In order to install thermocouples at two different depths within the subgrade, a 10.2 cm (4 in) hole was augured 1.52 m (5 ft) deep, and fine sand was compacted in the base of the hole to provide a cushion. Two thermocouples were attached to opposite sides of a PVC pipe (Figure 4.15), the pipe (with probes attached) was lowered into the hole, and with the exception of the top 30.5 cm (1 ft), the void space surrounding the instrumented pipe was backfilled with sand. Subsequently, two thermocouples were installed at the surface of the subgrade and backfilled with subgrade material. Similarly, a hole was hand excavated in the base course to install two thermocouples (Figure 4.16). The three asphalt thermocouples were positioned on

the surface of the base course and protected with the same pre-mixed asphalt that was used to cushion the asphalt strain gages using a procedure identical to the one described in the previous section (Figure 4.17).

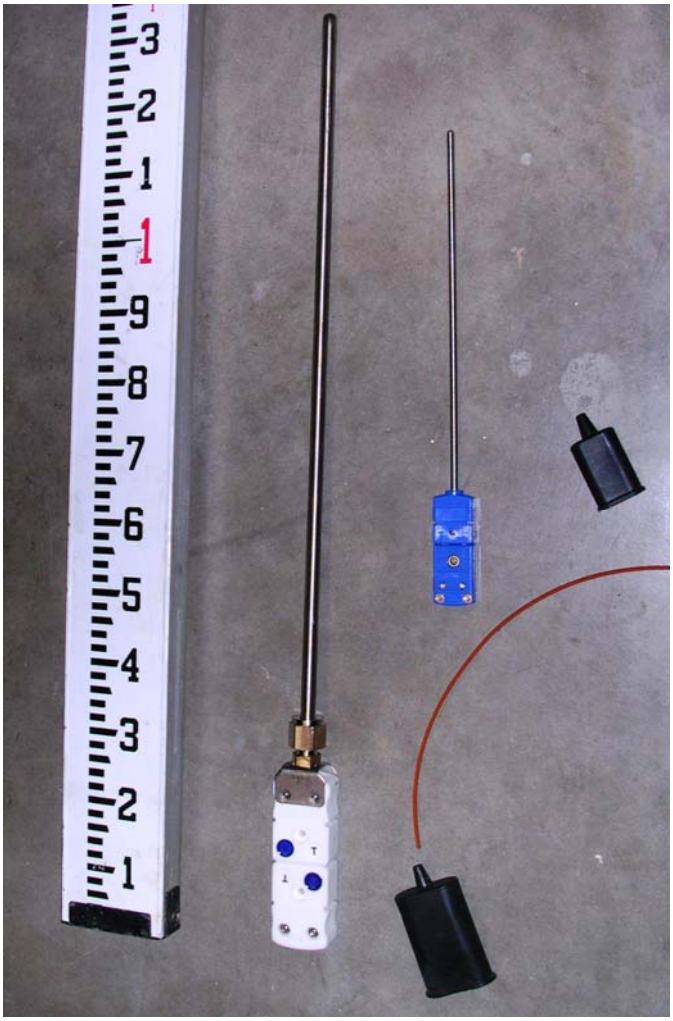

Figure 4.14 – Geotextile Strain Gage in the Field

Figure 4.15 – Subgrade Thermocouples Attached to a PVC Pipe

Figure 4.16 – Base Course Thermocouples

Figure 4.17 – Asphalt Thermocouples

4.7 Moisture Content Probes

A Decagon (model ECH$_2$O) capacitance moisture content probe was purchased at a cost of $100 per sensor and the cable was $1.31/m ($0.40/ft). This particular gage averages the volumetric moisture content along the length of the probe. The specifications of the Decagon gage (supplied by the manufacturer) are shown in Table 4.5 and Figure 4.18 illustrates the moisture content probe. A survey rod is displayed in Figure 4.18 so each major increment is one tenth of a foot.

Table 4.5 - Decagon EC-20 Product Specifications

Measurement Time	10 ms
Accuracy	$\pm$ 3%
Resolution	0.002 m^3/m^3 (0.1%)
Power	2.5-5 VDC
Output	10-40% of Excitation Voltage
Temperature Range	0-50 ^oC (32-122 ^oF)
Operating Range	0- Saturated
Dimensions	20 x 3.17 x 0.15 cm (8.00 x 1.25 x 0.06 in)

Figure 4.18 – Moisture Content Probe

Five moisture content probes were installed in Section 7 (three were positioned in the subgrade and two were positioned in the base course). The top of all three subgrade probes was located approximately 75-250 mm (3-10 in) from the surface of the subgrade and all gages were positioned vertically. Due to the length of the probe, the two base course probes could not be oriented vertically. They were installed at an angle so the probes still averaged the moisture content over the full depth of the base course layer.

Before inserting the moisture content probe into subgrade, a small hole was excavated at each location to ensure the top of the gage was recessed. Water was poured into the hole and permitted to infiltrate the soil to soften it up. A rectangular metal bar (machined to dimensions slightly larger than that of the probe with a hole at the top big enough to fit a threaded steel rod through it) was driven into the soil using a mallet. The steel rod was inserted horizontally through the hole (Figure 4.19), and the bar was extracted using the leverage provided by the rod. Since the soil was

cohesive, the void space remained intact, and the moisture content probe was easily inserted (Figure 4.20). In order to push the adjacent soil back into the void space to ensure full soil contact with the probe, the same metal bar was then driven into the soil adjacent to the gage a short distance away on both sides. A trench was then excavated for the cables, and the remaining hole was backfilled with fine sand, which was compacted using the hand tamper.

Figure 4.19 – Insertion of Metal Bar with Leverage Rod

Figure 4.20 – Insertion of Subgrade Moisture Content Probe

The same method was unsuccessful in the base course since there was insufficient cohesion to keep the void space open and the material was coarser and stiffer. Therefore, a hole just large enough to install the probe was excavated for each probe (Figure 4.21), and the finer portion of the crusher run was used to backfill the hole. All other procedures were the same.

The gages were manually calibrated using the subgrade and aggregate materials obtained from the site. Samples were compacted in standard concrete cylinders using five lifts and a 150 mm (6 in) Marshall Hammer that delivered six blows per lift. When each sample was prepared, the steel bar (described previously) was driven into the sample, removed, and the probe was inserted into the remaining hole (similar to the procedure described previously). The cylinder was manually squeezed to ensure there was contact between the soil and the probe before data acquisition.

4.8 Piezometers

Geokon (model 3400-2) piezometers were purchased at a cost of $517.50 per sensor and $2.45/m ($0.90/ft) for the cable. The sensor consisted of a semi-conductor pressure transducer housed in a 32 mm (1.25 in) diameter 304 stainless steel tube. A

filter was located at one end of the tube to permit water flow into the sensor but prevent the passage of soil particles. The piezometers were used in this project qualitatively to determine if the materials were at or near saturation (they were not used for effective stress calculations). Both piezometers were calibrated in a laboratory setting, prior to installation. The manufacturer specifications are summarized in Table 4.6 and Figure 4.22 displays the piezometer.

Figure 4.21 – Insertion of Base Course Moisture Content Probe

Table 4.6 – Piezometer Specifications

Output	0-5 Volts
Accuracy	± 0.25 % F.S. or Better
Linearity	< 0.5 % F.S.
Temperature Range	-20 °C to + 80 °C [-4 to 176 ^{0}F]
Length x Diameter	194 x 32 mm (7 5/8 x 1 ¼ in)

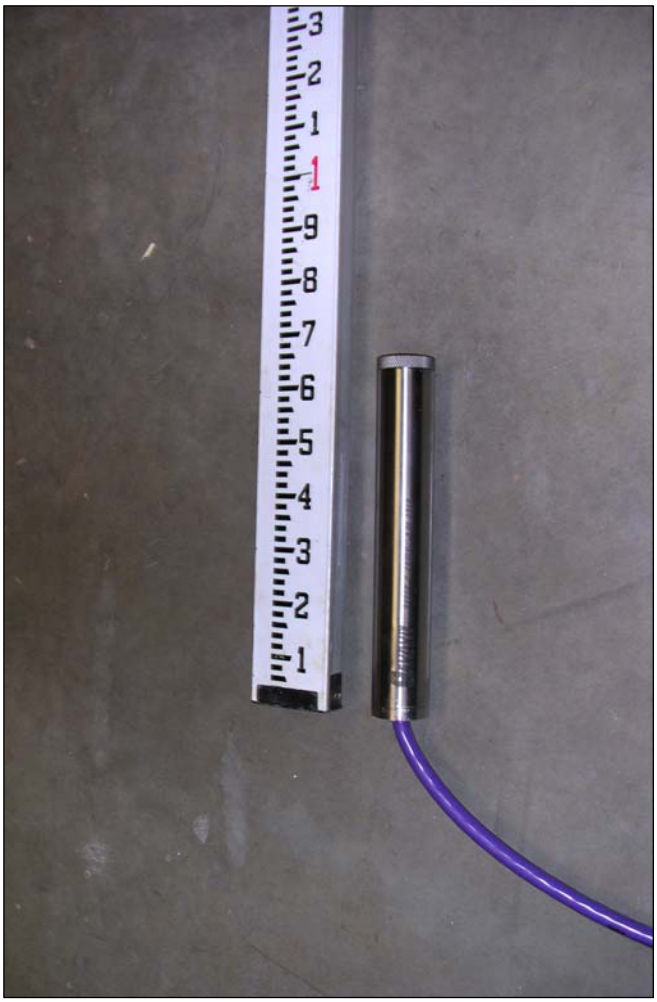

Figure 4.22 - Piezometer

Two piezometers were installed in the transition section (near the surface of the subgrade and in the middle of the base course). A hole with the following dimensions was excavated in each layer: 150-200 mm (6-8 in) deep, 450 mm (18 in) long, and 200 mm (8 in) wide. A piezometer was then placed inside the geotextile bag and filled with clean sand (Figure 4.23). After placing the bag in the hole (Figure 4.24), it was backfilled with sand (in the subgrade) or aggregate (in the base course) and a trench was excavated for the cables. Bentonite plugs were installed within the trenching pattern to ensure the piezometers were only reading values representative of the subgrade conditions.

Figure 4.23 – Geotextile Bag for the Piezometer

Figure 4.24 – Placement of the Piezometer

4.9 Tipping Bucket

A Texas Electronics tipping bucket (model TR-525M) was secured to a small concrete pad near the data acquisition system to monitor daily precipitation, and the instrument was calibrated in the laboratory, prior to installation. A Spectrum Technologies 115 Watch Dog® Rain Logger was connected to the tipping bucket (as a stand alone device), and the data was periodically downloaded using SpecWare 6.0 software. Table 4.7 summarizes the manufacturer product specifications and a photograph of the device is displayed in Figure 4.25.

Table 4.7 - Tipping Bucket and Collector Product Specifications

Accuracy	1% Up to 50 mm/hr (2 in/hr)
Funnel Depth	163 mm (6.4 in)
Collector Diameter	200 mm (8 in)
Operating Temperature	0-50 $^{\circ}$C (32-125 ^{o}F)
Height	300 mm (12 in)
Switch Closure Time	135 ms

Figure 4.25 – Installed Tipping Bucket

4.10 Piezoelectric Sensors

Two piezoelectric sensors were installed (as part of a Weight-In-Motion system) to independently assess the type and the number of vehicles passing through the test site. Piezoelectric materials produce a voltage when strained and the induced voltage is related to stress knowing the capacitance of the material. The MSI Roadtrax® Brass Linguini® (BL) Class 1 axle sensor was purchased from MSI Sensors for $668, and the AS475 grout necessary for installation cost $125. The price included all necessary cable (91 m [300 ft]). All signals were monitored by the AHTD using an ADR 3010 - 190 logger and the data was downloaded using 32-bit, Windows-based application software that handled binary data. The manufacturer supplied specifications are summarized in Table 4.8 and a photograph of the sensor is displayed in Figure 4.26.

AHTD installed and calibrated two 3.65 m (12 ft) spaced piezoelectric tubes near the middle of the test site. In general two 19 mm (0.75 in) square grooves were cut in the pavement using the apparatus displayed in Figure 4.27. The grooves were then pressure washed and blown dry using an air compressor. The sensor was properly aligned within the groove using clips provided by the manufacturer. The AS475 grout was then used to fill the groove and the installation was complete when the grout was cured. Figure 4.28 displays one of two finished products. The calibration of the piezoelectric tubes was performed using a loaded single axle truck. The front axle weighed 37.6 KN (8,460 lb) while the back axle weighed 90 KN (20,200 lb) at the time of calibration.

Table 4.8 – MSI Roadtrax® BL Class 1 Sensor Product Specifications

Output Uniformity	< ± 7% for Class 1 Weigh in Motion
Operating Temperature	-4 to 70 °C (-40 to 160 °F)
Passive Signal Cable	RG 58C/U; HDPE Outer Jacket
Product Life	40 Million ESAL's
Dimensions	6.6 mm (0.26 in) wide by 1.6 mm (0.063 in) thick
Piezoelectric Coefficient	> 20pC/N

Figure 4.26 - Piezoelectric Sensor

Figure 4.27 – Pavement Saw

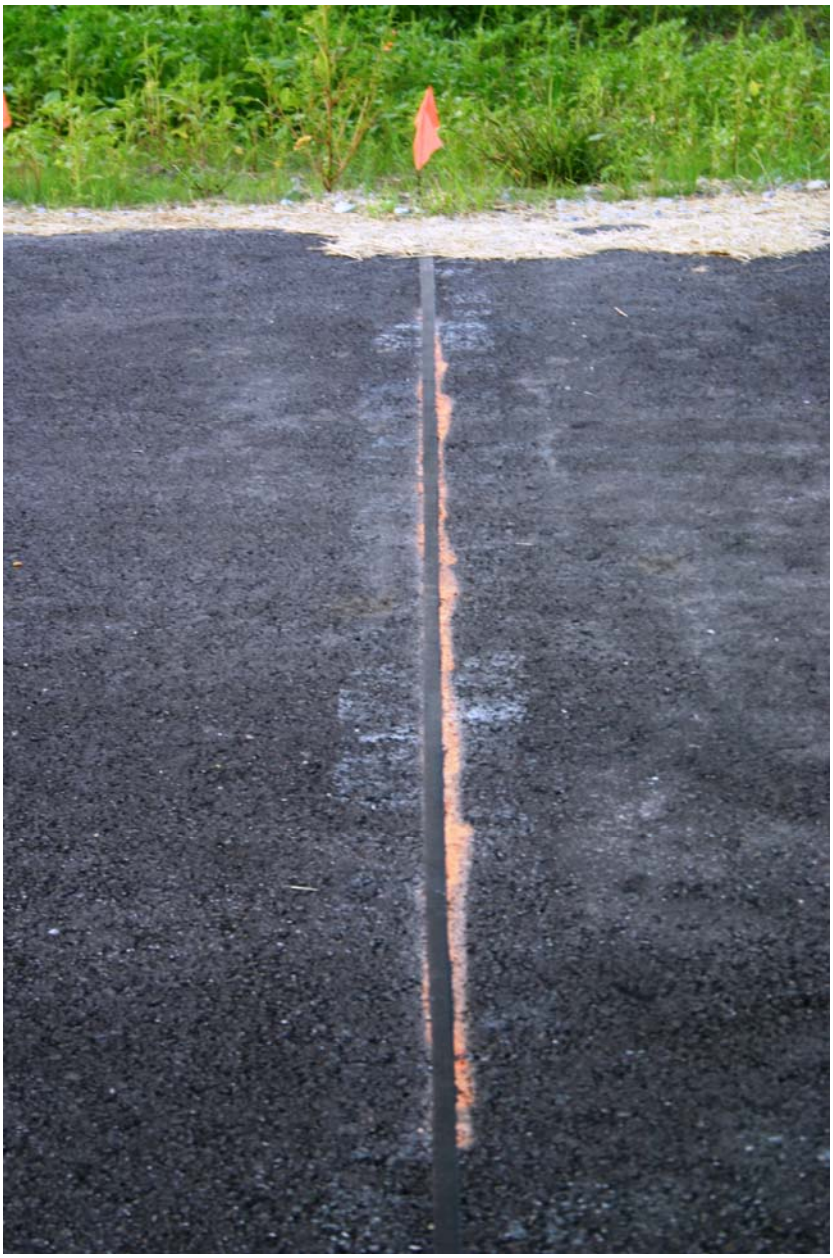

Figure 4.28 – Installed Piezoelectric Sensor

5. FULL-SCALE FIELD CONSTRUCTION

5.1 Introduction

The construction of a pavement structure containing instrumentation requires careful planning and execution. Detailed installation procedures were developed for each sensor to ensure it was protected during construction and modifications were made to each construction phase and communicated to the contractor to maximize gage survivability. Approximately 5,000 m (16,400 ft) of cable and 370 m (1210 ft) of protective conduit were installed for all 129 gages. While the previous chapter describes the type of instrumentation and the installation procedure developed for each gage, this chapter outlines the methods that were used to construct each phase of the pavement structure (subgrade, geosynthetic placement, base course, and asphalt) and install the protective conduit system.

5.2 Subgrade Preparation

The subgrade was graded and compacted by the contractor in October of 2004 using standard methods (as outlined in the AHTD specifications). The research team then used hand tools to excavate the holes and trenches necessary to install the subgrade instrumentation (earth pressure cells, thermocouples, moisture content probes, and piezometers) using the methods outlined in Chapter 4. Prior to placing the geosynthetics on the surface of the subgrade, it was swept to avoid installation damages to the geosynthetic materials. Figure 5.1 displays a photograph of the finished subgrade.

However, contractor issues and weather conditions prevented completion of the roadway before the end of the construction season. Since the subgrade would have to be re-worked the following season, all subgrade instrumentation that had already been installed had to be removed and subsequently re-calibrated or replaced. The subgrade preparation phase and instrumentation installation was successfully repeated in the summer of 2005.

Figure 5.1 – Finished Subgrade

5.3 Geosynthetic Placement

Before moving the geosynthetic test materials to the site, the instrumented geosynthetics were folded so that the foil strain gages were protected during transportation and could be easily positioned on-site (some of these materials were heavy and cumbersome). In other words, the ends of the test section materials were folded into the middle (where the gages were located) instead of folding these large geosynthetic sections from one end to the other. Additionally, wooden dowel rods were temporarily attached to the materials in the vicinity of the gage to prevent bending of the foil strain gages during transit, and were removed after the geosynthetics were placed on site.

The full length of each geosynthetic section was unfolded and aligned with the roadway after positioning the gages in the approximate location. The gage locations were then finalized using the previously determined survey coordinates (Figure 5.2) and then two people stood on each side of the material at the gage location (center of the test section) and pulled the material taunt so that the center of the material could be

tacked down. An alignment mark (for additional pins) was then painted on the edge of the material every 2.4 m (8 ft) from the center position on both sides of the gage.

Figure 5.2 – Relocation of the Instrumentation Location

The procedure used to manually tension the woven geotextiles was labor intensive and required two pick-up trucks. An illustration of the following components is displayed in Figure 5.3. A 10.2 cm (4 in) diameter PVC pipe was cut in half (length-wise) and attached to the top of a wooden board to provide a smooth surface for the geotextile to slide across as it was lapped over the board. Each end of this modified board rested on the open tailgate of a pick-up truck that was positioned on each side of the geosynthetic and this board was referred to as the "extension". The geosynthetic material was draped over the extension. While the two trucks and the "extension" simultaneously moved away from the gage (center of the section), a PVC

pipe (referred to as the "tensioner") was pushed against the draping geotextile near the ground surface to tighten the material behind it as the system proceeded forward. In Figure 5.3, there is an individual standing on the "tensioner", the "extension" is resting on the two tailgates under the fabric, the strain gages are located in the outside wheel path (to the left of the bucket), and the trucks are getting ready to move forward.

Figure 5.3 – Geosynthetic Lay Down Technique

At every alignment mark, the tensioning process was temporarily delayed, and six pins were driven into the subgrade across the geotextile. This process was repeated on both sides of the gage until the trucks reached the end of the geosynthetic. Due to the stiffness of the geogrids and the elongation capability of the nonwoven geotextiles, the lay down and tensioning process for these materials was performed by pulling the materials taunt by hand and pinning them every 2.4 m (8 ft).

The geotextile foil strain gages were protected from the sharp aggregate during the construction phase using a neoprene cushion and the geogrid gages were protected using a small piece of a geosynthetic strip drain. Since the geosynthetic cables (now located on top of each geosynthetic) could not be buried, crushed stone was manually placed and compacted over a layer of fine sand placed on top of the cables, prior to the

base course installation. The contractor was required to place the base course aggregate immediately, thereafter, to prevent damage to the materials and the instrumentation.

5.4 Base Course

The contractor dumped enough aggregate on the non-instrumented lane to provide a working platform adjacent to the test sections and generate the first lift of compacted material on both lanes. The aggregate was laterally bladed across the test sections by an experienced operator (Figure 5.4). After compaction of the first lift, the contractor proceeded normally to bring the entire test section to the appropriate grade and density. A preliminary study was conducted prior to the full-scale installation to verify that compaction vibration would not affect the survivability of the geosynthetic instrumentation (with the described gage protection). As a result, vibration was used to compact each lift. The final base course thickness for each test section is summarized in Table 5.1.

Figure 5.4 – Aggregate Placement

Table 5.1 – Final Base Course Thicknesses

Station	*Section*	*Thickness (cm)*	*Thickness (in)*
137+75	1	29.4	11.58
138+25	2	22.3	8.76
138+75	3	23.1	9.10
139+25	4	24.3	9.55
139+75	5	25.1	9.87
140+25	6	23.3	9.16
140+75	7	Transition	Transition
141+25	8	16.8	6.61
141+75	9	16.8	6.61
142+25	10	14.3	5.64
142+75	11	16.3	6.40
143+25	12	16.0	6.31
143+75	13	16.5	6.50

After the base course was compacted, the position of the instrumentation location in each test section was re-located using survey equipment, and the base course instrumentation was installed using the methods outlined in Chapter 4. Additionally, the asphalt strain gages and asphalt thermocouples were installed on the surface of the base course, clearly marked, and protected until the paving equipment could be mobilized. Figure 5.5 displays a photograph of the site, just prior to paving. The protective asphalt cushions (described in Chapter 4) have already been installed and the paving train is in progress.

5.5 Asphalt Concrete

Multiple asphalt dump trucks, a shuttle buggy (Road Tec 74-001 SB-25 00B), a paver (Cedaraphids CR 461R), a breakdown roller (Ingersol Rand DD-138 steel wheel roller), and a finish roller (Ingersol Rand DD-130 steel wheel roller) were on site during the paving phase. Modifications to the paving procedure were required to avoid damaging the gages at the bottom of the 5 cm (2 in) asphalt surface course, which was a 12.7 mm (0.5 in) Superpave mix. In order to protect the gages, the contractor paved the southbound lane first (the same lane containing the instrumented

test sections) from AR Hwy 75 to the end of these test sections, and then subsequently paved the adjacent lane. The contractor paved the instrumented lane without modification until they reached the vicinity of the test sections, and then operation was temporarily halted to wait for asphalt and reposition the equipment. The position of the shuttle buggy and paver was shifted slightly from the norm to avoid tire/track contact with the gage locations. Paving continued when there was enough asphalt on-site to pave all 17 test section.

Figure 5.5 – Final Base Course with Asphalt Strain Gages

As discussed in Chapter 4, the asphalt strain gages and thermocouples were installed just before the paving train reached the test sections (Figure 5.5). A photograph of the paving train is displayed in Figure 5.6. All vehicles are moving northbound on the southbound traffic lane. The pipe network and the data acquisition enclosure are located to the right of this photograph. A line of dump trucks was formed in the background of this photograph before each truck was instructed to pull around the right side of the buggy (on the non-instrumented side) and back up into the shuttle buggy to unload (Figure 5.6) while avoiding the asphalt gages that exist on the base course surface. There is an asphalt strain gage located next to the cone displayed in this photograph. Note that the truck drivers had to be carefully monitored/watched

to ensure they did not run over the gages. A single static pass preceded three vibratory passes with a breakdown roller and then two static passes were made with the finish roller.

Figure 5.6 – Paving in Progress

During this process, the paving train was only forced to stop once after a careless driver spilled material from his truck while he was dumping into the shuttle buggy, but this occurred between instrumentation locations so the effect it had on the study was negligible. The air temperature was approximately 38 ^{0}C (100 ^{0}F), the heat index approximately 46 ^{0}C (115 ^{0}F), and the temperature of the asphalt patches (installed prior to paving) cooled to only 52 ^{0}C (126 ^{0}F). Cores were extracted mid-way between the instrumentation locations (at the boundaries of each test section) to determine the variability in the asphalt mat and these results are summarized in Table 5.2.

5.6 Cable Management and Protection

Two 90 cm x 120 cm x 34 cm (36 in x 48 in x 13 in) enclosures were purchased to house and protect the data acquisition system (Figure 5.7). The lockable top panel of each enclosure (lined with a gasket around the inside edge) formed a lid

that had hinges on the back side. Holes were tapped into all four sides of the box and flanges were mounted on each hole to allow for entry of the instrumentation and power cables. Wooden blocks were attached to the bottom of each enclosure before attaching it to a concrete foundation pad. Wooden blocks were also attached to the top of the box so that a tin roof could be used to provide shade to the box. Finally, a muffin fan and a filtered vent were installed on the bottom side of each box to permit air circulation inside the enclosures. The header pipe for Sections 8-13b (full of instrumentation cable) is attached to the box in Figure 5.7.

Table 5.2 – Final Asphalt Thickness

Station	*Asphalt Thickness (cm)*	*Asphalt Thickness (in)*
144+00	6.31	2.49
143+50	5.89	2.32
143+00	6.07	2.39
142+50	5.36	2.11
142+00	6.03	2.38
141+50	5.52	2.18
141+00	5.61	2.21
140+50	-	-
140+00	5.89	2.32
139+50	6.07	2.39
139+00	6.25	2.46
138+50	5.77	2.27
138+00	5.58	2.20
137+50	5.77	2.27

All gages were manufactured with a lead wire that was long enough to reach the shoulder of the road. Therefore, a longer cable that extended from the shoulder to the data acquisition enclosure had to be spliced to each gage lead. This was the only reasonable option since the cable lengths were significant and it would have been impossible to handle this amount of cable for all sensors during the transition and construction process, and since the dimensions required were unknown at the time that the instrumentation was purchased.

While the task of handling this amount of cable may seem trivial to someone who has not done so before, the effort required to handle, organize, and splice the cables was overwhelming. Approximately 5,000 m (16,400 ft) of cable was spliced to

the gages and incorporated into a piping system that contained approximately 370 m (1210 ft) of conduit. Prior to splicing, the appropriate length of each cable was measured, cut, and strung out in an area adjacent to the conduit trenches. The cables for each test section were bundled separately in this area and positioned so that the cable bundle for the test section farthest from the enclosure was also the bundle farthest from the trench. The importance of this step will become evident in the following discussion.

Figure 5.7 – Data Acquisition Enclosures

Before splicing, the leads cables were all trimmed to a convenient location near the shoulder of the road. The individual conductors in the cable were spliced with a solder connection, individually protected with clear heat shrink tubing (Alpha Fit 221), and individually wrapped with electrical tape. Any braid or wire shield was preserved

and spliced separately. Adhesive lined, heat shrink tubing (manufactured by Raychem) was used to seal the exterior of the cable, the ends of the Raychem product were wrapped with Aqua Seal, and the entire splice was wrapped with electrical tape. While this procedure was overly excessive, it was important to ensure the splices were fully waterproofed.

A PVC pipe network was constructed to protect the cables underground but this phase of the construction was extremely labor intensive due to the amount of cable (up to 32 cables at any one location within the pipe network) and the design of the pipe network. Eight test sections lie on either side of the enclosure (located adjacent to section 7) and cables extended up to approximately 125 m (410 ft) on both sides (Figure 3.7). The 10.2 cm (4 in) diameter pipe network consisted of a series of "laterals" attached to a main "header" pipe on each side of the enclosure. The system was eventually buried in a 0.6 m (2 ft) deep trench. The "header" ran parallel to the road from the enclosure to the mid-point of the farthest test section on each side of the enclosure. The joining of the "header" pipe with one of the enclosures is displayed in Figure 5.7. One "lateral" pipe extended from the shoulder to the header (perpendicular to the roadway) at the mid-point of each test section (Figure 5.8). The "lateral" protected the cables from the shoulder to the main conduit, and the main conduit carried the cables to the enclosure that housed the data acquisition system.

Since the "lateral" pipe was positioned at the bottom of a 0.6 m (2 ft) square trench, there was an elevation change that existed between the sensor cables that day lighted from the roadway at multiple elevations within the pavement structure and the "lateral" pipe at the bottom of the trench near the shoulder of each test section. Therefore, a 45^0 elbow was attached to the top of each "lateral" to turn the pipe up towards the cables and create a smooth transition from the buried cables into the pipe network.

While the geosynthetic and subgrade sensors were deep enough to be protected, shallow sensors in the base course and asphalt were more susceptible to damage from construction equipment. As a result, a combination of vinyl tubing and pipe insulation was used to protect the cables day lighting near the surface as they

transitioned into the “lateral” pipe. This cable entrance at the head of the “lateral” was then waterproofed to prevent water from infiltrating into the pipe network.

Figure 5.8 – Lateral Pipe Extending From the Shoulder to the Header

The intersection of each “lateral” and “header” was referred to as a “junction point”. Access points were incorporated into the pipe network at select locations to ensure easy access to the cables for repair when necessary. An access point was constructed using a T-fitting (with the stem of the “T” facing up), and the access stem was sealed with a flexible, rubber cap (tightened with a hose clamp) for easy access. In general, access points were placed at the top of each “lateral” (near the roadway), and on all three legs of the “junction point” in every test section (Figure 5.9).

Figure 5.9 – Junction Located at the Base of the Lateral

The pipe network had to be constructed in a specific sequence (from the sections furthest away to the sections adjacent to the enclosure) in order to seamlessly incorporate each "lateral" cable bundle into the "header" cable bundle. Pipe sections and fittings were manually pulled down the cable bundles (Figure 5.10) in the following order. Beginning with Section 13b, the fittings and pipe sections necessary to construct the "lateral" for Section 13b were pulled down and constructed inside the trench. The pipe section between Section 13b and Section 13a was constructed and this cable bundle was now considered to be the "header" cable bundle. It gets a little trickier from this point on. The pipe sections necessary to construct Section 13a were then pulled down the next "lateral" cable bundle and constructed (the reason for good organization of the cable bundles should be apparent at this point). Then a "junction" (displayed in Figure 5.9) was constructed and pulled down both the "header" and the Section 13a "lateral" cable bundles as follows: referring to Figure 5.9, the end of the "lateral" cable bundle was fed through the stem of the junction and out the side of the "T" facing the enclosure; the "header" cable was fed through the "T" and both cable bundles were combined at this point, becoming the main "header" cable bundle. This

process was then repeated for each test section, and the "header" cable bundle continued to grow as the process moved towards the enclosure.

Figure 5.10 – Pipe Feeding Process

Cable slack was deliberately incorporated in case repair a gage was necessary during testing. Colored electrical tape was wrapped around the cables to easily identify the cables at the future repair location (the access point located closest to the shoulder). Additionally, a signed post was driven into the ground behind every "junction point" before the pipes were buried, and a string line was pulled from a bolt attached to the bottom of the post to a concrete nail driven into the paved shoulder. While the sign on the post identified the test section and geosynthetic configuration, the string line was used to map the location of each access point (to be buried) for future reference.

During the re-dress of the unpaved shoulder, slope, and drainage ditch, all sensitive areas were passed over by the motor grader with a raised blade and subsequently dressed by hand. Figure 5.11 illustrates the final test site while the side slopes are being re-dressed. The tipping bucket is centered in the photograph, the utility pole is located next to the data acquisition tent and enclosures on the right side

of the picture, and the location of the each measurement location is marked with a cone on the newly paved road. These cones remained on the roadway during the traffic phase to give the driver something to align with.

Figure 5.11 – Redressing the Side Slopes

During the construction of this project, the construction of a brand new nursing home was initiated adjacent to the site. Unfortunately, the access road for the nursing home was going to intersect Section 8, which would have compromised the integrity of the data. No longer would a vehicle travel from one end of the test area to the other end without turning. The nursing home was scheduled to open March 1, 2006. As a result, the type, frequency, and duration of the test traffic had to be adjusted. AHTD agreed to delay the opening of the frontage road to keep the nursing home construction traffic off the frontage road and allow the research team to collect data before they were forced to permit access to the nursing home. Therefore, the data collection phase was accelerated. Instead of collecting true traffic over the course of a year, an AHTD dump truck was used to traffic the instrumented lane under controlled loading conditions over the course of three testing phases.

6. DATA ACQUISITION

6.1 Introduction

Similar studies have utilized the "all sensors on", "all sensors off" approach for the majority of their dynamic data collection. A single trigger (such as a piezoelectric tube) is often used to trigger data collection for all sensors in all test sections simultaneously, and a significant amount of data is subsequently collected from the time a vehicle enters the first test section to the time is exits the last test section. Due to the size of this project and the anticipated wealth of data, extensive programming was developed to 1) seamlessly acquire and monitor continuous streams of structural data from each axle and test section independently using section-specific trigger sensors, 2) trigger environmental data collection concurrent with each vehicle pass, 3) and manipulate and organize the data to some extent in an effort to soften the post-processing effort.

While Chapter 4 discussed the selection and installation of the instrumentation, this chapter will describe the selection of the data acquisition hardware and software, the data acquisition logic and code, the details of some pilot scale testing that was performed prior to construction, problems encountered with the hardware, and the process of implementing the system into the field. Data collection and management is addressed in Chapter 7.

6.2 Data Acquisition Hardware

In choosing a data acquisition system, options were evaluated based on cost, product quality, processing speed, and the ability to accommodate a wide range of input modules and obtain measurements from a variety of different sensors. The data acquisition system developed for this project was manufactured by National Instruments™. The configuration consisted of one PXI-1002 chassis and three SCXI-1000 chassis to accommodate the necessary number of channels. Figure 6.1 displays the PXI chassis and two of the three SCXI chassis.

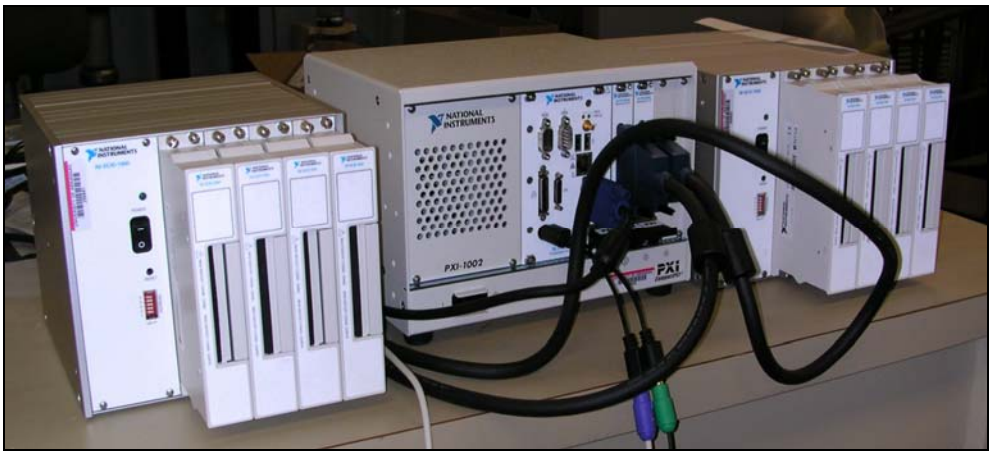

Figure 6.1 - Data Acquisition System

The PXI-1002 chassis contained four slots that were occupied by the system controller (PXI-8186) and three PXI-6052E analog input data acquisition (DAQ) cards. The controller (the internal computer) had a Pentium 4, 2.2 GHz processor that ran on Windows XP Pro. The controller was remotely accessed using the phone line, high speed DSL internet connection, and a static IP address established on site. The DSL connection was used to communicate with all hardware except for the Weigh-In-Motion and tipping bucket data loggers. It was equipped with 256 MB RAM, but it was upgraded to 1 GB to increase the processing speed for this application.

Each PXI-6052E DAQ card had the capability of sampling at a rate of 333,000 Hz, received an analog signal from each measurement module, and simultaneously digitized the signal. The 16 bit card divided the input range into 2^{16} (65,536) pieces of resolution. However, PXI-6052E DAQ cards do not isolate internal components from out of range signals, which can lead to charge saturation of amplifiers. Isolation cards are recommended for future applications since minor problems resulted during the acquisition of data as a result of this issue.

To better understand the complexity of the programming involved for this project, it is important to note that only one independent hardware command can be executed at any one time for each DAQ card, but recall that the goal was "to acquire and monitor continuous streams of structural data from all 16 test sections independently using section-specific trigger sensors". This was a challenge with only

three DAQ cards. While it would have been easier to purchase one DAQ card for each test section, it would have also increased the total cost of the project significantly.

While the PXI chassis contained the power supply and was the processing power house, each SCXI chassis was cabled to one DAQ card and contained four slots for the insertion of the measurement modules. Each measurement module was selected and purchased separately based on the number and type of gages to be monitored. Of the 10 input modules purchased for this system, one 32 channel SCXI 1102 input module (with an SCXI 1303 terminal block) was utilized for the measurement of temperature. Each channel of the SCXI 1102 was equipped with low pass filtering options and the input ranged from $\pm$ 100 mV at a gain of 1 to $\pm$ 10V at a gain of 100.

The remaining nine modules measured stresses and strains using an eight channel, SCXI 1520 analog input module (with an SCXI 1314 terminal block). This multifunction measurement module enabled a user to vary the wiring configuration, input code, and calibration equations for each channel so it easily accommodated a variety of sensor types simultaneously. A programmable 0-10V excitation source and a programmable 4-pole Butterworth filter were inclusive with each channel. There were 49 possible input ranges from $\pm$ 10 mV to $\pm$ 10 V depending on the programmable gain setting that was used.

6.3 Data Acquisition Software Overview

Lab VIEW™ 7 Express software (a package developed specifically for National Instruments hardware) was selected for this project due to the graphical programming capability, user-friendly interface, programming flexibility, and existing software libraries. The program consists of a front panel that permits the user to monitor data as it is collected, observe errors, and control the overall program flow (user interface). Additionally, it contains a block diagram that displays the graphical code. Lab VIEW™ uses tools (referred to as virtual instruments) to perform a wide variety of tasks that may include (as just a few examples) writing data to files, reading signal inputs, performing calculations, storing large groups of data in arrays, grouping

data, or continuously monitoring the time and date. A designer can use the VI tools directly or lump them together in a series of commands for simple data acquisition applications, but for projects of this scale, the designer will need to generate new code to customize the data acquisition capabilities. The modular nature of graphical programming allows portions of the code to be tested independently. Lab VIEW™ can also handle "while" loops, "for" loops, and many other features common to most programming languages. Each component of the program is graphically wired together between terminals to allow data to pass between the desired locations within the program.

6.4 Data Acquisition Logic

To best introduce the data acquisition logic, consider a two-axle vehicle traveling across all 17 test sections. As the front axle approaches the first section, the asphalt strain gage triggers the data acquisition of all gages in this section for a specified time period to capture data from the front axle (the triggering logic and programming details will be discussed in the following sections). At the end of the time period, the load response to the vehicle returns to the baseline level (in theory), and data collection terminates. Subsequently, the back axle triggers data acquisition a second time and the process is repeated. The goal was to separate the responses from each axle to soften the post-processing effort. Therefore, it was important to select a time interval that could capture the entire response while re-triggering in the time that passes between the two axles. This process was repeated in each test section as the vehicle proceeded from section 1b to 13b.

The raw data array from each axle in each test section was written to a separate file (16 files total) and then a separate file that contained minor statistical data calculated from the raw data arrays was also generated for each test section (an additional 16 files). The intent was to generate a raw data file for future reference but soften the post-processing effort by generating a complimentary file with pertinent statistical information. The environmental data was triggered by a single test section

for each vehicle pass and the environmental data was written to a separate file. In total, there were 33 total files generated for each day of testing.

The program was designed to evaluate the incoming signals in each test section against a known threshold and any data that fell below a specified magnitude was neglected. The goal was to collect data associated with meaningful responses and eliminate data associated with noise or vehicle wander. For this reason, each individual test section may have had a slightly different traffic count for the same traffic interval (some vehicle passes may not have triggered the system due to slight wander). However, the actual number of vehicle passes was monitored independently using the piezoelectric sensors.

Based on the programming logic described herein, there were several key programming challenges: the ability to incorporate an independent trigger for all 16 structural test sections using only three DAQ cards, the selection of an accurate threshold strain response to trigger data collection, the optimum sampling speed necessary to collect enough data that will sufficiently define the critical points of a response, and the sampling time interval necessary to capture the event. These parameters were investigated during a pilot scale study prior to construction and finalized during field implementation exercises preceding the traffic phase of this project. The pilot-scale test is described in the following section.

6.5 Pilot Scale Study

In order to address the programming challenges listed in the previous section prior to construction, an asphalt strain gage and a subgrade earth pressure cell were installed in the pavement structure of a newly constructed parking lot on the University campus. The instrumentation was installed using the same procedures outlined in Chapter 4, and the pavement was loaded with passenger vehicles. Each vehicle had an axle spacing equal to 2.75 m, and the pavement structure consisted of a 7.6 cm (3 in) asphalt and a 20.3 cm (8 in) aggregate layer. While the pavement structure and loading conditions were not identical to the full-scale field conditions in Marked Tree, this opportunity provided a place work out timing, triggering, and

logistical problems associated with the gages and the software. All parameters were then adjusted on-site during the field implementation of the system using the full-scale test vehicle.

There were two phases to the pilot-scale study: 1) continuous signal acquisition to assess the overall sensor response, and 2) development and evaluation of the independent triggering philosophy. During the first phase, approximately 45 data sets were acquired at different frequencies ranging between 100-500 Hz while vehicles traveled at speeds ranging from 11-89 km/h. The goal was to 1) select a sampling frequency that minimized the number of data points while ensuring that the resolution of the curve and the critical data points were not compromised, and 2) select a data collection time period that would capture the response of one axle and terminate before the arrival of the second axle for a range of axle speeds. Figure 6.2 displays a representative (unfiltered) signal acquired for one of two axles at a frequency of 500 Hz and a speed of 48 km/h. The annotations on this figure will be discussed in the following sections.

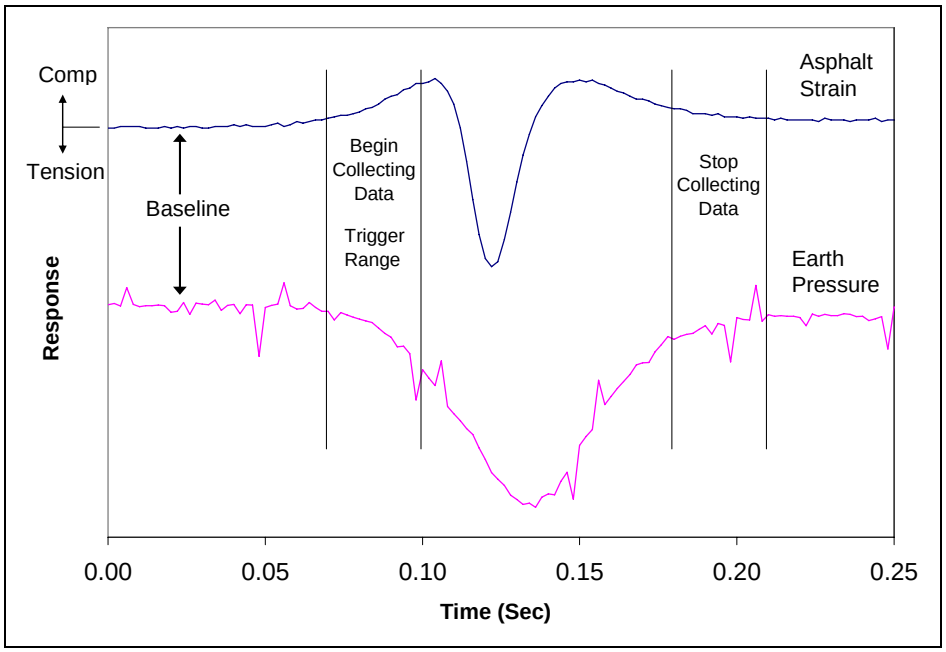

Figure 6.2 – Pilot Scale Traffic Responses in the Asphalt and Subgrade

Based on the results, there was an increase in data resolution with an increase in sampling frequency until the 400-500 Hz range. Therefore, a conservative 500 Hz sampling frequency was implemented for the duration of the full-scale field test. At the 500 Hz sampling frequency, the data acquisition (DAQ) card was utilizing only a fraction of the available capacity.

For this frequency, it was determined that a sampling time period equal to 0.11 seconds provided an adequate number of data points (500 samples/second * 0.11 seconds = 55 total data points) to fully describe the stress and strain response resulting from each axle load for vehicles traveling 32-80 km/hr (a wide range of anticipated speeds for the full-scale pavement). For vehicles traveling at slower speeds, the latter part of the response would be incomplete, and if the vehicle speed exceeded this range, the response from axle 2 would be affected. Therefore, selection of this time period was critical and was adjusted for full-scale loading conditions in the field.

The triggering philosophy was investigated during the second phase of this preliminary study. While some triggering options are typically available within software codes, a custom triggering routine was needed for this application since data obtained from 16 structural test sections was going to be processed and gages from these sections would be triggered independently using only three multiplexing DAQ cards. While the concept of triggering each test section individually made sense in theory, it was necessary to assess the feasibility of the concept in conjunction with the current hardware and instrumentation.

The asphalt strain gage was the most desirable trigger due to the near surface location of the gage. It was selected after reviewing results obtained during the first phase of this preliminary study. Figure 6.2 displays a typical asphalt strain response (top curve). At the beginning of the time interval displayed above, the axle is too far from the measurement location to produce a response higher than the baseline reading. As the axle approaches the gage, the response begins to increase until it reaches the first compression peak (just before it passes over the gage). As the axle travels over the gage, the signal rapidly descends to a tension peak, and then the compression peak spikes again but decreases as the axle moves away from the instrumentation.

Based on the data collected, it took approximately 0.03 seconds (designated as the trigger range in Figure 6.2) for the asphalt strain response to deviate from the horizontal baseline signal to a critical response level that required data acquisition, thereafter. During the axle detection process, the difference in the signal magnitude between two consecutive executions is compared to a predetermined threshold value so the trigger range must be long enough to handle at least two program executions. Since the timing of the vehicle and program initiation is arbitrary, three 0.01 second executions were conservatively enabled within the 0.03 second trigger range and five data points were evaluated during each 0.01 second execution. This enabled three detection opportunities during the trigger range.

Figure 6.3 is an exaggerated view of the initial portion of the signal in Figure 6.2 (500 Hz sampling frequency). As described in the previous paragraph, each execution of the program evaluated five data points and the complete execution (acquisition and analysis of the data) occurred over 0.01 seconds. Therefore, there are 11 executions displayed in Figure 6.3. During the first execution, the hardware reads five data points and passes them to the software program for analysis. The software subsequently took the average of those five data points and compared the average to a threshold value (which was determined to be 5 με for the pilot-scale conditions). While the software did the analysis on the first five points, the hardware initiated the second program execution, acquired an additional five data points, and passed those points on to the software as soon as the software was finished analyzing the data from the first execution. It is important to understand that one timing sequence exists for hardware and a separate timing sequence exists for software. This process was repeated to allow seamless handling of the incoming dynamic signal.

The average for each execution is displayed near the top of Figure 6.3. The averages for executions 1 and 2 are 1.3 με and 1.2 με, respectively (a difference equal to -0.1 με). Since the difference is less than the 5.0 με threshold value, the program concludes that there is no axle present and the triggering scheme continues to search for an axle during subsequent executions. In Figure 6.3, an axle was detected during execution 10 so data collection began at 0.09 seconds and continued for 0.11 seconds,

thereafter. Recall that the 0.11 second time interval and 500 Hz sampling frequency were determined during the first phase of this investigation. During the 0.11 second data collection period, triggering was disabled, but it commenced immediately following data collection.

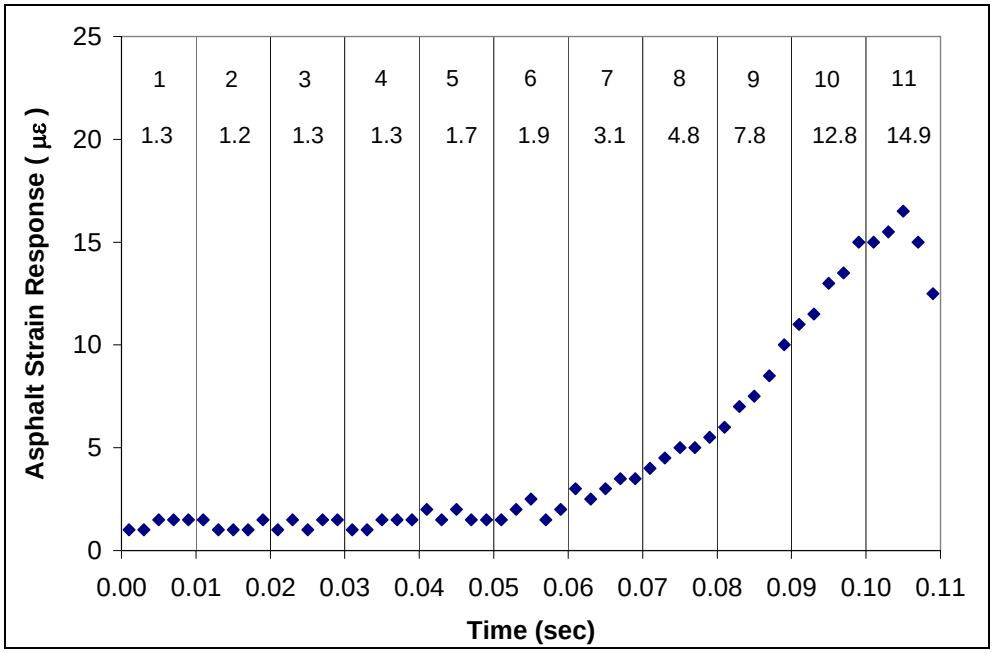

Figure 6.3 – Detailed Asphalt Strain Response

The trigger methodology developed herein is designed to detect individual vehicle axles within the trigger range depicted in Figure 6.2 to ensure peak responses (at a minimum) will be measured real-time for vehicles traveling 32-80 km/hr. Note that for full scale conditions many of the parameters were adjusted (trigger threshold, data points processed per execution, and data collection period), but the methodology remained the same. The following section will describe the technical details of the program methodology.

6.6 Data Acquisition Programming

Hierarchical (top down) procedures are an efficient programming approach, and were employed to acquire, trigger, and process data independently from each vehicle axle in each test section. Figure 6.4 displays a flow chart of the general

hierarchy and order of operations for the software program. It contains three levels of hierarchy (outlined in bold black borders on Figure 6.4). Hierarchy 1 represents the main program (which begins in the top left corner of Figure 6.4), and Hierarchy 2 and 3 represent supporting subroutines. The following sections describe each level of hierarchy in general form, but in reality, the program is much more complex. For example, "Hierarchy 1" has 17 additional "Hierarchy 2" subroutines (each additional subroutine is responsible for one test section). Within each "Hierarchy 2" subroutine, the program has multiple "Hierarchy 3" subroutines (each additional subroutine is responsible for one sensor). Figure 6.5 displays a block diagram from the program that represents a simplified form of Hierarchy 1 and serves as an example of the visual programming required to acquire continuous data acquisition signals.

Hierarchy 1 controls the main program and communicates directly with the DAQ cards. One program was developed for each DAQ card to simplify programming, and each DAQ card was associated with a single SCXI chassis. In order to generalize the following discussion, only one of the three programs is discussed. Additionally, the methodology used to handle the environmental sensors is not discussed since it is a simplified version of Hierarchy 2. The program begins in the top left corner of Figure 6.4 where and all variables are initialized. During each execution of the program (completion of Hierarchy 1, 2, and 3), the hardware acquires (X) data points every (X / frequency) seconds from each sensor, which generates a data matrix.

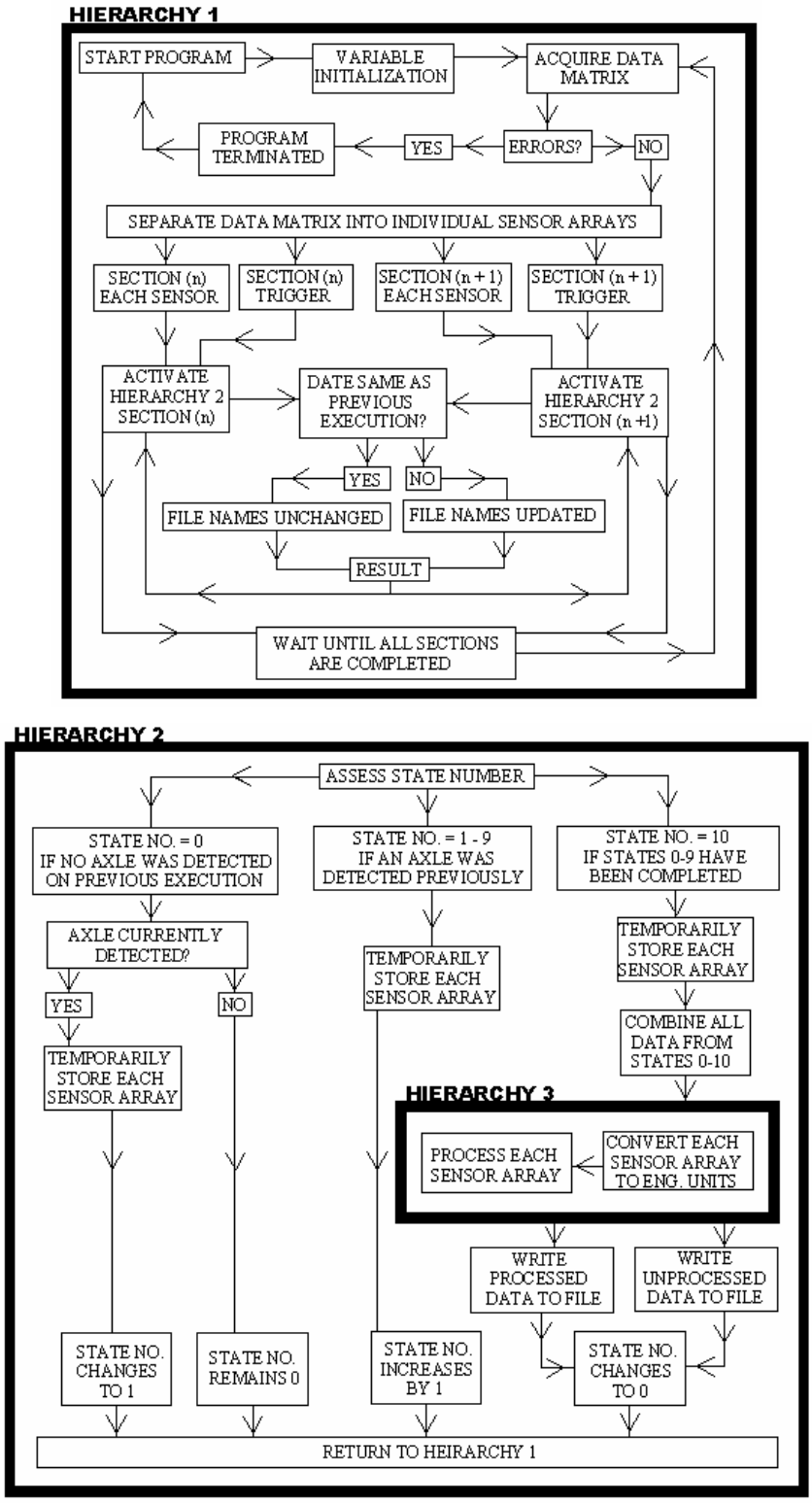

Figure 6.4 – Programming Flow Chart

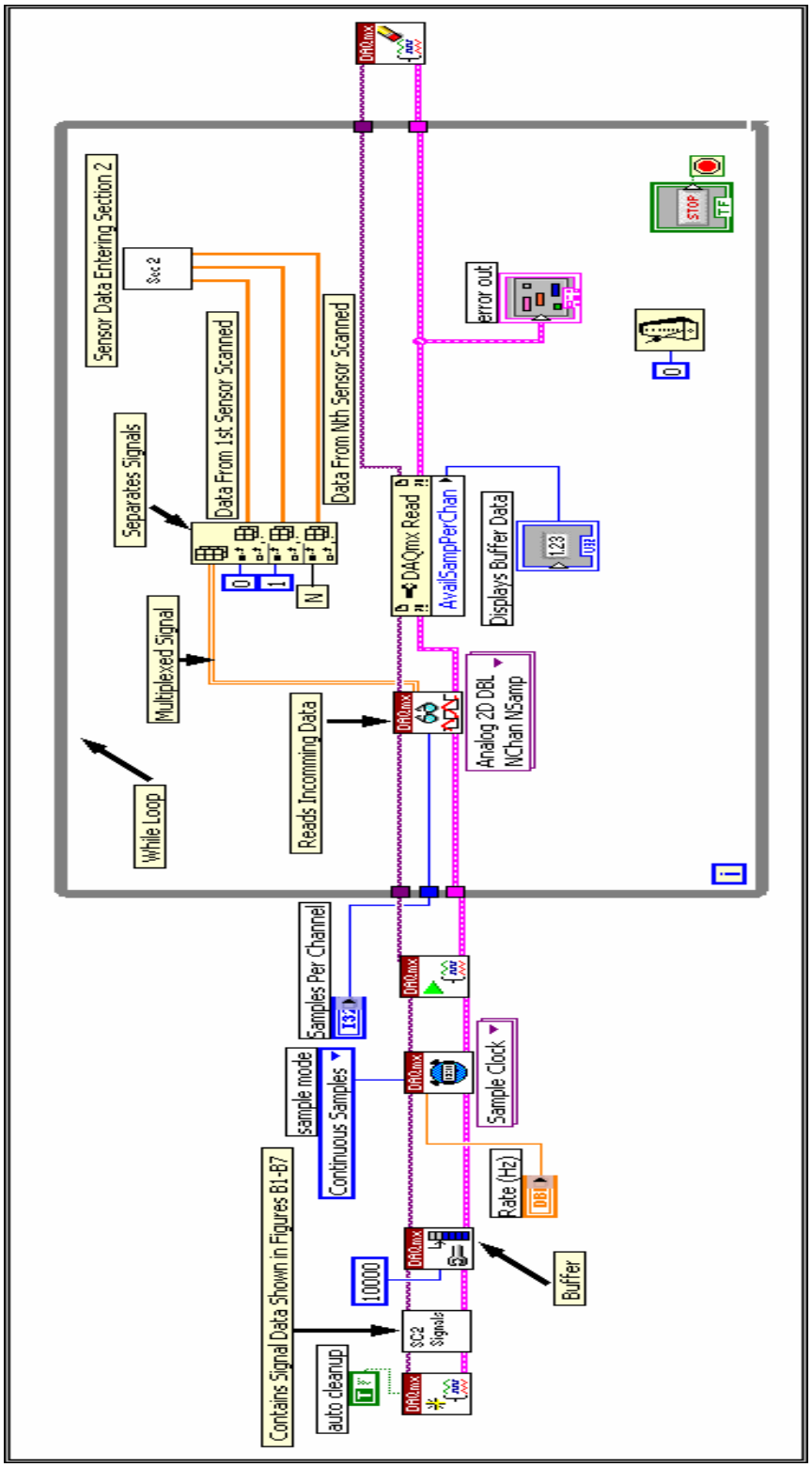

Figure 6.5 – Example Block Diagram

The data matrix is immediately separated into individual data arrays for each sensor (each array consists of (X) data points) and the sensor arrays are grouped by test section, and subsequently analyzed in Hierarchy 2. Figure 6.4 displays a generic flow chart consisting of two test sections (Section (n) and Section (n+1)) and each test section has multiple sensors in addition to a trigger sensor. As soon as Hierarchy 2 operations are activated, Hierarchy 1 operations simultaneously evaluate the time stamp and send the results to Hierarchy 2 before Hierarchy 2 operations are completed so that a new set of files can be created if the calendar date changed. Only when Hierarchy 2 and 3 operations have terminated for all test sections will the data acquisition process described above move forward and be repeated to ensure seamless monitoring of the test sections (reference the bottom of Hierarchy 1 in Figure 6.4). It is important to note that each test section is able to access a separate set of operations for Hierarchy 2 and each test section is able to perform these operations independently.

Hierarchy 2 is executed by each test section independently, and evaluates trigger status using a concept known as "state number" before the data arrays are processed in Hierarchy 3 and written to file within Hierarchy 2 operations. The "state number" allows each test section to handle the data independently without interfering with the continuous DAQ card data retrieval. The first task of Hierarchy 2 operations is to asses the "state number", which is 0 if a vehicle axle has not been detected on the previous execution and the trigger sensor is still actively searching (according to the previously discussed trigger methodology). If the trigger sensor detects a vehicle axle, the "state number" begins to climb. The "state number" increases to 1 after a vehicle axle is detected and the program begins to store data in temporary storage containers. The "state number" automatically increases by 1 for each subsequent execution time interval (X / frequency) until a "state number" equal to 10 is achieved and (11X) data points have been collected for each sensor over a total of (11X / frequency) seconds. This corresponds with the 0.11 second time interval determined during the pilot-scale study.

For example, if a test section initially detects an axle during execution 200, it will pass through "state number 0", automatically increase to "state number 1" for execution 201, and consecutively pass through "state numbers 1-9" during executions 201-209 while collecting 10 data arrays for each sensor in the test section. The last data array is collected during execution 210 (referred to as "state number 10"). The data from all 11 executions are subsequently combined, and Hierarchy 3 is accessed to process the data. The "state number" is restored to 0 before execution 211 begins and the triggering routine begins actively searching for the next vehicle axle (as previously discussed). It is important to note that all test sections are able to complete this process independently.

While Hierarchy 2 manipulated each test section, Hierarchy 3 operations handled the data processing for each sensor. Hierarchy 3 (located within Hierarchy 2) received all (11X) data points for each sensor, converted each analog signal to meaningful engineering units using laboratory determined calibration factors, and analyzed the data to determine the important statistical information (maximum, minimum, average, and standard deviation values). Subsequently, the data was written to file during Hierarchy 2 operations.

In order to ensure efficient data retrieval and management, data was processed and written to two types of files for each calendar day. While one file type contained the initial data output from each combined sensor data array of size (11X), the second file type contained the essential statistics of these data (they were referred to as "raw" and "processed" files, respectively). After the date was evaluated in Hierarchy 1, 33 files were generated and all data was appended to these files during that 24 hour period. "Raw" and "processed" data files were generated for each structural test section, and one file was generated for all environmental data (a total of 33 data files). Due to this file organization, data was easily retrieved since each file was clearly identified by date and test section.

For continuous data acquisition at a remote location, it was important to incorporate an error handling routine (in case of a buffer overflow or power surge, for example). Extensive code was incorporated into the current program to handle all

errors by allowing Hierarchy 1 operations to utilize a separate subroutine (not displayed in Figure 6.4) to clear the error with minimal data loss prior to program termination. The routine called for the main program(s) to terminate in the presence of any error. Hierarchy 1 requested the assistance of a separate Lab VIEW™ subroutine and subsequently began to shut down. The activated subroutine was programmed to wait five seconds to ensure sufficient time for Hierarchy 1 to terminate, and then requested Hierarchy 1 to re-open and continue operation.

While graphic indicators that allow the user to view real-time data for each sensor were desirable, they quickly exhausted the memory and processing speed during full-scale acquisition. As a compromise, Hierarchy 1 was equipped with code that enabled switching capabilities that permitted graphics to be turned on during pertinent program development and trouble shooting activities and turned off during full-scale acquisition to avoid buffer overflows or other undesirable processing problems.

6.7 Hardware Glitches

While developing the program, there were a few hardware problems encountered. The purpose of this section is to disclose this information in hope that the same issues can be avoided in future research projects.

1. A National Instruments™ "error code 200152" (improper hardware configuration) occurred inconsistently in one of the SCXI-1000 chassis. While this error is typically solved by re-booting the system, it did not provide a solution in this case. The entire system was re-booted multiple times and the error re-appeared each time. Due to the inconsistency of the error message, it was difficult to diagnose the problem. Initially, the system drivers for the DAQ cards were updated but this did not have an effect. Numerous code modifications were unsuccessfully tested. NI technical support indicated that the problem had to be located in one of the DAQ cards or in the SCXI-1000 chassis. Each DAQ card-SCXI chassis combination was therefore evaluated to identify the malfunctioning component (software or hardware). One of the

SCXI chassis was identified so cables were reconfigured and sensors were removed from the scan order individually until a problem was identified with one of the SCXI slots. The SXCI chassis was replaced.

2. A problem also occurred with one of the SCXI-1520 measurement modules. When channel 4 was not hooked up to a sensor but remained in the scan order, readings could not be acquired for the four subsequent sensors in the scan order regardless of the input range. However, when a sensor was engaged in channel 4, it worked properly. This module was temporarily replaced with an identical module located in a different slot and it did not error. Additionally the functionality of the terminal block was tested. After struggling with this problem, the SCXI 1520 measurement modules purchased for this project were recalled by the manufacturer. While the modules performed properly under most conditions, they were susceptible to channel skipping and the likelihood of failure increased as the number of 1520 modules increased in an SCXI chassis. Failures occurred intermittently, with symptoms varying significantly. However, the recall indicated that the most common problem was reading data from an incorrect channel during a continuous acquisition.
3. While trying to fix the SCXI-1520 measurement module problems, it was determined that the current data acquisition system did not have the ability to protect against out of range signals. If the input signal from any channel was out of range, the amplifier in the PXI-6052E DAQ card became saturated with charge and by the time the charge had dissipated, four additional channels had been scanned unsuccessfully (resulting in a loss of data). In the future, M-series (instead of E-series) DAQ cards should be utilized to isolate out of range signals.

6.8 Full-Scale Field Implementation

In preparation of the full-scale field implementation, a few tasks were completed to ensure there were no details missed. A battery back-up was incorporated into the system to prevent loss of data from power surges during the full-scale field

test. Additionally, the magnitude of the load response and the response time of each gage was verified in the laboratory after the program was complete. File appending capabilities were checked in detail to ensure that data was not lost if the program was interrupted.

The data acquisition system was transported to the field site in August of 2005 to begin field implementation. While a pilot-scale study was performed to analyze the signal response and timing requirements, an adjustment of the program parameters was necessary to accommodate the full-scale pavement structure and loading scheme. Recall that the pavement structure and the types of vehicles used during the pilot-scale study were different than the field conditions.

Data was collected and evaluated in three phases. During the first phase, the system was set to acquire signals continuously (no triggering) from variably loaded, single axle dump trucks, similar to the methods used during the first phase of the pilot-scale study. Subsequently, data was collected continuously over multiple days in the absence of traffic using various combinations of trigger thresholds, filter settings, and data points processed per execution. Lastly, data was acquired in the presence of vehicular traffic to evaluate trigger performance using the pilot-scale input parameters initially, and then these parameters were adjusted to achieve optimum performance based on full-scale testing conditions.

During this process, the asphalt strain, geosynthetic strain, and earth pressure signals were filtered. Sensors were also wired to the terminal blocks in differential (floating) mode to reduce noise infiltration. Low pass hardware filters were found to be adequate for all sensors, which was a desirable outcome since other alternatives (such as smoothing filters) alter the incoming signal and require software processing (a resource heavily taxed in the current application). Both the asphalt and geosynthetic strain signals were filtered with a 4 Hz low pass cut-off frequency. A filter for the asphalt strain signal was used to improve triggering consistency while the filter for the geosynthetic strain signal was used to decrease the signal baseline to a value that was within the precision of the instrument calibration. In both cases, filter cut-off frequencies higher and lower than 4 Hz were investigated.

Noise was more significant in the earth pressure signals, but was filtered more successfully. The primary source of noise was due to 60 Hz electromagnetic oscillations (commonly caused by electric power lines, which were located on-site). A 0.01 Hz low pass cut-off filter frequency was selected for the earth pressure signals, which significantly improved the quality of the signal acquired from vehicular traffic. Other filter cut-off frequencies were examined, but the 0.01 Hz frequency appeared to remove random noise events better than the other frequencies investigated that were below 60 Hz.

While it will be necessary to perform a final check on site, a more comprehensive noise evaluation during the pilot-scale test would have likely saved time during the field implementation phase. Long cable lengths, wire splices, and similar interferences (such as nearby power lines) can cause noise in the signals. All data acquired during this evaluation process was utilized to ensure insignificant events due to noise were not triggered without compromising the efficiency of the trigger mechanism and data collection.

In comparison to the pilot-scale study, the data collection period increased from 0.11 seconds to 0.176 seconds with the increase in axle weight due to the larger deflection basins resulting from the heavier loads, which would affect the distance that each sensor was impacted by the load. The number of data points processed per execution increased from five to eight, and the trigger threshold increased to 10 με to minimize the ability for noise to trigger the gages.

Prior to traffic, the tipping bucket was manually exercised to validate the logger response, the asphalt strain gage trigger was checked in each test section, the time stamp recorded while acquiring data was compared to the computer clock, and all trigger sensors were repetitively loaded to ensure that sensor overextension was not an issue.

The hardware and software were carefully selected, sophisticated programming logic and code was developed to independently trigger 16 different test sections using only three DAQ cards to soften the post-processing effort, a pilot-scale study was performed to establish optimum sampling and triggering parameters, multiple

hardware and software problems were encountered and eliminated, functionality checks for every component of the data acquisition system were performed, and a second preliminary investigation was performed to adjust the timing parameters for full-scale conditions. In conclusion, the data acquisition code efficiently acquired dynamic data signals using section specific triggering, it processed the data within the flow of acquisition, and it wrote the data to an organized set of files to easily compare test section performance (an improvement over previous data acquisition approaches). The next chapter will discuss the data collection and management of over 2,000 truck passes on this heavily instrumented test section.

7. DATA COLLECTION AND MANAGEMENT

7.1 Data Collection

A wealth of data was collected during three test phases (four full test weeks). All vehicles were weighed prior to each test, all structural and environmental responses were acquired during 2000 passes of a fully loaded truck (which generated approximately 800 files of data), Weigh-In-Motion data was collected continuously, FWD testing was performed before and after each test week, and rut measurements were collected using two different methods. This section describes the details of each data collection process.

Initially, data was going to be acquired from actual traffic on the frontage road, supplemented with data collected during select times of the year under controlled traffic conditions. However, the contractor fell behind schedule due to wet weather conditions and poor planning so the test sections were constructed approximately one year behind schedule (in 2005 instead of 2004). During the installation of the frontage road, the construction of a new nursing home adjacent to the site began and it was scheduled to open March 1, 2006. Unfortunately, the access road for the nursing home was designed to intersect this frontage road in Section 8, which would have compromised the integrity of the data. No longer would a vehicle be obligated to travel from one end of the test area to the other end to ensure that all test sections received the same amount of damage.

As a result, the research team was forced to adjust the current data acquisition plan and accelerate testing. AHTD agreed to delay the opening of the frontage road to keep the nursing home construction traffic off of it and allow the research team to collect data in a controlled manner before they were forced to permit access on March 1, 2006. Instead of collecting traffic on the frontage road over the course of a year, an AHTD dump truck was used to traffic the instrumented lane under controlled loading conditions over the course of three testing phases. Testing took place in September of 2005 (Phase A), December of 2005 (Phase B), and February of 2006 (Phase C), and it

encompassed four full weeks of continuous loading (over 2000 passes of a fully loaded dump truck).

During each test phase, data responses were obtained from a single axle dump truck with a 4.6 m^3 (6 yd^3) capacity, and from a tandem axle dump truck with a 7.6 m^3 (10 yd^3) capacity in the following order: 1) lightly loaded (half capacity) tandem, 2) fully loaded tandem, 3) lightly loaded (half capacity) single, and 4) fully loaded single. Approximately 10 passes were made with the lightly loaded tandem, fully loaded tandem, and lightly loaded single, and approximately 500 passes were performed with the loaded single during each test week. Full capacity was approximately equal to the legal limit for each type of rear axle. A fully loaded, single axle carried approximately 89 KN (20 kips) and a fully loaded tandem axle carried approximately 151 KN (34 kips) on the rear axle.

Before each testing phase, the dump truck was weighed at a nearby agricultural facility using a stationary scale (WEIGH-TRONIX). The scale was calibrated according to National Institute of Standards and Technology (NIST) specifications using a 107 KN (24 kip) known weight. Therefore, the maximum error in the scale reading was 0.9 KN (200 lb). Figure 7.1 displays an AHTD single axle dump truck on the scale.

Traffic cones were placed along the wheel path and an orange dot was positioned at each instrumentation location to provide a reference for the driver in an attempt to minimize wander. The AHTD was able to supply one truck and the truck was only able to gain the required speed going northbound over the instrumented test sections (which were in the southbound land) due to the status of the frontage road construction at the time that testing occurred. The truck traveled 56 km/h (35 mph) through the entire test section, and was forced to brake shortly after the test sections (since the pavement ended) and return to the start position using the non-instrumented lane before the process was repeated. There was always one member of the research team on site to observe and address problems as necessary. Two-way radios were used to facilitate communication between the research team and the driver.

Figure 7.1 – Single Axle Dump Truck on the Scale

The data acquisition system was used to acquire the responses of over 2000 passes of a loaded, single axle dump truck. During the course of testing, over 800 files of data were generated, and these files were organized in terms of test phase, test sequence, and test section. While a test phase lasted one to two work weeks (five to ten days), a test sequence was defined as the test interval corresponding to a continuous data acquisition period. Ideally, a test sequence would be one full work day, but there were a few days that had more than one sequence. For example, if the truck had mechanical problems and there was a break in data collection, the program was terminated, and a new sequence was initiated when data collection resumed.

Additional data was collected by the Weight-In-Motion system during each testing phase to provide an independent count of traffic and verify the speed of the AHTD truck. Rainfall data from the tipping bucket were also recorded using a Watch Dog data logger, and supplemented with information provided by the contractor and the AHTD inspector on site.

A controlled Falling Weight Deflectometer (FWD) evaluation of pavement condition was conducted before and after each traffic phase using a Dynatest 8000. FWD data was obtained to quantify the response of the roadway, compare FWD responses to vehicular wheel load responses, provide controlled data for use in finite element modeling (Chapter 9), and back calculate in-situ subgrade moduli. The FWD applied a 0.025-0.030 second, single impulse transient load by dropping a 100 mm (11.8 in) diameter steel plate onto the pavement. The sensors used to measure the deflection profile for the pavement surface were positioned 0, 207, 310, 639, 923, 1222, 1524, 1835, and 2136 mm from the loading point. The deflections were inversely proportional to the layer moduli (the greater the deflection, the lower the moduli).

All 16 structural test sections were loaded with the FWD using 27, 40, and 53 KN (6, 9, and 12 kip) weights at two different locations within each test section: directly over the sensor and 30 cm (1 ft) to the side of the instrumentation location. At each location, three seating drops were performed using the 27 KN (6 kips) load prior to each test, and then each of the three load levels was repeated two times for consistency (a total of nine drops). While the FWD apparatus measured surface pressures and deflections, the data acquisition system simultaneously collected data from all sensors. Figure 7.2 displays an FWD test in progress.

Figure 7.2 – Falling Weight Deflectometer Test

FWD surface pressure and deflection data were provided in a format that required minimal reduction and analysis. Figures 7.3 and 7.4 display asphalt strain and earth pressure responses during the full FWD loading sequence (all nine drops occurring at a single location). Figures 7.5 and 7.6 display the response to only one of the nine drops for the asphalt strain and earth pressure responses, respectively. The full responses in Figure 7.5 and 7.6 are equal to the distance between the signal baseline (designated with a (1) in either figure) and the signal peak (designated with a 2 in either figure). For each FWD drop in Figure 7.5 and 7.6, the weight drops and produces the maximum response (2), and then the weight bounces a few times, thereafter. The anomaly of the signal change between (1) and (3) was not fully understood.

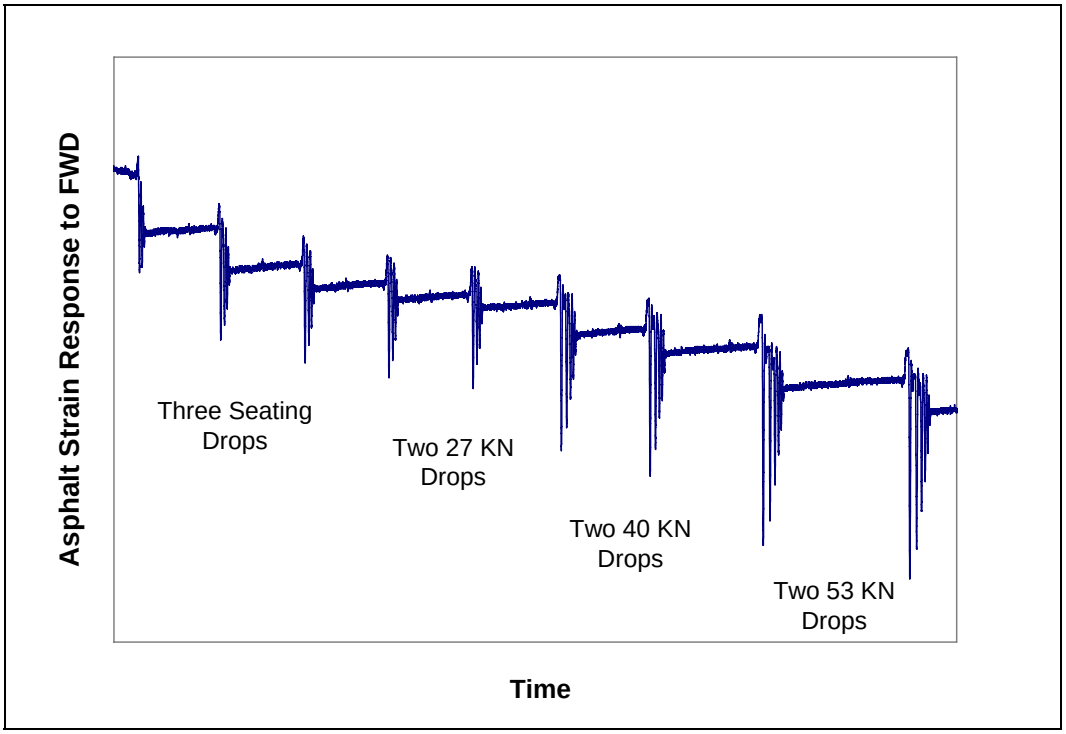

Figure 7.3 - Asphalt Strain Response to FWD Testing Sequence

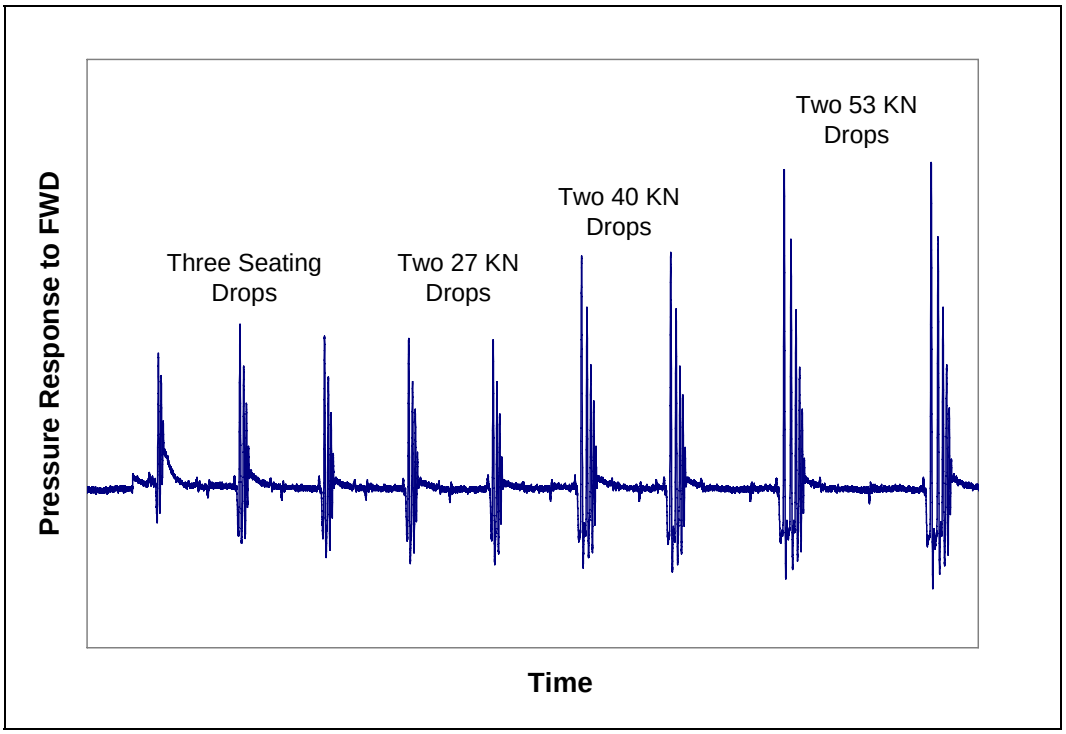

Figure 7.4 – Earth Pressure Response to FWD Testing Sequence

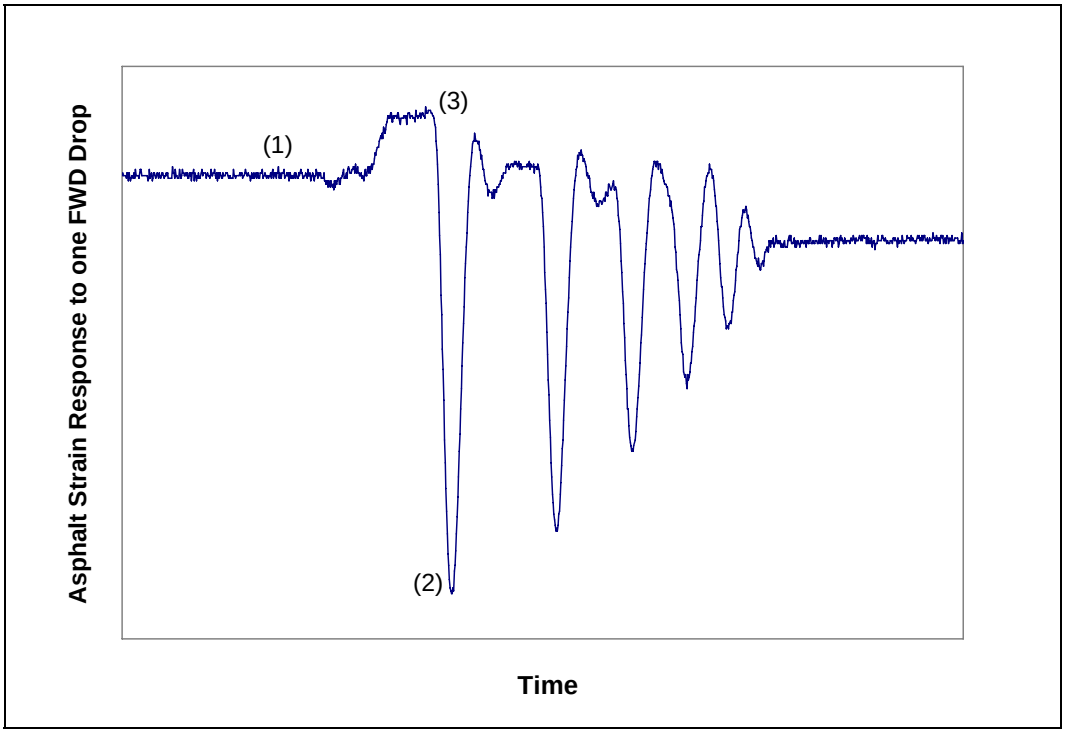

Figure 7.5 - Asphalt Strain Response to One FWD Drop

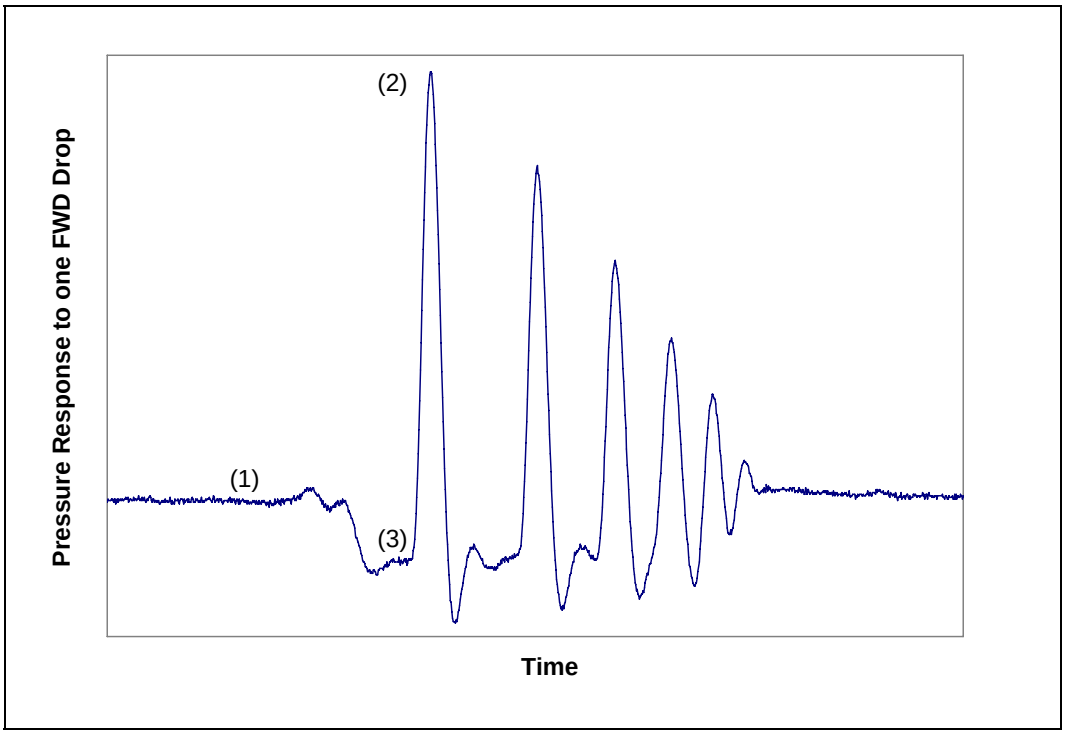

Figure 7.6 - Earth Pressure Response to One FWD Drop

In addition to FWD testing, a visual assessment of the wheel paths was performed and photographs were taken to qualitatively assess fatigue. Rut depths were measured at each sensor location using standard survey equipment before and after each traffic phase. Additional surveying was performed in the wheel rut, approximately 1.2 m (4 ft) away from the measurement location before and after Phase C.

Rut depths were also measured using the procedure outlined in ASTM E 1703 at the end of the testing phase, midway between sensors, directly over the sensors, and approximately 1.2 m (4 ft) from the sensors. Three measurements were obtained at each point using this method and the results were averaged.

During the last two traffic phases, coring was performed in the transition section and samples of the crushed stone and subgrade surface were obtained to determine an accurate value of in-situ moisture content (Figure 7.7).

Figure 7.7 – Asphalt Coring

7.2 File Identification and Description

The data acquisition system was programmed to generate 33 Lab VIEW™ files during each test sequence, and there was 1 - 2 test sequences per day. Of these 33 files, 16 files contained the raw data arrays (one file for each structural test section), 16 files contained the processed data from the raw data arrays (one file for each structural test section), and there was one environmental file. There were a total of 24 sequences generated during four weeks of testing, and a total of 792 files were generated by the data acquisition system. Additionally, one file was generated by the Weigh-In-Motion system for each test phase, and the rainfall data was downloaded as needed.

All 33 files were subsequently identified and formatted. The file name included a description of the file type (environmental, raw data, or processed data), measurement location (test section), and the full date (day of the week, month, day, and year). A new suite of 33 files was generated for each of the 24 test sequences. If

data acquisition had been performed continuously, a new suite of files would be generated every 24 hours to allow for easy organization, storage, retrieval, manipulation, and analysis of the data.

"Raw" data files contained the unprocessed data from each sensor in each test section. Each raw file included a counter, a $\pm$ 55 ms time stamp, and multiple data points for each sensor in that test section as a result of each vehicle axle load. The counter recorded the number of times that each sensor was triggered, which was not necessarily equal to the number of axles that passed through the test section. For example, the number of recorded axles could have been higher than the true count if the data acquisition system was triggered by noise or it could have been lower if a vehicle wandered from the predetermined wheel path and failed to trigger the system all together. For this reason, the Weigh-In-Motion system was utilized to provide an independent count of traffic. The responses recorded in the "Raw" data files were used to calculate key statistical information (maximums, minimums, and standard deviations) for each sensor to soften the post-processing and data manipulation effort. The results of the statistical calculations are reported in the "Processed" data files.

Table 7.1 displays the output file reference table. Column 1 displays the type of file and corresponding test section. For example, "P1b", "R1b", and "Env" represents the "Processed" file for Section 1b, the "Raw" data file for Section 1b, and the file that summarizes all environmental data, respectively. The remaining columns in Table 7.1 detail the type of data that was calculated or the type of gage responses acquired from each test section.

Table 7.1 – Data Acquisition Output Format

File	33 Files/Day: 16 Processed, 16 Raw, 1 Environmental														
P1b	AS_max	AS_min	AS_blm	EPC_B_max	EPC_B_min	EPC_B_blm	EPC_S_max	EPC_S_min	EPC_S_blm	GT_max	GT_min	GT_blm			
P1a	AS_max	AS_min	AS_blm	EPC_B_max	EPC_B_min	EPC_B_blm	EPC_S_max	EPC_S_min	EPC_S_blm	GG_max	GG_min	GG_blm			
P1	AS_max	AS_min	AS_blm	EPC_B_max	EPC_B_min	EPC_B_blm	EPC_S_max	EPC_S_min	EPC_S_blm	AS_7_avg	AS_7_stdev	EPC_S_7_avg	EPC_S_7_stdev		
P2	AS_max	AS_min	AS_blm	EPC_B_max	EPC_B_min	EPC_B_blm	EPC_S_max	EPC_S_min	EPC_S_blm	GT_max	GT_min	GT_blm			
P3	AS_max	AS_min	AS_blm	EPC_B_max	EPC_B_min	EPC_B_blm	EPC_S_max	EPC_S_min	EPC_S_blm	GT_max	GT_min	GT_blm			
P4	AS_max	AS_min	AS_blm	EPC_B_max	EPC_B_min	EPC_B_blm	EPC_S_max	EPC_S_min	EPC_S_blm	GT_max	GT_min	GT_blm			
P5	AS_max	AS_min	AS_blm	EPC_B_max	EPC_B_min	EPC_B_blm	EPC_S_max	EPC_S_min	EPC_S_blm	GT_max	GT_min	GT_blm	GG_max	GG_min	GG_blm
P6	AS_max	AS_min	AS_blm	EPC_B_max	EPC_B_min	EPC_B_blm	EPC_S_max	EPC_S_min	EPC_S_blm	GG_max	GG_min	GG_blm			
P8	AS_max	AS_min	AS_blm	EPC_S_max	EPC_S_min	EPC_S_blm	GG_max	GG_min	GG_blm						
P9	AS_max	AS_min	AS_blm	EPC_S_max	EPC_S_min	EPC_S_blm	GT_max	GT_min	GT_blm	GG_max	GG_min	GG_blm			
P10	AS_max	AS_min	AS_blm	EPC_S_max	EPC_S_min	EPC_S_blm	GT_max	GT_min	GT_blm	GTW1_max	GTW1_min	GTW1_blm	GTW2_max	GTW2_min	GTW2_blm
										GTW3_max	GTW3_min	GTW3_blm	GTW4_max	GTW4_min	GTW4_blm
P11	AS_max	AS_min	AS_blm	EPC_S_max	EPC_S_min	EPC_S_blm	GT_max	GT_min	GT_blm						
P12	AS_max	AS_min	AS_blm	EPC_S_max	EPC_S_min	EPC_S_blm	GT_max	GT_min	GT_blm	GGTC7_avg	GGTC7_stdev	GTNWTC7_avg	GTNWTC7_stdev	GTWTC7_avg	GTWTC7_stdev
P13	AS_max	AS_min	AS_blm	EPC_S_max	EPC_S_min	EPC_S_blm									
P13a	AS_max	AS_min	AS_blm	EPC_S_max	EPC_S_min	EPC_S_blm	GG_max	GG_min	GG_blm						
P13b	AS_max	AS_min	AS_blm	EPC_S_max	EPC_S_min	EPC_S_blm	GT_max	GT_min	GT_blm	GGTCa7_avg	GGTCa7_stdev	GTWTCa7_avg	GTWTCa7_stdev		
Env	TH_A1	TH_A2	TH_A3	TH_B1	TH_B2	TH_S1	TH_S2	TH_Air	TH_Box	TH_D1	TH_D2	w_B	w_S	U_B	U_S
R1b	AS	EPC_B	EPC_S	GT											
R1a	AS	EPC_B	EPC_S	GG											
R1	AS	EPC_B	EPC_S	AS_7	EPC_S_7										
R2	AS	EPC_B	EPC_S	GT											
R3	AS	EPC_B	EPC_S	GT											
R4	AS	EPC_B	EPC_S	GT											
R5	AS	EPC_B	EPC_S	GT	GG										
R6	AS	EPC_B	EPC_S	GG											
R8	AS	EPC_S	GG												
R9	AS	EPC_S	GT	GG											
R10	AS	EPC_S	GT	GTW1	GTW2	GTW3	GTW4								
R11	AS	EPC_S	GT												
R12	AS	EPC_S	GT	GGTC7	GTNWTC7	GTWTC7									
R13	AS	EPC_S													
R13a	AS	EPC_S	GG												
R13b	AS	EPC_S	GT	GGTCa7	GTWTCa7										

The definition of each acronym used to describe the output in Table 7.1 is defined in Table 7.2. For the "Processed" files, one acronym from the top half of Table 7.2 is combined with one acronym from the bottom half of Table 7.2. For example, the "maximum" data point measured from one vehicle axle response acquired by the asphalt strain gage located in Section 1b will be displayed in the first output data column for the Section 1b "Processed" file (AS_max). For the "Raw" and "Environmental" data files, one acronym from the top half of Table 7.2 is utilized to describe the output parameters. For example, an array of asphalt strain gage responses will consume the first portion of data in the Section 1b raw data file.

Table 7.2 – Data Acquisition Nomenclature

Instrumentation	
Acronym	*Description*
AS	Asphalt strain gage
EPC_B	Earth Pressure Cell (Base)
EPC_S	Earth Pressure Cell (Subgrade)
GT	Geotextile Strain
GG	Geogrid Strain
GTW	Geotextile Strain Wander
GGTC	Geogrid Strain Temperature Compensation
GTNWTC	Non-Woven Geotextile Temperature Compensation
GTWTC	Woven Geotextile Temperature Compensation
TH	T-type Thermocouple
w	Moisture Content Probe
U	Pore Water Pressure Piezometer
Statistical Information	
Acronym	*Description*
avg	Average
blm	Base Line Mean
max	Maximum
min	Minimum
stdev	Standard Deviation

While the "Environmental" file listed in Table 7.1 contained all temperature, moisture content, and piezometer data, the rainfall data were acquired separately using a WatchDog data logger so precipitation information was downloaded on site using

the SpecWare software package. Each data line included the day of the month, number of hours that passed since midnight, number of minutes that passed since the last full hour, and the amount of rainfall recorded during a preset time interval.

The Weigh-In-Motion data was downloaded by the AHTD and file printouts were forwarded to the University as requested. The printouts provided a count of vehicle traffic independent of the data acquisition system, which was useful during the filtering process.

7.3 File conversion and Hierarchy

The Lab VIEW™ files (*.lvm file format) were converted into a usable platform for data reduction and analysis using Microsoft Excel software. The data acquisition files were imported into Excel and saved as Excel workbooks while retaining the same file names. One copy of this file was archived to protect the original data, and one file was used to carry out the following data manipulation.

After the files were formatted, they were organized in the following hierarchy. There was a folder for each of the three test phases (Phase A, B, and C). For each test phase, there were subfolders for each test sequence (Sequence 1-11, for example). In each test sequence folder, there were sub-folders for each of the 17 test sections and one folder that contained all original Lab VIEW™ files. For example, the file hierarchy for Phase B, Sequence 2, Section 5 is presented in Figure 7.8. The Lab VIEW™ "*.lvm" files were placed in the top "Labview Files" folder in Sequence 2 of Phase B, the "Environmental" file was placed in the Section 7 folder (the transition section), and the "Processed" and "Raw" data files were placed in the corresponding test section folders.

7.4 File Formatting

The input format (type and order) varied in each "Processed" file (Table 7.1) so one data reduction template file (containing a series of Excel Macro functions) was created separately for each test section to format the initial data prior to manipulation. The data from each "Processed" and "Environmental" data file was subsequently

copied into the appropriate data reduction template file (depending on test section), the macros were executed in each file to format the data, and the file was renamed to preserve the original data reduction template file. For example, the formatted file (post macro execution) for the "P5, Tues, Dec 13, 2005.xls" file (Phase B, Sequence 7, Section 5) is illustrated in Figure 7.9. Row 1 of the Excel spreadsheet contains user-friendly column headings, columns "F", "G" and "H" were inserted to assess the axle location and calculate the asphalt and ambient temperature from temperature regressions to be performed in a subsequent step, and all data was formatted.

After each file was formatted, an AutoFilter was created for each column of the spreadsheet by highlighting the full data range and enabling the AutoFilter function. The AutoFilter is an Excel function that enables the user to sort spreadsheet data using advance input parameters.

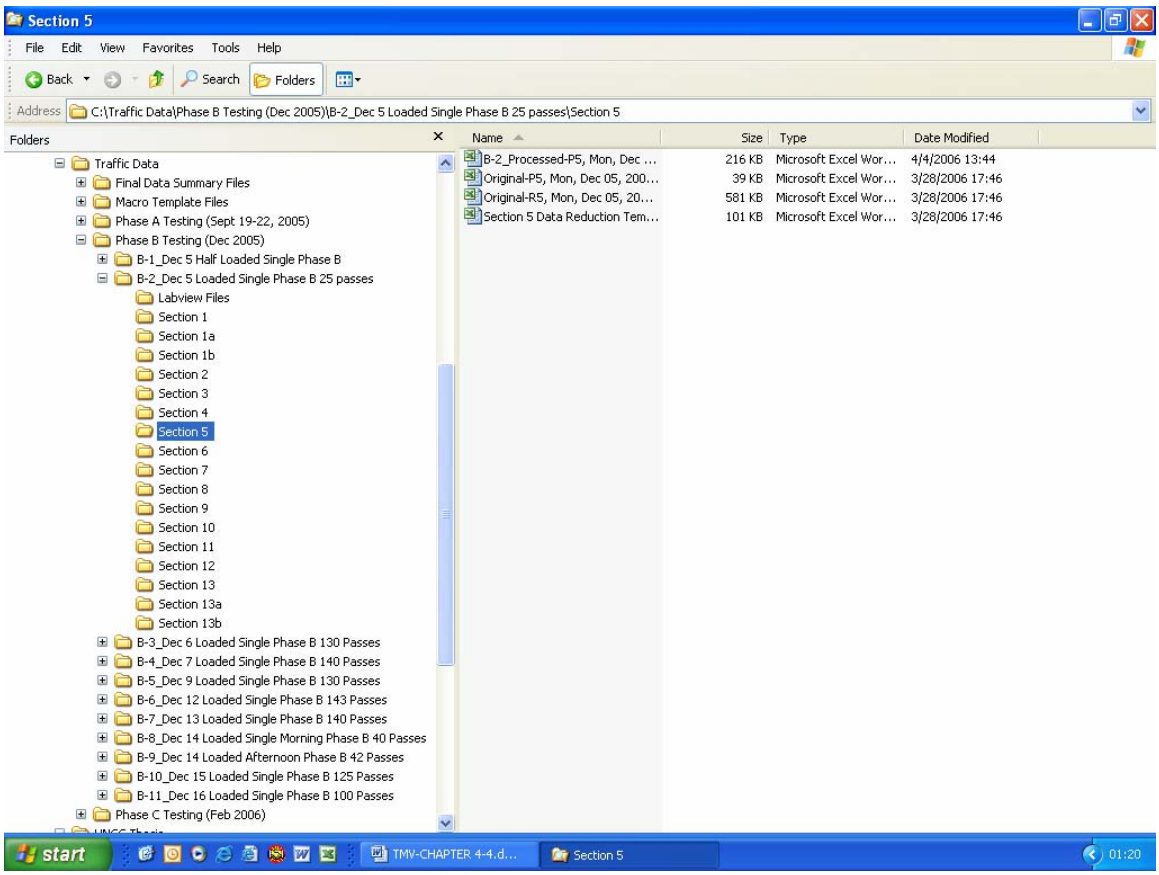

Figure 7.8 – File Hierarchy for Phase B, Sequence 2, Section 5

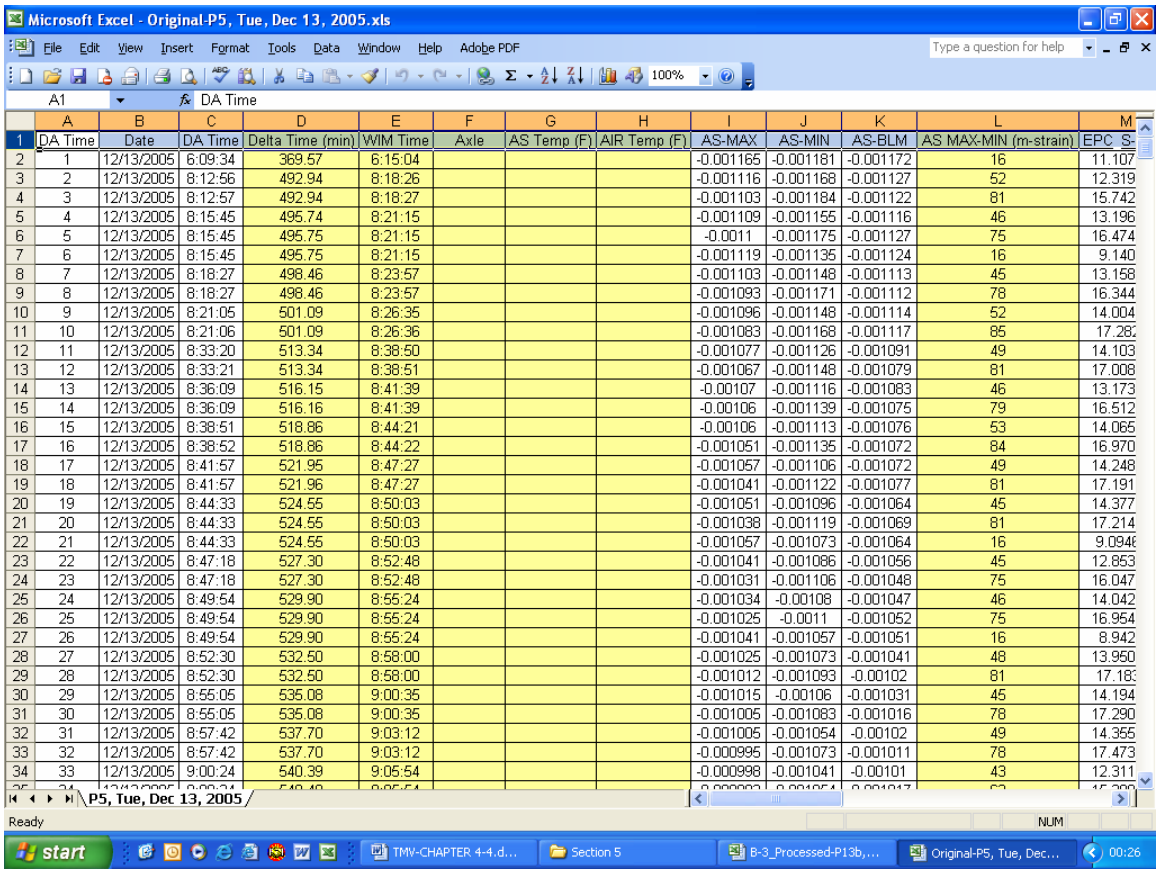

Microsoft Excel - Original-P5, Tue, Dec 13, 2005.xls

File Edit View Insert Format Tools Data Window Help Adobe PDF

A1 DA Time

	A	B	C	D	E	F	G	H	I	J	K	L	M
1	DA Time	Date	DA Time	Delta Time (min)	WIM Time	Axle	AS Temp (F)	AIR Temp (F)	AS-MAX	AS-MIN	AS-BLM	AS MAX-MIN (m-strain)	EPC S-
2	1	12/13/2005	6:09:34	369.57	6:15:04				-0.001165	-0.001181	-0.001172	16	11.107
3	2	12/13/2005	8:12:56	492.94	8:18:26				-0.001116	-0.001168	-0.001127	52	12.319
4	3	12/13/2005	8:12:57	492.94	8:18:27				-0.001103	-0.001184	-0.001122	81	15.742
5	4	12/13/2005	8:15:45	495.74	8:21:15				-0.001109	-0.001155	-0.001116	46	13.196
6	5	12/13/2005	8:15:45	495.75	8:21:15				-0.0011	-0.001175	-0.001127	75	16.474
7	6	12/13/2005	8:15:45	495.75	8:21:15				-0.001119	-0.001135	-0.001124	16	9.140
8	7	12/13/2005	8:18:27	498.46	8:23:57				-0.001103	-0.001148	-0.001113	45	13.158
9	8	12/13/2005	8:18:27	498.46	8:23:57				-0.001093	-0.001171	-0.001112	78	16.344
10	9	12/13/2005	8:21:05	501.09	8:26:35				-0.001096	-0.001148	-0.001114	52	14.004
11	10	12/13/2005	8:21:06	501.09	8:26:36				-0.001083	-0.001168	-0.001117	85	17.282
12	11	12/13/2005	8:33:20	513.34	8:38:50				-0.001077	-0.001126	-0.001091	49	14.103
13	12	12/13/2005	8:33:21	513.34	8:38:51				-0.001067	-0.001148	-0.001079	81	17.008
14	13	12/13/2005	8:36:09	516.15	8:41:39				-0.00107	-0.001116	-0.001083	46	13.173
15	14	12/13/2005	8:36:09	516.16	8:41:39				-0.00106	-0.001139	-0.001075	79	16.512
16	15	12/13/2005	8:38:51	518.86	8:44:21				-0.00106	-0.001113	-0.001076	53	14.065
17	16	12/13/2005	8:38:52	518.86	8:44:22				-0.001051	-0.001135	-0.001072	84	16.970
18	17	12/13/2005	8:41:57	521.95	8:47:27				-0.001057	-0.001106	-0.001072	49	14.248
19	18	12/13/2005	8:41:57	521.96	8:47:27				-0.001041	-0.001122	-0.001077	81	17.191
20	19	12/13/2005	8:44:33	524.55	8:50:03				-0.001051	-0.001096	-0.001064	45	14.377
21	20	12/13/2005	8:44:33	524.55	8:50:03				-0.001038	-0.001119	-0.001069	81	17.214
22	21	12/13/2005	8:44:33	524.55	8:50:03				-0.001057	-0.001073	-0.001064	16	9.094
23	22	12/13/2005	8:47:18	527.30	8:52:48				-0.001041	-0.001086	-0.001056	45	12.853
24	23	12/13/2005	8:47:18	527.30	8:52:48				-0.001031	-0.001106	-0.001048	75	16.047
25	24	12/13/2005	8:49:54	529.90	8:55:24				-0.001034	-0.00108	-0.001047	46	14.042
26	25	12/13/2005	8:49:54	529.90	8:55:24				-0.001025	-0.0011	-0.001052	75	16.954
27	26	12/13/2005	8:49:54	529.90	8:55:24				-0.001041	-0.001057	-0.001051	16	8.942
28	27	12/13/2005	8:52:30	532.50	8:58:00				-0.001025	-0.001073	-0.001041	48	13.950
29	28	12/13/2005	8:52:30	532.50	8:58:00				-0.001012	-0.001093	-0.00102	81	17.183
30	29	12/13/2005	8:55:05	535.08	9:00:35				-0.001015	-0.00106	-0.001031	45	14.194
31	30	12/13/2005	8:55:05	535.08	9:00:35				-0.001005	-0.001083	-0.001016	78	17.290
32	31	12/13/2005	8:57:42	537.70	9:03:12				-0.001005	-0.001054	-0.00102	49	14.355
33	32	12/13/2005	8:57:42	537.70	9:03:12				-0.000995	-0.001073	-0.001011	78	17.473
34	33	12/13/2005	9:00:24	540.39	9:05:54				-0.000998	-0.001041	-0.00101	43	12.311

P5, Tue, Dec 13, 2005

Ready NUM

start TMV-CHAPTER 4-4.d... Section 5 B-3_Processed-P13b,... Original-P5, Tue, Dec... 00:26

Figure 7.9 – Formatted File for Section 5

7.5 Temperature Analysis

There was one "Environmental" file in each test sequence folder and it contained the temperature, moisture content, and pore pressure data generated for each vehicle pass. In other words, there was only one environmental data file for all 16 structural test sections. Therefore, a regression line was established for the ambient and asphalt temperature data using a polynomial function, and the equations for the trend lines were programmed into the appropriate columns (columns G and H in Figure 7.9) in each "Processed" data file to determine the ambient and asphalt temperatures for every data point in every file. The order of the polynomial was adjusted until the R^2 value was as close to 1 as possible. Figure 7.10 illustrates a typical temperature plot for Phase B, Sequence 7. The trend line, polynomial

equation, and R^2 information are displayed on this figure. Tables 7.3 and 7.4 summarize the regression equations that were programmed into the ambient and asphalt temperature columns in each file for all three phases.

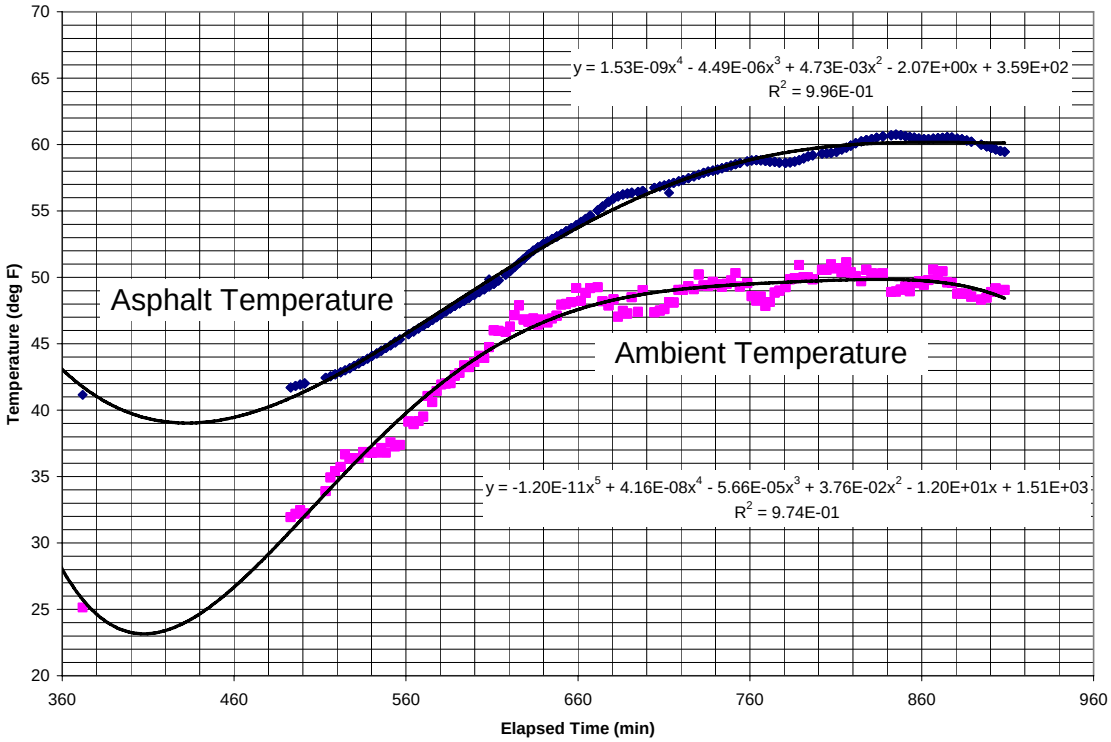

Figure 7.10 – Sequence B-7 Ambient and Asphalt Temperature Curves

7.6 Data Filtering

The data was filtered to eliminate any data rows that represented noise rather than a true signal response. Filtering was accomplished using the data acquired from the earth pressure cells in the subgrade (EPC_S). A two stage filtering process was established after some refinement to the method. The goal of the first stage was to identify and filter the majority of the meaningless data without purging traffic data. First, the Excel "AutoFilter" feature (a pull down menu) was used to view all values within that column of data (EPC_S), and the lowest value in the higher group of numbers was used if a gap existed between two clearly defined groups of numbers. For example, if a group of data ranging from 0 to 1.4 existed and another group of values ranging from 4.5 to 11 was observed, all rows that had a value less than 4.5 in

the EPC_S column would be filtered (or hidden). Secondly, the earth pressure data in each remaining row was manually evaluated until the number of axles recorded by the data acquisition system closely matched the number of axles independently counted by the Weigh-In-Motion system. The goal was to identify two axle readings for each vehicle pass.

Table 7.3 – Ambient Temperature Regression Equations

Phase-Sequence	*Ambient Temperature Regression Equation*	R^2
A-1	$-4.315E\text{-}04\ t^2 + 0.63\ t - 141.62$	0.7938
A-2	$-1.33E\text{-}04\ t^2 + 0.2412\ t - 11.66$	0.6555
A-3	$-1.18E\text{-}04\ t^2 + 0.2089\ t + 6.04$	0.9424
A-4	$-8.2E\text{-}05\ t^2 + 0.1601\ t + 17.64$	0.9715
A-5	$4.29E\text{-}05\ t^2 - 0.0831\ t + 138.61$	0.2376
A-6	$4.29E\text{-}05\ t^2 - 0.0831\ t + 138.61$	0.2376
B-1	$-3.33E\text{-}03\ t^2 + 5.21\ t - 2003.68$	0.3988
B-2	$-7.27E\text{-}05\ t^3 + 0.191\ t^2 - 168.48\ t + 49354.09$	0.4259
B-3	$-1.16E\text{-}04\ t^2 + 0.21064201\ t - 44.74$	0.9832
B-4	$-9.52E\text{-}05\ t^2 + 0.16\ t - 30.79$	0.9763
B-5	$1.96E\text{-}05\ t^2 + 0.004.604343\ t + 9.89$	0.9145
B-6	$-1.03E\text{-}04\ t^2 + 0.17081927\ t - 13.39$	0.9631
B-7	$-1.20E\text{-}11\ t^5 + 4.16E\text{-}08\ t^4 - 5.66E\text{-}05\ t^3 + 0.04\ t^2 - 12.04\ t + 1505.35$	0.9737
B-8	$1.01E\text{-}06\ t^3 - 1.48E\text{-}03\ t^2 + 0.73\ t - 74.83$	0.9886
B-9	$-7.77\ t^3 + 1.67E\text{-}03\ t^2 - 1.18\ t + 324.54$	0.7851
B-10	$-1.32E\text{-}04\ t^2 + 0.22\ t - 38.08$	0.9846
B-11	$-1.85E\text{-}04\ t^2 + 0.28\ t - 58.54$	0.9610
C-1	$2.58E\text{-}04\ t^3 – 0.51\ t^2 + 337.61\ t - 74250.72$	0.5799
C-2	$-1.15E\text{-}06\ t^3 + 2.78E\text{-}03\ t^2 - 2.22\ t + 633.029$	0.2358
C-3	$2.33E\text{-}04\ t^2 – 0.19\ t + 70.56$	0.9913
C-4	$1.14E\text{-}04\ t^2 – 0.20\ t + 131.28$	0.5433
C-5	$-9.09E\text{-}06\ t^2 + 0.04\ t + 10.55$	0.9763
C-6	$-5.35E\text{-}05\ t^2 + 0.11\ t - 11.12$	0.9872
C-7	$-9.43E\text{-}07\ t^3 + 1.65E\text{-}03\ t^2 - 0.88\ t + 182.53$	0.9942

Subsequently, a “1” was assigned to each identified front axle, a “2” was assigned to each identified back axle, and a “3” was assigned to a data row that contained only one reading for each vehicle pass. For example, rows 102 and 103 in Figure 7.11 both have the same time stamp (9:52:25 in Column E), and there were only two rows that corresponded to this time stamp after the filtering process was completed so axle 1 and 2 were easily identified and labeled in Column F of this file. Occasionally, only one data line was available for a time stamp so the axle

identification was unclear. For this case, the row was assigned a value equal to 3, indicating it could be either the front or rear axle (see rows 96, 97 and 98 in Figure 7.11). For these cases, the same response was assigned to both the front and the back axle. If more than two data lines still existed for the same time stamp after this evaluation was complete, either the initial filter was re-evaluated or engineering judgment was used to determine which line was "noise".

Table 7.4 – Asphalt Temperature Regression Equations

Phase-Sequence	*Asphalt Temperature Regression Equation*	R^2
A-1	$1.07E\text{-}04\ t^2 - 0.0257465t + 72.75$	0.9999
A-2	$-2.81E\text{-}04\ t^2 + 0.53\ t - 126.40$	0.9970
A-3	$-4.4E\text{-}07\ t^3 + 8.5E\text{-}04\ t^2 - 0.44\ t + 154.48$	0.9960
A-4	$-5.03E\text{-}07\ t^3 + 9.9E\text{-}04\ t^2 - 0.54\ t + 177.56$	0.9957
A-5	$-2.33E\text{-}04\ t^2 + 0.44\ t - 83.96$	0.9821
A-6	$-2.33E\text{-}04\ t^2 + 0.44\ t - 83.96$	0.9821
B-1	$-0.001.77E\text{-}03\ t^2 + 2.84\ t - 1081.40$	0.9034
B-2	$-0.0002.49E\text{-}04\ t^2 + 0.43\ t - 126.25$	0.7912
B-3	$-6.65E\text{-}07\ t^3 + 1.26\ t^2 - 0.69\ t + 153.09$	0.9994
B-4	$3.71E\text{-}09\ t^4 - 1.06E\text{-}05\ t^3 + 0.01\ t^2 - 4.96\ t + 841.06$	0.9938
B-5	$-6.52E\text{-}10\ t^4 + 1.21E\text{-}06\ t^3 - 6.76E\text{-}04\ t^2 + 0.13\ t + 22.55$	0.9986
B-6	$7.53E\text{-}10\ t^4 - 2.52E\text{-}06\ t^3 + 2.92E\text{-}03\ t^2 - 1.34\ t + 253.16$	0.9994
B-7	$1.53E\text{-}09\ t^4 - 4.49E\text{-}06\ t^3 + 4.73E\text{-}03\ t^2 - 2.07\ t + 3.58.73$	0.9960
B-8	$3.05E\text{-}07\ t^3 - 4.16E\text{-}04\ t^2 + 0.20\ t + 18.26$	0.9642
B-9	$-7.76E\text{-}09\ t^4 + 2.40E\text{-}05\ t^3 - 0.03\ t^2 + 14.21\ t - 2674.31$	0.9377
B-10	$-5.14E\text{-}07\ t^3 + 9.57E\text{-}04\ t^2 - 0.52\ t + 131.63$	0.9969
B-11	$-6.31E\text{-}07\ t^3 + 1.17E\text{-}03\ t^2 - 0.65\ t + 152.21$	0.9988
C-1	$-9.26E\text{-}05\ t^2 + 0.23\ t - 54.26$	0.9997
C-2	$-2.77E\text{-}03\ t^2 + 0.49\ t - 143.55$	0.9885
C-3	$1.30E\text{-}03\ t^2 - 0.11\ t + 68.58$	0.9952
C-4	$1.68E\text{-}06\ t^3 - 0.004.01\ t^2 + 3.16\ t - 771.42$	0.9608
C-5	$-5.77E\text{-}07\ t^3 + 0.001.10\ t^2 - 0.61\ t + 139.67$	0.9998
C-6	$8.09E\text{-}10\ t^4 - 2.76E\text{-}06\ t^3 + 3.23E\text{-}03\ t^2 - 1.49\ t + 268.06$	0.9958
C-7	$-8.40E\text{-}07\ t^3 + 1.57E\text{-}03\ t^2 - 0.87\ t + 188.50$	0.9999

After the data was filtered and the axle assignments were complete (Figure 7.11), the filtered rows (currently hidden within Excel) were backed out (unhidden) to further evaluate the data rows adjacent to the axle-type "3" responses to ensure that valid data was not filtered out. Figure 7.12 displays the same worksheet with all filtered data backed out.

Additional quality checks were performed to determine the number of "1", "2" and "3" axle assignments. If the number of axle "1" assignments was not identical to the number of axle "2" assignments, then the assignments were revisited to determine the error. This evaluation was then compared to the count provided by the Weigh-In-Motion data file and the count from the other test sections within the same test sequence. If there was a conflict between either of these, then the filtered data was further evaluated to determine the cause of error (if any). Figure 7.13 displays a summary of this evaluation in the top black box: 282 axle counts were recorded from the Weigh-In-Motion piezoelectric tubes ($N_{A\text{-}WIM}$); 141 passes were recorded for the front and for the back axles by the data acquisition system ($N_{A\text{-}DA(F/B)}$); therefore, were no missing data points ($N_{A\text{-}DA(missed)}$) for Phase B, Sequence 7, Section 3. This type of check was performed in each data file.

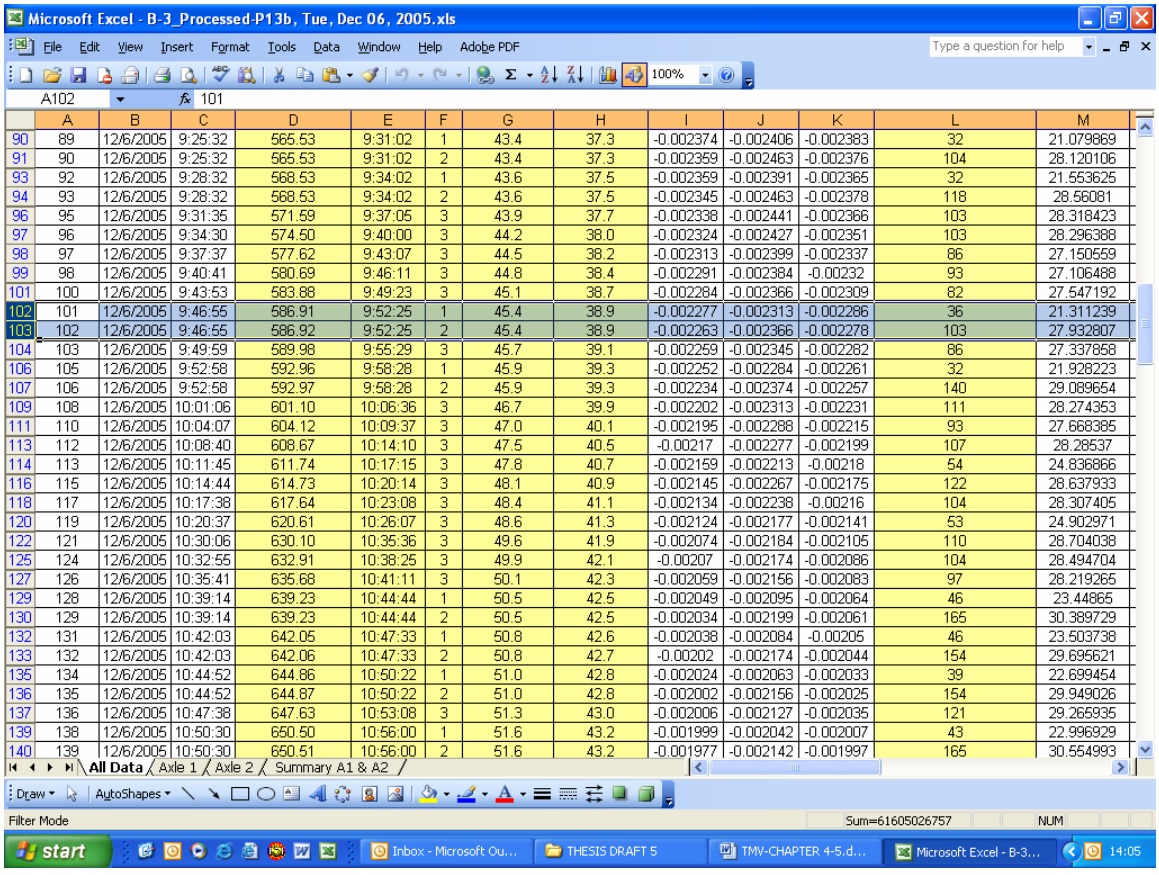

	A	B	C	D	E	F	G	H	I	J	K	L	M
90	89	12/6/2005	9:25:32	565.53	9:31:02	1	43.4	37.3	-0.002374	-0.002406	-0.002383	32	21.079869
91	90	12/6/2005	9:25:32	565.53	9:31:02	2	43.4	37.3	-0.002359	-0.002463	-0.002376	104	28.120106
93	92	12/6/2005	9:28:32	568.53	9:34:02	1	43.6	37.5	-0.002359	-0.002391	-0.002365	32	21.553625
94	93	12/6/2005	9:28:32	568.53	9:34:02	2	43.6	37.5	-0.002345	-0.002463	-0.002378	118	28.56081
96	95	12/6/2005	9:31:35	571.59	9:37:05	3	43.9	37.7	-0.002338	-0.002441	-0.002366	103	28.318423
97	96	12/6/2005	9:34:30	574.50	9:40:00	3	44.2	38.0	-0.002324	-0.002427	-0.002351	103	28.296388
98	97	12/6/2005	9:37:37	577.62	9:43:07	3	44.5	38.2	-0.002313	-0.002399	-0.002337	86	27.150559
99	98	12/6/2005	9:40:41	580.69	9:46:11	3	44.8	38.4	-0.002291	-0.002384	-0.00232	93	27.106488
101	100	12/6/2005	9:43:53	583.88	9:49:23	3	45.1	38.7	-0.002284	-0.002366	-0.002309	82	27.547192
102	101	12/6/2005	9:46:55	586.91	9:52:25	1	45.4	38.9	-0.002277	-0.002313	-0.002286	36	21.311239
103	102	12/6/2005	9:46:55	586.92	9:52:25	2	45.4	38.9	-0.002263	-0.002366	-0.002278	103	27.932807
104	103	12/6/2005	9:49:59	589.98	9:55:29	3	45.7	39.1	-0.002259	-0.002345	-0.002282	86	27.337858
106	105	12/6/2005	9:52:58	592.96	9:58:28	1	45.9	39.3	-0.002252	-0.002284	-0.002261	32	21.928223
107	106	12/6/2005	9:52:58	592.97	9:58:28	2	45.9	39.3	-0.002234	-0.002374	-0.002257	140	29.089654
109	108	12/6/2005	10:01:06	601.10	10:06:36	3	46.7	39.9	-0.002202	-0.002313	-0.002231	111	28.274353
111	110	12/6/2005	10:04:07	604.12	10:09:37	3	47.0	40.1	-0.002195	-0.002288	-0.002215	93	27.668385
113	112	12/6/2005	10:08:40	608.67	10:14:10	3	47.5	40.5	-0.00217	-0.002277	-0.002199	107	28.28537
114	113	12/6/2005	10:11:45	611.74	10:17:15	3	47.8	40.7	-0.002159	-0.002213	-0.00218	54	24.836866
116	115	12/6/2005	10:14:44	614.73	10:20:14	3	48.1	40.9	-0.002145	-0.002267	-0.002175	122	28.637933
118	117	12/6/2005	10:17:38	617.64	10:23:08	3	48.4	41.1	-0.002134	-0.002238	-0.00216	104	28.307405
120	119	12/6/2005	10:20:37	620.61	10:26:07	3	48.6	41.3	-0.002124	-0.002177	-0.002141	53	24.902971
122	121	12/6/2005	10:30:06	630.10	10:35:36	3	49.6	41.9	-0.002074	-0.002184	-0.002105	110	28.704038
125	124	12/6/2005	10:32:55	632.91	10:38:25	3	49.9	42.1	-0.00207	-0.002174	-0.002086	104	28.494704
127	126	12/6/2005	10:35:41	635.68	10:41:11	3	50.1	42.3	-0.002059	-0.002156	-0.002083	97	28.219265
129	128	12/6/2005	10:39:14	639.23	10:44:44	1	50.5	42.5	-0.002049	-0.002095	-0.002064	46	23.44865
130	129	12/6/2005	10:39:14	639.23	10:44:44	2	50.5	42.5	-0.002034	-0.002199	-0.002061	165	30.389729
132	131	12/6/2005	10:42:03	642.05	10:47:33	1	50.8	42.6	-0.002038	-0.002084	-0.00205	46	23.503738
133	132	12/6/2005	10:42:03	642.06	10:47:33	2	50.8	42.7	-0.00202	-0.002174	-0.002044	154	29.695621
135	134	12/6/2005	10:44:52	644.86	10:50:22	1	51.0	42.8	-0.002024	-0.002063	-0.002033	39	22.699454
136	135	12/6/2005	10:44:52	644.87	10:50:22	2	51.0	42.8	-0.002002	-0.002156	-0.002025	154	29.949026
137	136	12/6/2005	10:47:38	647.63	10:53:08	3	51.3	43.0	-0.002006	-0.002127	-0.002035	121	29.265935
139	138	12/6/2005	10:50:30	650.50	10:56:00	1	51.6	43.2	-0.001999	-0.002042	-0.002007	43	22.996929
140	139	12/6/2005	10:50:30	650.51	10:56:00	2	51.6	43.2	-0.001977	-0.002142	-0.001997	165	30.554993

Figure 7.11 – Filtered Data (Phase B, Sequence 3, Section 13b)

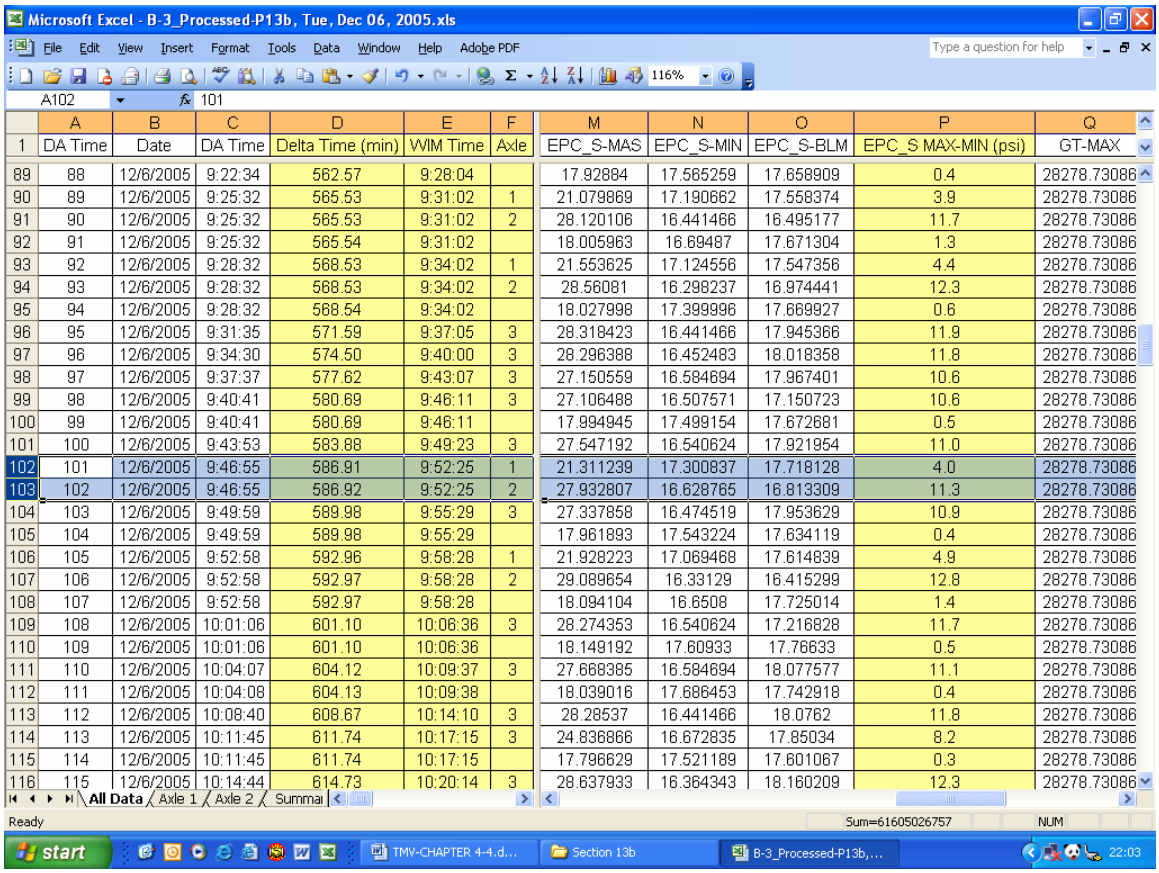

	A	B	C	D	E	F	M	N	O	P	Q
1	DA Time	Date	DA Time	Delta Time (min)	WIM Time	Axle	EPC_S-MAS	EPC_S-MIN	EPC_S-BLM	EPC_S MAX-MIN (psi)	GT-MAX
89	88	12/6/2005	9:22:34	562.57	9:28:04		17.92884	17.565259	17.658909	0.4	28278.73086
90	89	12/6/2005	9:25:32	565.53	9:31:02	1	21.079869	17.190662	17.558374	3.9	28278.73086
91	90	12/6/2005	9:25:32	565.53	9:31:02	2	28.120106	16.441466	16.495177	11.7	28278.73086
92	91	12/6/2005	9:25:32	565.54	9:31:02		18.005963	16.69487	17.671304	1.3	28278.73086
93	92	12/6/2005	9:28:32	568.53	9:34:02	1	21.553625	17.124556	17.547356	4.4	28278.73086
94	93	12/6/2005	9:28:32	568.53	9:34:02	2	28.56081	16.298237	16.974441	12.3	28278.73086
95	94	12/6/2005	9:28:32	568.54	9:34:02		18.027998	17.399996	17.669927	0.6	28278.73086
96	95	12/6/2005	9:31:35	571.59	9:37:05	3	28.318423	16.441466	17.945366	11.9	28278.73086
97	96	12/6/2005	9:34:30	574.50	9:40:00	3	28.296388	16.452483	18.018358	11.8	28278.73086
98	97	12/6/2005	9:37:37	577.62	9:43:07	3	27.150559	16.584694	17.967401	10.6	28278.73086
99	98	12/6/2005	9:40:41	580.69	9:46:11	3	27.106488	16.507571	17.150723	10.6	28278.73086
100	99	12/6/2005	9:40:41	580.69	9:46:11		17.994945	17.499154	17.672681	0.5	28278.73086
101	100	12/6/2005	9:43:53	583.88	9:49:23	3	27.547192	16.540624	17.921954	11.0	28278.73086
102	101	12/6/2005	9:46:55	586.91	9:52:25	1	21.311239	17.300837	17.718128	4.0	28278.73086
103	102	12/6/2005	9:46:55	586.92	9:52:25	2	27.932807	16.628765	16.813309	11.3	28278.73086
104	103	12/6/2005	9:49:59	589.98	9:55:29	3	27.337858	16.474519	17.953629	10.9	28278.73086
105	104	12/6/2005	9:49:59	589.98	9:55:29		17.961893	17.543224	17.634119	0.4	28278.73086
106	105	12/6/2005	9:52:58	592.96	9:58:28	1	21.928223	17.069468	17.614839	4.9	28278.73086
107	106	12/6/2005	9:52:58	592.97	9:58:28	2	29.089654	16.33129	16.415299	12.8	28278.73086
108	107	12/6/2005	9:52:58	592.97	9:58:28		18.094104	16.6508	17.725014	1.4	28278.73086
109	108	12/6/2005	10:01:06	601.10	10:06:36	3	28.274353	16.540624	17.216828	11.7	28278.73086
110	109	12/6/2005	10:01:06	601.10	10:06:36		18.149192	17.60933	17.76633	0.5	28278.73086
111	110	12/6/2005	10:04:07	604.12	10:09:37	3	27.668385	16.584694	18.077577	11.1	28278.73086
112	111	12/6/2005	10:04:08	604.13	10:09:38		18.039016	17.686453	17.742918	0.4	28278.73086
113	112	12/6/2005	10:08:40	608.67	10:14:10	3	28.28537	16.441466	18.0762	11.8	28278.73086
114	113	12/6/2005	10:11:45	611.74	10:17:15	3	24.836866	16.672835	17.85034	8.2	28278.73086
115	114	12/6/2005	10:11:45	611.74	10:17:15		17.796629	17.521189	17.601067	0.3	28278.73086
116	115	12/6/2005	10:14:44	614.73	10:20:14	3	28.637933	16.364343	18.160209	12.3	28278.73086

Figure 7.12 – Unfiltered Data with Axle Assignments (Phase B, Sequence 3, Section 13b)

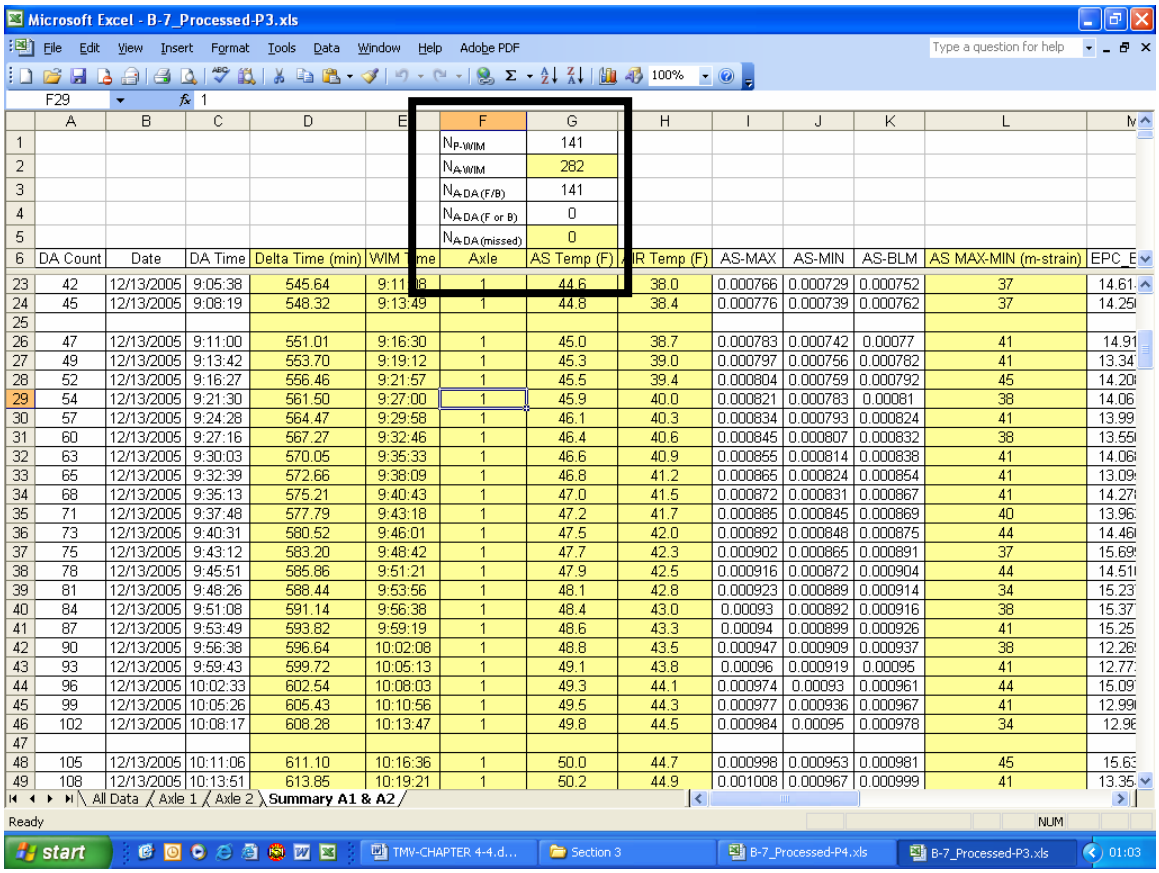

	F	G
1	$N_{P\text{-}WIM}$	141
2	$N_{A\text{-}WIM}$	282
3	$N_{A\text{-}DA\ (F/B)}$	141
4	$N_{A\text{-}DA\ (F\ or\ B)}$	0
5	$N_{A\text{-}DA\ (missed)}$	0

	A	B	C	D	E	F	G	H	I	J	K	L	M
6	DA Count	Date	DA Time	Delta Time (min)	WIM Time	Axle	AS Temp (F)	AIR Temp (F)	AS-MAX	AS-MIN	AS-BLM	AS MAX-MIN (m-strain)	EPC_E
23	42	12/13/2005	9:05:38	545.64	9:11:08	1	44.6	38.0	0.000766	0.000729	0.000752	37	14.61
24	45	12/13/2005	9:08:19	548.32	9:13:49	1	44.8	38.4	0.000776	0.000739	0.000762	37	14.25
25													
26	47	12/13/2005	9:11:00	551.01	9:16:30	1	45.0	38.7	0.000783	0.000742	0.00077	41	14.91
27	49	12/13/2005	9:13:42	553.70	9:19:12	1	45.3	39.0	0.000797	0.000756	0.000782	41	13.34
28	52	12/13/2005	9:16:27	556.46	9:21:57	1	45.5	39.4	0.000804	0.000759	0.000792	45	14.20
29	54	12/13/2005	9:21:30	561.50	9:27:00	1	45.9	40.0	0.000821	0.000783	0.00081	38	14.06
30	57	12/13/2005	9:24:28	564.47	9:29:58	1	46.1	40.3	0.000834	0.000793	0.000824	41	13.99
31	60	12/13/2005	9:27:16	567.27	9:32:46	1	46.4	40.6	0.000845	0.000807	0.000832	38	13.55
32	63	12/13/2005	9:30:03	570.05	9:35:33	1	46.6	40.9	0.000855	0.000814	0.000838	41	14.06
33	65	12/13/2005	9:32:39	572.66	9:38:09	1	46.8	41.2	0.000865	0.000824	0.000854	41	13.09
34	68	12/13/2005	9:35:13	575.21	9:40:43	1	47.0	41.5	0.000872	0.000831	0.000867	41	14.27
35	71	12/13/2005	9:37:48	577.79	9:43:18	1	47.2	41.7	0.000885	0.000845	0.000869	40	13.96
36	73	12/13/2005	9:40:31	580.52	9:46:01	1	47.5	42.0	0.000892	0.000848	0.000875	44	14.46
37	75	12/13/2005	9:43:12	583.20	9:48:42	1	47.7	42.3	0.000902	0.000865	0.000891	37	15.69
38	78	12/13/2005	9:45:51	585.86	9:51:21	1	47.9	42.5	0.000916	0.000872	0.000904	44	14.51
39	81	12/13/2005	9:48:26	588.44	9:53:56	1	48.1	42.8	0.000923	0.000889	0.000914	34	15.23
40	84	12/13/2005	9:51:08	591.14	9:56:38	1	48.4	43.0	0.00093	0.000892	0.000916	38	15.37
41	87	12/13/2005	9:53:49	593.82	9:59:19	1	48.6	43.3	0.00094	0.000899	0.000926	41	15.25
42	90	12/13/2005	9:56:38	596.64	10:02:08	1	48.8	43.5	0.000947	0.000909	0.000937	38	12.26
43	93	12/13/2005	9:59:43	599.72	10:05:13	1	49.1	43.8	0.00096	0.000919	0.00095	41	12.77
44	96	12/13/2005	10:02:33	602.54	10:08:03	1	49.3	44.1	0.000974	0.00093	0.000961	44	15.09
45	99	12/13/2005	10:05:26	605.43	10:10:56	1	49.5	44.3	0.000977	0.000936	0.000967	41	12.99
46	102	12/13/2005	10:08:17	608.28	10:13:47	1	49.8	44.5	0.000984	0.00095	0.000978	34	12.96
47													
48	105	12/13/2005	10:11:06	611.10	10:16:36	1	50.0	44.7	0.000998	0.000953	0.000981	45	15.63
49	108	12/13/2005	10:13:51	613.85	10:19:21	1	50.2	44.9	0.001008	0.000967	0.000999	41	13.35

Figure 7.13 – Axle Assignment Quality Control Checks

The next task was to separate the front axle data from the rear axle data. This was done by making two copies of the spreadsheet displayed in Figure 7.11, renaming the tabs of these worksheets ("Axle 1" and "Axle 2"), and further filtering the data using the axle column instead of the earth pressure cell column. For example, all axle "2" rows were filtered in the "Axle 1" worksheet, which left axle "1" and "3" rows only. Recall that axle "3" rows were accounted for on both axle worksheets.

For each "Axle" spreadsheet, the data rows were subsequently grouped into 5 degree temperature intervals using the asphalt temperature column. For example, all rows with an asphalt temperature ranging from 40-44, 45-49, and 50-54 degrees were grouped separately (as seen in Figure 7.13, rows 26 to 46). A row was simply inserted between each temperature subset.

7.7 Data Consolidation

After the front and rear axle data were separated, and the data were grouped into five degree asphalt temperature subsets, additional statistical data for each temperature subset in each axle worksheet was needed. A summary table was posted next to each temperature subset (shown inside the black box on Figure 7.14), and the desired statistical data for each temperature subset was calculated in this table. Figure 7.14 displays the summary table for the front axle, 45-49 °F asphalt temperature data subset during Sequence 7 of Phase B in Section 3 (same data from Figure 7.13). In general, the summary statistics included averages, standard deviations, medians, maximum and minimums, and ranges for all gages in that test section.

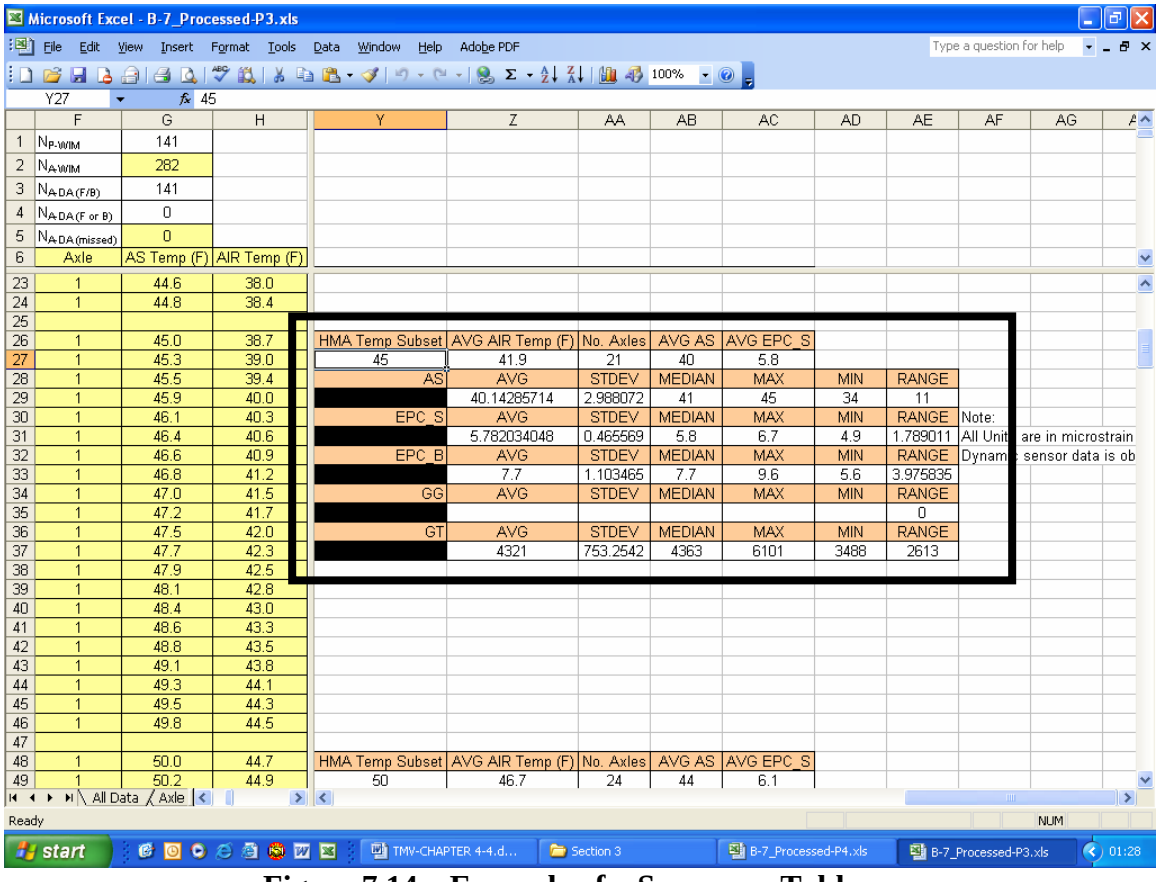

Figure 7.14 – Example of a Summary Table

After the critical statistical data was generated, further consolidation of the data was still necessary. The summary tables were located in multiple worksheets

inside 792 data files. The goal was to generate a separate data file for each structural test section and axle (a total of 32 files) that incorporated all important information needed for the empirical analysis described in Chapter 8.

To accomplish this task, the information from the summary table (Figure 7.14) for each temperature subset and axle in each "Processed" file was transferred to a separate "Summary Table" file that contained the information from all test sequences for that axle and test section. Figure 7.15 displays a full "Summary File" for a rear axle in test Section 5 (Phase A, Sequence 4). This file summarizes the previously calculated statistical information presented in Figure 7.14, and the following information was also calculated: number of repetitions to fatigue cracking failure (N_f), the Subgrade Stress Ratio (SSR), the number of repetitions to rutting failure (N_d), the amount of relative fatigue damage (D_f), the amount of relative rutting damage (D_d), the dynamic modulus of asphalt concrete(E^*), the resilient modulus (M_r), the compressive strain at the subgrade surface (ε_c), and the subgrade strength parameters.

This	5	1b,1a,1,2,3,4,5,6,8,9,10,11,12,13,13b,13a
Traffic Phase	A	A, B, OR C (Sept, Dec, March,
Truck Type	Single	Single or Tandem
Axle	Back	Front or Back
Axle Weight	20860	(lb)
Date	9-21(4)	Month-Day (Sequence)

w%_S	2.73	Representative subgrade water content
w%_B	8.73	Representative base course water content
$N_{P\text{-}WIM}$	149	Number of passes recorded by the WIM device (see additional data sheets)
$N_{A\text{-}WIM}$	298	Number of axles recorded by the WIM device (No. Passes * 2 Axles per
$N_{A\text{-}DA}$ (F/B)	148	Number of axle sets (front and back) triggered by the DA system
$N_{A\text{-}DA}$ (F or B)	0	Number of single axle readings (front or back) triggered by the DA system
$N_{A\text{-}DA}$ (missed)	1	Number of axles not triggered by the DA
First HMA Temp Subset	85	Beginning value of the lowest temperature subset (in 5 degree intervals)

HMA Temp Subset	AVG AIR	No. Axles	AS Strain	EPC_S	N_f	SSR	N_d	D_f	D_d	E*	M_r	ε_c (in/in)	Subgrade
85	76.9	1	211	8.10	2.375E+05	0.289248357	6.516E+04	4.210E-	1.535E-	492000	9200	0.000880321	28
90	79.4	17	190	8.48	3.943E+05	0.302840905	5.305E+04	4.311E-	3.205E-	409000	9200	0.00092169	28
95	82.9	13	187	8.79	4.891E+05	0.313907865	4.518E+04	2.658E-	2.878E-	339000	9200	0.000955372	28
100	86.1	15	171	8.70	7.660E+05	0.310633483	4.735E+04	1.958E-	3.168E-	282000	9200	0.000945406	28
105	88.6	15	168	8.99	9.541E+05	0.321142979	4.079E+04	1.572E-	3.677E-	235000	9200	0.000977392	28
110	90.5	11	167	8.95	1.124E+06	0.319796776	4.157E+04	9.788E-	2.646E-	196000	9200	0.000973295	28
115	94.1	20	188	10.45	8.777E+05	0.373103948	2.085E+04	2.279E-	9.595E-	165000	9200	0.001135534	28
120	95.2	56	177	10.27	1.239E+06	0.366899955	2.247E+04	4.519E-	2.492E-	139000	9200	0.001116652	28
							Sum	**1.870E-**	**5.024E-**				

N_f =No. of repetitions to fatigue cracking failure (calculated using a transfer

SSR =Subgrade Stress Ratio = EPC_S Stress (psi) / Subgrade Strength (psi)

N_d =No. repetitions to rutting failure (calculated using a transfer function)

D_f =Amount of relative fatigue damage = No. Axles / N_f

D_d =Amount of relative rutting damage = No. Axles / N_d

AS (με)

HMA Temp Subset	AVG	STDEV	MEDIAN	MAX	MIN	RANGE
85	211	#DIV/0!	211	211	211	0
90	190	11.33	192	208	169	39
95	187	13.04	179	209	173	36
100	171	16.02	169	202	137	65
105	168	10.06	170	182	150	32
110	167	13.01	170	182	137	45
115	188	24.40	179	229	146	83
120	177	30.08	180	219	26	193

EPC_S (psi)

HMA Temp Subset	AVG	STDEV	MEDIAN	MAX	MIN	RANGE
85	8.1	#DIV/0!	8.1	8.1	8.1	0.0
90	8.5	0.42	8.5	9.2	7.8	1.3
95	8.8	0.62	8.9	9.5	7.2	2.3
100	8.7	0.80	8.7	9.7	6.6	3.2
105	9.0	0.78	9.0	10.0	7.2	2.8
110	9.0	0.87	8.9	10.6	7.6	3.0
115	10.4	0.78	10.6	11.4	9.0	2.5
120	10.3	1.29	10.4	11.9	3.1	8.8

EPC_B (psi)

HMA Temp Subset	AVG	STDEV	MEDIAN	MAX	MIN	RANGE
85	10.665763	#DIV/0!	10.665763	10.665763	10.665763	0
90	11.64071912	0.941919	11.877955	12.914799	9.827141	3.087658
95	12.674354	0.9852705	12.907175	13.623816	10.32269	3.301126
100	12.79332527	1.8352007	13.204505	14.477687	7.097802	7.379885
105	13.94910053	1.8441221	14.607292	16.071071	9.453571	6.6175
110	13.49767645	1.7477158	13.921146	15.621265	9.987241	5.634024
115	15.4569706	1.1025899	15.2705675	17.550098	13.753422	3.796676
120	16.08019302	2.016311	16.368402	18.708923	5.519666	13.189257

GG (με)

HMA Temp Subset	AVG	STDEV	MEDIAN	MAX	MIN	RANGE
85	3258	#DIV/0!	3258	3258	3258	0
90	2776	326.14	2714	3258	2169	1089
95	3214	347.85	3255	3799	2710	1089
100	3074	392.54	3250	3799	2710	1089
105	3110	521.76	3255	3799	2169	1630
110	3057	365.68	3255	3795	2710	1085
115	3118	426.66	3255	3795	2169	1626
120	3245	457.71	3255	4885	2169	2716

GT (με)

HMA Temp Subset	AVG	STDEV	MEDIAN	MAX	MIN	RANGE
85	5181	#DIV/0!	5181	5181	5181	0
90	4575.764706	733.26611	4325	6048	3458	2590
95	4575.764706	733.26611	4325	6048	3458	2590
100	4266.666667	691.80609	4325	5193	3458	1735
105	4323	799.99062	4325	5193	2596	2597
110	4875.909091	584.64647	5187	6063	4325	1738
115	4454	757.75562	4325	6055	3458	2597
120	4370.142857	745.66296	4325	6063	2596	3467

Figure 7.15 Summary Table (Phase A, Rear Axle, Sequence 4, Section 5)

8. DATA ANALYSIS

8.1 Introduction

Analysis of the current data set consisted of an environmental characterization (that focused on the precipitation, moisture content of the subgrade soil and crushed stone, and the temperature of the air and hot mix asphalt), an analysis of over 2,000 passes of a loaded, single axle dump truck, and a comparison of the calculated versus measured permanent rutting fatigue. An assessment of pavement performance was conducted using Asphalt Institute (AI) transfer functions for fatigue cracking and subgrade rutting to predict the pavement service life. These functions were coupled with Miner's hypothesis to compare the sensor responses for all test sections. The primary objective of this chapter is to discuss the procedures employed and results obtained during the data analysis, which was part of a bigger effort to develop a mechanistic-empirical pavement design procedure for flexible pavement reinforced with geosynthetics.

8.2 Environmental Data

Field testing took place in September 2005, December 2005, and February 2006. Conditions were extremely dry and the seasonal changes required to weaken the subgrade soil were not observed. In fact, a river channel located in Marked Tree was completely dry during December 2005 (Phase B testing). The rainfall increased slightly in January of 2006, but much of the moisture was necessary to replenish groundwater, stream, and river levels so there was little affect on the subgrade soil moisture of the pavement structure.

The rainfall data acquired from the test site is displayed in Table 8.1 (from August 2005 – February 2006 in column 3). For comparison, additional rainfall data were obtained from the nearby city of Jonesboro, AR for 2004 and 2005. According to the Jonesboro data, the amount of rainfall in 2005 was well below typical levels. The annual precipitation in 2004 was equal to 128.5 cm (50.59 in), which was in line with the normal annual precipitation reported in Table 3.1 (125 cm (50 in)) by the

Chamber of Commerce in nearby Truman. However, Jonesboro received only 89.8 cm (35.35 in) of rainfall in 2005, which was approximately 70% of the normal value reported in Table 3.1. Furthermore, approximately 65.4 cm (25.76 in) of precipitation was recorded from January – July of 2005, and approximately 40.1 cm (15.79 in) of precipitation was recorded from August 2005 to February 2006 (a 40 % decrease over an equal period of time.

Table 8.1 – Rainfall Record for NE Arkansas

Month	*Year*	*Test Section*	*City of Jonesboro, AR*	
		Measured cm (in)	*Reported cm (in)*	*Total cm (in)*
Jan		No Data	6.9 (2.71)	
Feb		No Data	6.5 (2.57)	
Mar		No Data	8.7(3.42)	
April		No Data	19.5 (7.68)	
May	2004	No Data	11.9(4.68)	
June		No Data	9.4 (3.70)	
July		No Data	7.5(2.97)	128.5 (50.59)
Aug		No Data	11.9 (4.67)	
Sept		No Data	0.1 (0.03)	
Oct		No Data	13.3 (5.25)	
Nov		No Data	24.9 (9.82)	
Dec		No Data	7.8 (3.09)	
Jan		No Data	10.3 (4.05)	89.8 (35.35)
Feb		No Data	7.1 (2.80)	
Mar		No Data	12.5 (4.93)	
April	2005	No Data	15.1 (5.94)	
May		No Data	0.6 (0.22)	
June		No Data	6.5 (2.55)	
July		No Data	13.4 (5.27)	
Aug		11.8 (4.65)*	10.1 (3.97)	

Sept		4.7 (1.85)	6.9 (2.70)
Oct		0 (0.00)	0 (0.00)
Nov		6.7 (2.64)	6.4 (2.52)
Dec		2.2 (0.87)	1.0 (0.40)
Jan	2006	18.7 (7.36)	10.0 (3.92)
Feb		5.9 (2.32)**	5.8 (2.28)

** Approximately 10.9 cm (4.3 in) of this total fell within a 48 hr period*
*** First half of February only*

The compacted subgrade and crushed stone moisture content results are presented in Table 8.2. While water content sensors were installed, samples obtained from field core samples were deemed more reliable since testing was limited to isolated periods of time. A crushed stone sample was obtained from the lower half of the stone layer, and three shallow compacted subgrade samples were obtained from each cored hole in Section 7.

Table 8.2 –Moisture Contents Obtained from Section 7 Cores

Coring Date	*Material*	*w%*	*Corresponding Traffic Phase*	*Corresponding FWD Phase*
*	Compacted Subgrade	16.8	A	1, 2
*	Crushed Stone	6.5	A	1, 2
12/4/2005	Compacted Subgrade	17.2	B	
12/4/2005	Compacted Subgrade	18.3	B	
12/4/2005	Compacted Subgrade	16.4	B	
12/4/2005	Crushed Stone	1.7	B	
12/9/2005	Compacted Subgrade	15.8	B	
12/9/2005	Compacted Subgrade	16.4	B	
12/9/2005	Compacted Subgrade	15.6	B	
12/9/2005	Crushed Stone	2.2	B	
12/15/2005	Compacted Subgrade	17.1	B	3

12/15/2005	Compacted Subgrade	17.9	B	3
12/15/2005	Compacted Subgrade	18.8	B	3
12/15/2005	Crushed Stone	2.2	B	3
2/6/2006	Compacted Subgrade	20.4	C	
2/6/2006	Compacted Subgrade	20.5	C	
2/6/2006	Compacted Subgrade	20.6	C	
2/6/2006	Crushed Stone	3.7	C	
2/14/2006	Compacted Subgrade	16.9	C	4
2/14/2006	Compacted Subgrade	22.7	C	4
2/14/2006	Compacted Subgrade	20.0	C	4
2/14/2006	Crushed Stone	3.8	C	4

** No coring performed since testing was performed shortly after construction and optimum properties used.*

While the moisture content from the compacted subgrade increased slightly during the test, the magnitude of the increase was insignificant in comparison to the range of acceptable optimum values. The moisture content in the subgrade varied 3.4 % - 7.1% from the beginning of construction through the end of testing. The 3.4% value was obtained by averaging the subgrade moisture data in each phase and taking the largest difference between Phases A, B, and C. The 7.1% value was the largest difference in any two single point measurements. The optimum moisture content determined for the subgrade by the AHTD and the contractor ranged from 16.8% to 20.4% (a difference of 3.6%). Therefore, it was concluded that the compacted subgrade moisture content failed to deviate significantly from the optimum. Under these conditions, the piezometer reading were meaningless and therefore, not reported. As a result of the dry conditions, the poor subgrade soils (designated CH using USCS soil classification methods) remained relatively stable and the geosynthetic load carrying capability was not able to mobilize in any of the test sections.

For each vehicle pass, ambient and asphalt temperature data was calculated from the temperature regression lines developed and reported in Chapter 7 (Tables 7.3 and 7.4). The temperature in the asphalt dropped slightly below freezing for two brief periods in the night, but freezing with depth did not occur.

8.3 Transfer Functions

Details regarding the procedure used to collect and organize the data are described in Chapter 7. In general, the data was retrieved, formatted, and consolidated so that key statistical information for each five degree temperature subset and each axle was contained within 32 summary data files (1 file per axle for all 16 structural test sections). Figure 7.15 displays an example of a summary table for all rear axles in test Section 5 during test Phase A (Sequence 4). Following this procedure, one representative value was calculated for each sensor response, axle, and temperature subset. The average value was (50% reliability) was selected after plotting several of the distributions and observing no real statistical pattern. Furthermore, many of the subsets had small amounts of data and so the use of advanced statistical techniques was unnecessary. The mean was selected instead of the median since representation of the overall value of the sample was more important than representation of the overall range of values in the sample. However, the mean and median were relatively close for the temperature subsets that were investigated.

Asphalt Institute transfer functions (fatigue cracking and subgrade rutting) were coupled with Miner's Concept to determine the damage produced by the critical representative responses. It should be noted that the final data sets can be directly compared to the FWD results since the traffic was generated at 56 km/h (35 mph). A Falling Weight Deflectometer (FWD) typically has a load pulse of 0.025-0.030 seconds in length (Fetten and Humphrey, 1998; Huang, 1993; Al-Qadi and Appea, 2003), which simulates a load-time pulse similar to an axle moving 56 km/h (35 mph) (Bhutta 1998).

To further reduce the data, weighted averages were calculated for 1) asphalt temperature, 2) front and back axle weights, 3) subgrade stress ratios (defined as the

ratio of the repeated deviator stress to the ultimate subgrade strength), 4) asphalt strain, 5) base course earth pressure, 6) subgrade earth pressure, and 7) geosynthetic strain using Equation 8.1. The weights (w_i) in Equation 8.1 represent the number of axles (number of data points) per temperature subset and the representative measured data (x_i) would be the average asphalt strain value reported on Figure 7.15 for the same temperature subset if the asphalt strain data was being evaluated, for example.

$$Average_{(weighted)} = \frac{\sum_{i=1}^{n} w_i x_i}{\sum_{i=1}^{n} w_i} = \frac{\sum_{i=1}^{n} w_1 x_1 + w_2 x_2 + \ldots + w_n x_n}{\sum_{i=1}^{n} w_1 + w_2 + \ldots + w_n} \qquad (8.1)$$

Where,

w_i = Weights
x_i = Representative Measured Data

The asphalt temperature, front and back axle weights, and the total number of passes recorded by the Weigh-In-Motion device remained constant for all test sections during a single testing phase so these values are summarized in Table 8.3. The procedures used to analyze the remaining data will be discussed throughout this chapter and results (pertinent statistical information and damage calculations) will be summarized in the tables that follow for each test section and test phase.

Table 8.3 – Test Section Constant Weighted Average Values

Traffic Phase	*Total Number of Passes*	*Asphalt Temp °C (°F)*	*Front Axle KN (lb)*	*Back Axle KN (lb)*
A	544	43.8 (110.8)	39.6 (8,900)	91.2 (20,500)
B	1074	11.7 (53.0)	34.3 (7,700)	92.1 (20,700)
C	551	12.2 (54.0)	34.7 (7,800)	88.5 (19,900)

It is paramount to recognize that the analysis conducted herein is based on single point, dynamic measurements taken at a full-scale, remote location. Since there were no duplicate dynamic measurements (only one gage was active for each test

section), the following assumptions must be advanced unless the gage was physically malfunctioning: the response from a single sensor at a single location is the true reading, the sensor is absent of installation, fabrication, or other defects, and the localized area adjacent to the gage accurately represents the entire test section. .

Transfer functions were used to predict the damage induced in terms of alligator fatigue cracking (parameters associated with fatigue cracking will be referred to using the subscript "f" in the following discussion) and subgrade rutting (parameters associated with subgrade rutting will be referred to using the subscript "d" in the following discussion). For example, N_f represents the number of repetitions to failure resulting from alligator fatigue cracking, and N_d represents the number of passes to failure resulting from subgrade rutting. For both distresses, accumulation of damage was performed using Miner's hypothesis: the total damage was the sum of the relative damage values for all subsets of interest (Equation 8.2). According to Newcomb and Timm (2001), permanent pavement damage is represented by the accumulation of thousands or millions of load repetitions.

$$D_i = \frac{n_i}{N_{ji}} \tag{8.2}$$

Where,

D_i = Relative damage in temp subset i
n_i = Number of axles in temp subset i
N_{ji} = Number of passes to failure from the transfer function of axle j (f or d) represented in subset i

8.3.1 Fatigue Cracking

Carpenter (2005) provides a summary of available transfer functions. The Asphalt Institute (AI, 1982) approach was chosen for this application and the basic equations have the following form:

$$N_f = 18.4\,C\left(0.004325\right)\varepsilon_t^{-3.291}\left|E^*\right|^{-0.854} \tag{8.3}$$

$$C = 10^M \tag{8.4}$$

$$M = 4.84\left(\frac{V_b}{V_a + V_b} - 0.69\right) \tag{8.5}$$

Where,

N_f = Number of repetitions to failure
ε_t = Tensile strain in horizontal direction at bottom of asphalt mat (in/in)
E^* = Dynamic modulus of asphalt concrete (psi)
C = Function of Volume of voids and volume of asphalt
V_b = Asphalt volume (11.5%)
V_a = Air void volume (9.3%)

The 0.004325 constant in Equation (8.3) must be multiplied by 18.4 to adjust this relationship for field conditions, which results in a constant value equal to 0.0796. This relationship is representative of asphalt mats that are at least 150 mm (6 in) thick. Furthermore, Equation 8.3 was developed using stress controlled testing, which is more representative of thicker asphalt mats. Strain controlled fatigue testing is more desirable for thinner asphalt mats. Craus et al. (1984) recommended reducing the 0.0796 constant to 0.0636 to account for the aforementioned differences and the fact that thinner pavements go from crack onset to limiting failure faster than thicker pavements.

Using the asphalt and air void volume numbers displayed in Equation 8.5 to calculate it, the value of C in Equation 8.4 was equal to 0.2169. When this value is multiplied by the 0.0636 constant (discussed in the previous paragraph), the final constant in Equation 8.3 is equal to 0.0138 and the final transfer function used to predict alligator fatigue cracking is displayed in Equation 8.6.

$$N_f = 0.0138\varepsilon_t^{-3.291}\left|E^*\right|^{-0.854} \quad (8.6)$$

Equation 8.6 is only used when the representative strain from a temperature subset is 60 με or higher. This endurance limit was set slightly below the limit recommended by Carpenter (2005). When mean parameters are used, a relative fatigue damage (D_f) value of 1.0 means there is a 50% probability of failure or 50% of the wheel path will experience cracking.

8.3.2 Subgrade Rutting

Two approaches are often considered for the analysis of permanent strain accumulation, which produces subgrade rutting (Thompson and Nauman 1993). The

first approach computes the rut depth directly while assuming a standard failure criteria. Equation 8.7 (Asphalt Institute, 1982) was utilized with a 13 mm (0.5 in) failure criteria.

$$N_d = 1.365\left(10^{-9}\right)\varepsilon_c^{-4.477} \tag{8.7}$$

Where,

N_d = Number of repetitions to permanent deformation (rutting) failure

ε_c = Compressive strain at subgrade surface

$$\varepsilon_c = \frac{\sigma_d}{M_r} \tag{8.8}$$

Where,

σ_d = Representative measured subgrade surface pressure of a subset

M_r = Resilient Modulus back calculated from corresponding FWD testing

The second approach is similar in concept, but the deviator stress is controlled to limit rut progression rather than calculating it for each vehicular load. The typical strain accumulation model is displayed in Equation 8.9

$$\varepsilon_p = (A)N^b \tag{8.9}$$

Where,

ε_p = Permanent strain

N = Number of repeated loads

A, b = Coefficients

Thompson and Nauman (1993) report that the (A) term in Equation 8.9 could be associated with repeated deviator stress and that there is a threshold level above which permanent deformation occurs rapidly. To quantify this threshold, a subgrade stress ratio (SSR) was defined as the ratio of the repeated deviator stress and ultimate subgrade strength. Thompson and Nauman (1993) recommended a SSR value of 0.5-0.6, and noted that a statistically significant but somewhat inaccurate correlation with rutting was observed for SSR values as low as 0.4. Thompson and Bejarano (1997) reported SSR values for airfields from 0.4-0.7, depending upon the strain criteria, agency, and several other factors.

8.4 Asphalt Strain Response

Figure 8.1 contains two typical (but unrelated) asphalt strain responses for the purpose of displaying the two extremes of the trigger interval. One of the curves (solid triangles) represents a response that is triggered late while the other curve (open squares) represents an early response. While the timing of the trigger was not always perfect (one gage may be triggered slightly later than the other), and a part of the curve may be absent on one end or the other, the data acquisition that followed a triggered response always collected enough data to determine the difference between the peak and the baseline value for each axle response. ***The difference between the peak and the baseline was then used to calculate all statistical data (weighted averages, maximums, minimums, and ranges) presented in the following tables, and will be referred to as the "response interval".***

As discussed previously, the representative weighted average (Equation 8.1) of the "response interval" was calculated for each gage, axle, test section, and test phase. Additionally, the corresponding maximum, minimum, and range (maximum – minimum) was determined (Table 8.4). The damage values in Table 8.4 were reported in a decimal form of the percentage of damage anticipated for the roadway during the service life. These numbers were converted to a percentage in the summary tables presented at the end of the analysis.

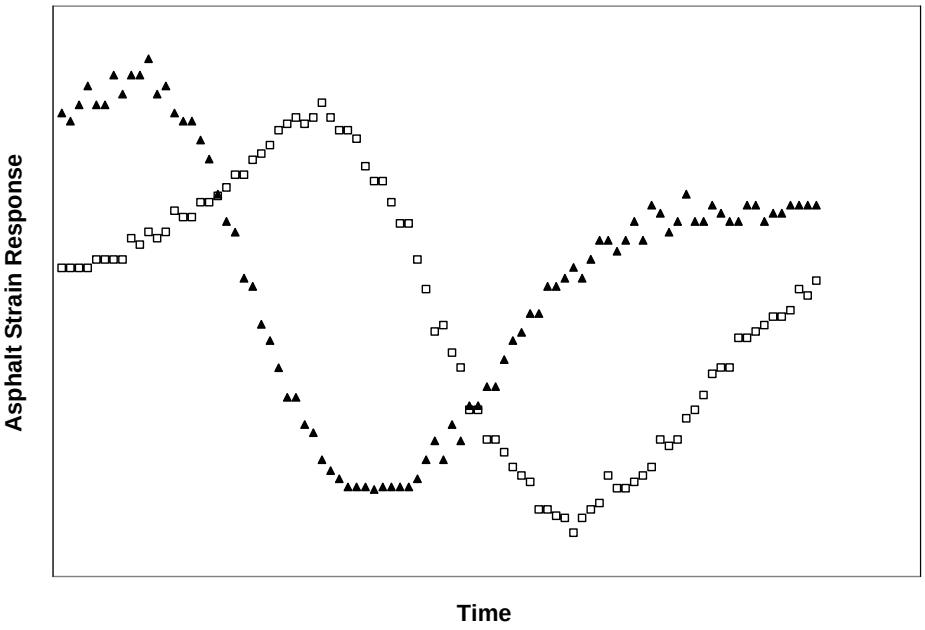

Figure 8.1 - Two Triggered Asphalt Strain Responses

The variability of the data in Table 8.4 was substantial between test sections. The difference in the asphalt strain readings between test sections was the primary variable in performance assessment relative to fatigue cracking, and the differences observed were higher than anticipated. However, the data set as a whole appears to be sound, with the exception of Section 9. The readings in Section 9 remain fairly steady, failing to decrease with temperature similar to the other test sections. For example, the weighted average for the asphalt strain response (peak minus baseline) for phases A, B, and C in Section 10 were 344, 91, and 88. Note that the temperature was much lower in phases B and C. However, the corresponding values from Section 9 were 387, 319, and 352 (they remained fairly consistent).

Since temperature can significantly affect asphalt concrete, the effect of temperature on the variability of the current readings was investigated. According to Table 8.4, the range values (column 6 in Table 8.4) in each test section of a single phase varied significantly in some cases even though the calculated temperature was the same for all test sections within any one test phase. Recall that temperature was only measured once for each vehicle and this temperature was used for all test sections

alike. For example, values equal to 177 με, 396 με, and 521 με were measured in Sections 1a, 2, and 4 during Phase A. However, the sensors with higher weighted averages (column 3 in Table 8.4) tend to have higher ranges, implying that the variability in the Table 8.4 "Range" is linked to the variability in the "Weighted Average" rather than temperature.

The variability within the temperature subsets of select test sections was investigated to verify that temperature was not the cause of the variation in "Range" values from section to section in Table 8.4. Data from Sections 1, 11, and 13 were selected for this evaluation since Sections 1 and 13 were the control sections (with relatively low readings), and Section 11 had a functional sensor with a high reading. Values from these test sections were evaluated for test Phases A and B since the entire temperature range was covered during this test interval (see the footnote at the bottom of Table 8.4).

Figure 8.2 displays the ***average*** asphalt strain gage "response interval" for each temperature subset as a function of the corresponding asphalt temperature. Section 11 readings are consistently higher than Sections 1 and 13. Similarly, Figure 8.3 displays the corresponding "response interval" ***range*** for each asphalt temperature subset. Sections 1 and 13 are very similar and Section 11 is consistently higher. However, when each sensor was normalized relative to the corresponding ***weighted average*** in Table 8.4, differences between test sections were minimized. Figure 8.4 illustrates this point for the "response interval" range data. Therein, all data at a given temperature was combined to provide a more concise description. As a result, it was concluded that the variability in range between sections was linked to the variability in average reading.

Table 8.4 - Asphalt Strain Response Calculations

		Response Interval = Peak – Baseline Value (με)				*Fatigue Cracking (D_f)***		
*Phase**	*Test Section*	*Weighted Average (με)*	*Maximum (με)*	*Minimum (με)*	*Range (με)*	*Front Axle*	*Back Axle*	*Total*
A	1b	263	333	139	194	1.04E-03	2.53E-03	3.58E-03
B	1b	106	157	65	92	2.48E-04	1.47E-03	1.72E-03
C	1b	81	126	47	79	5.26E-05	2.76E-04	3.29E-04
A	1a	203	287	111	177	3.54E-04	1.03E-03	1.39E-03
B	1a	76	104	45	59	3.56E-05	4.51E-04	4.87E-04
C	1a	58	88	40	48	3.56E-05	5.98E-05	9.54E-05
A	1	170	259	39	220	1.12E-04	6.47E-04	7.63E-04
B	1	44	55	31	24	0.00E+00	0.00E+00	0.00E+00
C	1	43	55	29	27	0.00E+00	0.00E+00	0.00E+00
A	2	231	491	95	396	3.07E-04	1.53E-03	1.84E-03
B	2	61	99	39	60	0.00E+00	1.67E-04	1.67E-04
C	2	50	70	38	31	0.00E+00	1.99E-05	1.99E-05
A	3	378	790	179	610	2.70E-03	7.51E-03	1.02E-02
B	3	97	148	48	100	2.88E-05	1.09E-03	1.12E-03
C	3	88	126	66	60	8.60E-06	3.46E-04	3.55E-04
A	4	295	672	151	521	1.90E-03	4.31E-03	6.21E-03
B	4	61	107	32	75	6.46E-06	1.91E-04	1.97E-04
C	4	55	65	38	27	0.00E+00	1.03E-05	1.03E-05
A	5	173	211	109	102	1.73E-04	6.75E-04	8.39E-04
B	5	78	122	40	82	4.13E-05	5.35E-04	5.76E-04
C	5	73	104	57	44	7.34E-06	1.84E-04	1.92E-04
A	6	142	193	59	135	1.97E-04	3.37E-04	5.34E-04
B	6	65	85	30	55	0.00E+00	2.67E-04	2.67E-04
C	6	64	95	48	47	2.73E-06	8.01E-05	8.28E-05
A	8	210	330	52	278	4.02E-04	1.29E-03	1.69E-03
B	8	56	80	29	51	2.23E-05	7.77E-05	1.00E-04
C	8	61	86	34	53	2.24E-	9.79E-	1.20E-

						05	05	04
A	9	387	474	160	314	3.27E-03	9.45E-03	1.27E-02
B	9	319	457	41	416	8.93E-03	5.53E-02	6.42E-02
C	9	352	424	269	155	7.46E-03	3.30E-02	4.05E-02
A	10	344	421	145	277	4.04E-03	5.85E-03	9.89E-03
B	10	91	127	44	83	1.04E-04	8.65E-04	9.69E-04
C	10	88	120	56	63	2.27E-04	6.49E-04	8.76E-04
A	11	379	545	114	430	9.31E-04	7.86E-03	8.79E-03
B	11	118	142	49	93	4.17E-05	1.83E-03	1.87E-03
C	11	118	157	76	81	2.59E-05	8.92E-04	9.18E-04
A	12	293	394	93	301	8.16E-04	3.33E-03	4.15E-03
B	12	98	125	36	89	2.09E-04	1.04E-03	1.25E-03
C	12	103	131	65	66	1.03E-04	5.85E-04	6.88E-04
A	13	157	216	46	170	2.11E-04	4.46E-04	6.59E-04
B	13	61	70	43	27	7.30E-06	1.68E-04	1.75E-04
C	13	70	83	51	32	0.00E+00	1.59E-04	1.59E-04
A	13a	361	427	154	273	2.29E-03	7.11E-03	9.40E-03
B	13a	169	222	45	177	6.08E-04	6.25E-03	6.86E-03
C	13a	225	290	148	142	1.18E-03	7.42E-03	8.60E-03
A	13b	514	646	210	436	1.51E-03	2.09E-02	2.24E-02
B	13b	149	199	50	149	4.72E-04	4.18E-03	4.66E-03
C	13b	194	260	98	162	5.15E-04	5.06E-03	5.58E-03

** AS Temperature Ranges: Phase A (70-125 ^{0}F); Phase B (30-70 ^{0}F); Phase C (30-70 ^{0}F)*

Calculated fatigue cracking damage values are presented in Tables 8.5 -8.7. Additionally, the test sections were ranked in terms of their ability to resist damage (the lower the number, the better the ranking). Table 8.5 summarizes all test sections while Tables 8.6 and 8.7 separate the first eight test sections (25.4 cm thick base course) from the last eight sections (15.2 cm thick base course). The damage data presented in Table 8.5 represent the summation of the "Total Fatigue Cracking (D_f)" values for all three phases for each test section (last column of Table 8.4). For

example, values equal to 3.57E-03, 1.71E-03, and 3.22E-04 are reported for Phases A, B, and C, respectively in Section 1b (Table 8.4). The sum of these values was equal to 0.005602 (0.56% in Tables 8.5 and 8.6). Note that the data presented for Section 9 was omitted from the analysis but has been included in Table 8.5 have been highlighted because the gage appeared to be malfunctioning. The D_r value is an order of magnitude higher than the other test sections. Section 9 results were omitted from the analysis, but data was included in the tables to illustrate this point.

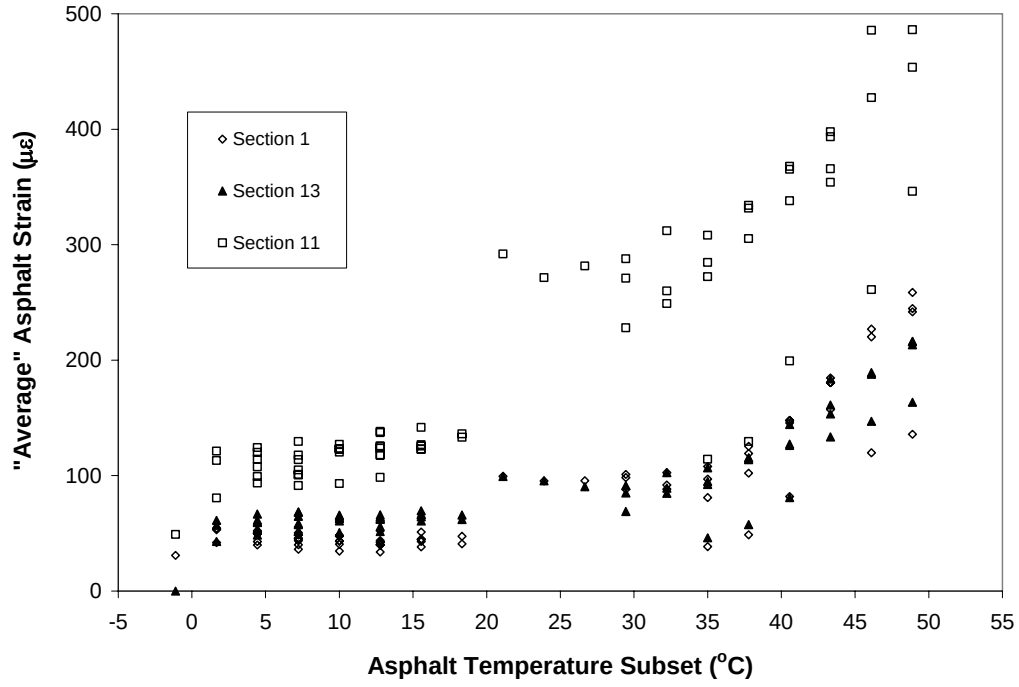

Figure 8.2 – Average Asphalt Strain "Response Interval" Per Subset

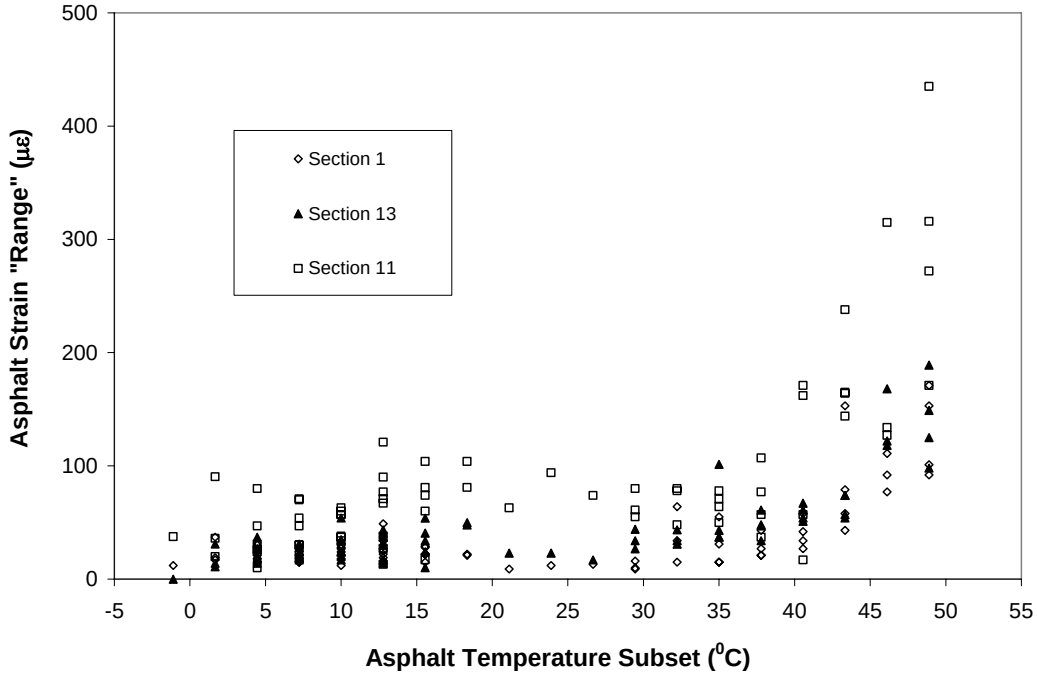

Figure 8.3 – Range of Asphalt Strain "Response Interval" Per Subset

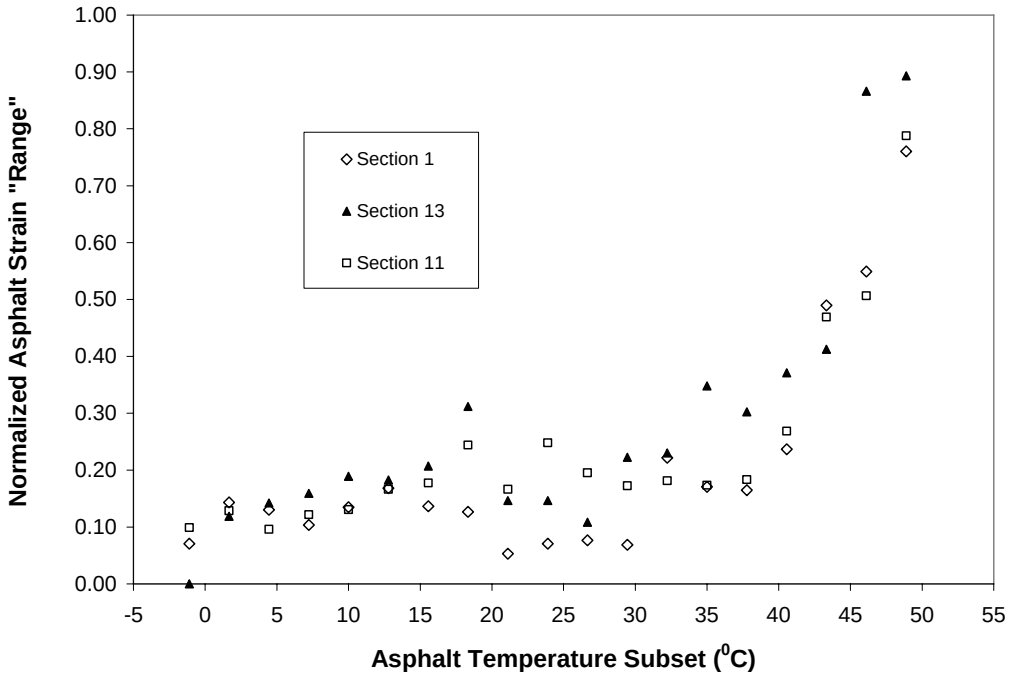

Figure 8.4 – Normalized Asphalt Strain Range

Table 8.5 – Relative Fatigue Cracking Performance for All Test Sections

Section	*Reinforcement*	*Total Damage - D_f (%)*	*Ranking*
1b	Mirafi Geolon HP 570	0.56	8
1a	Mirafi BasXgrid 11	0.20	6
1	None	0.08	1
2	Propex 2044	0.20	7
3	Propex 2006	1.16	12
4	Propex 4553	0.64	10
5	Tensar BX1200 / Propex 4553	0.16	4
6	Tensar BX 1200	0.09	2
8	Tensar BX 1200	0.19	5
9	Tensar BX1200 / Propex 4553	11.74	16
10	Propex 4553	1.12	11
11	Propex 2006	1.16	13
12	Propex 2044	0.61	9
13	None	0.10	3
13a	Mirafi BasXgrid 11	2.49	14
13b	Mirafi Geolon HP 570	3.26	15

Table 8.6 – Relative Fatigue Cracking Performance for Sections 1b-6

Test Section	*Reinforcement*	*Total Damage - D_f(%)*	*Ranking*
1b	Mirafi Geolon HP 570	0.56	6
1a	Mirafi BasXgrid 11	0.20	4
1	None	0.08	1
2	Propex 2044	0.20	5
3	Propex 2006	1.16	8
4	Propex 4553	0.64	7
5	Tensar BX1200 over Propex 4553	0.16	3
6	Tensar BX 1200	0.09	2

Table 8.7 – Relative Fatigue Cracking Performance for Sections 8-13b

Section	*Reinforcement*	*Total Damage - D_f (%)*	*Ranking*
8	Tensar BX 1200	0.19	2
9	Tensar BX1200 / Propex 4553	11.74	8
10	Propex 4553	1.12	4
11	Propex 2006	1.16	5
12	Propex 2044	0.61	3
13	None	0.10	1
13a	Mirafi BasXgrid 11	2.49	6
13b	Mirafi Geolon HP 570	3.26	7

This analysis was based on single point dynamic measurements. Since there was only one response per location, it must be assumed that the response from a single sensor at a single location is the true reading, the sensor is absent of installation, fabrication, or other defects, and the localized area where the instrument is installed accurately represents the entire test section and is identical to the localized areas of all test sections unless the response is deemed erroneous due to sensor failure.

While the rankings were displayed in Tables 8.5 – 8.7 as part of the overall objective, ***the information was not meaningful for any type of geosynthetic comparison*** since the magnitude of the damage in each test section (omitting Section 9) was relatively small and there was no meaningful pattern in the results. The control section with a 25.4 cm thick base course thickness (test Section 1) had the lowest fatigue damage value (0.08%) while Section 3 (ranked the worst test section for the same base course thickness) had a fatigue damage value equal to 1.16%. Similarly, the lowest fatigue damage was reported for the control section with a 15.2 cm base course thickness (Section 13) and the test section with the highest value of damage was only 3% higher. While the site had poor quality subgrade soils, the material was not weakened due to the dry conditions described in Chapter 3. Therefore, the strength and benefit of the geosynthetic materials (as a whole across the site) was not mobilized.

8.5 Earth Pressure Response

Figure 8.5 contains two typical (but unrelated) earth pressure responses for the purpose of displaying the two extremes of the trigger interval. One of the curves (solid triangles) represents a response that is triggered late while the other curve (open squares) represents an early response. While the timing of the trigger was not always perfect (one gage may be triggered slightly later than the other), the data acquisition that followed a triggered response always collected enough data to determine the difference between the peak and the baseline value for each axle response. ***The difference between the peak and the baseline was then used to calculate all statistical data (weighted averages, maximums, minimums, and ranges) presented in***

the following tables, and will be referred to as the "response interval". As discussed previously, the representative weighted average (Equation 8.1) of the "response interval" was calculated for each gage, axle, test section, and test phase, and the corresponding maximum, minimum, and range (maximum – minimum) was also reported for the earth pressure cells in the base course and the subgrade layers.

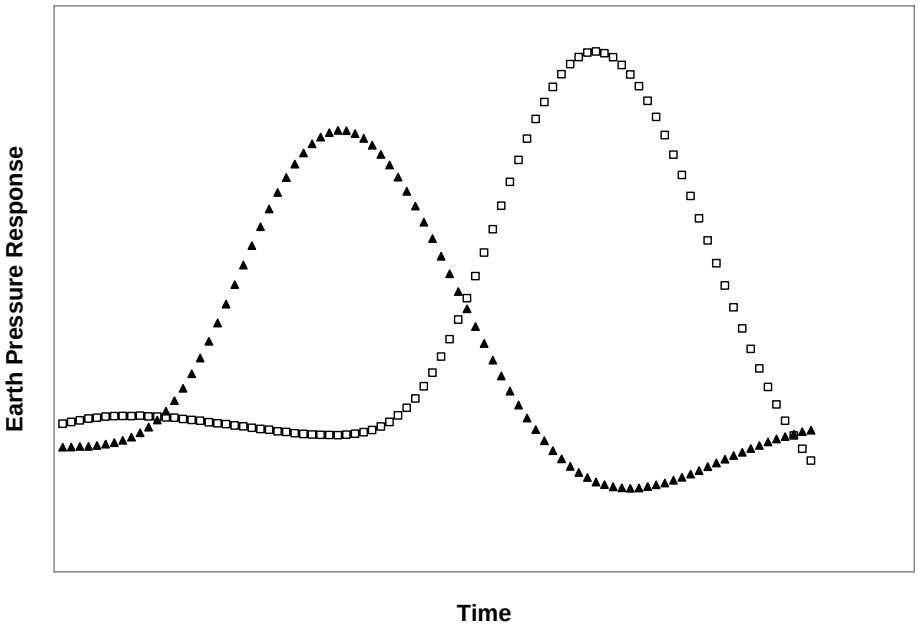

Figure 8.5 - Two Triggered Earth Pressure Responses

Table 8.8 summarizes the data for the earth pressure cells located in the base course. Recall that base course earth pressure cells were only installed in Section 1b through Section 6 of the base course. Overall, the crushed stone earth pressure responses were consistent, and all sensors provided reasonable responses. There was some variability from section to section, but no major discrepancies existed. Furthermore, the data ranges were reasonable in light of the type and nature of the loads.

The same data was also calculated for the subgrade earth pressure cells and summarized in columns 3-6 in Table 8.9. The subgrade rutting damage values in Table 8.9 were reported in a decimal form of the percentage of damage anticipated for

the roadway during the service life. These numbers were converted to a percentage in the summary tables presented at the end of the analysis.

Table 8.8 – Base Course Earth Pressure Responses*

Phase	*Test Section*	*Average kPa (psi)*	*Maximum kPa (psi)*	*Minimum kPa (psi)*	*Range kPa (psi)*
A	1b	79.2 (11.5)	102.7 (14.9)	35.8 (5.2)	66.8 (9.7)
	1a	85.4 (12.4)	97.8 (14.2)	35.8 (5.2)	62.0 (9.0)
	1	91.7 (13.3)	111.0 (16.1)	42.7 (6.2)	68.3 (9.9)
	2	88.2 (12.8)	129.6 (18.8)	44.8 (6.5)	84.8 (12.3)
	3	99.3 (14.4)	145.5 (21.1)	62.0 (9.0)	83.4 (12.1)
	4	113.8 (16.5)	135.8 (19.7)	86.2 (12.5)	49.6 (7.2)
	5	91.7 (13.3)	111.0 (16.1)	51.7 (7.5)	59.3 (8.6)
	6	109.6 (15.9)	135.1 (19.6)	58.6 (8.5)	76.5 (11.1)
B	1b	67.5 (9.8)	84.8 (12.3)	34.5 (5.0)	50.3 (7.3)
	1a	75.8 (11.0)	96.5 (14.0)	36.5 (5.3)	59.9 (8.7)
	1	79.9 (11.6)	93.0(13.5)	29.6 (4.3)	63.4 (9.2)
	2	80.6 (11.7)	98.5 (14.3)	43.4 (6.3)	55.1 (8.0)
	3	95.8 (13.9)	112.3 (16.3)	58.6 (8.5)	53.7 (7.8)
	4	107.5 (15.6)	131.6 (19.1)	53.1 (7.7)	78.5 (11.4)
	5	60.6 (8.8)	81.3 (11.8)	28.2 (4.1)	53.1 (7.7)
	6	81.3 (11.8)	104.7 (15.2)	32.4 (4.7)	72.3 (10.5)
C	1b	64.1 (9.3)	75.1 (10.9)	35.8 (5.2)	39.3 (5.7)
	1a	77.9 (11.3)	88.2 (12.8)	60.6 (8.8)	27.6 (4.0)
	1	75.8 (11.0)	86.1 (12.5)	62.0 (9.0)	24.1 (3.5)
	2	90.3 (13.1)	99.9 (14.5)	64.8 (9.4)	35.1 (5.1)
	3	99.9 (14.5)	109.6 (15.9)	75.8 (11.0)	33.8 (4.9)
	4	112.3 (16.3)	128.2 (18.6)	81.3 (11.8)	46.9 (6.8)
	5	64.1 (9.3)	79.2 (11.5)	46.9 (6.8)	32.4 (4.7)
	6	77.9 (11.3)	94.4 (13.7)	53.1 (7.7)	41.3 (6.0)

** Rear Single Axle Data Only*

While there was inherent variability in the data between test sections, there was erroneous subgrade earth pressure response behavior in Sections 6, 9, 10, 11, 12, and 13a. The response curves for these sensors were smooth, consistent, and appeared

normal. However, when the magnitude of the responses from these sensors was compared to other sensors, it was determined that Sections 6, 9, 10, 11, 12, and 13a were not responding appropriately to the applied dynamic loads. Since the base course thickness varied between test Sections 1b – 6 (25.4 cm thick base course) and Sections 8 through 13b (15.2 cm thick base course), the earth pressure cells in Section 8-13b should have been exposed to higher pressures resulting from the applied dynamic loads since the gages were closer to the surface, but this was not the case for Sections 9-12 and 13a.

Table 8.9 – Subgrade Earth Pressure Responses*

		Compacted Subgrade Pressure				*Permanent Deformation (D_d)**		
Phase	*Section*	*Weighted Average kPa(psi)*	*Maximum kPa(psi)*	*Minimum kPa(psi)*	*Range kPa(psi)*	*Front Axle*	*Back Axle*	*Total*
A	1b	77.9(11.3)	91.6 (13.3)	37.9 (5.5)	53.7 (7.8)	6.23E-03	1.30E-02	1.92E-02
B	1b	79.9 (11.6)	93.7 (13.6)	52.4 (7.6)	41.3 (6.0)	1.24E-02	5.86E-02	7.10E-02
C	1b	72.4 (10.5)	84.1 (12.2)	40.0 (5.8)	44.1 (6.4)	3.40E-03	1.25E-02	1.59E-02
A	1a	44.1 (6.4)	52.4 (7.6)	18.6 (2.7)	33.8 (4.9)	7.44E-04	1.00E-02	1.08E-02
B	1a	49.6 (7.2)	60.6 (8.8)	30.3 (4.4)	30.3 (4.4)	1.27E-03	7.18E-03	8.45E-03
C	1a	50.3 (7.3)	55.1 (8.0)	37.2 (5.4)	17.9 (2.6)	4.94E-04	2.23E-03	2.72E-03
A	1	62.7(9.1)	77.9(11.3)	29.6(4.3)	48.2(7.0)	1.29E-02	2.21E-02	3.50E-02
B	1	67.5(9.8)	84.7(12.3)	37.2(5.4)	47.5(6.9)	1.44E-02	3.13E-02	4.57E-02
C	1	73.0(10.6)	86.8(12.6)	54.4(7.9)	32.4(4.7)	5.79E-03	1.45E-02	2.03E-02
A	2	90.3(13.1)	106.1(15.4)	46.9(6.8)	59.3(8.6)	2.46E-02	5.23E-02	7.70E-02
B	2	86.1(12.5)	102.0(14.8)	51.0(7.4)	51.0(7.4)	1.53E-02	8.92E-02	1.04E-01
C	2	93.0(13.5)	102.7(14.9)	65.5(9.5)	37.2(5.4)	7.81E-03	5.01E-02	5.79E-02
A	3	71.7(10.4)	81.3(11.8)	42.7(6.2)	38.6(5.6)	7.09E-03	2.11E-02	2.82E-02
B	3	75.1(10.9)	86.8(12.6)	43.4(6.3)	43.4(6.3)	2.71E-03	4.83E-02	5.10E-02
C	3	77.9(11.3)	86.1(12.5)	43.4(6.3)	42.7(6.2)	1.58E-03	1.87E-02	2.03E-02
A	4	59.3(8.6)	76.5(11.1)	33.1(4.8)	43.4(6.3)	7.11E-03	1.45E-02	2.16E-02
B	4	58.6(8.5)	71.0(10.3)	31.7(4.6)	39.3(5.7)	2.14E-03	1.68E-02	1.90E-02
C	4	63.4(9.2)	71.7(10.4)	47.5(6.9)	24.1(3.5)	8.44E-04	6.35E-03	7.20E-03
A	5	62.7(9.1)	75.1(10.9)	38.6(5.6)	36.5(5.3)	3.80E-03	1.54E-02	1.92E-02

B	5	48.2(7.0)	59.9(8.7)	24.8(3.6)	35.1(5.1)	4.64E-04	7.97E-03	8.43E-03
C	5	51.0(7.4)	58.6(8.5)	39.3(5.7)	19.3(2.8)	2.69E-04	3.54E-03	3.81E-03
A	6	10.3(1.5)	12.4(1.8)	6.2(0.9)	6.2(0.9)	2.27E-06	4.45E-06	6.72E-06
B	6	6.9(1.0)	9.0(1.3)	3.4(0.5)	5.5(0.8)	5.62E-05	5.73E-05	1.14E-04
C	6	8.3(1.2)	10.3(1.5)	5.5(0.8)	4.8(0.7)	1.94E-07	9.75E-07	1.17E-06
A	8	99.9(14.5)	115.1(16.7)	48.2(7.0)	66.8(9.7)	1.04E-02	2.72E-02	3.76E-02
B	8	95.8(13.9)	115.1(16.7)	37.2(5.4)	77.9(11.3)	1.78E-02	1.33E-01	1.51E-01
C	8	87.5(12.7)	105.4(15.3)	53.7(7.8)	51.7(7.5)	3.16E-03	3.23E-02	3.55E-02
A	9	28.9(4.2)	37.9(5.5)	15.2(2.2)	22.7(3.3)	6.18E-05	1.18E-04	1.80E-04
B	9	12.4(1.8)	15.8(2.3)	5.5(0.8)	10.3(1.5)	1.53E-04	2.86E-04	4.39E-04
C	9	13.8(2.0)	15.8(2.3)	10.3(1.5)	5.5(0.8)	1.30E-04	4.86E-04	6.15E-04
A	10	37.9(5.5)	42.7(6.2)	18.6(2.7)	24.1(3.5)	3.55E-04	1.12E-03	1.47E-03
B	10	28.2(4.1)	32.4(4.7)	9.6(1.4)	22.7(3.3)	7.32E-05	6.09E-04	6.82E-04
C	10	29.6(4.3)	33.8(4.9)	19.3(2.8)	14.5(2.1)	4.14E-06	2.27E-04	2.31E-04
A	11	39.3(5.7)	46.2(6.7)	24.1(3.5)	22.0(3.2)	3.19E-04	7.12E-04	1.03E-03
B	11	24.1(3.5)	27.6(4.0)	13.1(1.9)	14.5(2.1)	1.03E-05	3.02E-04	3.12E-04
C	11	25.5(3.7)	28.2(4.1)	17.9(2.6)	10.3(1.5)	5.58E-06	6.89E-05	7.45E-05
A	12	48.2(7.0)	57.9(8.4)	24.8(3.6)	33.1(4.8)	1.89E-03	2.71E-03	4.60E-03
B	12	20.7(3.0)	24.8(3.6)	10.3(1.5)	14.5(2.1)	3.41E-05	1.58E-04	1.92E-04
C	12	24.1(3.5)	31.0(4.5)	18.6(2.7)	12.4(1.8)	5.78E-06	4.54E-05	5.12E-05
A	13	124.0(18.0)	144.0(20.9)	66.1(9.6)	77.9(11.3)	2.91E-02	9.77E-02	1.27E-01
B	13	113.0(16.4)	126.8(18.4)	83.4(12.1)	43.4(6.3)	5.79E-02	2.67E-01	3.25E-01
C	13	116.4(16.9)	135.0(19.6)	81.3(11.8)	53.7(7.8)	9.27E-03	1.11E-01	1.20E-01
A	13a	37.9 (5.5)	46.9 (6.8)	15.2 (2.2)	31.7 (4.6)	2.83E-04	5.79E-04	8.62E-04
B	13a	15.9 (2.3)	18.6 (2.7)	6.2 (0.9)	12.4 (1.8)	2.27E-06	4.30E-05	4.53E-05
C	13a	17.9 (2.6)	20.7 (3.0)	13.1 (1.9)	7.6 (1.1)	1.12E-06	1.07E-05	1.18E-05
A	13b	121.3(17.6)	141.3(20.5)	69.6(10.1)	71.6 (10.4)	3.49E-02	9.81E-02	1.33E-01
B	13b	88.9(12.9)	102.0(14.8)	42.7 (6.2)	59.3 (8.6)	1.14E-02	1.00E-01	1.11E-01
C	13b	90.9 (13.2)	106.1(15.4)	64.8 (9.4)	41.3 (6.0)	1.73E-03	1.58E-02	1.75E-02

** Total damage from both single and tandem axles; Remaining data from back single axle only*

The amount of permanent deformation (rutting) damage that accumulated in each test section and the rankings for each test section performance are presented in Tables 8.10 - 8.12. Table 8.10 summarizes all test sections while Tables 8.11 and 8.12 separate the first eight test sections (25.4 cm) from the last eight sections (15.2 cm). The damages presented in Table 8.10 are the summations of the "Permanent Deformation (D_d)" values for all three phases for a specific test section (last column of Table 8.9). For example, permanent deformations equal to 1.92E-02, 7.10E-02, and 1.59E-02 were reported in Section 1b during Phase A, B, and C testing, respectively. The summation of these values is equal to 0.1061 (10.61% in Tables 5.10 and 5.11).

The analysis conducted herein is based on single point dynamic measurements so it must be assumed that the response from a single sensor at a single location is the true reading, the sensor is absent of installation, fabrication, or other defects, and the localized area where the instrument is installed accurately represents the entire test section and is identical to the localized areas of all test sections unless the response is deemed erroneous due to sensor failure. It is important that the information presented in Tables 8.10 – 8.12 be reviewed with skepticism for the same reasons that were discussed previously. The dry environmental conditions did not weaken the soils to a point that the benefits of the geosynthetics could be realized.

Excluding test Section 6, Section 1a had the lowest damage value in Table 8.11, and Sections 2 and 1b were out performed by the control section. Due to the problems with 5 of the 8 responses in Sections 8-13b (Table 8.12), it can only be concluded that Section 8 and 13b out performed the control section. When comparing test sections with the same geosynthetic configuration, there were test sections with the 25.4 cm crushed stone base (sections 1b and 1) that outperformed the complementary test sections with the 15.2 cm crushed stone base thickness (sections 13b and 13) as would be expected.

Table 8.10 – Relative Permanent Deformation Performance for All Sections

Section	*Reinforcement*	*Total Damage - D_d (%)*	*Ranking*
1b	Mirafi Geolon HP 570	10.61	12
1a	Mirafi BasXgrid 11	2.20	7
1	None	10.09	11
2	Propex 2044	23.90	14
3	Propex 2006	9.92	10
4	Propex 4553	4.78	9
5	Tensar BX1200 over Propex 4553	3.13	8
6	Tensar BX 1200	0.01	1
8	Tensar BX 1200	23.39	13
9	Tensar BX1200 over Propex 4553	0.03	2
10	Propex 4553	0.24	5
11	Propex 2006	0.14	4
12	Propex 2044	0.48	6
13	None	57.20	16
13a	Mirafi BasXgrid 11	0.09	3
13b	Mirafi Geolon HP 570	26.15	15

Table 8.11 – Relative Permanent Deformation Performance for Sections 1b-6

Test Section	*Reinforcement*	*Total Damage - D_d (%)*	*Ranking*
1b	Mirafi Geolon HP 570	10.61	7
1a	Mirafi BasXgrid 11	2.20	2
1	None	10.09	6
2	Propex 2044	23.90	8
3	Propex 2006	9.92	5
4	Propex 4553	4.78	4
5	Tensar BX1200 over Propex 4553	3.13	3
6	Tensar BX 1200	0.01	1

Table 8.12 – Relative Permanent Deformation Performance for Sections 8-13b

Section	*Reinforcement*	*Total Damage - D_d (%)*	*Ranking*
8	Tensar BX 1200	23.39	6
9	Tensar BX1200 over Propex 4553	0.03	1
10	Propex 4553	0.24	4
11	Propex 2006	0.14	3
12	Propex 2044	0.48	5
13	None	57.20	8
13a	Mirafi BasXgrid 11	0.09	2
13b	Mirafi Geolon HP 570	26.15	7

As discussed in Section 8.3.2, SSR values greater than 0.4-0.7 typically indicate that there is a stress condition for which rutting is probable under repeated loading, but this trend is somewhat inaccurate at the lower end of this range 0.4 – 0.7. Table 8.13 contains the weighted average Subgrade Stress Ratio (SSR) data computed from the measured responses. Recall that the SSR is the ratio of the repeated deviator stress to the ultimate subgrade strength. The SSR values computed were (at most) in the lower end of the 0.4-0.7 range discussed previously, and are typically well below the range. For example, values as high as 0.48, 0.40, and 0.40 were calculated for the rear axle in test Sections 2, 3, and 13, respectively, following Phase C. However, values as low as 0.24 were calculated for the rear axle in Section 1a after Phase C, and values as low as 0.15-0.18 were calculated for test Sections 1a, 5, 8, and 13b, respectively, for the front axle. It should be noted that Sections 6, 9-12, and 13a were suspects for erroneous sensor behavior, and were not considered. Furthermore, test sections with the highest rutting are, in general, the test sections that have SSR values closer to the 0.4–0.7 range (the higher the SSR value, the more rutting was an issue).

8.6 Geosynthetic Strain Response

Due to the dry conditions, the geosynthetic strength was not mobilized. While a signal existed in the data acquisition system, the geosynthetic strain gage response

was only a noise band, implying that no load outside of the measurement and/or calibration tolerances was detected. The benefits from geosynthetic materials are only realized through deformation so when all pavement layers are stable, movements are insignificant and the benefits of the geosynthetics are not observed. The lack of response from the geosynthetics was verified using finite element analysis (Chapter 9).

Table 8.13 – Subgrade Stress Ratios

Section	*Single Axle Phase A*		*Single Axle Phase B*		*Single Axle Phase C*	
	Front	*Rear*	*Front*	*Rear*	*Front*	*Rear*
1b	0.22	0.27	0.25	0.40	0.24	0.35
1a	0.14	0.15	0.17	0.25	0.17	0.24
1	0.28	0.32	0.29	0.35	0.30	0.38
2	0.39	0.47	0.29	0.45	0.33	0.48
3	0.29	0.37	0.20	0.39	0.23	0.40
4	0.26	0.31	0.19	0.30	0.21	0.33
5	0.24	0.33	0.13	0.25	0.15	0.26
6	0.05	0.05	0.02	0.04	0.03	0.04
8	0.27	0.34	0.20	0.33	0.18	0.30
9	0.09	0.10	0.02	0.04	0.03	0.05
10	0.10	0.13	0.04	0.10	0.05	0.10
11	0.11	0.13	0.04	0.08	0.04	0.09
12	0.15	0.16	0.05	0.07	0.05	0.08
13	0.32	0.42	0.25	0.38	0.22	0.40
13a	0.11	0.13	0.03	0.05	0.03	0.06
13b	0.31	0.41	0.18	0.30	0.18	0.31

8.7 The Observed Versus the Calculated Pavement Condition

The rut depths that were determined from the survey measurements before and after each test phase are presented in Tables 8.14 and 8.15, and the rut depths that were determined after the field testing was completed using ASTM E1703 (specification for manual measurement of rut depth without survey equipment) are presented in Table 8.16. In general, rut depths were measured in the outside wheel path at three possible locations in each test section: 1) directly over each sensor location, 2) midway between the sensor and the end of the test section, and 3) approximately 1.2 m from each sensor. These three locations will be termed “On Sensors,” “Midpoint,” and “Near Sensor,” respectively, in the following tables. The

rut depths were measured at only two of the three locations using the survey crew; measurements were taken at all three locations using the ASTM E 1703 method.

In general, rut depths were higher directly over each sensor location using both measurement methods. They were also higher in Sections 1b-6 since the crushed stone had to be excavated and re-compacted to install the earth pressure cells. Recall that the earth pressure cells were not installed in the base course of Sections 8-13b. Due to the installation procedures required for the gages, the rut depth precision of the caliper (nearest 3.05 mm), and the small magnitude of these values, the average of the "midpoint" and "near sensor" values in Table 8.16 was calculated and presented in the last column (the "on sensor" data was ignored).

Table 8.14 – Surveyed Rut Depths (On Sensors)

Section	*Pre Phase A*		*Post Phase A*		*Post Phase B*		*Post Phase C*	
	mm	*in*	*mm*	*in*	*mm*	*in*	*mm*	*in*
1b	0.00	0.00	6.10	0.24	9.15	0.36	9.15	0.36
1a	0.00	0.00	6.10	0.24	9.15	0.36	9.15	0.36
1	0.00	0.00	12.20	0.48	15.25	0.60	12.20	0.48
2	0.00	0.00	9.15	0.36	12.20	0.48	12.20	0.48
3	0.00	0.00	12.20	0.48	15.25	0.60	12.20	0.48
4	0.00	0.00	15.25	0.60	12.20	0.48	12.20	0.48
5	0.00	0.00	9.15	0.36	9.15	0.36	9.15	0.36
6	0.00	0.00	9.15	0.36	9.15	0.36	9.15	0.36
8	0.00	0.00	6.10	0.24	6.10	0.24	9.15	0.36
9	0.00	0.00	9.15	0.36	6.10	0.24	6.10	0.24
10	0.00	0.00	9.15	0.36	6.10	0.24	9.15	0.36
11	0.00	0.00	9.15	0.36	3.05	0.12	6.10	0.24

12	0.00	0.00	9.15	0.36	3.05	0.12	6.10	0.24
13	0.00	0.00	3.05	0.12	0.00	0.00	0.00	0.00
13a	0.00	0.00	9.15	0.36	3.05	0.12	6.10	0.24
13b	0.00	0.00	9.15	0.36	3.05	0.12	3.05	0.12

Table 8.15 – Surveyed Rut Depths (Near Sensors)

Section	Pre Phase A		Post Phase A		Post Phase B		Post Phase C	
	mm	in	mm	in	mm	in	mm	in
1b	0.00	0.00	-	-	3.05	0.12	3.05	0.12
1a	0.00	0.00	-	-	3.05	0.12	0.00	0.00
1	0.00	0.00	-	-	9.15	0.36	6.10	0.24
2	0.00	0.00	-	-	6.10	0.24	0.00	0.00
3	0.00	0.00	-	-	9.15	0.36	6.10	0.24
4	0.00	0.00	-	-	3.05	0.12	3.05	0.12
5	0.00	0.00	-	-	6.10	0.24	6.10	0.24
6	0.00	0.00	-	-	9.15	0.36	6.10	0.24
8	0.00	0.00	-	-	6.10	0.24	6.10	0.24
9	0.00	0.00	-	-	0.00	0.00	3.05	0.12
10	0.00	0.00	-	-	3.05	0.12	6.10	0.24
11	0.00	0.00	-	-	0.00	0.00	3.05	0.12
12	0.00	0.00	-	-	0.00	0.00	3.05	0.12
13	0.00	0.00	-	-	0.00	0.00	3.05	0.12
13a	0.00	0.00	-	-	3.05	0.12	3.05	0.12
13b	0.00	0.00	-	-	3.05	0.12	3.05	0.12

Table 8.16 – Final Measured Rut Depth (ASTM E1703)

Section	On Sensors		Midpoint		Near Sensors		Average*	
	mm	in	mm	In	mm	in	Mm	in
1b	12.7	0.5	2.4	0.1	3.4	0.1	3.0	0.1

	0	0	6	0	7	4	5	2
1a	10.8	0.4	3.0	0.1	3.3	0.1	3.1	0.1
	4	3	5	2	0	3	8	3
1	11.4	0.4	2.6	0.1	5.8	0.2	4.2	0.1
	3	5	2	0	4	3	3	7
2	13.2	0.5	6.1	0.2	4.4	0.1	5.3	0.2
	9	2	8	4	9	8	3	1
3	12.9	0.5	6.6	0.2	5.4	0.2	6.0	0.2
	5	1	0	6	2	1	1	4
4	13.1	0.5	2.3	0.0	4.2	0.1	3.3	0.1
	2	2	7	9	3	7	0	3
5	8.21	0.3	3.1	0.1	3.4	0.1	3.3	0.1
		2	3	2	7	4	0	3
6	7.11	0.2	1.9	0.0	1.5	0.0	1.7	0.0
		8	5	8	2	6	4	7
8	5.00	0.2	5.9	0.2	5.2	0.2	5.5	0.2
		0	3	3	5	1	9	2
9	7.37	0.2	4.7	0.1	5.0	0.2	4.8	0.1
		9	4	9	0	0	7	9
10	7.11	0.2	3.2	0.1	5.0	0.2	4.1	0.1
		8	2	3	0	0	1	6
11	10.9	0.4	7.3	0.2	6.7	0.2	7.0	0.2
	2	3	7	9	7	7	7	8
12	11.0	0.4	8.3	0.3	7.4	0.2	7.8	0.3
	1	3	0	3	5	9	7	1
13	3.22	0.1	3.0	0.1	6.1	0.2	4.6	0.1
		3	5	2	8	4	1	8
13a	6.10	0.2	4.7	0.1	3.8	0.1	4.3	0.1
		4	4	9	9	5	2	7
13b	8.38	0.3	7.4	0.2	5.4	0.2	6.4	0.2
		3	5	9	2	1	3	5

** Average of "Midpoint" and "Near Sensors" Only*

Tables 8.17 - 8.19 compare the relative performance of the rut data measured using ASTM E1703 to the values calculated using the transfer functions. The two columns for Sections 1b-6 compare favorably while the two columns for Sections 8-13b are somewhat variable. For example, Sections 1b-6 typically differ by 1-3 ranking levels while Sections 8-13b typically differ by 3-5 ranking levels. A repeated number indicates equal rank of multiple sections.

Rutting fatigue calculations were ultimately performed to determine the number of repetitions necessary to achieve the 13 mm (0.5 in) failure criteria

established while assuming that all rutting occurred as a result of subgrade deformation (asphalt deformation was neglected). Therefore, the measured rut depths were divided by the 13 mm (0.5 in) failure criteria to calculate the percent rut damage for comparison with the values calculated using the transfer functions. For example, the average of the measured rut depth in Section 1b (column 8 in Table 8.16) was 3.05 mm (0.12 in). When this value was divided by the 13 mm (0.5 in) failure criteria, the measured damage was 24.0% of the expected service life using a 13 mm (0.5 in) failure criteria (column 2 in Table 8.20). Table 8.20 summarizes the results from this evaluation.

Table 8.17 – Rut Damage Evaluation for All Test Sections

Section	*Ranking for Measured Rutting**	*Ranking for Calculated Damage*
1b	2	12
1a	3	7
1	7	11
2	11	14
3	13	10
4	3	9
5	3	8
6	1	1
8	12	13
9	10	2
10	6	5
11	15	4
12	16	6
13	9	16
13a	7	3
13b	14	15

** Based on the "Average" Column in Table 8.16*

Table 8.18 – Rut Damage Evaluation for Sections 1b-6

Section	*Ranking for Measured Rutting**	*Ranking for Calculated Damage*
1b	2	7
1a	3	2
1	6	6
2	7	8
3	8	5
4	3	4
5	3	3
6	1	1

** Based on the "Average" Column in Table 8.16*

Table 8.19 – Rut Damage Evaluation for Sections 8-13b

Section	*Rank Relative to Least Measured Rutting**	*Rank Relative to Least Calculated Damage*
8	5	6
9	4	1
10	1	4
11	7	3
12	8	5
13	3	8
13a	2	2
13b	6	7

** Based on the "Average" Column in Table 8.16*

The measured damage (ASTM E1703) exceeded the calculated damage in all test sections except Section 13 in Table 8.20, which is reasonable since asphalt deformations were neglected in the calculations. Table 8.20 also provides further evidence of the erroneous responses for Sections 6, 9, 10, 11, 12 and 13a. In absence of asphalt material rutting data, observations beyond qualitative assessments are impractical. Qualitatively, it was observed that the measured and calculated values had similar trends and were on the same order of magnitude.

Table 8.20 – Measured and Calculated Permanent Deformation Damage

Section	*Measured Damage* (%)*	*Calculated Damage** (%)*	*Measured / Calculated*
1b	24.0	10.61	2.3
1a	26.0	2.20	11.8
1	33.3	10.09	3.3
2	42.0	23.90	1.8
3	47.3	9.92	4.8
4	26.0	4.54	5.7
5	26.0	3.13	8.3
6	13.7	0.01	1370.0
8	44.0	23.39	1.9
9	38.3	0.03	1276.7
10	32.3	0.24	134.6
11	55.7	0.14	397.9
12	62.0	0.48	129.2
13	36.3	55.78	0.7
13a	34.0	0.09	377.8
13b	50.0	26.15	1.9

** Values from the "Average" Column in Table 8.16 have been divided by the 13 mm (0.5") failure criteria*
*** Table 8.10*

Fatigue cracking caused by traffic loads was observed after any of the traffic phases. Only very minor to moderate cracking was observed within a few centimeters of some sensor and trench locations, indicating that these cracks were inevitable due to the sensor installation process. During the instrumentation installation, material was excavated and re-compacted after the gages were installed so the density of the re-compacted material was likely less than optimum.

When comparing the observed pavement condition from this discussion to the pavement distress calculated using transfer functions, the observed and calculated values align well with one another. Even though minimal damages were *calculated* for fatigue cracking (less than 3.5% for all sensors believed to be functioning properly in Table 8.5), fatigue cracking would likely not be *observed* during a visual inspection in the field.

In contrast to the fatigue evaluations, the calculated rutting damages showed noticeable distress. Based on the average measured responses (Table 8.20), up to half of the service life of the pavement was expended (in terms of rutting) in Sections 3, 11, 12 and 13b (25% of all sections), assuming a 13 mm (0.5 in) failure criteria.

9. FINITE ELEMENT MODEL DEVELOPMENT

9.1 Methodology

A variety of modeling and analysis techniques exist for all layers in a pavement system as well as for the system as a whole. As a result, it is important to define the scope of the model. The objective of the current model was not to predict the accumulation of permanent strain for a series of loads occurring over a period of time. If it were, isotropic hardening plasticity models (for example) would not be an ideal choice since they don't predict permanent deformation well after the first load has been applied. Perkins et al. (2000) discusses this type of strain accumulation technique, which would be truly mechanistic. Additionally, Chazallon (2000) uses an elasto-plastic model to describe the cyclic behavior of a pavement system.

Alternatively, the mechanistic-empirical approach used in this study determines the critical responses (mechanistic) under a specific type of load and relates them to the number of repetitions to failure using empirical transfer functions. The maximum response is determined for each type of load to predict the design life of the pavement.

Finite element and layered elastic analysis are the two most commonly used techniques for mechanistic pavement evaluations. A layered elastic analysis is fairly simplistic and fails to consider non-linear or stress dependent behavior. Finite element analysis (FEA) models are able to handle non-linear, anisotropic, stress hardening, and stress softening material models, and simulate a variety of other behaviors that cannot be incorporated using layered elastic analysis. As a result of the layered elastic analysis limitations and the desire to incorporate geosynthetics, a finite element method was selected for this research project. While a FEA can be performed using a three-dimensional, plane strain (not applicable for this application), or axis-symmetric model, a three-dimensional mesh can be computationally intensive and may be more precise than the quality of the input parameters used to perform the analysis so an axis-symmetric approach was utilized (Figure 9.1).

In order to simulate an axis-symmetric approach, a two-dimensional plane extending from the center point to the outside of the loaded area and extending with depth was analyzed. The behavior of this plane was computed and then rotated around the vertical axis of the center point to simulate a three-dimensional (circular) loaded area. In Figure 9.1, the width of the analysis plane extends from the center point to the outside of the circular area (3.05 m wide) and it is 4.57 m in depth. The majority of the FEA models in the literature use this same axis-symmetric approach. Furthermore, ILLI-PAVE (1990), Hornych et al. (2000), Tutumler et al. (2003), and Helwany et al. (1998) have all used this technique as part of their analytical investigations.

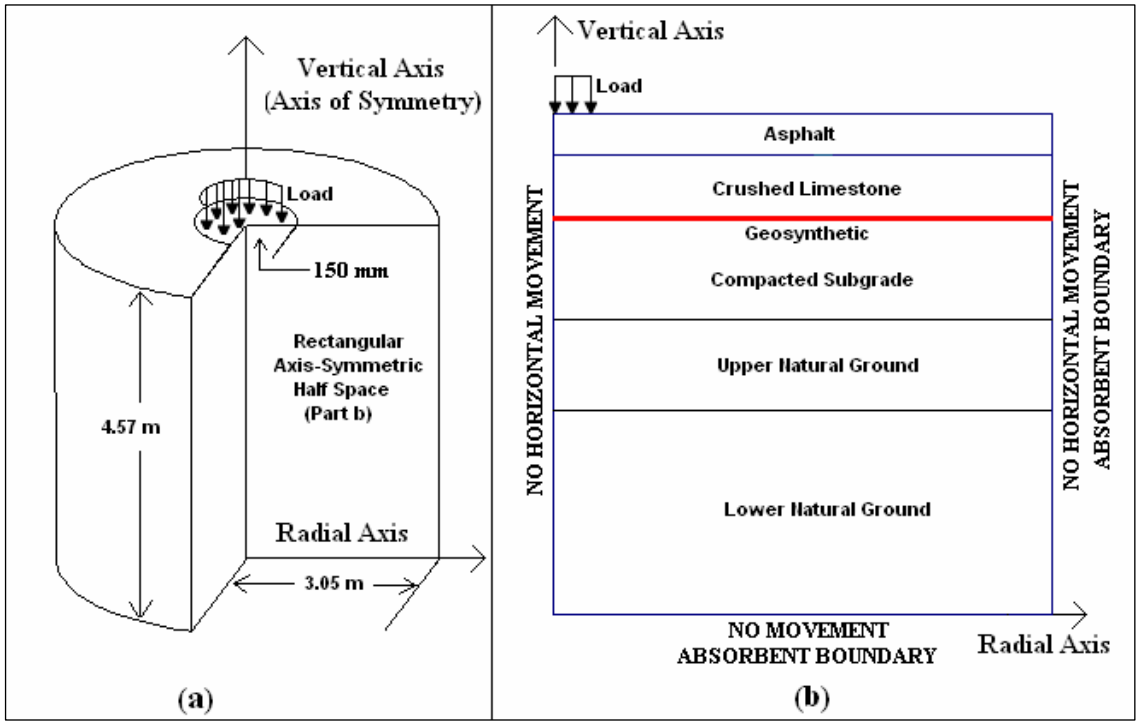

Figure 9.1 – Axis-Symmetric Configuration in 3D (a) and as a Single Plane (b)

Plaxis 2D Professional Version 8.2 (combined with the 2D Dynamics Module) is fairly comprehensive so it was used to model the flexible pavement for this study. It is equipped with a variety of features that lend themselves well to the current application. For example, the code contains elements to handle geosynthetics, automatic mesh generation, and a variety of material models that parallel the behavior(s) being investigated in the current work. The code can also be run in

automatic step size mode, which keeps the user from having to select suitable plastic calculation load increments.

After selecting the appropriate material models for each layer, the pavement structure was divided up into a series of elements (connected by nodes) and each element was independently assigned a set of material properties. In general, the objective was to determine the nodal displacements of the elements as a result of the assigned material properties and applied loading configuration. The nodal displacements were then used to calculate the stresses and strains in each element. A discussion of the material constitutive models, material properties, element configuration, boundary conditions, geometry, mesh configuration, and the load application technique will be discussed in the following sections of this chapter.

9.2 Material Constitutive Models

9.3.1 Asphalt Concrete

The asphalt concrete was modeled as a linear elastic material. The 5.1 cm (2 in) thick asphalt layer was very thin, which made temperature adjustment with depth impractical. Furthermore, since temperature effects were accounted for in the asphalt properties entered into the model, temperature non-linearity was of little significance, thereafter. The asphalt concrete was also modeled as a linear elastic material in numerous other studies (Table 9.1). It should be noted that Hornych et al. (2000) used both linear elastic and visco elastic models (to account for temperature and loading frequency) and did not indicate a preference between them. Additionally, Gonzalez (1994) set all non-linear properties equal to zero so it was essentially linear elastic.

9.3.2 Base Course Aggregate

The unbound aggregate in the base course layer plays a critical structural role in pavements, particularly when a thin asphalt layer exists. True behavior of granular material is non-linear, anisotropic, stress dependent, and inelastic, but often these behaviors are approximated or simplifying assumptions are made to simplify the constitutive material model, reduce computational time, and/or reduce the need for additional material properties.

Hornych et al. (2000) used a non-linear elastic model that was modified to allow anisotropy. While the anisotropy improved the results, the effect was limited. Tutumluer et al. (2003) modeled anisotropic behavior for both linear-elastic and non-linear, stress sensitive modeling under repeated loading. Barksdale et al. (1989) took anisotropy into account in a linear-elastic model. Most analytical investigations using geosynthetics in flexible pavements, however, assumed isotropy and used non-linear models. Furthermore, Perkins and Ismeik (1997) conducted a review of analytical methods on geosynthetic reinforced sections and reported un-paved studies were also using elastoplastic models with assumed isotropy.

Table 9.1 - Asphalt Concrete Constitutive Models

Pavement Model	*Geosynthetic*	*Reference*
Linear Elastic	No	Helwany et al. (1998)
Linear Elastic	No	Qiu et al. (2000)
Linear Elastic	No	Tutumuler et al. (2003)
Linear Elastic	Yes	Dondi (1994)
Linear Elastic	Yes	Miura et al. (1990)
Linear Elastic & Visco Elastic	No	Hornych et al. (2000)
Duncan Hyperbolic*	Yes	Gonzalez (1994)
Non-Linear Elastic	Yes	Barksdale et al. (1989)
Elasto-Plastic, Drucker Prager	Yes	Wathulala et al. (1996)
Elastic-Perfect Plastic	Yes	Ling and Liu (2003)

The K-Theta-n model is a common model that represents the stress hardening behavior of granular materials and is often used in finite element programs such as ILLI-PAVE (Thompson 1994; ILLI-PAVE 1990) and ARKPAVE (Qiu et al. 2000). This type of model utilizes Mohr-Coulomb failure criteria. Garg et al. (2000) used ILLI-PAVE to perform unbound granular base modeling using different resilient modulus, stress hardening models (σ_3 model, K-Theta-n model, and Uzan's model) and found no effect of practical engineering significance between them. While the

particular model utilized was not critical, characterizing the stress hardening behavior of the granular material was important.

As an extension of the K-Theta-n model, Hall and Elliott (2000) incorporated a stress ratio that accounted for the drop off in resilient modulus of unbound granular materials above failure. The modulus value of the material was permitted to taper off after failure instead of continuing to increase with bulk stress. Again, the stress dependency of the modulus was the critical parameter investigated.

Duncan and Chang (1970) proposed a model that depicted both non-linear and stress dependent behavior. The non-linearity was approximated with a hyperbolae that asymptotically approached the term defined as $(\sigma_1 - \sigma_3)_{ult}$, but never obtained it. A fitting factor defines the difference between this value and the applied stress difference at failure ($(\sigma_1 - \sigma_3)_{failure}$) as displayed in Equation 9.1. Helwany et al. (1998) determined that the finite element analysis results from this model for granular material were significantly different than the results acquired using a linear elastic assumption for both vertical subgrade strain and vertical stress at the bottom of the base.

$$(\sigma_1 - \sigma_3)_{failure} = R_f (\sigma_1 - \sigma_3)_{ult} \tag{9.1}$$

Where,

$(\sigma_1 - \sigma_3)_{failure}$ = Applied stress difference at failure
$(\sigma_1 - \sigma_3)_{ult}$ = Asymptotic stress difference at failure
R_f = Fitting factor (Ranges from 0.75-1.0; 0.9 typically used)

When this hyperbolic concept is combined with stress dependency and coupled with Mohr-Coulomb failure criteria, the following equation (Equation 9.2) for the tangent modulus of the material is developed. This form of the equation is convenient to use in incremental stress analysis.

$$E_t = \left[1 - \frac{R_f (1 - \sin\phi)(\sigma_1 - \sigma_3)}{(2c)\cos\phi + (2\sigma_3)\sin\phi}\right]^2 (K) p_a \left(\frac{\sigma_3}{p_a}\right)^n \tag{9.2}$$

Where,

E_t = Tangent modulus
R_f = Fitting factor
ϕ = Friction angle

σ_1 = Major principal stress
σ_3 = Minor principal stress
c = Cohesion
K = Modulus number for primary loading
p_a = Atmospheric pressure
n = Exponent

The Hardening-Soil (HS) model used in this work is an extension of the aforementioned work by Duncan and Chang (1970) and it was contained in the Plaxis library (Brinkgreve et al. 2002). While the hyperbolic model described by Duncan and Chang (1970) formed the basis of this model, it also incorporated additional features to improve the overall model adequacy. The model was non-linear, isotropic, stress dependent, and was developed using the theory of plasticity. It also accounted for soil dilatancy and the yield surface was able to expand due to plastic straining (neither of which were originally accounted for). The stress dilatancy was based on Rowe (1962): the material contracted for small stress ratios, and if a dilatancy potential ($\psi \neq 0$) was present, it expanded for high stress ratios.

9.3.3 Geosynthetics

Both the material constitutive model and the interface conditions were considered for the geosynthetic materials. Geosynthetics can be modeled as one-dimensional tension elements (Cancelli et al., 2000; Gonzalez, 1994; and Ling and Liu, 2003) or membrane elements, which are used primarily for unpaved roads (Perkins and Ismeik, 1997; and Barksdale et al., 1989). Other approaches include a composite modulus concept, truss elements (Miura et al. 1990), and solid continuum modeling (Wathugala et al. 1996). It should be noted that membrane elements are typically utilized in applications with large deformations. Since rut failure criteria for a flexible pavement is typically on the order of 13 mm (0.5 in) (NCHRP 1990), the value of the membrane element is lessoned for this application.

Interface conditions are often not considered at all, implying a perfect bond between the geosynthetic and adjacent layers. Alternatively, linear elastic or elastoplastic interface elements can be used to simulate geosynthetic-adjacent layer

interaction. Furthermore, geogrid confinement can be simulated by restraining lateral movement of the geogrids (Gonzalez 1994).

Tension elements were used to model the geosynthetics in the current study. The tension elements were linear elastic in the direction parallel to the longitudinal axis, which was perpendicular to the traffic and FWD direction. As a result of the one dimensional behavior, only axial force was carried by the tension elements and unlike a true geosynthetic, the stiffness remained constant regardless of the elongation.

9.3.4 Subgrade

A model for a true cohesive soil would be non-linear, inelastic, anisotropic, and stress softening. However, models typically assume isotropic conditions and model either elastoplastic or non-linear behaviors. Hornych et al. (2000) used a K-θ non-linear elastic model. Bodhinayake and Hadi (2003) used a non-linear isotropic hardening model that utilized Mohr-Coulomb failure criteria, similar to the work performed by Gonzalez (1994) using the Duncan and Chang (1970) model previously described. ILLI-PAVE (1990) and Qiu et al. (2000) used a bi-linear stress softening model of deviator stress versus resilient modulus coupled with Mohr-Coulomb failure criteria. The adequacy of a pure linear-elastic model (problematic at high strain levels) improves when a yield function is introduced. Miura et al. (1990) reported problems with linear-elastic models that incorporated geosynthetics. A linear-elastic model was also used by Helwany et al. (1998). The following two paragraphs describe the models used for the compacted subgrade and the natural subgrade material, respectively.

A non-linear hyperbolic model available in the Plaxis library (the Hardening Soil model) was selected for the ***compacted subgrade*** (based on the Duncan and Chang (1970) model). Details were previously provided since this model is also used for the base course layer. This model is an advanced technique that can be used for soils ranging from soft to hard. Previous versions of the Plaxis code used what was termed a Soft Soil Model for materials similar to a compacted subgrade. While this

model is still available, the same capabilities are contained in the Hardening Soil model.

The Mohr-Coulomb model (perfect plasticity), which was also available in the Plaxis library, was used to model the ***natural subgrade***. This model contained six fixed Mohr-Coulomb yield functions that could be represented as a hexagonal cone in principal stress space. Three additional yield functions were present to allow tensile soil stresses to be set to zero, a desirable condition for long term analysis. Six plastic potential functions were also incorporated to permit either: associated plasticity ($\varphi = \psi$) where plastic strain rates were perpendicular to the yield surface or non-associated plasticity where ($\varphi \neq \psi$) and dilatancy is not over predicted. Note that φ represents the friction angle and ψ is equal to the angle of dilatancy. Within the yield surface, isotropic linear elastic behavior (that satisfies Hooke's law) was incorporated.

The linear elastic-perfect plastic model selected for the natural soil subgrade was less complex than the hardening soil model used in the compacted subgrade and crushed stone base. However, the accuracy of the results in the natural soil layer (in comparison to the compacted subgrade and aggregate layers) does not need to be as high. The natural soil subgrade was only providing a "reasonably" representative foundation for the compacted subgrade and pavement layers. The material properties for this lower layer were not determined with the accuracy of the compacted subgrade material and they were not as repeatable as the crushed stone data. Therefore, selection of a material model more sophisticated than the quality of the material properties was deemed irrational.

9.3 Boundary Conditions and Geometry

The boundary conditions selected for this model were fairly standard for an axis-symmetric analysis with a transient load (Figure 9.1). The triangular elements contained six nodes. The vertical boundaries were only allowed to move vertically, and movement was not permitted at the horizontal base. Since rotations were not considered, the horizontal base was fixed against displacement only.

In order to set zero displacement boundaries, the effects of load must either be dissipated or some physical parameter must be present (such as bedrock) to merit this condition. Due to the axis symmetric configuration, absorbent boundaries were assigned to the bottom and right side of the analysis plane depicted in Figure 9.1(b) to prevent (or at least reduce) reflection of the transient dynamic loads back into the pavement and subgrade body. A reflection of the transient load would not be realistic since the boundaries do not actually exist. Based on the final soil profile generated from the soil borings, it was determined that bedrock would have little to no effect on this application.

Based on the site conditions, information obtained from the literature, and a preliminary linear-elastic sensitivity analysis of load induced deflections as a function of depth (performed using Kenlayer and ELSYM5), the model was sized 4.57 m (15 ft) deep and 3.05 m (10 ft) wide (Figure 9.1). The layer thicknesses were established from the top down. Average asphalt thicknesses were calculated using the asphalt cores obtained on both sides of each instrumentation location (Table 5.2). Survey data were used to determine the thickness of the crushed stone (Table 5.1). The thickness of the compacted subgrade was equal to the difference between the final grade and natural grade elevation in each test section along the centerline of the road. The compacted subgrade values were grouped into two categories: 0.76 m (2.5 ft) thick in Sections 1b - 6 and 1.07 m (3.5 ft) thick in Sections 8 - 13b. The upper natural ground was allocated 0.61m (2 ft) since the material properties of this layer were determined from remolded Shelby tube samples at this depth, and the remainder of the 4.57 m (15 ft) depth was considered to be lower natural ground (Figure 9.1).

9.4 Mesh

The individual layers described in the previous section were further divided into zones (Figure 9.2) to better allocate the coarseness of the finite element mesh and the variation of material properties within the model. Each zone is drawn to scale relative to the other and Table 9.2 provides further description of each zone.

Figure 9.3 illustrates the zones and variation in the coarseness of the entire mesh. The mesh is finest near the load and gets progressively coarser as the distance

from the load increases. In order to optimize mesh coarseness, the elements were made progressively smaller (by trial and error) until there were no significant changes in load response resulting from a reduction in size. Figure 9.4 displays a localized view of the mesh area directly beneath the load in Figure 9.3.

Plaxis uses a global and local coarseness value to generate the mesh. The global coarseness is defined by Equation 9.3.

$$L_e = \sqrt{\frac{(x_{max} - x_{min})(y_{max} - y_{min})}{n_c}} \tag{9.3}$$

Where,

L_e = average element size

$x_{max, min}$ $y_{max, min}$ = outer model dimensions

n_c = global coarseness setting

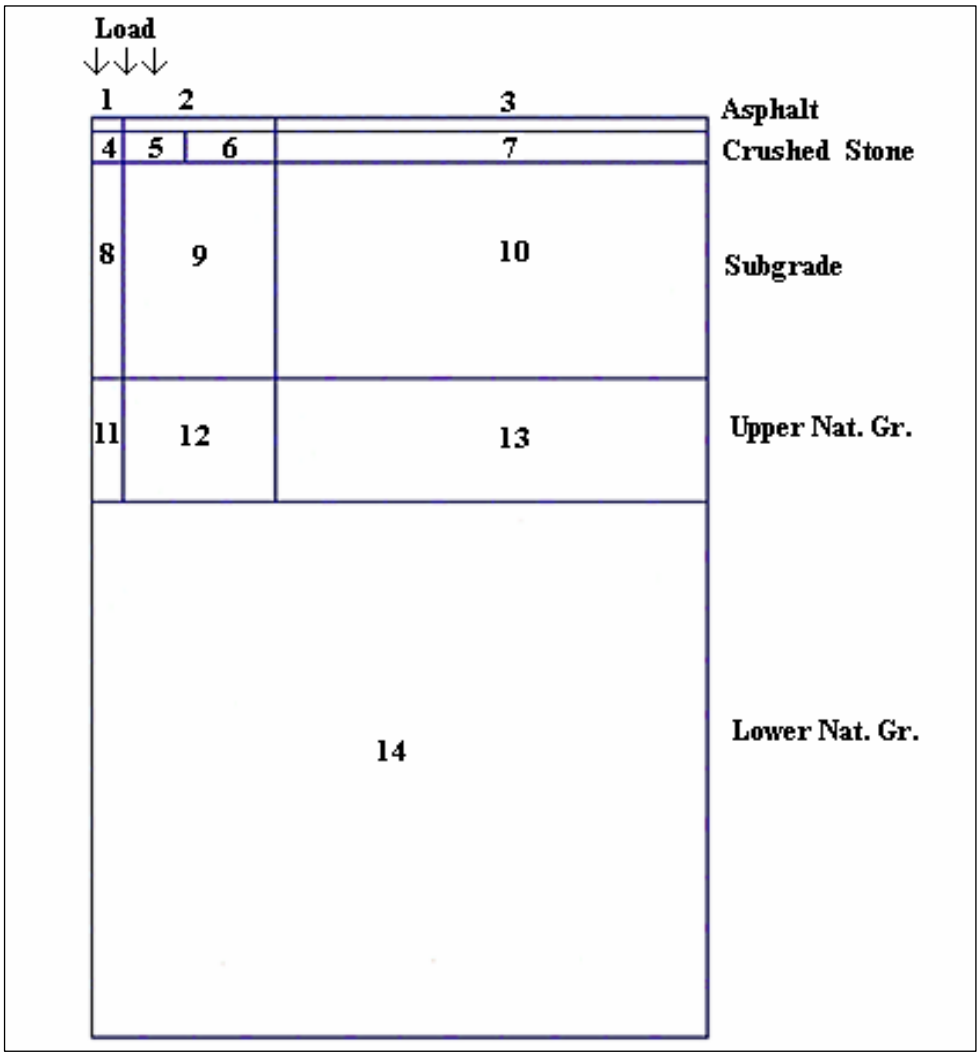

Figure 9.2 - Geometric Zones Created for the Model

Table 9.2 – Geometric Zones Used in the Model

Zone	*Layer*	*Width cm (in)*
1	Asphalt Concrete	15.0 (5.9)
2	Asphalt Concrete	78.5 (30.9)
3	Asphalt Concrete	213.4 (84.0)
4	Crushed Stone	15.0 (5.9)
5	Crushed Stone	30.7 (12.1)
6	Crushed Stone	45.7 (18.0)
7	Crushed Stone	213.4 (84.0)
8	Compacted Subgrade	15.0 (5.9)
9	Compacted Subgrade	78.5 (30.9)
10	Compacted Subgrade	213.4 (84.0)
11	Upper Natural Ground	15.0 (5.9)
12	Upper Natural Ground	78.5 (30.9)
13	Upper Natural Ground	213.4 (84.0)
14	Lower Natural Ground	304.8 (120.0)

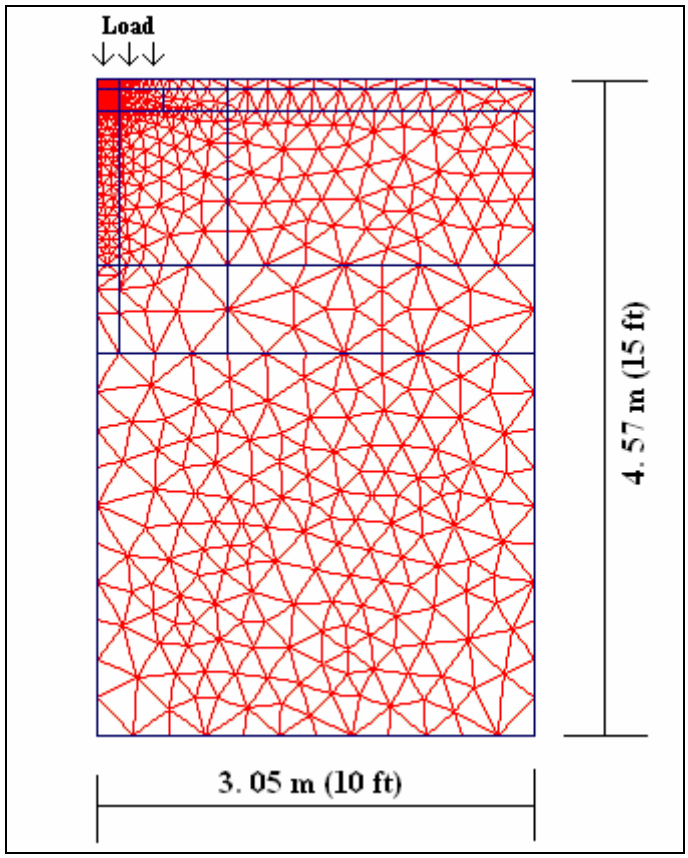

Figure 9.3 - Mesh Configuration

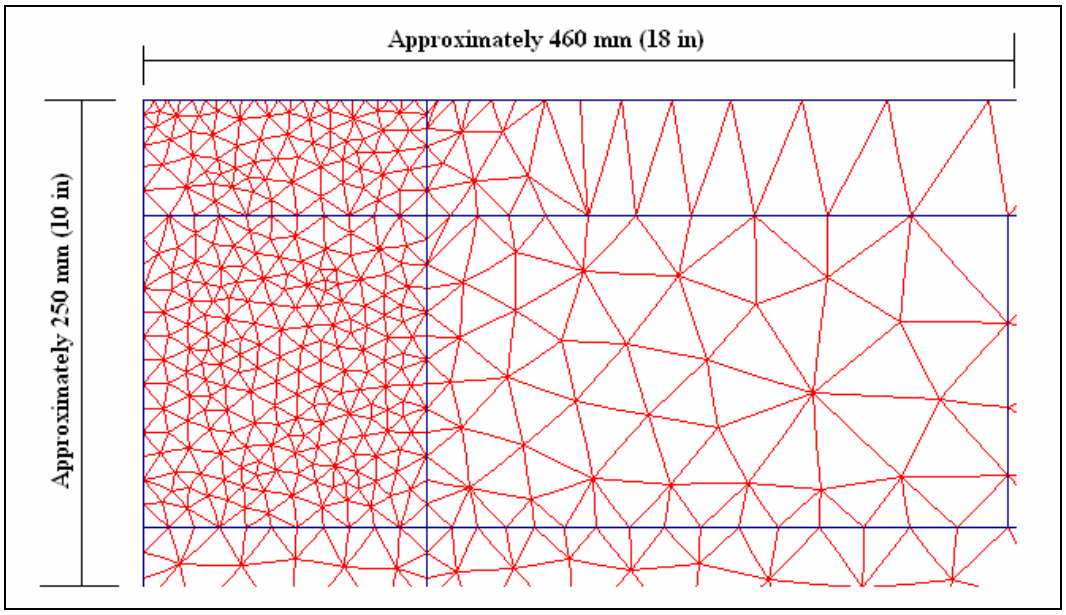

Figure 9.4 – Localized Mesh Near the Load

The global coarseness was set to "fine" (n_c of 200), which created approximately 500 elements, but this number was further increased due to local refinement. Plaxis allows "local element size factors" at each point used to define the model geometry. A "local element size factor" equal to 1.0 does not alter the globally generated mesh, if (for example) the factor for a given geometry point was reduced to 0.25, the adjacent element lengths computed by Equation 9.3 would be reduced to 25% of the original size.

Directly under the load, a minimum "local element size factor" equal to 0.05 was used. Moving horizontally away from the load, a value equal to 0.05 was used in Zone 1, it increased to 0.5 at the edge of Zone 2, and increased to 1.0 at the edge of Zone 3. Moving vertically away from the load, a value equal to 0.05 was utilized in Zone 1, it increased to 0.1 at the edge of Zone 4, increased to 0.25 at the edge of Zone 8, and increased to 1.0 at the edge of Zone 11. As a result of the local refinement, the number of elements in each test section varied between 1194 and 1824. Sections 1 and 13 were control sections, they had the lowest element count. The test sections with the thickest asphalt layers had the highest element count due to the fine mesh directly under the load.

9.5 Load Application

While a transient, dynamic pressure is applied in the field, a static load is commonly used to simulate traffic in a finite element analysis model. The authors are unaware of an analytical solution that is able to simulate a transient force applied to a flexible pavement system. Al-Khoury et al. (2001) used a spectral analysis technique to analyze a three layer pavement and treated each layer as one element under an FWD load. The results were positive when compared to an axis-symmetric finite element model. The paper stated that the axis-symmetric model was capable of linear or non-linear analysis, but the reported properties indicated that the materials were modeled as linear.

The variable dynamic loading rate of the vehicle axles coupled with the various loading rates used to obtain the properties of each material further complicate the simulation of true pavement behavior. The typical load duration for a resilient modulus test (AASHTO T 294 or T 307) is 0.1 seconds while the load is applied significantly slower for a triaxial test. The haversine shape (required by the resilient modulus test) provides a good representation of the measured compressive stress pulse for a moving vehicle (Loulizi et al., 2002). Furthermore, a Falling Weight Deflectometer typically has a load pulse duration equal to 0.025-0.030 seconds (Fetten and Humphrey, 1998; Huang, 1993; Al-Qadi and Appea, 2003), which simulates a load-time pulse similar to an axle moving 56 km/h (35 mph) (Bhutta 1998). In general, as the load interval increases, the material stiffness properties decrease since larger strains develop during the longer loading periods.

Figure 9.5 contains the normalized transient pulse used to represent FWD and vehicular loading conditions, which was applied to a 300 mm (11.8 in) diameter area. The load pulse encompassed a 0.05 second time interval (0.03 seconds of transient loading (16.67 Hz frequency) followed by 0.02 seconds of free field conditions). Equation 9.4 defines the transient pulse.

$$F = M \sin\left(2\pi f t + \phi_o\right) \quad (9.4)$$

Where,

F = Applied pressure at time (t)

M = Maximum amplitude of transient pressure

f = Loading frequency (Hz)

ϕ_o = Initial phase angle

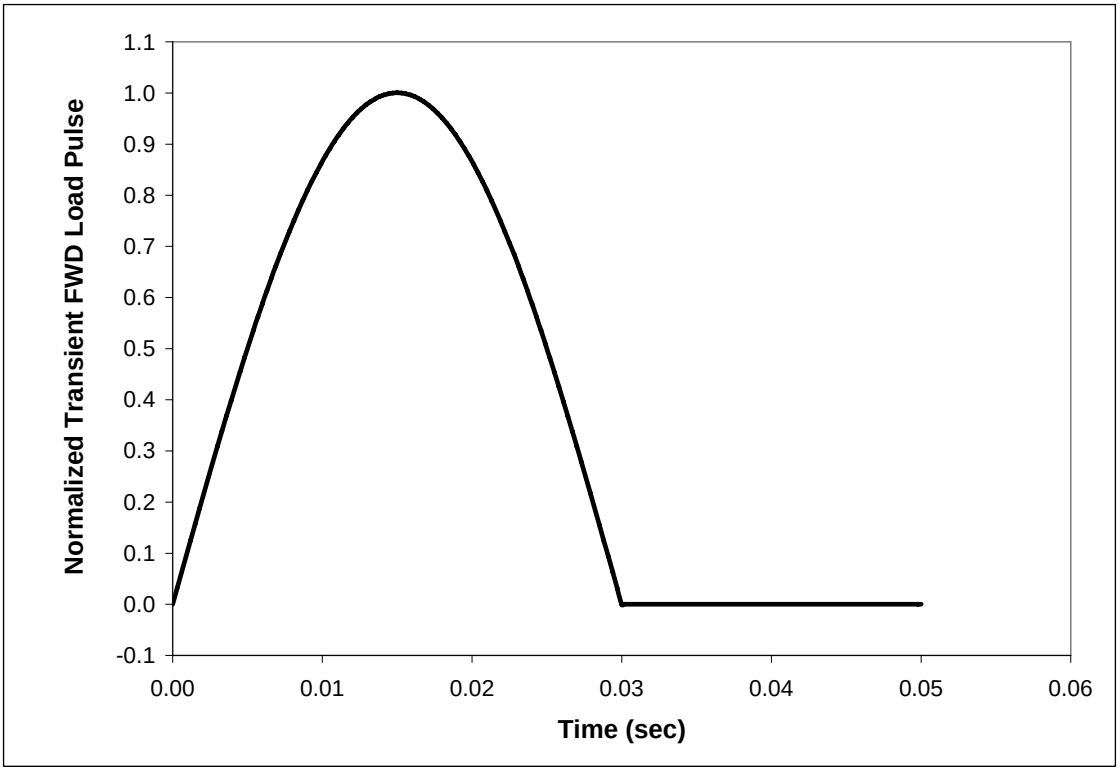

Figure 9.5 - Transient Force Representing an FWD Load Pulse

9.6 Constant Material Model Inputs

Table 9.3 summarizes the constant model inputs for the asphalt, crushed stone, compacted subgrade, and the upper and lower natural subgrade soil. The origination of many of these values was discussed in Chapter 3. The cohesion and reference stiffness values selected for the lower natural ground were measured using soil samples obtained from Zone 6 in Figure 3.3. The discussion provided by Brinkgreve et al. (2002) was used to help select the stress dependency (m) coefficients for the compacted subgrade and crushed stone. The subgrade coefficient of 1.0 simulates a

logarithmic stress dependency and a crushed stone coefficient of 0.5 simulated superior stress dependency and stiffness characteristics. The damping values were selected to aid the absorbent boundaries in wave reflection.

Table 9.3 - Constant Inputs Used in the FEA Model

Material	*Parameter*	*Value Used*
Asphalt	Total Unit Weight (γ)	22 KN/m^3 (140 pcf)
Asphalt	Poisson's Ratio (ν)	0.33
Asphalt	Rayleigh Damping (α)	0.1
Asphalt	Rayleigh Damping (β)	5E-3
Crushed Stone	Total Unit Weight (γ)	23.6 KN/m^3 (150 pcf)
Crushed Stone	Rayleigh Damping (α)	0.1
Crushed Stone	Rayleigh Damping (β)	5E-3
Crushed Stone	Stress Dependency (m)	0.5
Crushed Stone	Cohesion (c)	41.4 kPa (6 psi)
Crushed Stone	Internal Friction Angle (φ)	43^0
Crushed Stone	Dilatancy Angle (ψ)	7^0
Subgrade	Total Unit Weight (γ)	18.5 KN/m^3 (118 pcf)
Subgrade	Rayleigh Damping (α)	0.1
Subgrade	Rayleigh Damping (β)	5E-3
Subgrade	Stress Dependency (m)	1.0
Subgrade	Dilatancy Angle (ψ)	0
Upper Nat. Gr.	Total Unit Weight (γ)	15.4 KN/m^3 (98 pcf)
Upper Nat. Gr.	Rayleigh Damping (α)	0.1
Upper Nat. Gr.	Rayleigh Damping (β)	0.1
Upper Nat. Gr.	Internal Friction Angle (φ)	0
Upper Nat. Gr.	Dilatancy Angle (ψ)	0
Upper Nat. Gr.	Poisson's Ratio (ν)	0.4
Lower Nat. Gr.	Total Unit Weight (γ)	19 KN/m^3 (121 pcf)
Lower Nat. Gr.	Rayleigh Damping (α)	0.1
Lower Nat. Gr.	Rayleigh Damping (β)	0.1
Lower Nat. Gr.	Poisson's Ratio (ν)	0.45
Lower Nat. Gr.	Internal Friction Angle (φ)	0
Lower Nat. Gr.	Dilatancy Angle (ψ)	0
Lower Nat. Gr.	Cohesion (c)	120.6 kPa (17.5 psi)
Lower Nat. Gr.	Reference Stiffness (E_{ref})	89.6 MPa (13 ksi)

9.7 Variable Material Model Inputs

Each material model required a unique set of carefully selected inputs that varied over the course of the finite element modeling. Inputs depended on stress level, test section, environmental conditions, and/or test phase. Most of the details regarding material properties are presented in Chapter 3. Clarification of this information with regard to the variable inputs is provided below.

The dynamic modulus (E^*) was the only variable input for the ***asphalt concrete***. The variable inputs for the ***crushed stone*** were determined using Equations 9.5 - 9.10. All parameters that were varied were related to the material stiffness. Equation 9.5 describes the fundamental relationship between the crushed stone modulus and the corresponding stress state (refer to Section 3.7). The general relationship in Equation 9.5 is modified for the HS material model used to represent the crushed stone behavior and presented in Equation 9.6. Both the confining pressure dependency (incorporated into the material model) and deviator stress dependency (incorporated into Equation 9.5) are represented in the finite element model. In essence, the estimated stress state at the time of modeling is used to determine the reference stiffness of the crushed stone at a reference confining pressure. The remaining equations compliment the aforementioned relationship in the HS material model.

The crushed stone layer of the model was divided into four zones (zones 4-7 in Figure 9.2), which enabled a more accurate estimate of the stress state in each zone. The stress state of the crushed stone under the load (zone 4 in Figure 9.2) was the highest and it decreased with distance from the load. The stress state in Zone 4 was estimated using the measured responses from FWD tests performed directly over the sensors while the stress state in Zone 5 was determined using measured responses from FWD tests performed 0.3 m (1 ft) offset from the sensors. The stress states in Zones 6 and 7 were represented by the overburden pressure (no deviator stress).

$$M_r = 2.5983(\theta)^{0.7081} \quad (9.5)$$

$$E_{50}^{ref} = 2.5983(3k_o(x) + x)^{0.7081} \quad (9.6)$$

$$k_o = 1 - \sin\phi \quad (9.7)$$

$$p_{ref} = x(k_o) \quad (9.8)$$

$$E_{oed}^{ref} = E_{50}^{ref} \quad (9.9)$$

$$E_{ur}^{ref} = 3E_{50}^{ref} \quad (9.10)$$

Where,

M_r = Resilient modulus (ksi)

θ = Bulk stress (psi)

E_{50}^{ref} = Reference secant stiffness at corresponding reference confining pressure p_{ref}

x = Average measured stress in center of base course for a given FWD load level, testing phase, and position relative to sensors (directly above or offset)

φ = Internal friction angle (43^0)

The values displayed in Table 9.4 were used to model the axial stiffness of the ***geosynthetics***. The algebraic sum of the values was used if more than one geosynthetic was located within a test section. The stiffness remained constant regardless of the elongation.

Table 9.4 - Geosynthetic Axial Stiffness Values

Material	*Test Method*	*Axial Stiffness KN/m (lb/ft)*
ProPex 4553	Propex Recommended	70 (4800)
ProPex 2006	ASTM D 4595	205 (14,000)
ProPex 2044	ASTM D 4595	701 (48,000)
Tensar BX1200	ASTM D 6637	400 (27,400)
Mirafi BasXgrid 11	ASTM D 6637	365 (25,000)
Mirafi Geolon HP 570	ASTM D 4595	701 (48,000)

Similar to the base course calculations, variable ***compacted subgrade*** stiffness related inputs were determined using Equations 9.11-9.15. However, stiffness moduli

back-calculated from FWD test data were used for the subgrade in lieu of a statistical relationship derived from extensive laboratory testing.

$$E_{50}^{ref} = M_{r(FWD)} \tag{9.11}$$

$$k_o = 1 - \sin\phi \tag{9.12}$$

$$p_{ref} = x(k_o) \tag{9.13}$$

$$E_{oed}^{ref} = E_{50}^{ref} \tag{9.14}$$

$$E_{ur}^{ref} = 3E_{50}^{ref} \tag{9.15}$$

Where,

E_{50}^{ref} = Reference secant stiffness at the reference confining pressure p_{ref}

$M_{R(FWD)}$= Resilient modulus (Chapter 3)

x =Average subgrade stress per FWD load level and test phase

φ = Internal friction angle

The average cohesion at 2% strain was determined by testing soil samples obtained from the compacted subgrade in zones 1 and 2 of Figure 3.3. The average value of Zone 1 (test Section 1) was used for test Sections 1b - 6, and the average value of Zone 2 (test Section 13) was used for test Sections 8-13b. Note that the cohesion was equal to half of the failure deviator stress (φ = 0 conditions).

Variable material inputs for the ***upper natural ground*** were determined from laboratory testing performed on soil samples obtained from soil Zone 4 in Figure 3.3. Estimates of the water content and deviator stress state were made using measurements from the compacted subgrade.

10. FINITE ELEMENT ANALYSIS RESULTS

10.1 Introduction

The previous chapter outlined the details associated with the finite element analysis (FEA) model development. It is important to note that model "calibration" was completed using limited data and environmental conditions and therefore, should not be used to generate design charts from the data collected during this study alone. While the initial objective of this study was to collect enough FWD data to calibrate the model over a variety of environmental conditions, and then validate the model independently with traffic data, the research team encountered several major obstacles that prevented this goal from coming to fruition: 1) the contractor delays in construction, 2) the dry environmental conditions that existed during construction and testing that protected the poor subgrade soils, and 2) the construction of a nursing home adjacent to this test section that forced the project to be expedited.

As a result, the model was developed and calibrated (on a very limited basis) during Phase 1 using data from Section 13 since the majority of the material characterization and laboratory testing was performed on soils obtained from this control test section. Since some of the model material inputs were back-calculated from results generated during FWD testing (discussed in Section 9.7), Section 13 was a good choice since there was no influence of a geosynthetic. With the limited data that was available, the ***modified*** goal of this work was to adjust the model after the first phase of FWD testing and use this model (as is) on all test sections for all FWD and traffic loads, thereafter. During the preliminary adjustment period, reasonable changes to the geometric zones, damping coefficients, and calculation tolerances were performed until satisfactory agreement was obtained between the measured and calculated deflection basins.

In order to ensure the finite element model was performing as intended, all material models were initially set to linear elastic and the results from this analysis were compared to the solution generated from two commonly used linear elastic pavement analysis programs (Kenlayer and ELSYM5). The results from all three

programs were nearly identical. The dimensions and properties used during this quality control analysis were approximated, and geosynthetic were excluded to avoid unnecessary complications within the linear elastic programs.

Following this adjustment period, over 250 executions of the FEA model were performed. The majority of the effort was focused on computing load responses during controlled FWD testing (conducted after each traffic phase), and subsequently comparing the predicted (calculated) responses to the measured responses from the instrumentation in the field. The measured and calculated data comparisons from the FWD and traffic loads will be displayed in summary tables and figures throughout this chapter. Model calibration factors were developed from these data and summarized. Additionally, a significant amount of additional data that supports/compliments the results in this chapter has been organized and presented in a separate data addendum. While the data analysis presented in this chapter is complete, it is important to note again that this information should be used with caution as it applies to a very limited data set.

10.2 FEA Model Responses

Figure 10.1 displays the final deflection basins (measured and calculated) for a nominal FWD drop of 40 KN (9 kip) after the first phase of testing. Similar results were obtained for the 27 and 53 KN drops. The difference between the measured and calculated values was approximately 3% directly under the load. Thereafter, the curves followed the same trend, but the difference between the values increased slightly with distance from the center of the load (until 750 mm (2.5 ft) point). Note that FWD experimental error can easily be in the range of a few percent, and the reliability of the readings decreases as you move away from the load.

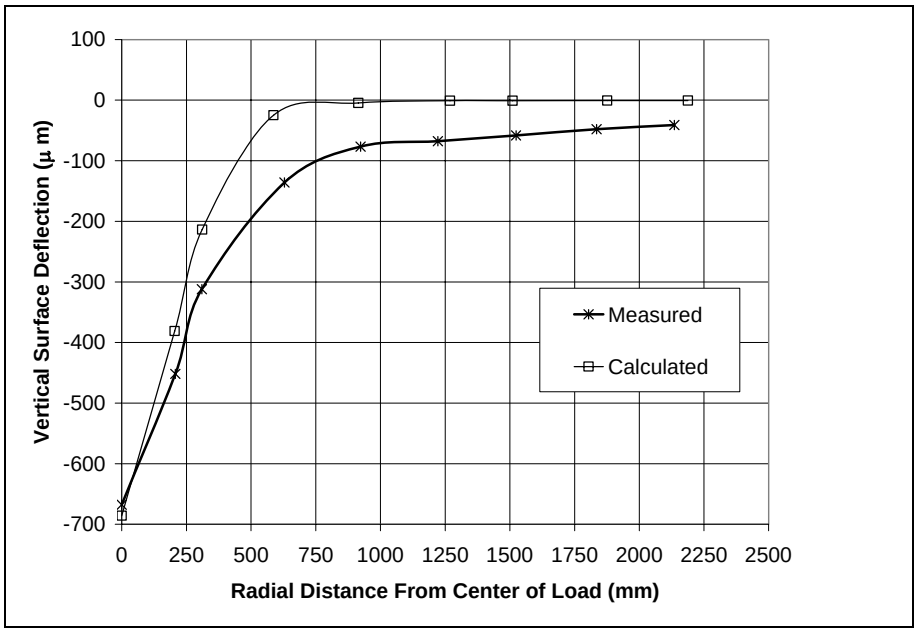

Figure 10.1 - Deflection Basin under a 40 KN Drop Load in Section 13

The sensitivity of the measured response location in the model was investigated. Early in the process, it was determined that the pressure response of the stress points in the finite element model were not sensitive to small vertical position changes that were within the tolerance of the pressure cell installation. As long as the point of interest was under the loaded area, the magnitude of the calculated stress anywhere under this area did not vary significantly. Note that the entire 230 mm (9 in) diameter pressure cell would be located under the loaded area designated in the model. The magnitude of the pressure difference between the center and the edge of the cell was only a few percent and well within measurement tolerances.

The model calculated pressure response was intended to be the absolute maximum pressure at the elevation of the gage providing the comparable response. While the effect of overburden was not removed from the results (providing a small amount of additional pressure), the overburden pressure was less than 6.89 kPa (1 psi) and considered insignificant. Figure 10.2 and Figure 10.3 display representative responses from the compacted subgrade and crushed stone layers in the model. The responses displayed in Figure 10.2 are located directly under the center of the load and the responses in Figure 10.3 are offset 300 mm (1 ft) from the center of the load.

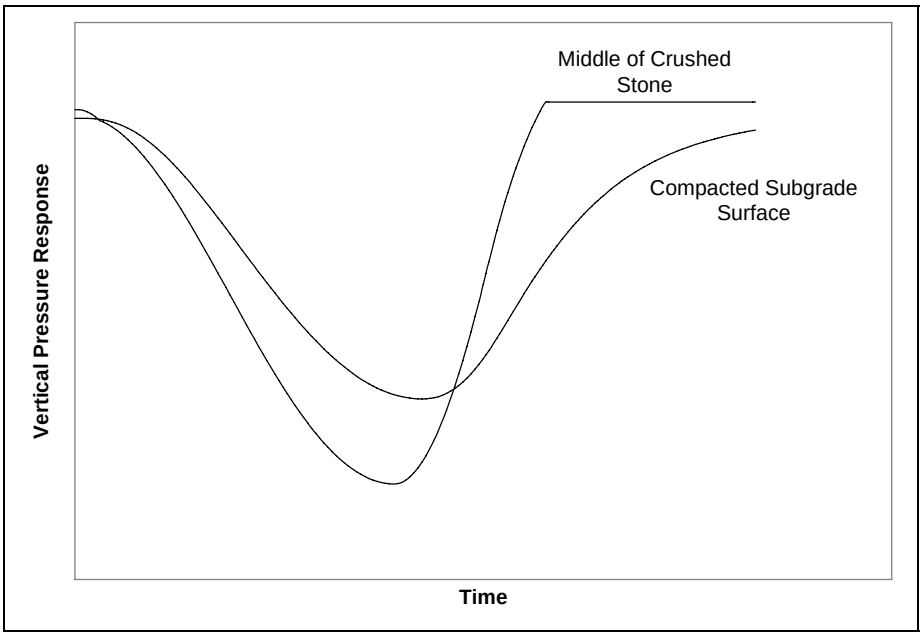

Figure 10.2 – Calculated Vertical Pressure Responses (Under Load)

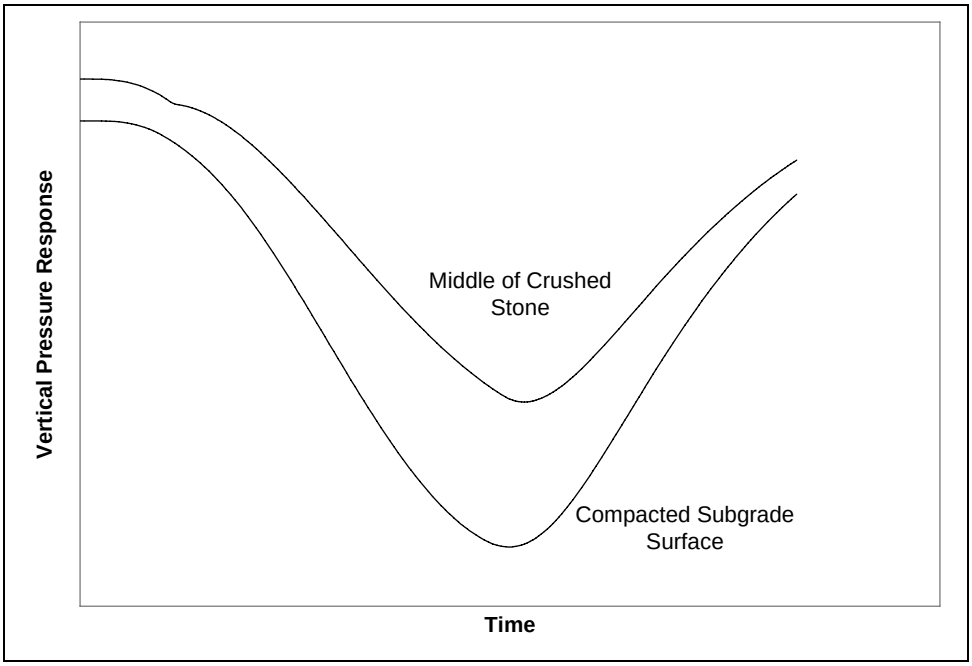

Figure 10.3 – Calculated Vertical Pressure Responses (Offset)

Unlike the vertical pressure responses, the horizontal strain in the asphalt was sensitive to vertical position, even within the installation tolerances. As a result, three points were selected at various depths to establish a strain profile with depth versus time. Due to the mesh configuration, these points were not perfectly aligned (vertically), but minor misalignments were practically insignificant. Figure 10.4 displays the horizontal asphalt strain response from points located directly under the center of the load. The finite element mesh was very fine so the intended depth of each point was more controlled and all three points were located in the bottom half of the asphalt. Figure 10.5 displays the horizontal asphalt strain response of three points located 300 mm (1 ft) from the center of the load. Due to the coarser mesh at this location, the same depth locations could not be replicated. These points had to be positioned within the full depth of the asphalt. Note that the intermediate depth displayed in Figure 10.5 was located in the top half of the asphalt layer.

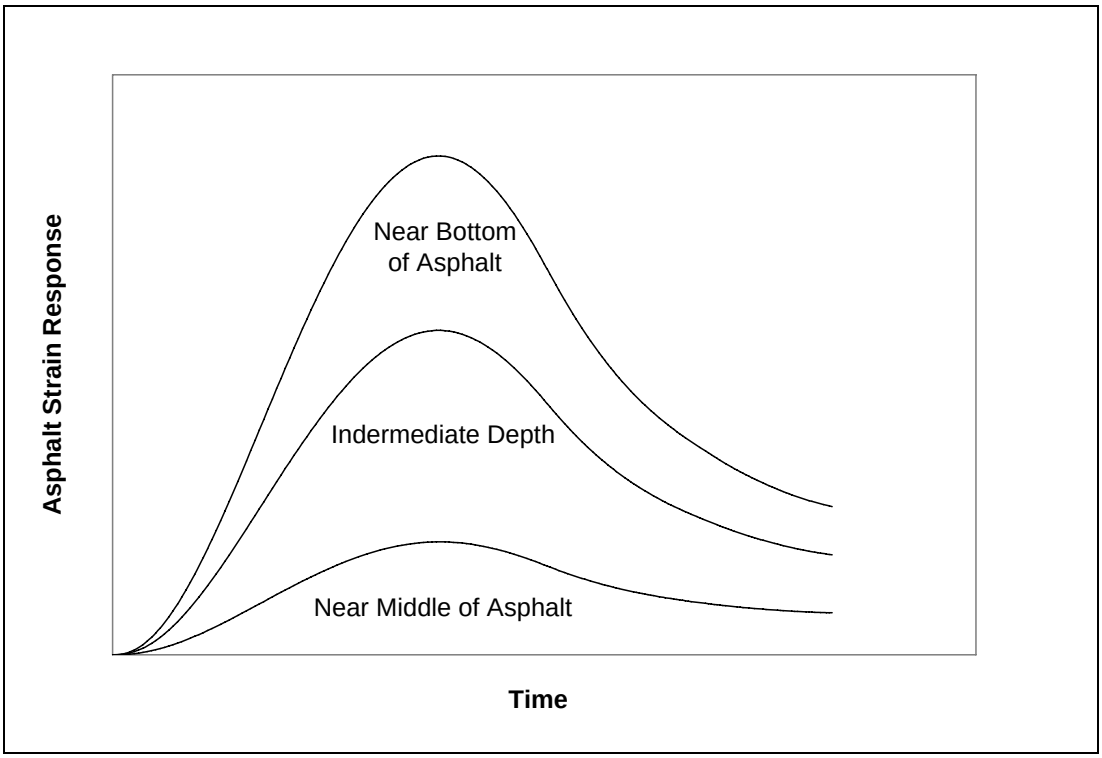

Figure 10.4 - Asphalt Strain Responses with Depth (Under Load)

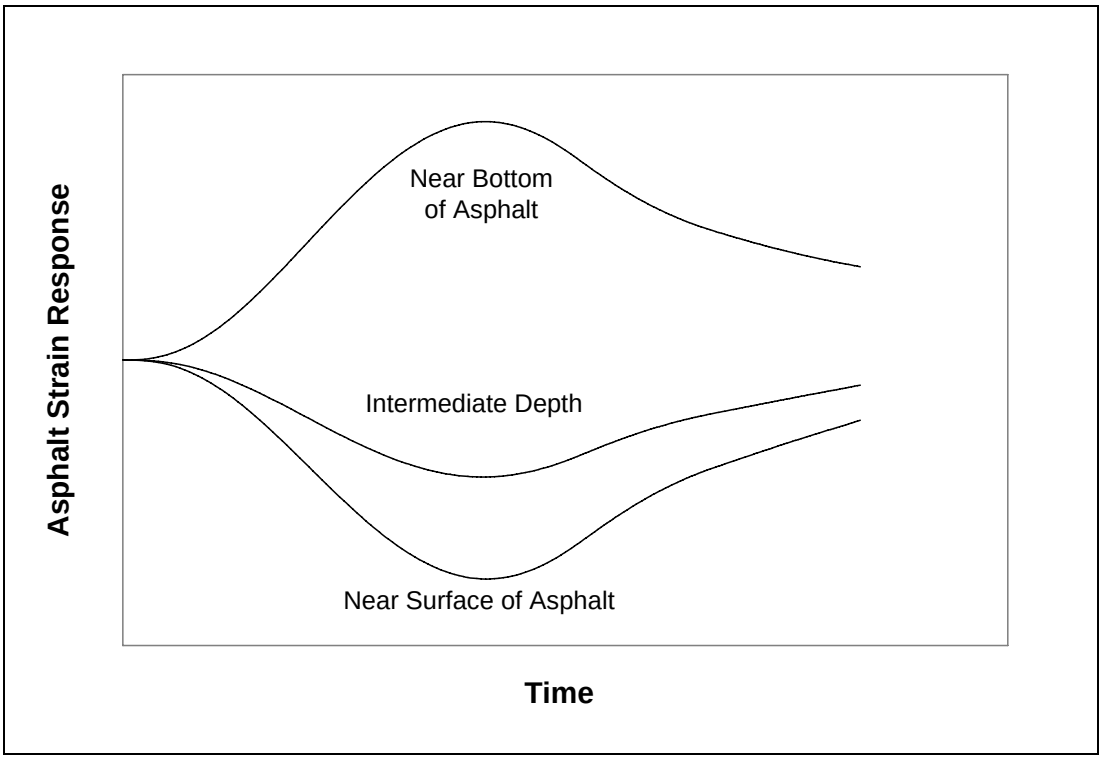

Figure 10.5 - Asphalt Strain Responses with Depth (Offset)

The horizontal asphalt strains displayed in Figure 10.4 (located directly under the load) were parallel to the radial axis shown in Figure 9.1. However, when the center of the FWD load plate was in the offset location (300 mm (1 ft) from the sensor), out-of-plane strains were generated in the axis symmetric coordinate system. Therefore, the horizontal strains in Figure 10.5 were not parallel to the radial axis displayed in Figure 9.1.

Figure 10.6 displays the normalized asphalt strain values calculated during the preliminary model development as a function of depth. In this figure, the asphalt strain values were normalized with respect to the maximum strain value. The linearity of the figure provides a good check of model quality (asphalt modeled as linear elastic). Based on the installation details and the gage geometry, it was assumed that the actual strain gage measurement was obtained approximately 13 mm (0.5 in) from the bottom of the asphalt layer. Linear equations were fit to each series of three points and the strain predicted at 13 mm (0.5 in) was used for comparison to measured values. It should be noted that the purpose of the model was to predict the absolute

maximum asphalt strain at the anticipated height of measurement. However, it was not possible to measure the true asphalt thickness or embedment depth of the sensor subsequent to the final installation. As a result, some discrepancy between the measured and calculated responses was anticipated due only to a slight variation in the vertical location.

Figure 10.7 displays a typical geosynthetic tensile strain response generated by the model as a function of distance from the center of the load. The majority of the induced strain is under the load and the response dissipates rapidly. As with the asphalt and pressure responses, the response directly under the load and 300 mm (1 ft) offset were of primary interest.

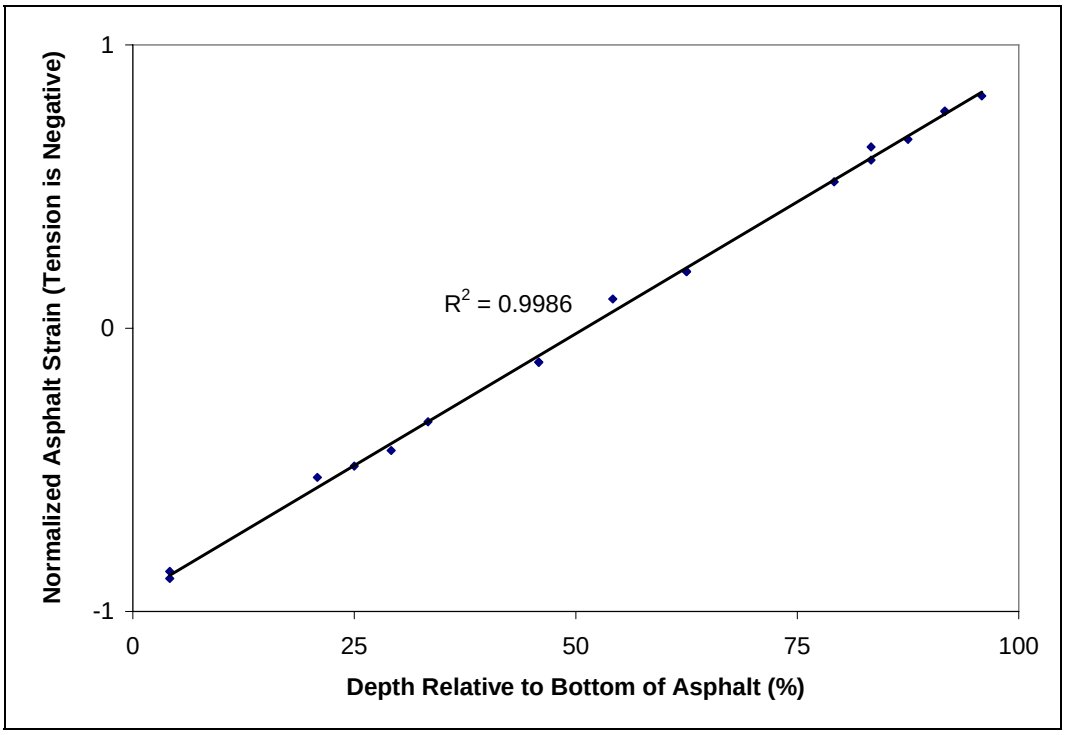

Figure 10.6 - Normalized Asphalt Strain with Depth (Section 13)

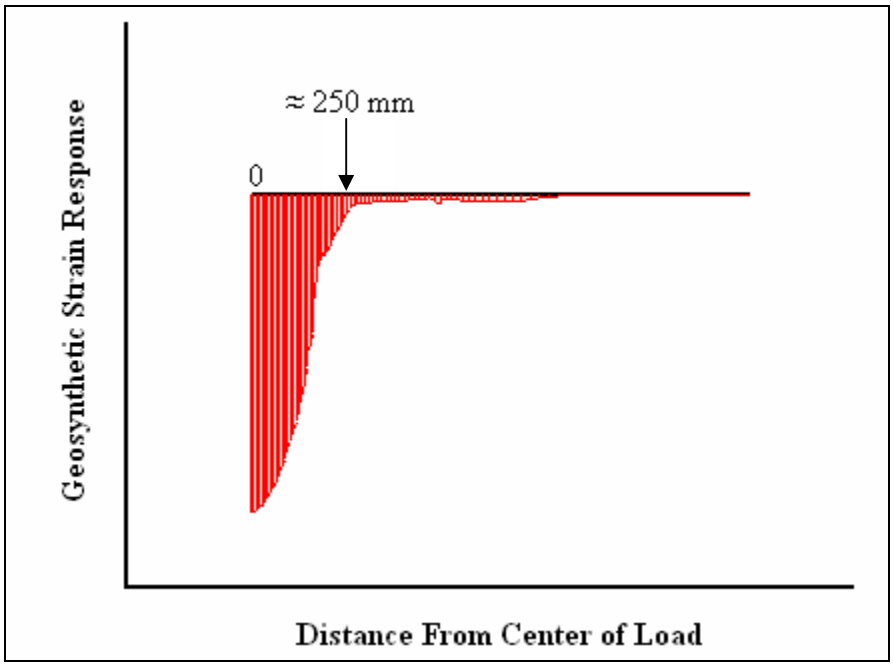

Figure 10.7 – Typical Geosynthetic Strain Response

10.3 Comparison of FEA and Measured Responses under FWD Loads

This section summarizes and compares the measured responses from the FWD loads to the data generated from the finite element model. Finite element calculations were performed to simulate every FWD test that was conducted in the field. Recall that FWD drops were performed at two locations within each test section: the center of the load plate was positioned directly over and 30 cm (1 ft) to one side of the embedded sensors. The following sections compare and contract measured (FWD) versus calculated responses in terms of 1) surface deflection, 2) asphalt strain, 3) crushed stone pressure, 4) compacted subgrade pressure, and 5) geosynthetic strain. Complete data sets can be found in the data addendum.

10.3.1 Surface Deflection:

Table 10.1 summarizes the average measured (FWD testing) and calculated vertical surface deflection response for each target load, test phase, and crushed stone thickness directly under the load. Figures 10.8 – 10.15 display the radial variations in the average deflection response resulting from the 40 KN (9 kip) FWD load. Figure

10.8 and 10.9 display test Phase 1 curves for Sections 1b-6 and Sections 8-13b, respectively. Figures 10.10 – 10.15 depict the same information for Phases 2-4. Overall deflection was under predicted for each condition. The last column of Table 10.1 also contains the ratio of the average measured and calculated values (M/C) directly under the load for the 27, 40, and 53 KN load levels during each test phase.

Calculated deflections were more consistent than the measured values, and the degree of variability for the measured deflections was higher than expected. Complete tables that summarize the variability of the measured deflection were provided in the data addendum, but are summarized as follows. The calculated vertical surface deflection values ranged between 51 μm and 102 μm directly under the load while the corresponding measured vertical deflection values ranged from 160 μm to 2040 μm. Similar ranges existed for radial distances that were less than 639 mm (24.76 in). Calculated deflections approached zero approximately 0.9 m -1.2 m (3-4 ft) from the load center, but measured deflections values stabilized near the 25-75 μm range.

Table 10.1 – Measured (FWD) and Calculated Vertical Surface Deflections (Under the Load)

Phase	*Test Section*	*Target Load KN (kip)*	*Measured, M*		*Calculated, C*		$\frac{M}{C}$
			μm	*Mils*	*μm*	*Mils*	
1	1b-6*	27 (6)	612.1	24.1	566.4	22.3	1.08
		40 (9)	944.9	37.2	749.3	29.5	1.26
		53 (12)	1292.9	50.9	927.1	36.5	1.39
	8-13b**	27 (6)	764.5	30.1	485.1	19.1	1.58
		40 (9)	1170.9	46.1	668.0	26.3	1.75
		53 (12)	1600.2	63.0	845.8	33.3	1.89
2	1b-6	27 (6)	607.1	23.9	454.7	17.9	1.34
		40 (9)	934.7	36.8	599.4	23.6	1.56
		53 (12)	1267.5	49.9	751.8	29.6	1.69
	8-13b	27 (6)	866.1	34.1	401.3	15.8	2.16
		40 (9)	1320.8	52.0	543.6	21.4	2.43
		53 (12)	1833.9	72.2	693.4	27.3	2.64
3	1b-6	27 (6)	482.6	19.0	325.1	12.8	1.48
		40 (9)	723.9	28.5	454.7	17.9	1.59
		53 (12)	1010.9	39.8	594.4	23.4	1.70
	8-13b	27 (6)	558.8	22.0	289.6	11.4	1.93
		40 (9)	843.3	33.2	406.4	16.0	2.08
		53 (12)	1193.8	47.0	533.4	21.0	2.24
4	1b-6	27 (6)	523.2	20.6	381.0	15.0	1.37
		40 (9)	787.4	31.	528.	20.	1.4

			0	3	8	9
	53 (12)	1102.4	43.4	675.6	26.6	1.63
	27 (6)	675.6	26.6	327.7	12.9	2.06
8-13b	40 (9)	1023.6	40.3	447.0	17.6	2.29
	53 (12)	1458.0	57.4	596.9	23.5	2.44

** Base course thickness = 25.4 cm*
*** Base course thickness = 15.2 cm*

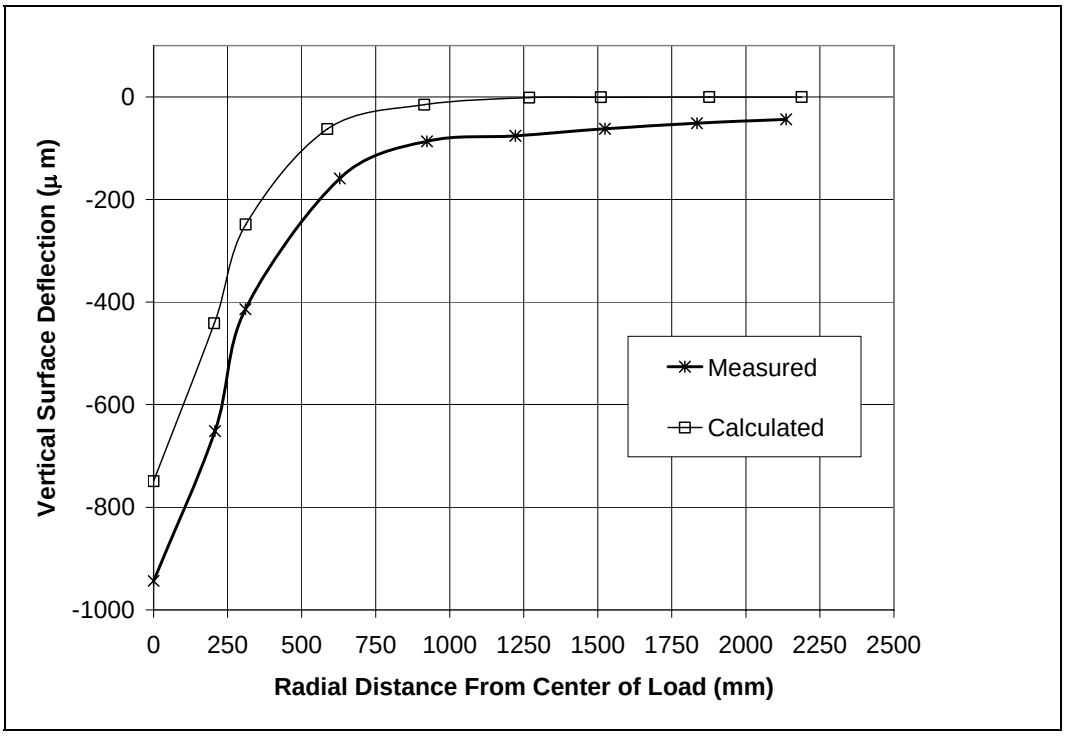

Figure 10.8 - Average Deflection Basins (Phase 1, Sections 1b-6, 40 KN Load)

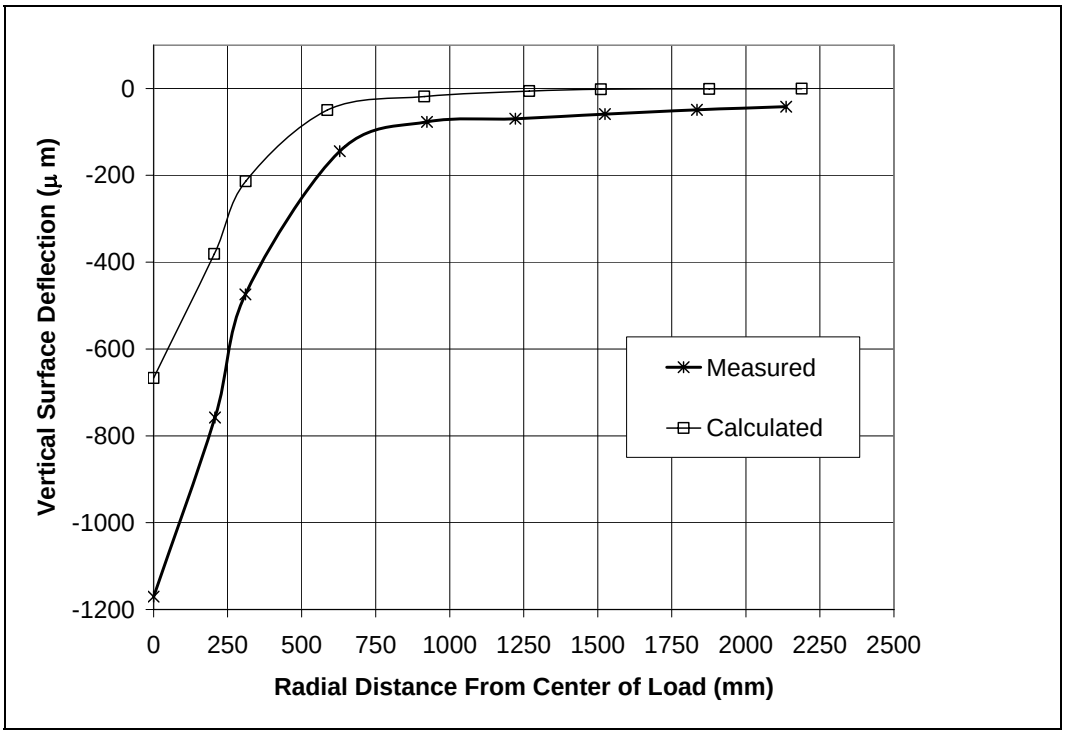

Figure 10.9 - Average Deflection Basins (Phase 1, Sections 8-13b, 40 KN Load)

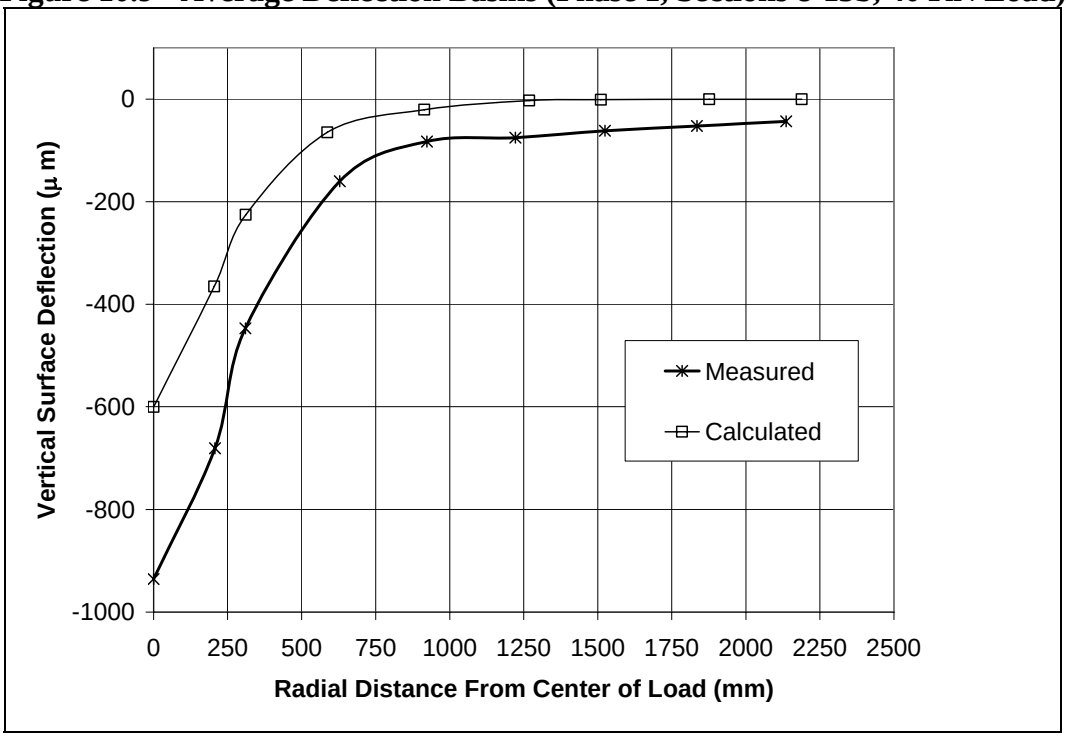

Figure 10.10 - Average Deflection Basins (Phase 2, Sections 1b-6, 40 KN Load)

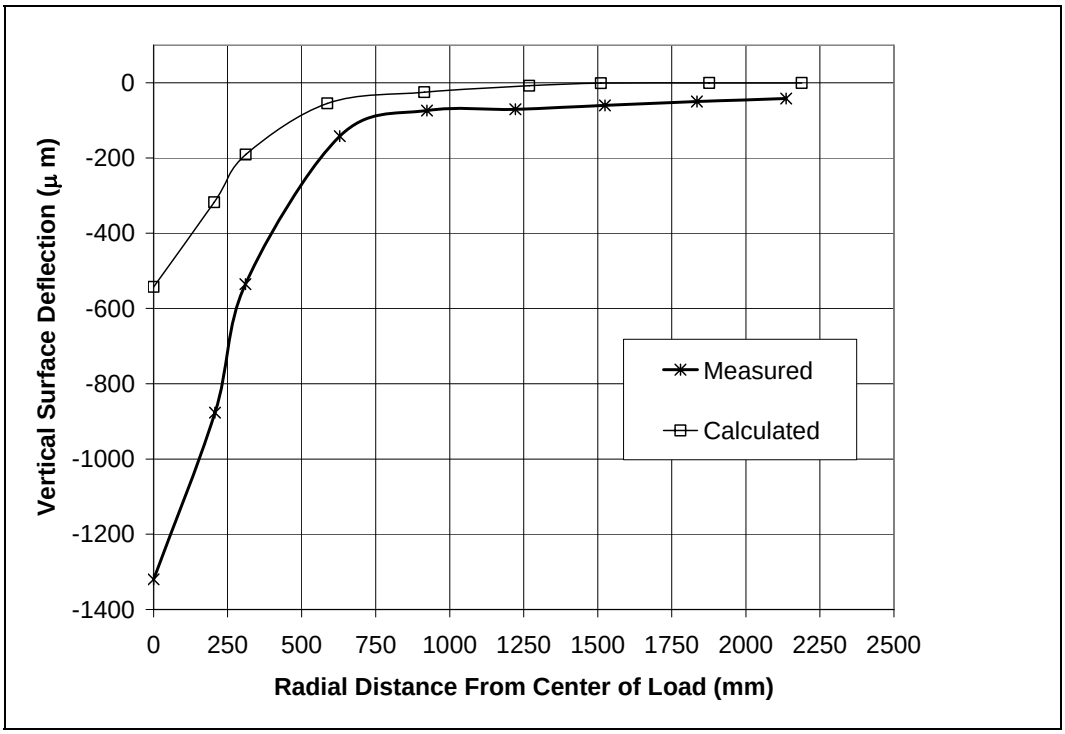

Figure 10.11 - Average Deflection Basins (Phase 2, Sections 8-13b, 40 KN Load)

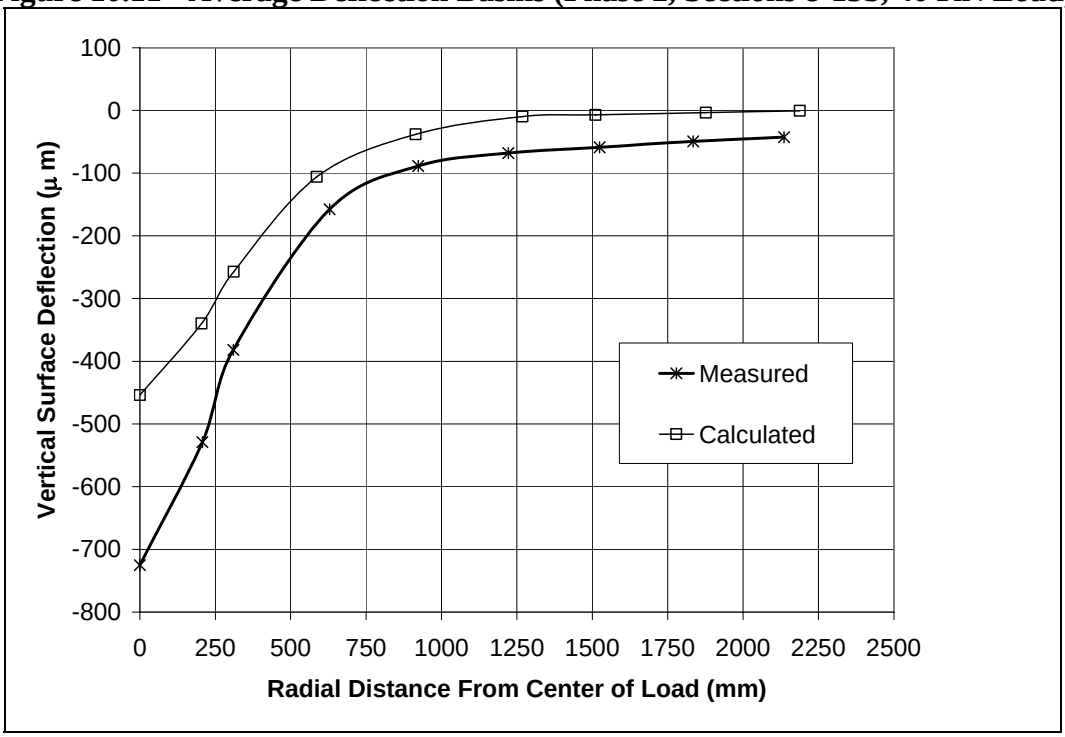

Figure 10.12 - Average Deflection Basins (Phase 3, Sections 1b-6, 40 KN Load)

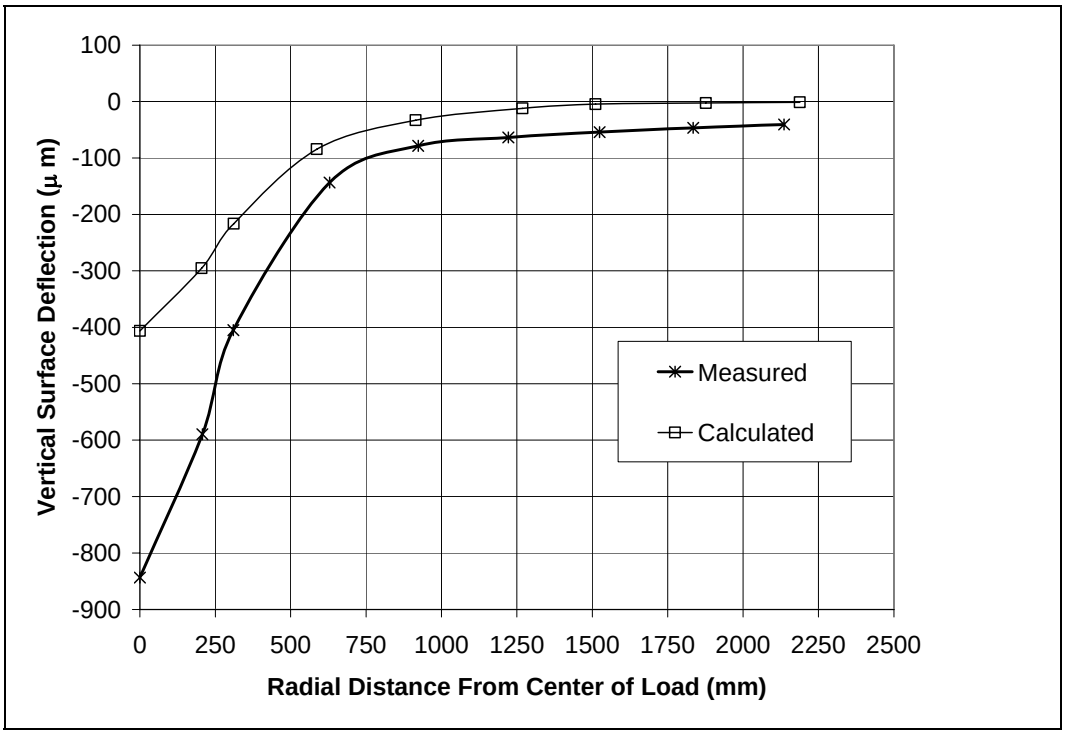

Figure 10.13 - Average Deflection Basins (Phase 3, Sections 8-13b, 40 KN Load)

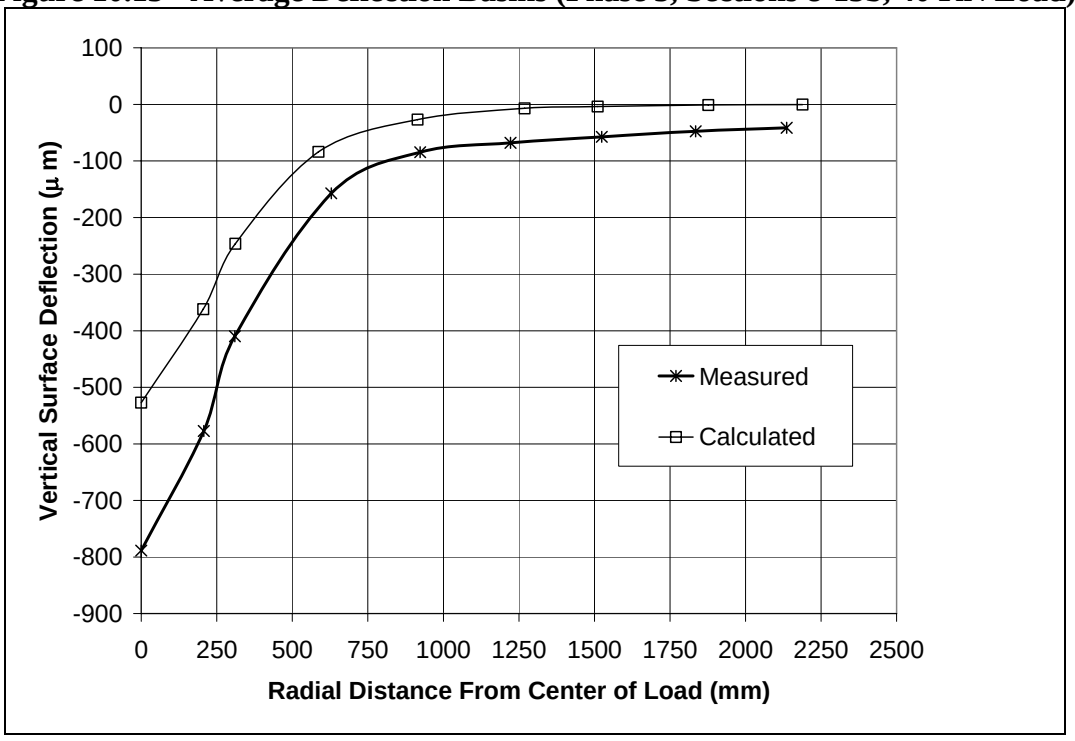

Figure 10.14 - Average Deflection Basins (Phase 4, Sections 1b-6, 40 KN Load)

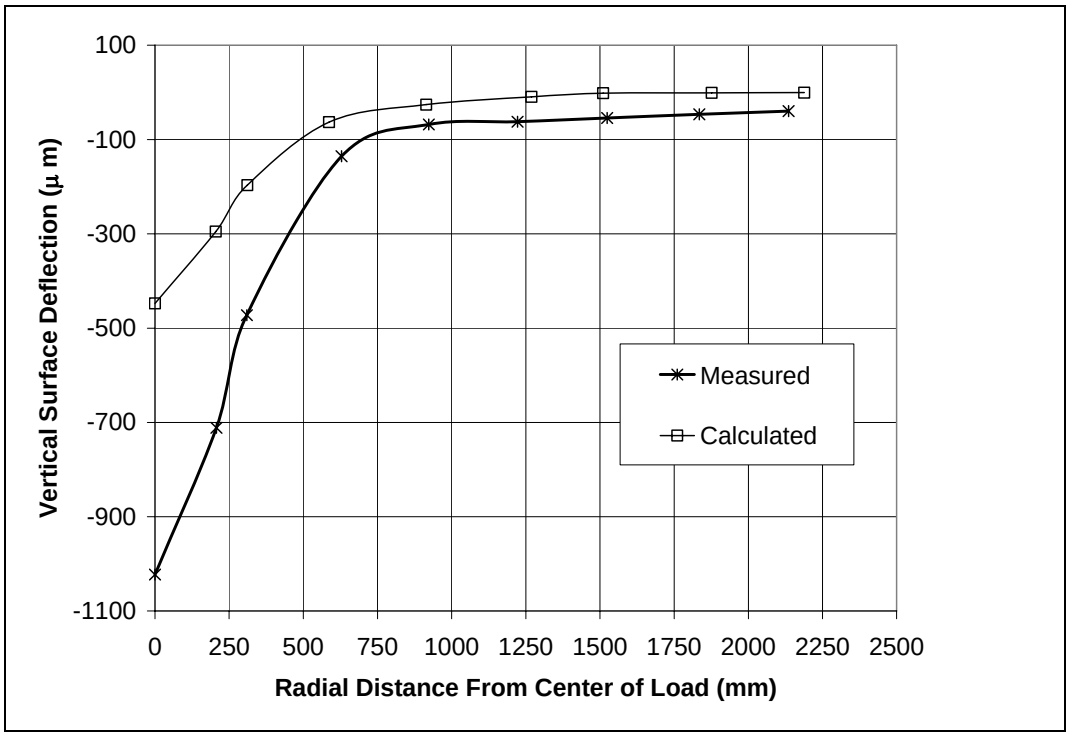

Figure 10.15 - Average Deflection Basins (Phase 4, Sections 8-13b, 40 KN Load)

10.3.2 Asphalt Strain:

Table 10.2 and Table 10.3 summarize the average measured (FWD) and calculated asphalt strain response for each target load, test section, and test phase under the load and 30 cm (1 ft) from the load, respectively. Generally, strains were over predicted (the calculated to measured ratio in the last column of both tables was typically greater than 1.0) with few exceptions in Sections 8-13b. In comparison to Sections 1b-6, the measured responses were closer to the calculated responses in Sections 8-13b. It should be noted that the majority of the material characterization was performed using soil samples from Section 13.

Complete tables that summarize the variability of the asphalt strain data for each FWD load level and base course thickness were provided in the data addendum, but are summarized as follows. Calculated asphalt strains varied between 6 - 65 με while measured values varied between 41- 474 με. As the temperature increased, the variability of both the measured and calculated values increased. A more complete discussion regarding measured asphalt strain variability can be found in Section 8.4.

Table 10.2 - Measured (FWD) and Calculated Asphalt Strain Responses (Under the Load)

Phase	*Sections*	*Target Load KN (kip)*	*Measured,M (με)*	*Calculated, C (με)*	$\frac{C}{M}$
1	1b-6	27 (6)	85	217	2.54
		40 (9)	138	267	1.94
		53 (12)	193	306	1.59
	8-13b	27 (6)	125	204	1.63
		40 (9)	191	259	1.35
		53 (12)	258	305	1.18
2	1b-6	27 (6)	58	180	3.13
		40 (9)	91	234	2.57
		53 (12)	121	277	2.29
	8-13b	27 (6)	132	169	1.28
		40 (9)	207	222	1.08
		53 (12)	271	270	1.00
3	1b-6	27 (6)	25	87	3.49
		40 (9)	35	123	3.49
		53 (12)	50	159	3.16
	8-13b	27 (6)	88	81	0.93
		40 (9)	130	115	0.89
		53 (12)	184	152	0.83
4	1b-6	27 (6)	37	127	3.44
		40 (9)	53	174	3.29
		53 (12)	72	219	3.04
	8-13b	27 (6)	111	117	1.06
		40 (9)	163	161	0.99
		53 (12)	223	211	0.95

Table 10.3 - Measured (FWD) and Calculated Asphalt Strain Responses (30 cm from the Load)

Phase	*Sections*	*Target Load KN (kip)*	*Measured,M (με)*	*Calculated, C (με)*	*C/M*
1	1b-6	27 (6)	23	60	2.57
		40 (9)	36	76	2.12
		53 (12)	50	90	1.81
	8-13b	27 (6)	35	54	1.54
		40 (9)	50	70	1.41
		53 (12)	74	85	1.16
2	1b-6	27 (6)	31	49	1.56
		40 (9)	49	61	1.25
		53 (12)	61	74	1.21
	8-13b	27 (6)	46	43	0.94
		40 (9)	68	56	0.83
		53 (12)	90	69	0.77
3	1b-6	27 (6)	17	34	2.03
		40 (9)	22	48	2.24
		53 (12)	29	62	2.13
	8-13b	27 (6)	32	31	0.98
		40 (9)	50	44	0.89
		53 (12)	74	57	0.77
4	1b-6	27 (6)	18	43	2.35
		40 (9)	27	58	2.17
		53 (12)	34	73	2.12
	8-13b	27 (6)	28	38	1.35
		40 (9)	39	51	1.31
		53 (12)	53	66	1.25

10.3.3 Crushed Stone Earth Pressure:

Table 10.4 and Table 10.5 summarize the average measured (FWD testing) and calculated total earth pressure response in the crushed stone under the load and 30 cm (1 ft) from the load, respectively. In all cases, pressure was over predicted but the over prediction was somewhat consistent from section to section. Tables that summarize the variability of the total earth pressure response in the base course aggregate for each FWD load level and base course thickness were included in the data addendum. Earth pressures varied between 10.3-47.5 kPa (1.5-6.9 psi) while measured values varied between 12.4-55.8 kPa (1.8-8.1 psi).

Table 10.4 - Measured (FWD) and Calculated Crushed stone Pressure Responses (Under the Load)

Phase	*Sections*	*Target Load KN (kip)*	*Measured, M kPa (psi)*	*Calculated, C kPa (psi)*	$\frac{C}{M}$
1	1b-6	27 (6)	35.8 (5.2)	117.8 (17.1)	3.30
		40 (9)	49.6 (7.2)	173.6 (25.2)	3.52
		53 (12)	68.9 (10.0)	222.5 (32.3)	3.22
	8-13b	27 (6)	-	144.7 (21.0)	-
		40 (9)	-	208.1 (30.2)	-
		53 (12)	-	259.8 (37.7)	-
2	1b-6	27 (6)	29.6 (4.3)	88.9 (12.9)	3.03
		40 (9)	44.8 (6.5)	132.3 (19.2)	2.94
		53 (12)	61.3 (8.9)	170.2 (24.7)	2.78
	8-13b	27 (6)	-	108.2 (15.7)	-
		40 (9)	-	158.5 (23.0)	-
		53 (12)	-	201.2 (29.2)	-
3	1b-6	27 (6)	25.5 (3.7)	64.8 (9.4)	2.53
		40 (9)	38.6 (5.6)	100.6 (14.6)	2.61
		53 (12)	53.1 (7.7)	133.0 (19.3)	2.53
	8-13b	27 (6)	-	76.5 (11.1)	-
		40 (9)	-	116.4 (16.9)	-
		53 (12)	-	153.0 (22.2)	-
4	1b-6	27 (6)	31.0 (4.5)	80.6 (11.7)	2.61
		40 (9)	44.8 (6.5)	121.3 (17.6)	2.71
		53 (12)	59.9 (8.7)	155.7 (22.6)	2.59
	8-13b	27 (6)	-	95.1 (13.8)	-

40 (9)	-	142.6 (20.7)	-
53 (12)	-	188.1 (27.3)	-

Table 10.5 - Measured (FWD) and Calculated Crushed stone Pressure Responses (30 cm from the Load)

Phase	*Sections*	*Target Load KN (kip)*	*Measured, M kPa (psi)*	*Calculated, C kPa (psi)*	$\frac{C}{M}$
1	1b-6	27 (6)	6.9 (1.0)	20.7 (3.0)	2.89
		40 (9)	10.3 (1.5)	28.2 (4.1)	2.68
		53 (12)	13.8 (2.0)	35.1 (5.1)	2.57
	8-13b	27 (6)	-	20.0 (2.9)	-
		40 (9)	-	28.2 (4.1)	-
		53 (12)	-	35.8 (5.2)	-
2	1b-6	27 (6)	13.8 (2.0)	24.1 (3.5)	1.74
		40 (9)	20.7 (3.0)	33.1 (4.8)	1.57
		53 (12)	28.2 (4.1)	40.7 (5.9)	1.45
	8-13b	27 (6)	-	23.4 (3.4)	-
		40 (9)	-	32.4 (4.7)	-
		53 (12)	-	41.3 (6.0)	-
3	1b-6	27 (6)	9.0 (1.3)	24.1 (3.5)	2.82
		40 (9)	11.7 (1.7)	33.8 (4.9)	2.89
		53 (12)	17.2 (2.5)	44.8 (6.5)	2.59
	8-13b	27 (6)	-	25.5 (3.7)	-
		40 (9)	-	35.8 (5.2)	-
		53 (12)	-	48.9 (7.1)	-
4	1b-6	27 (6)	11.0 (1.6)	24.8 (3.6)	2.28
		40 (9)	16.5 (2.4)	35.1 (5.1)	2.13
		53 (12)	22.0 (3.2)	44.8 (6.5)	2.00
	8-13b	27 (6)	-	24.8 (3.6)	-
		40 (9)	-	35.8 (5.2)	-
		53 (12)	-	46.9 (6.8)	-

10.3.4 Compacted Subgrade Earth Pressure:

Table 10.6 and Table 10.7 summarize the average measured (FWD testing) and calculated compacted subgrade total earth pressure response under the load and 30 cm (1 ft) from the load, respectively. In all cases, pressure was over predicted, but the extent of over prediction was higher in Sections 8-13b. For example, the calculated to measured ratios displayed in the last column of Table 10.6 for Phase 1 are equal to 5.99, 5.80, and 5.53 in Sections 1b-6, and they are 7.20, 6.53, and 5.99 in Sections 8-13b. Tables that summarize the variability of the total earth pressure response in the

compacted subgrade for each FWD load level and base course thickness were included in the data addendum. Calculated compacted subgrade pressures varied between 9.0 and 38.0 kPa (1.3-5.5 psi) while measured values varied between 19.3 and 62.7 kPa (2.8-9.1 psi).

Table 10.6 - Measured (FWD) and Calculated Compacted Subgrade Pressure Responses (Under the Load)

Phase	*Sections*	*Target Load KN (kip)*	*Measured, M kPa (psi)*	*Calculated, C kPa (psi)*	$\frac{C}{M}$
1	1b-6	27 (6)	15.2 (2.2)	90.3 (13.1)	5.99
		40 (9)	21.4 (3.1)	122.6 (17.8)	5.80
		53 (12)	28.2 (4.1)	157.1 (22.8)	5.53
	8-13b	27 (6)	16.5 (2.4)	118.5 (17.2)	7.20
		40 (9)	24.8 (3.6)	163.3 (23.7)	6.53
		53 (12)	33.1 (4.8)	199.8 (29.0)	5.99
2	1b-6	27 (6)	15.2 (2.2)	70.3 (10.2)	4.65
		40 (9)	22.7 (3.3)	97.1 (14.1)	4.32
		53 (12)	29.6 (4.3)	118.5 (17.2)	4.02
	8-13b	27 (6)	16.5 (2.4)	93.0 (13.5)	5.63
		40 (9)	24.8 (3.6)	130.9 (19.0)	5.22
		53 (12)	33.8 (4.9)	161.9 (23.5)	4.83
3	1b-6	27 (6)	13.8 (2.0)	57.9 (8.4)	4.30
		40 (9)	20.0 (2.9)	83.4 (12.1)	4.18
		53 (12)	26.9 (3.9)	104.0 (15.1)	3.88
	8-13b	27 (6)	11.0 (1.6)	71.7 (10.4)	6.64
		40 (9)	16.5 (2.4)	104.7 (15.2)	6.30
		53 (12)	23.4 (3.4)	133.7 (19.4)	5.78
4	1b-6	27 (6)	15.9 (2.3)	67.6 (9.8)	4.29
		40 (9)	22.7 (3.3)	93.8 (13.6)	4.15
		53 (12)	30.3 (4.4)	115.1 (16.7)	3.81

	27 (6)	13.8 (2.0)	84.7 (12.3)	6.05
	40 (9)	21.4 (3.1)	121.3 (17.6)	5.78
8-13b				
	53 (12)	28.9 (4.2)	155.7 (22.6)	5.41

Table 10.7 - Measured (FWD) and Calculated Compacted Subgrade Pressure Responses (30 cm from the Load)

Phase	*Sections*	*Target Load KN (kip)*	*Measured, M kPa (psi)*	*Calculated, C kPa (psi)*	$\frac{C}{M}$
1	1b-6	27 (6)	4.8 (0.7)	26.2 (3.8)	5.56
		40 (9)	6.9 (1.0)	35.8 (5.2)	5.07
		53 (12)	9.6 (1.4)	45.5 (6.6)	4.66
	8-13b	27 (6)	8.3 (1.2)	26.2 (3.8)	3.18
		40 (9)	12.4 (1.8)	36.5 (5.3)	2.89
		53 (12)	16.5 (2.4)	46.9 (6.8)	2.79
2	1b-6	27 (6)	7.6 (1.1)	29.6 (4.3)	3.89
		40 (9)	11.7 (1.7)	40.7 (5.9)	3.54
		53 (12)	15.2 (2.2)	50.3 (7.3)	3.35
	8-13b	27 (6)	8.3 (1.2)	29.6 (4.3)	3.57
		40 (9)	12.4 (1.8)	40.7 (5.9)	3.25
		53 (12)	16.5 (2.4)	51.7 (7.5)	3.13
3	1b-6	27 (6)	6.9 (1.0)	28.9 (4.2)	4.10
		40 (9)	8.3 (1.2)	39.3 (5.7)	4.74
		53 (12)	12.4 (1.8)	51.7 (7.5)	4.17
	8-13b	27 (6)	4.8 (0.7)	29.6 (4.3)	6.08
		40 (9)	7.6 (1.1)	42.0 (6.1)	5.58
		53 (12)	10.3 (1.5)	56.5 (8.2)	5.37
4	1b-6	27 (6)	7.6 (1.1)	29.6 (4.3)	3.98
		40 (9)	11.0 (1.6)	40.7 (5.9)	3.68
		53 (12)	17.2 (2.5)	52.4 (7.6)	3.06
	8-13b	27 (6)	6.2 (0.9)	29.6 (4.3)	4.73
		40 (9)	9.7 (1.4)	42.0 (6.1)	4.31
		53 (12)	13.1 (1.9)	55.8 (8.1)	4.15

10.3.5 Geosynthetic Strain:

The measured geosynthetic strain responses were deemed negligible for all three testing phases. The only measured reading obtained was the inherent noise band in the signal, implying that no load outside of the measurement and/or calibration tolerances was detected. The values calculated by the FEA model were in agreement. Table 10.8 summarizes the range of calculated values, but all values were at or below 0.06% strain.

Table 10.8 –Calculated Geosynthetic Strain Response Ranges from FWD Loads

	Under Load		*Offset 300 mm (1 ft)*	
Phase	*Geotextile (με)*	*Geogrid (με)*	*Geotextile (με)*	*Geogrid (με)*
1	118-600	120-445	1-13	2-9
2	107-377	98-343	5-18	5-13
3	44-220	47-223	1-21	2-21
4	68-302	73-302	3-21	3-21

10.4 Comparing FEA and Measured Responses under Traffic Loads

This section summarizes and compares the measured responses from traffic loads to the data generated from the finite element model. One simulation was performed for each test section and traffic test phase using weighted average conditions calculated for axle weights, asphalt temperature, and all gage responses measured in the field (discussed in Chapter 8). This methodology provides a weighted average of representative values under similar testing conditions to determine model inputs and for comparison with finite element modeling results.

The majority of the variable inputs necessary to perform the modeling were obtained from the 40 KN (9 kip) FWD inputs discussed in the previous section. However, the asphalt modulus and applied pressure were obtained using data from Table 8.3 (back axle) to simulate actual traffic conditions as close as possible. The following sections compare and contract measured (traffic) versus calculated responses in terms of 1) asphalt strain, 2) crushed stone total earth pressure, 3) compacted subgrade total earth pressure, and 4) geosynthetic strain. Complete data sets are located in the data addendum.

10.4.1 Asphalt Strain:

Table 10.9 summarizes the average measured (traffic) and calculated asphalt strain response in each test section for all three test phases directly under the load. Strains were over predicted (the ratio of calculated to measured was greater than 1.0) in all but nine cases. Note that Section 9 (the asphalt strain gage that was not functioning properly) was under predicted during all three traffic phases. There also appears to be more variability (from section to section) in the measured values.

Table 10.9 - Measured (Traffic) and Calculated Asphalt Strain Responses (Under the Load)

Phase	*Test Section*	*Measured,M (με)*	*Calculated, C (με)*	$\frac{C}{M}$
A	1b	263	310	1.2
	1a	203	308	1.5
	1	170	310	1.8
	2	231	308	1.3
	3	378	332	0.9
	4	295	355	1.2
	5	173	332	1.9
	6	142	310	2.2
	8	210	292	1.4
	9	387	298	0.8
	10	344	299	0.9
	11	379	293	0.8
	12	293	325	1.1
	13	157	324	2.1
	13a	361	346	1.0
	13b	514	337	0.7
B	1b	106	161	1.5
	1a	76	165	2.2
	1	44	174	4.0
	2	61	171	2.8
	3	97	167	1.7
	4	61	180	3.0
	5	78	168	2.2
	6	65	167	2.6
	8	56	161	2.9
	9	319	159	0.5
	10	91	164	1.8
	11	118	157	1.3
	12	98	162	1.7
	13	61	162	2.7
	13a	169	164	1.0
	13b	149	162	1.1
C	1b	81	151	1.9
	1a	58	155	2.7
	1	43	162	3.8
	2	50	158	3.2
	3	88	155	1.8
	4	55	168	3.1
	5	73	158	2.2
	6	64	155	2.4
	8	61	151	2.5
	9	352	148	0.4
	10	88	151	1.7
	11	118	145	1.2
	12	103	150	1.5
	13	70	153	2.2
	13a	225	153	0.7
	13b	194	152	0.8

10.4.2 Crushed Stone Pressure:

Table 10.10 summarizes the average measured (traffic) and calculated earth pressure response in the crushed stone for each test section and test phase directly under the load. Pressures were over predicted in all cases (the calculated to measured ratio was greater than 1.0), and the extent of over prediction remained reasonably consistent from section to section.

Table 10.10 - Measured (Traffic) and Calculated Crushed stone Pressure Responses (Under the Load)

Phase	*Test Section*	*Measured, M kPa (psi)*	*Calculated, C kPa (psi)*	$\frac{C}{M}$
A	1b	79.2 (11.5)	190.2 (27.6)	2.4
	1a	85.4 (12.4)	185.3 (26.9)	2.2
	1	91.7 (13.3)	156.4 (22.7)	1.7
	2	88.2 (12.8)	184.7 (26.8)	2.1
	3	99.3 (14.4)	176.4 (25.6)	1.8
	4	113.8 (16.5)	168.8 (24.5)	1.5
	5	91.7 (13.3)	159.8 (23.2)	1.7
	6	109.6 (15.9)	175.0 (25.4)	1.6
B	1b	67.5 (9.8)	133.0 (19.3)	2.0
	1a	75.8 (11.0)	130.2 (18.9)	1.7
	1	79.9 (11.6)	119.9 (17.4)	1.5
	2	80.6 (11.7)	137.1 (19.9)	1.7
	3	95.8 (13.9)	124.0 (18.0)	1.3
	4	107.5 (15.6)	122.6 (17.8)	1.1
	5	60.6 (8.8)	113.0 (16.4)	1.9
	6	81.3 (11.8)	124.7 (18.1)	1.5
C	1b	64.1 (9.3)	126.1 (18.3)	2.0
	1a	77.9 (11.3)	124.7 (18.1)	1.6
	1	75.8 (11.0)	116.4 (16.9)	1.5
	2	90.3 (13.1)	130.9 (19.0)	1.5
	3	99.9 (14.5)	122.0 (17.7)	1.2
	4	112.3 (16.3)	119.2 (17.3)	1.1
	5	64.1 (9.3)	107.5 (15.6)	1.7
	6	77.9 (11.3)	121.3 (17.6)	1.6

10.4.3 Compacted Subgrade Pressure:

Table 10.11 summarizes the average measured (traffic) and calculated earth pressure responses in the compacted subgrade for each test section and test phase. Pressures were over predicted (the ratio of calculated to measured was greater than 1.0) in all cases, and the extent of over prediction varied significantly from section to section. The ratio varied from slightly over 1.0 to approximately 14.4.

Table 10.11 - Measured (Traffic) and Calculated Compacted Subgrade Pressure Responses (Under the Load)

Phase	*Test Section*	*Measured, M kPa (psi)*	*Calculated, C kPa (psi)*	*C / M*
	1b	77.9 (11.3)	130.9 (19.0)	1.7
	1a	44.1 (6.4)	125.4 (18.2)	2.8
	1	62.7 (9.1)	102.7 (14.9)	1.6
	2	90.3 (13.1)	128.8 (18.7)	1.4
	3	71.7 (10.4)	124.7 (18.1)	1.7
	4	59.3 (8.6)	113.0 (16.4)	1.9
	5	62.7 (9.1)	115.1 (16.7)	1.8
A	6	10.3 (1.5)	122.0 (17.7)	11.8
	8	99.9 (14.5)	173.6 (25.2)	1.7
	9	28.9 (4.2)	170.9 (24.8)	5.9
	10	37.9 (5.5)	177.1 (25.7)	4.7
	11	39.3 (5.7)	165.4 (24.0)	4.2
	12	48.2 (7.0)	159.8 (23.2)	3.3
	13	124.0 (18.0)	166.7 (24.2)	1.3
	13a	37.9 (5.5)	163.3 (23.7)	4.3
	13b	121.3 (17.6)	177.1 (25.7)	1.5
	1b	79.9 (11.6)	106.1 (15.4)	1.3
	1a	49.6 (7.2)	102.7 (14.9)	2.1
	1	67.5 (9.8)	93.0 (13.5)	1.4
	2	86.1 (12.5)	110.2 (16.0)	1.3
	3	75.1 (10.9)	101.3 (14.7)	1.3
	4	58.6 (8.5)	97.1 (14.1)	1.7
	5	48.2 (7.0)	91.6 (13.3)	1.9
	6	6.9 (1.0)	99.2 (14.4)	14.4
B	8	95.8 (13.9)	133.0 (19.3)	1.4
	9	12.4 (1.8)	129.5 (18.8)	10.4
	10	28.2 (4.1)	137.8 (20.0)	4.9
	11	24.1 (3.5)	125.4 (18.2)	5.2
	12	20.7 (3.0)	124.7 (18.1)	6.0
	13	113.0 (16.4)	125.4 (18.2)	1.1
	13a	15.9 (2.3)	122.0 (17.7)	7.7
	13b	88.9 (12.9)	127.5 (18.5)	1.4
C	1b	72.4 (10.5)	98.5 (14.3)	1.3
	1a	50.3 (7.3)	95.8 (13.9)	1.9

1	73.0 (10.6)	89.6 (13.0)	1.2
2	93.0 (13.5)	104.0 (15.1)	1.1
3	77.9 (11.3)	98.5 (14.3)	1.3
4	63.4 (9.2)	93.7 (13.6)	1.5
5	51.0 (7.4)	86.1 (12.5)	1.7
6	8.3 (1.2)	96.5 (14.0)	11.7
8	87.5 (12.7)	126.1 (18.3)	1.4
9	13.8 (2.0)	125.4 (18.2)	9.1
10	29.6 (4.3)	137.8 (20.0)	4.7
11	25.5 (3.7)	124.0 (18.0)	4.9
12	24.1 (3.5)	124.0 (18.0)	5.1
13	116.4 (16.9)	118.5 (17.2)	1.0
13a	17.9 (2.6)	118.5 (17.2)	6.6
13b	90.9 (13.2)	125.4 (18.2)	1.4

10.4.4 Geosynthetic Strain:

The measured geosynthetic strain responses were deemed negligible for all three testing phases. The only measured reading obtained was the inherent noise band in the signal, implying that no load outside of the measurement and/or calibration tolerances was detected. The values calculated by the FEA model were in agreement. Table 10.12 contains ranges of values calculated, but all were at or below 0.05% strain.

Table 10.12 –Calculated Geosynthetic Strain Response Ranges from Traffic Loads

Phase	*Geotextile (με)*	*Geogrid (με)*
A	328-485	328-357
B	149-188	150-191
C	129-181	143-181

10.5 Model Calibration with Field Data

The data discussed in the previous section and presented in the separate data addendum were used to develop calibration equations for the finite element model under the limited environmental conditions encountered in the current study. Numerous plots were generated and will be displayed in the following sections to illustrate the differences between simulated (calculated) results from the FEA and measured data obtained during FWD and traffic loading conditions. Linear trend lines were generated using an intercept equal to zero, and the statistics from these equations

are summarized in Tables 10.13 and 10.14. An R^2 value equal to 1.0 indicates a perfect match between measured and calculated. If the slope of a regression line was less than 1.0, the model *over prediction* was equal to (1/slope). If the slope of a regression line was greater than 1.0, the model *under prediction* was still equal to (1/slope).

10.5.1 Model Calibration using FWD Load Data:

Tables 10.1 – 10.7 summarize and Figures 10.16 through 10.22 display the measured (FWD testing) and calculated response data. These tables and figures summarize ***all*** data including the responses associated with gages that were malfunctioning (the asphalt strain gage in Section 9 and the compacted subgrade pressure gages in Sections 6, 9, 10, 11, 12, and 13a). The magnitudes of the signals from these gages were unreasonable and did not compare well with trends exhibited by other gages that were functioning properly.

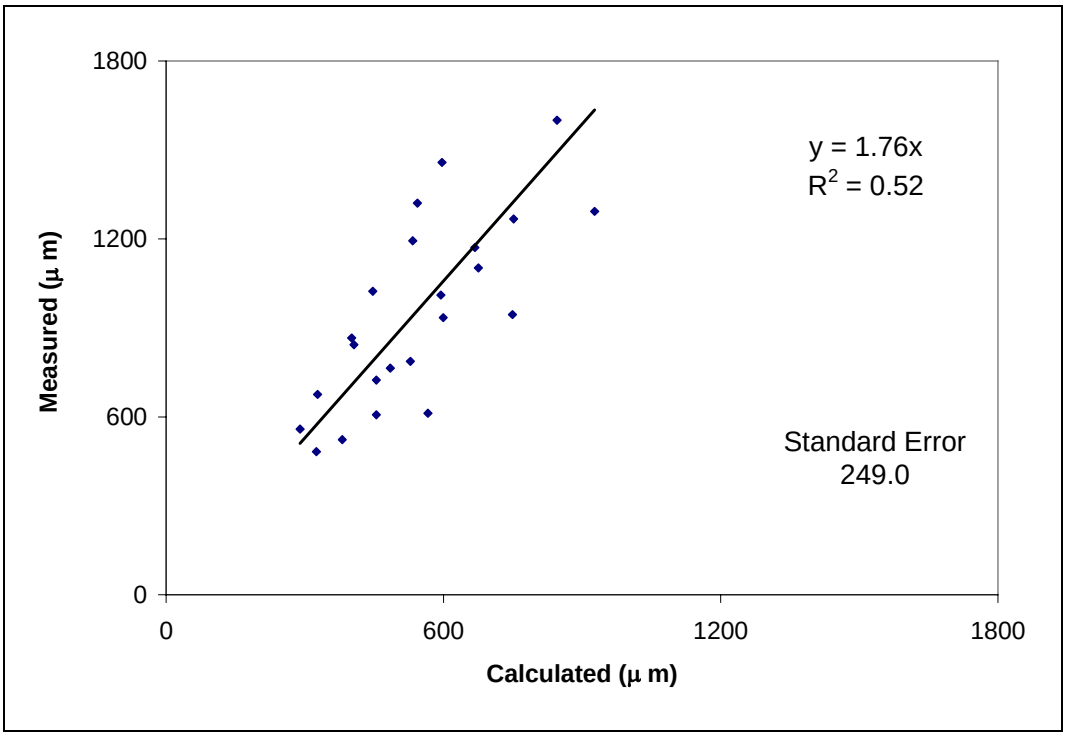

Figure 10.16 – All Measured (FWD) versus Calculated Deflections (Under Load)

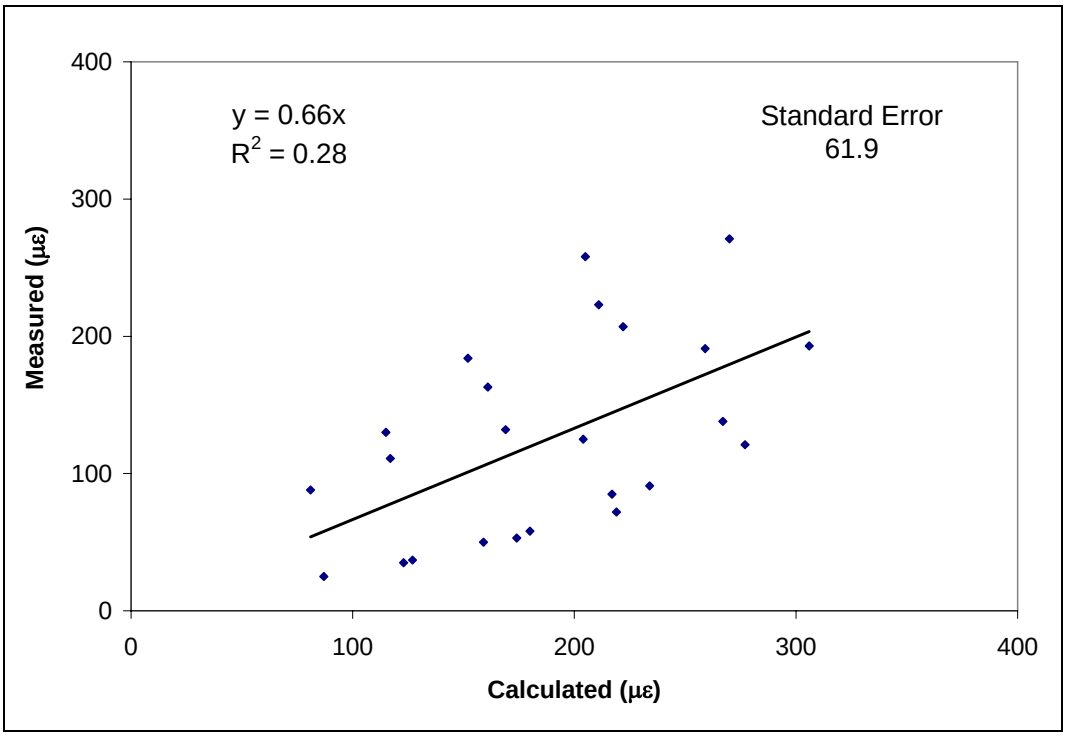

Figure 10.17 – All Measured (FWD) versus Calculated Asphalt Strains (Under Load)

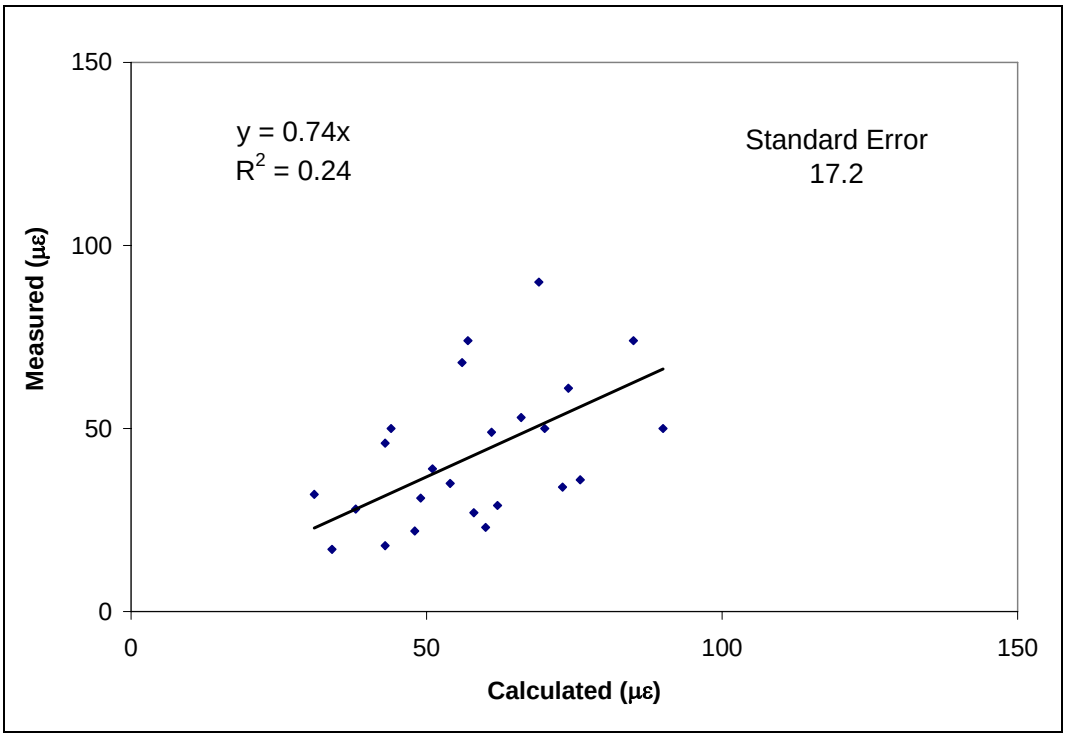

Figure 10.18 – All Measured (FWD) versus Calculated Asphalt Strains (Offset)

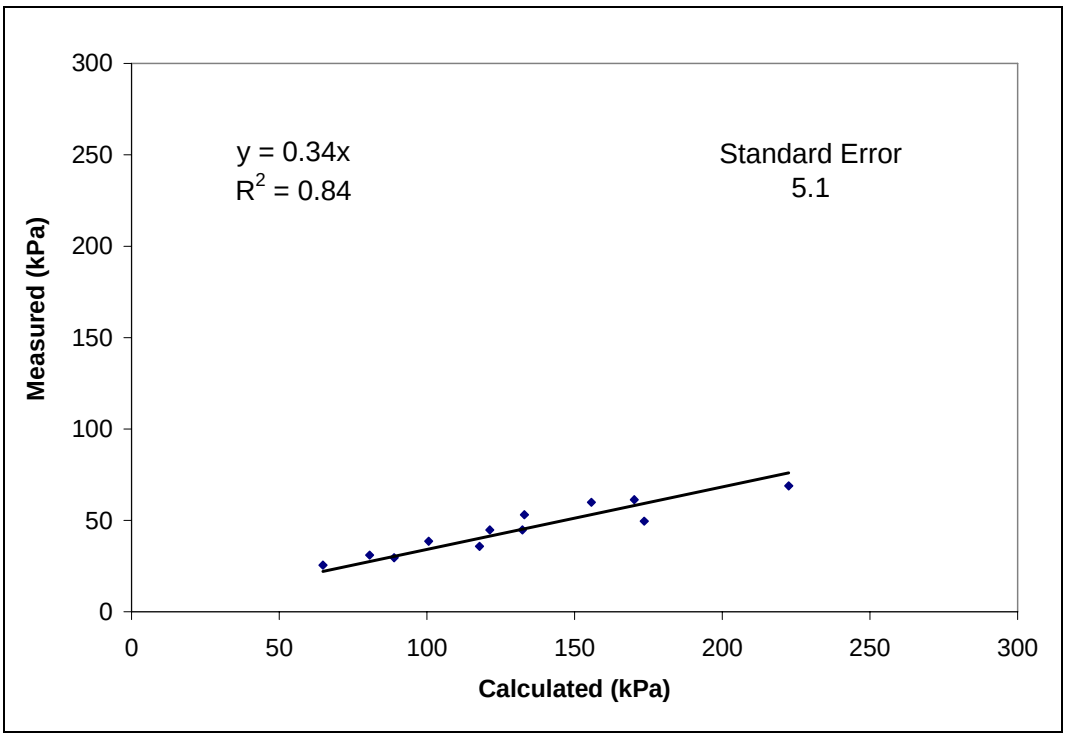

Figure 10.19 – All Measured (FWD) versus Calculated Crushed stone Pressures (Under Load)

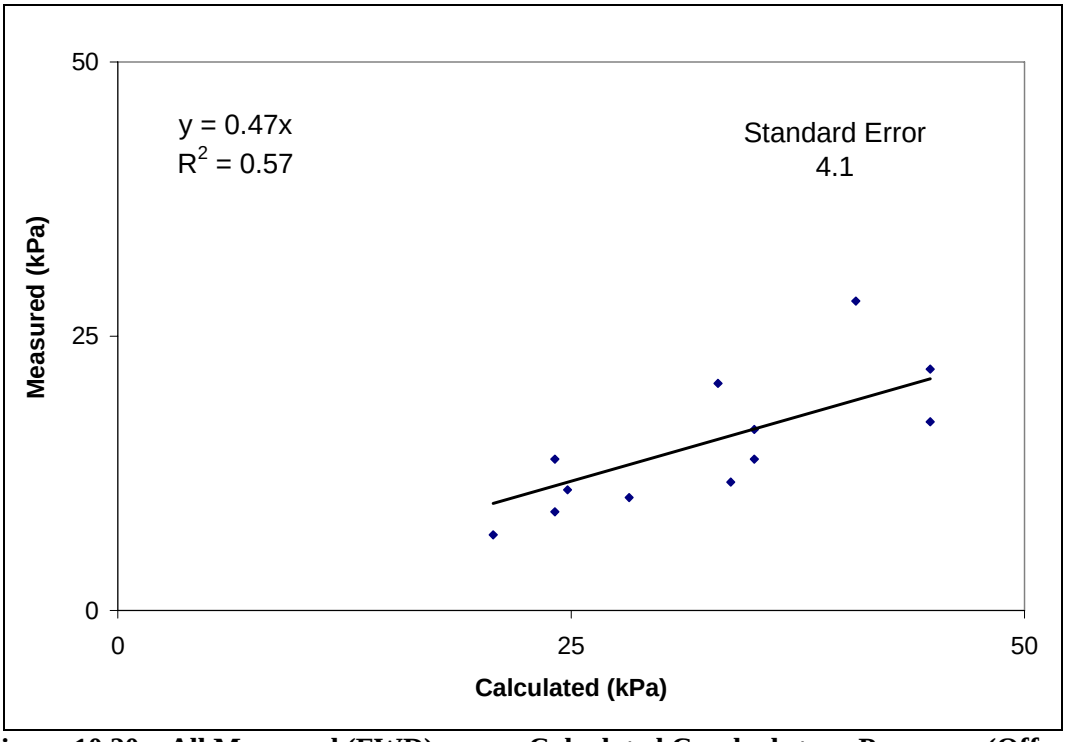

Figure 10.20 – All Measured (FWD) versus Calculated Crushed stone Pressures (Offset)

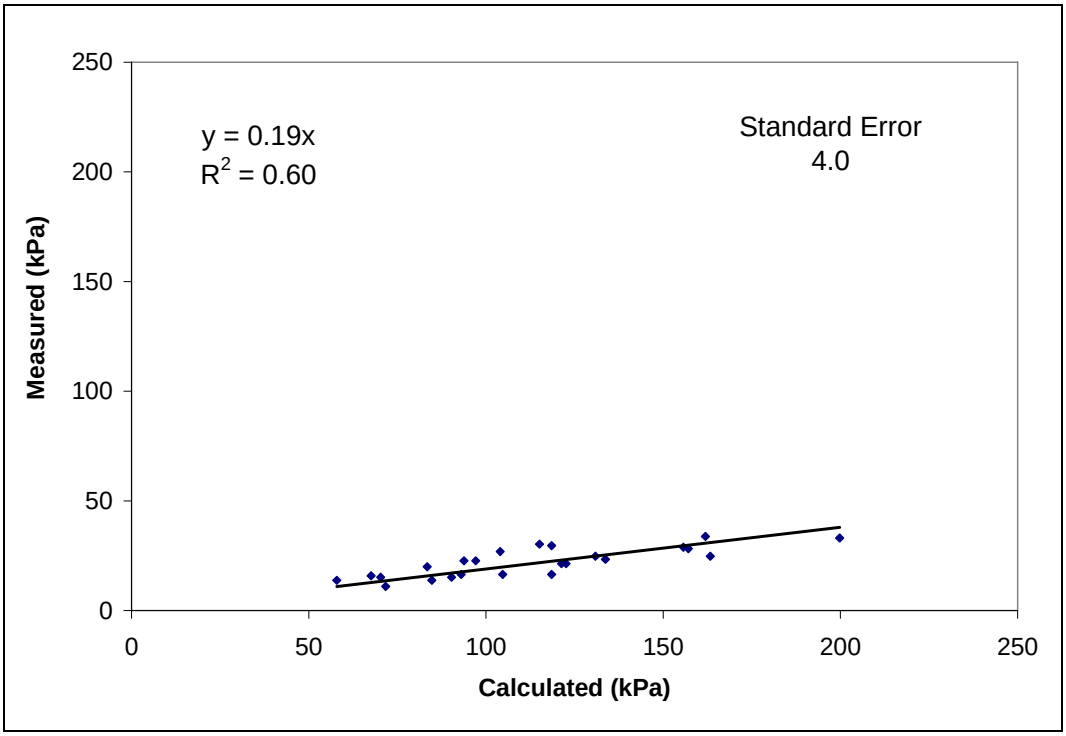

Figure 10.21 – All Measured (FWD) versus Calculated Subgrade Pressures (Under Load)

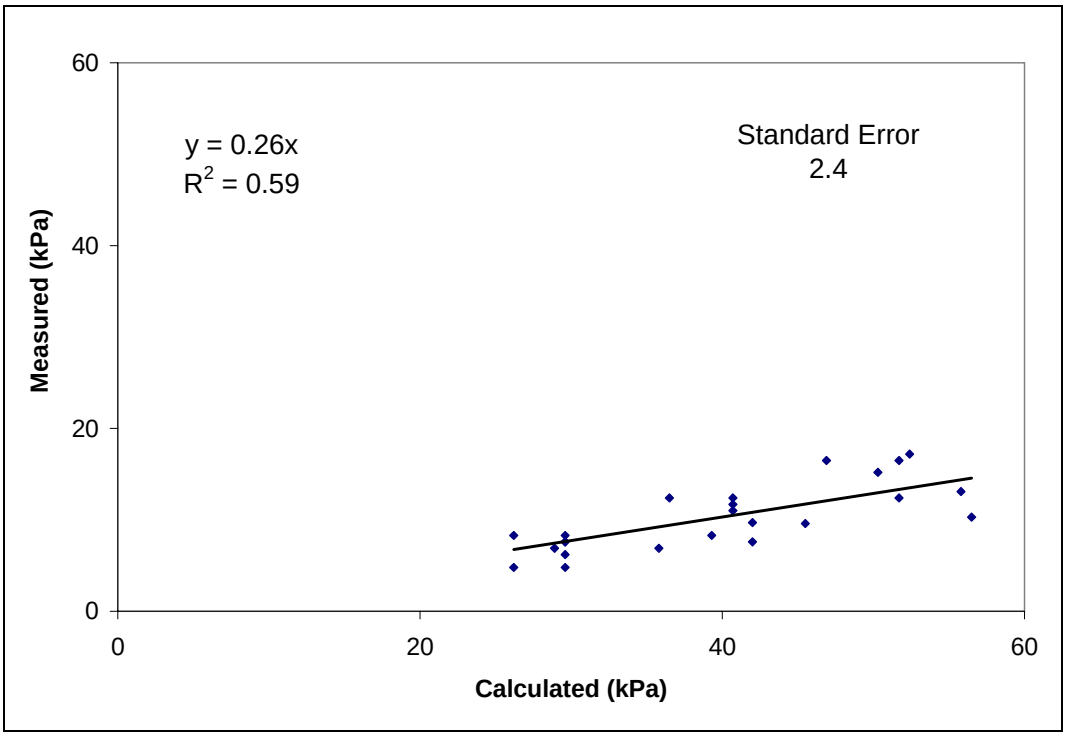

Figure 10.22 – All Measured (FWD) versus Calculated Subgrade Pressures (Offset)

As a result, the corresponding asphalt strain and compacted subgrade pressure plots were re-produced in Figures 10.23 - 10.26 without the questionable data. Note that the all inclusive data set is labeled with an "All" in the captions of Figures 10.16 – 10.22, and the data set that excludes the questionable data is labeled with a "Select" in the captions of Figures 10.23 – 10.26. Each test section was plotted individually in Figures 10.23 – 10.26 while Figures 10.16 – 10.22 combined sections with like crushed stone thicknesses (nearly identical results using either method). Table 10.13 summarizes the statistical data from Figures 10.16 – 10.26. Recall that the linear trend lines were generated using an intercept equal to zero. A data set that is all inclusive is described by "All" and a data set that excludes questionable data is described by "Select" in column 2 of Table 10.13. All responses were over predicted with the exception of surface deflection.

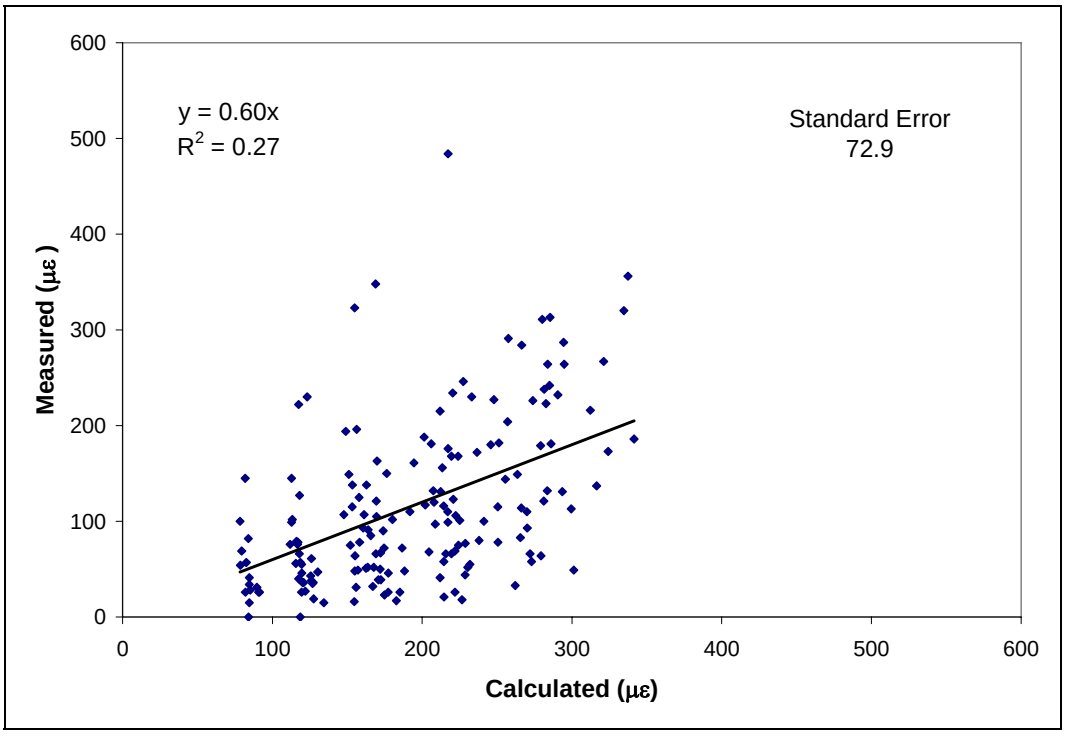

Figure 10.23 - Select Measured (FWD) versus Calculated Asphalt Strains (Under Load)

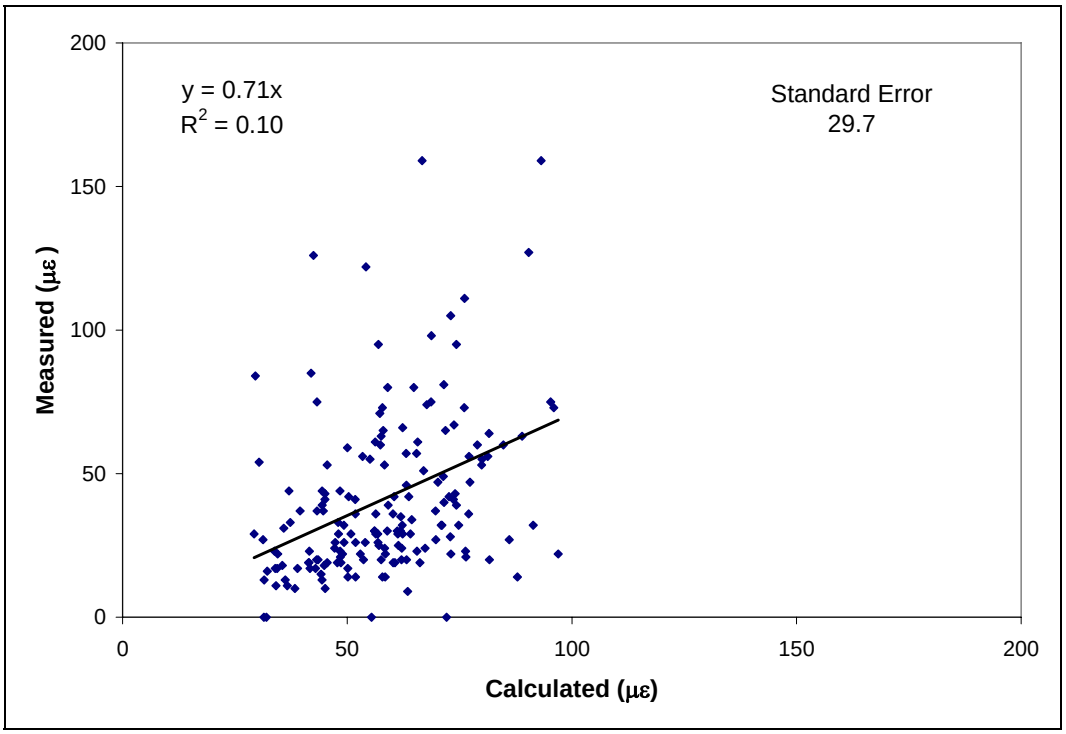

Figure 10.24 - Select Measured (FWD) versus Calculated Asphalt Strains (Offset)

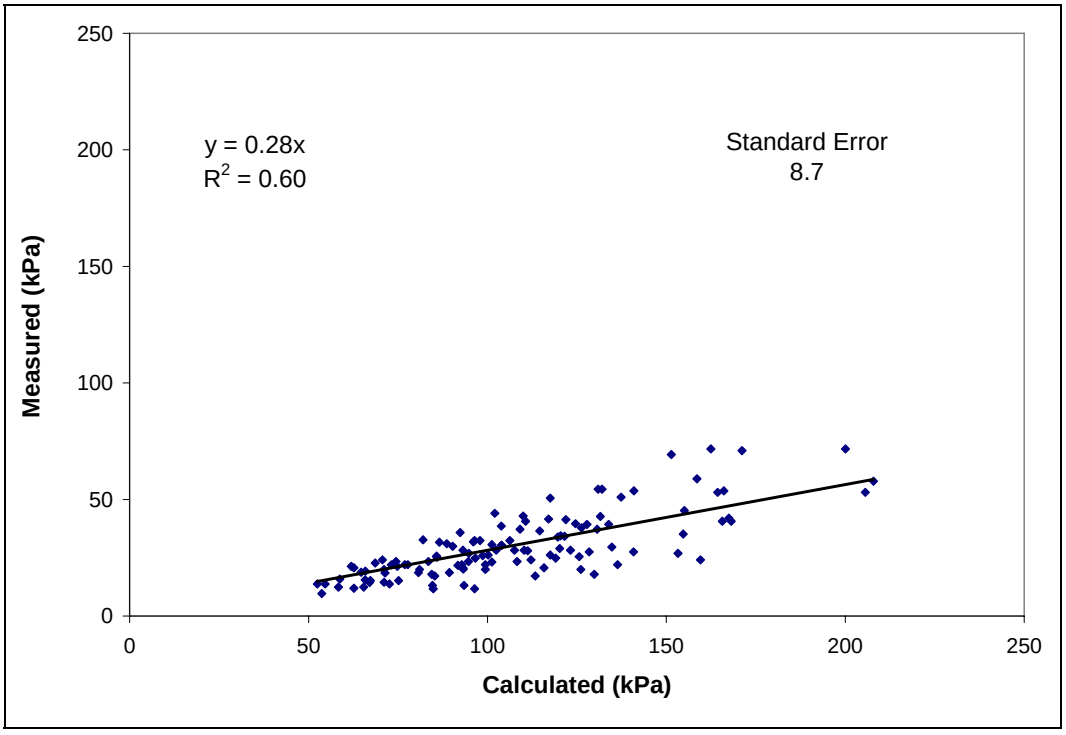

Figure 10.25 - Select Measured (FWD) versus Calculated Subgrade Pressured (Under Load)

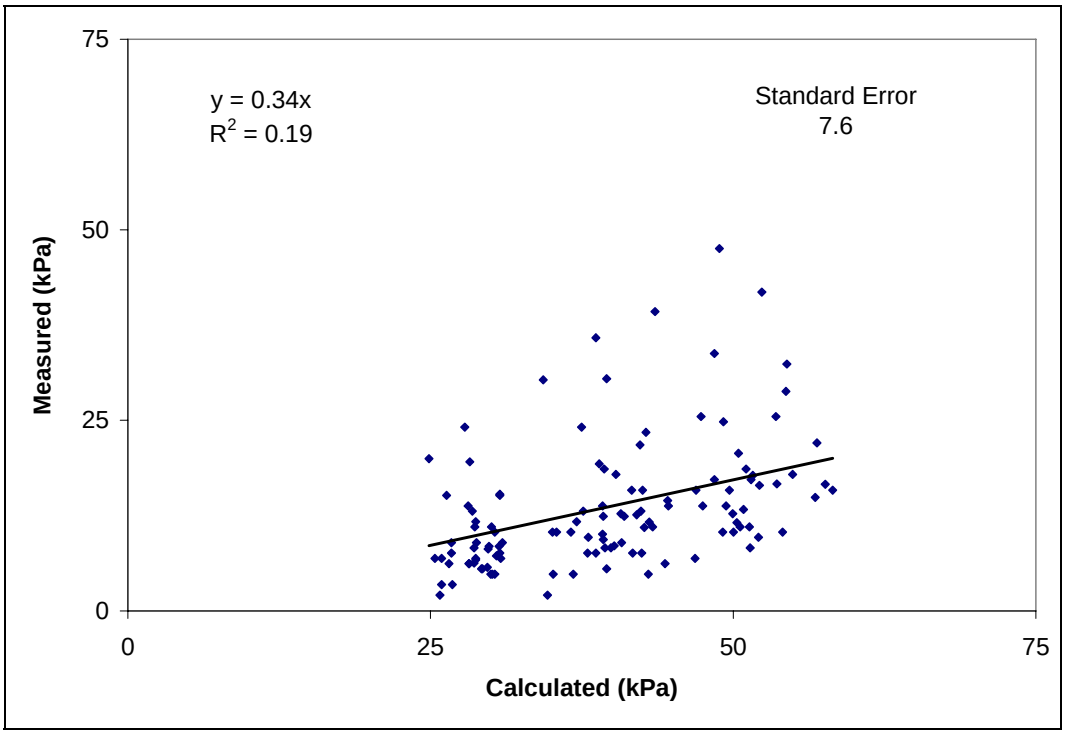

Figure 10.26 - Select Measured (FWD) versus Calculated Subgrade Pressures (Offset)

Table 10.13 - Model Calibration Equations under FWD Loads

Location	*Data*	*Slope*	*R^2*	*Units*
Deflection Under Load	All	1.76	0.52	μm
Asphalt Strain Under Load	All	0.66	0.28	με
Asphalt Strain Offset	All	0.74	0.24	με
Crushed Stone Pressure Under Load	All	0.34	0.84	kPa
Crushed Stone Pressure Offset	All	0.47	0.57	kPa
Compacted Subgrade Pressure Under Load	All	0.19	0.60	kPa
Compacted Subgrade Pressure Offset	All	0.26	0.59	kPa
Asphalt Strain Under Load	Select	0.60	0.27	με
Asphalt Strain Offset	Select	0.71	0.10	με
Compacted Subgrade Pressure Under Load	Select	0.28	0.60	kPa
Compacted Subgrade Pressure Offset	Select	0.34	0.19	kPa

The amount of scatter in the plots varied by response type and location. For example, R^2 values varied from 0.10 (Asphalt Strain, Select, Offset) to 0.84 (Crushed stone Pressure, All, Under Load). Note that the significance of the R^2 statistic is less significant for regression lines fit through the origin and the NCHRP 1-37a

Mechanistic Empirical Design Guide contains the same types of predicted versus estimated performance data with R^2 values ranging from less than 0.2 to greater than 0.6. If the data presented within the text is evaluated with the data presented in the additional addendum, it is apparent that the overwhelming majority of the scatter lies with the measured values. Generally speaking, there was more variability in the asphalt strain response, followed by surface deflection. The vertical pressure in the base course and compacted subgrade had the least amount of variability.

The slopes of the regression lines varied as well. Subgrade earth pressure was significantly over predicted, crushed stone earth pressure was moderately over predicted, and asphalt strain was slightly over predicted. These qualitative assessments (significant, moderate, and slight) of over prediction were made with the understanding that the calculated values simulate absolute maximum stress/strain states and a slope of slightly less than 1 would have been considered an excellent prediction.

Recall that if the slope of a regression line is less than 1.0, the model over predicted the value and the magnitude of the over prediction was equal to (1/slope). Therefore, the magnitude of the over prediction for the compacted subgrade pressure, crushed stone pressure, and the asphalt strain was 3.6, 2.9, and 1.7, respectively. These numbers were calculated using the "Select" data obtained "Under the Load" in Table 10.13 with the exception of the crushed stone pressure. There were no questionable data for the crushed stone earth pressure cells so the "All" group was used. The pertinent data used to calculate these numbers has been highlighted in Table 10.13 for clarity. Considering the environmental, measurement, test section, and calculation variables encountered, prediction/calibration of this order was considered reasonably accurate.

10.5.2 Model Calibration using Traffic Load Data:

Tables 10.9 – 10.11 summarize and Figures 10.27 - 10.29 display the measured (traffic) and calculated response data. These tables and figures summarize ***all*** data including the responses associated with gages that were malfunctioning (the asphalt

strain gage in Section 9 and the compacted subgrade pressure gages in Sections 6, 9, 10, 11, 12, and 13a). The magnitudes of the signals from these gages were unreasonable and did not compare well with trends exhibited by other gages that were functioning properly.

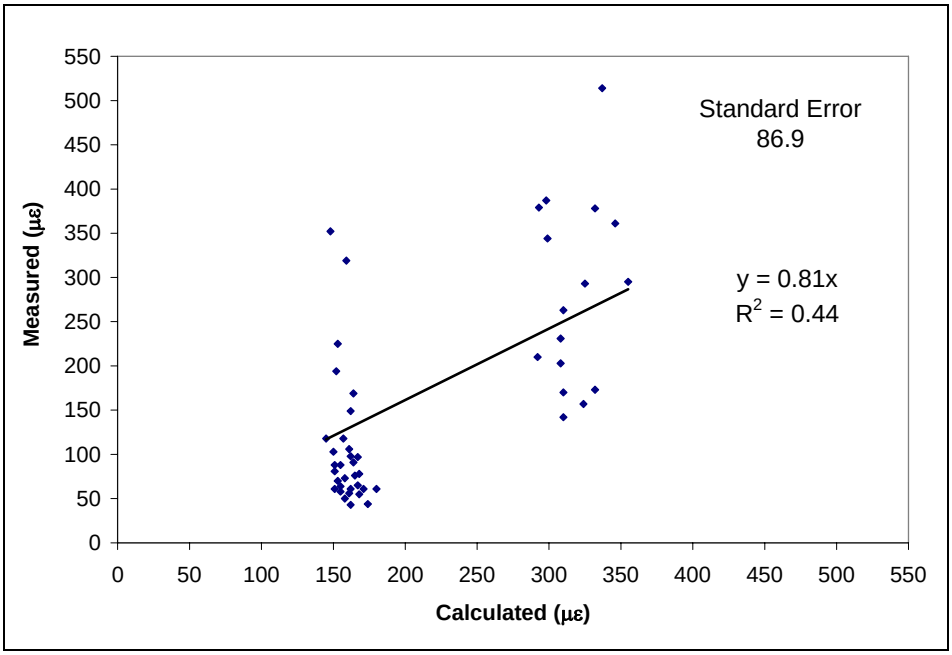

Figure 10.27 – All Measured (Traffic) versus Calculated Asphalt Strains (Under Load)

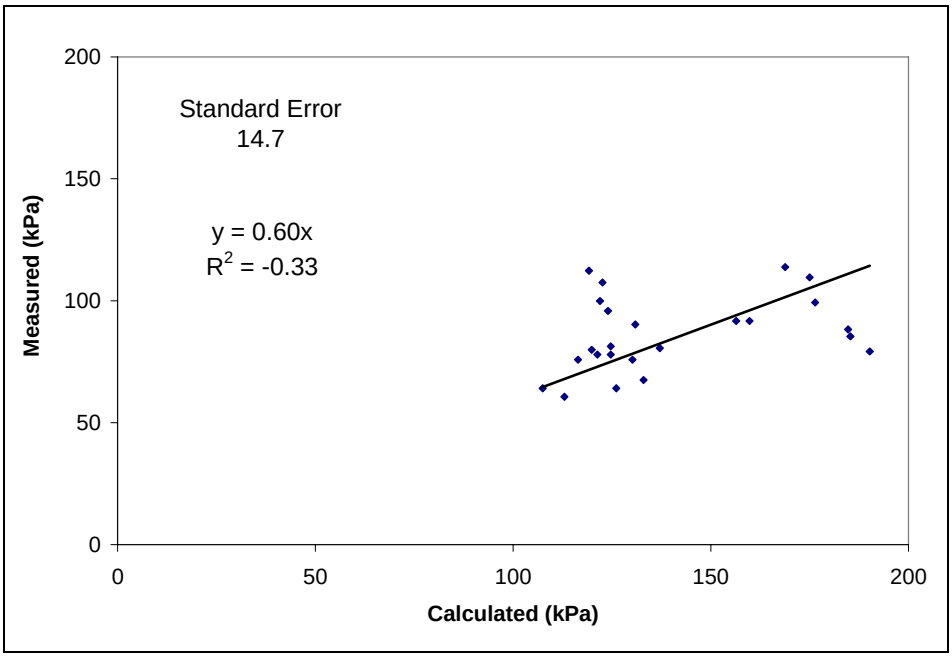

Figure 10.28 – All Measured (Traffic) versus Calculated Crushed stone Pressures (Under Load)

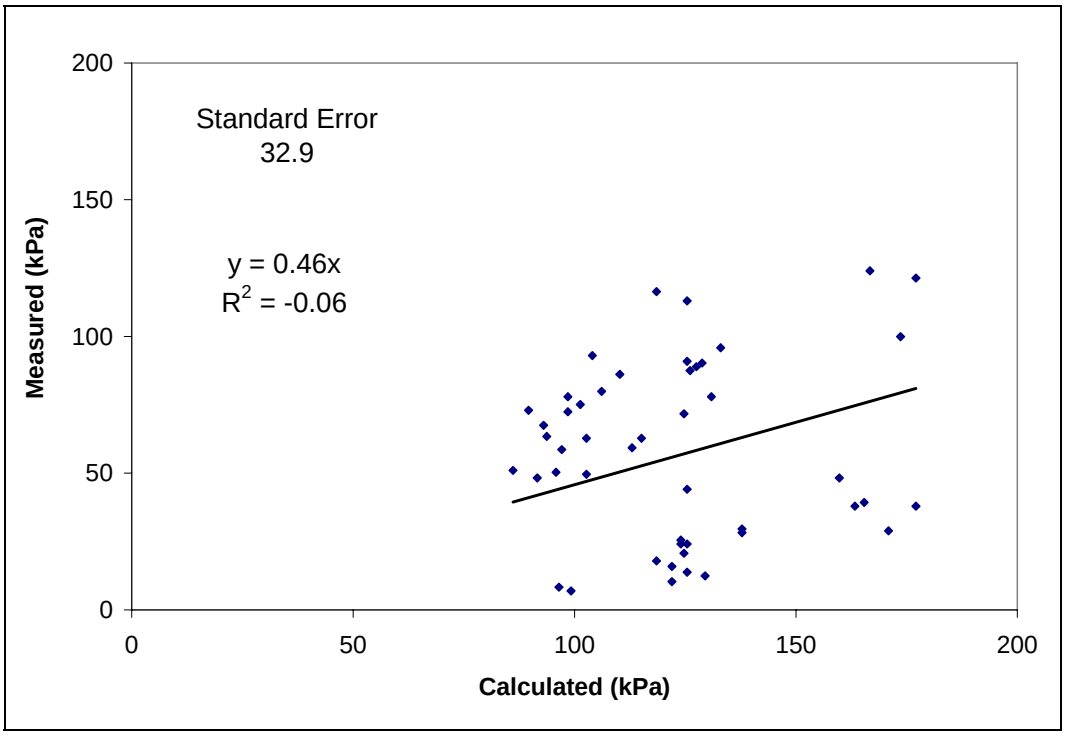

Figure 10.29 – All Measured (Traffic) versus Calculated Subgrade Pressures (Under Load)

As a result, the asphalt strain and compacted subgrade pressure plots were re-produced without the questionable data and displayed in Figure 10.30 and Figure 10.31. Table 10.14 summarizes the regression equations and statistical data from Figures 10.27 – 10.31. Recall that the linear trend lines were generated using an intercept equal to zero. A data set that is all inclusive is described by "All" and a data set that excludes questionable data is described by "Select" in column 2 of Table 10.14. All responses were over predicted (the slope was less than 1.0).

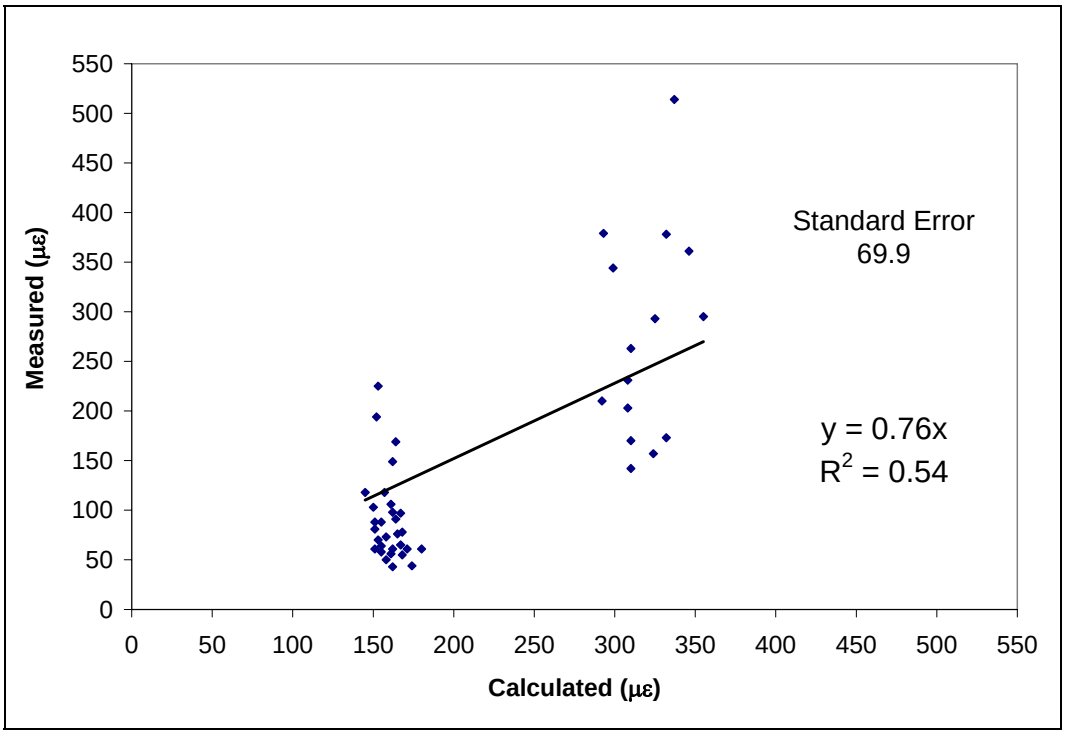

Figure 10.30 - Select Measured (Traffic) versus Calculated Asphalt Strains (Under Load)

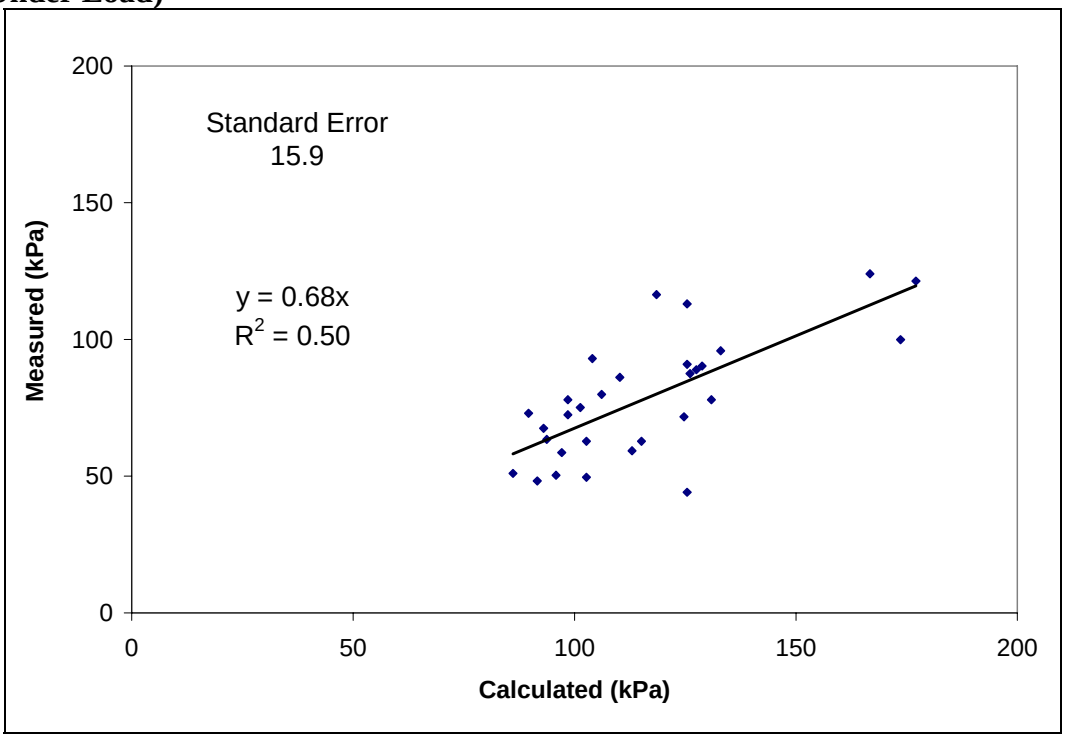

Figure 10.31 - Select Measured (Traffic) versus Calculated Subgrade Pressures (Under Load)

Table 10.14 - Model Calibration Equations under Traffic Loads

Location	*Data*	*Slope*	R^2	*Units*
Asphalt Strain Under Load	All	0.81	0.44	με
Crushed Stone Pressure Under Load	All	0.60	-0.33	kPa
Compacted Subgrade Pressure Under Load	All	0.46	-0.06	kPa
Asphalt Strain Under Load	Select	0.76	0.54	με
Compacted Subgrade Pressure Under Load	Select	0.68	0.50	kPa

Figure 10.29 was modified (Figure 10.32) to illustrate the affects of the questionable data obtained from the earth pressure cells in Sections 6, 9, 10, 11, 12, and 13a. Two lines were added to Figure 10.32. The first line exemplifies a perfect fit (or a match) between calculated and measured values (Equation of the line: Measured = 1.0 * Calculated). The second line represents a linear fit for all data in this figure (Equation of the line: Measured = 0.44 * Calculated). In other words, the slope of the line was reduced from 1.0 to 0.44 to accurately represent the relationship between measured and calculated for this data when the data set was all inclusive. Clearly, two distinct zones of data exist. Note that all measured data that falls below the linear fit line (dashed line) was obtained from the questionable gages in Sections 6, 9, 10, 11, 12, and 13a.

The amount of scatter in the plots varied by response type. For example, R^2 values varied from -0.06 (Subgrade Pressure, All) to 0.54 (Asphalt Strain, Select). Note that the significance of the R^2 statistic is less significant for regression lines fit through the origin. Note that negative R^2 values are possible since residuals will not sum to zero when the intercept is controlled, and the NCHRP 1-37a Mechanistic Empirical Design Guide contains the same types of predicted versus estimated performance data with R^2 values ranging from less than 0.2 to greater than 0.6. If the

data presented within the text is evaluated with the data presented in the additional addendum, it is apparent that the overwhelming majority of the scatter lies with the measured values.

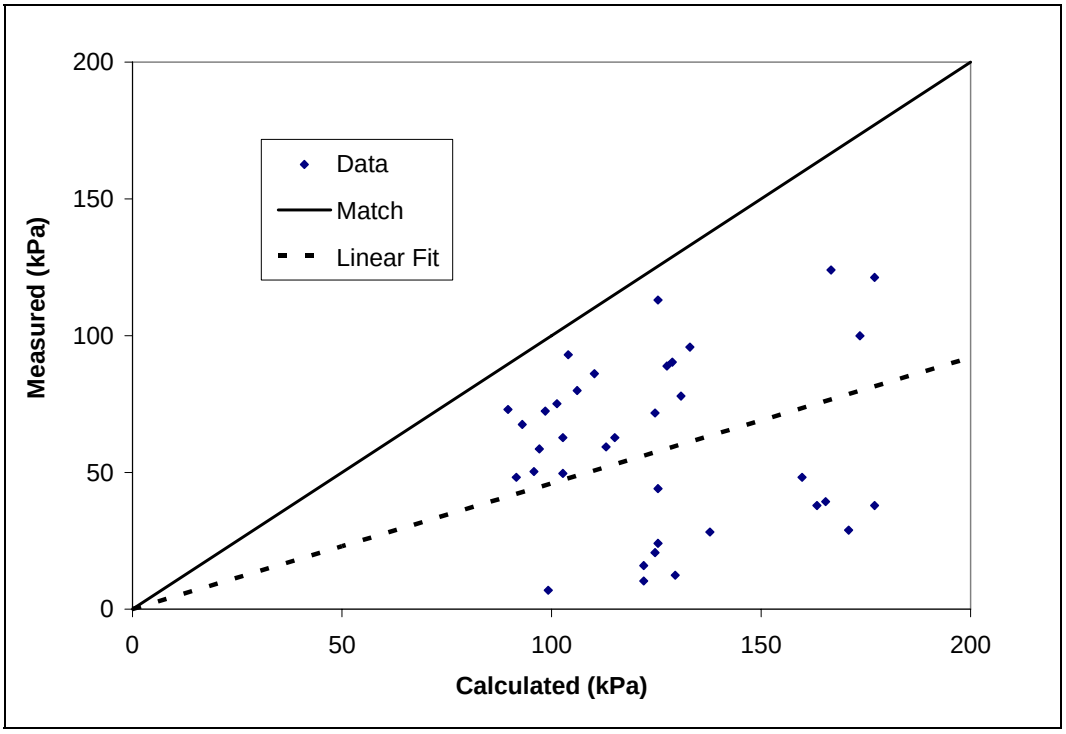

Figure 10.32 – Modified Measured (Traffic) Versus Calculated Subgrade Pressures (Under Load)

The highest variability existed in the asphalt strain responses even after the questionable data was removed (only three asphalt strain data points were removed between Figure 10.27 and Figure 10.30 due to Section 9). In Figure 10.30, two distinct clusters of data were present: a cluster with higher strain and variability, and a cluster with lower strain and variability. The high variability zone contained all Phase A data (which had higher temperatures), and the low variability zone contained all Phase B and C data (which had lower temperatures). If additional data were collected with time over a variety of seasonal conditions, the gap between the two distinct clusters in Figure 10.30 would likely close.

Aside from the aforementioned variability, the slopes of the regression lines produced were fairly consistent when the questionable data were removed. Asphalt strain, subgrade stress, and crushed stone stress were all slightly to moderately over predicted. These qualitative assessments (slight to moderate) of over prediction were established with the understanding that the calculated values simulate absolute maximum stress/strain states and a slope of slightly less than 1 would have been considered an excellent prediction.

Recall that if the slope of a regression line is less than 1.0, the model over predicted the value and the magnitude of the over prediction was equal to (1/slope). Therefore, the magnitude of the over prediction for the compacted subgrade pressure, crushed stone pressure, and the asphalt strain was 1.5, 1.7, and 1.3, respectively. These numbers were calculated using the "Select" data in Table 10.14 with the exception of the crushed stone pressure. There were no questionable data for the crushed stone earth pressure cells so the "All" group was used. The pertinent data used to calculate these numbers has been highlighted in Table 10.14 for clarity. Considering the environmental, measurement, test section, and calculation variables encountered, prediction/calibration of this order was considered reasonably accurate.

To elaborate on the expectation that calculated values would exceed measured values, the following rudimentary vehicle wander discussion is presented. Crude estimates of vehicle wander (based on the width of pavement that appeared worn post traffic) indicated that traffic deviated up to 450 mm (18 in) on either side of the instrumentation location. Therefore, the total wheel path was approximately 90 cm (36 in) wide. The edge to edge width of the dual tires on the back axle of the dump truck used to load the pavement was approximately 60 cm (24 in) so vehicle wander appeared to be relatively controlled in the field.

However, even in the finite element model, response dissipates rapidly from under the loaded area. Assuming the outer edge of a vehicle tire was at the edge of the estimated wander boundary, it is likely that some of the structural response gages would be outside of the representative loading area. Even a small number of vehicle

passes occurring at or near the estimated outer edge of vehicle wander could affect the measured responses relative to perfect vehicle position with each pass.

10.6 Comparison of Traffic and FWD Calibrations

Table 10.15 compares the response calibrations directly under the load for both the FWD and traffic loading conditions. There were minimal differences between the "All" inclusive data and the "Select" data. As a result, the remainder of the discussion will reference the "Select" data only.

Table 10.15 - Comparison of FWD and Traffic Calibrations (Under Load)

Sensors	*All*		*Select*		*All*	*Select*
Parameter	*FWD*	*Traffic*	*FWD*	*Traffic*	*Ratio (Traffic/FWD)*	
Asphalt Strain	0.66	0.81	0.60	0.76	1.23	1.27
Crushed stone Pressure	0.34	0.60	0.34	0.60	1.76	1.76
Subgrade Pressure	0.19	0.46	0.28	0.68	2.42	2.43

Traffic data calibration factors were higher than FWD calibration factors (closer to the desired value of 1.0). Asphalt strain did not appear to be extremely sensitive to load type (FWD or traffic). However, base course pressure and compacted subgrade pressure were sensitive to load type. It is also noteworthy that the magnitude of difference between the FWD and traffic response increased with depth. It was estimated that "true" pavement behavior fell somewhere between the "Select" traffic calibration factors (0.60-0.76) and a perfect match between measured and calculated responses (a slope of 1.0).

While no data is available to validate/dispute the previous statement, engineering judgment is considered sufficient to support the previous generalized statement when the scope of the this project is considered. Furthermore, a universal reduction factor within the 0.80 to 0.85 range for all calculated stress and strain responses under traffic would be reasonable and on the order of the precision and/or accuracy of the study. This range was selected since it conveniently falls between the two ranges just discussed (the 0.60-0.76 range for the "Select" traffic values and the perfect match of 1.0). Use of the "Select" ratios in Table 10.15 for each response type

should provide sufficient adjustment to the responses provided FWD loading is employed.

11. SUMMARY AND CONCLUSIONS

11.1 Summary

Seventeen test sections were designed and installed in a newly constructed flexible pavement frontage road in northeast Arkansas. All test sections were heavily instrumented and reinforced with various geosynthetic configurations (with the exception of the control test sections) to accomplish three main goals: to observe the difference in pavement performance with and without a geosynthetic on low volume roads constructed using poor subgrade soils, to establish the governing geosynthetic product and performance mechanism, and to develop a finite element analysis model that would contribute towards the on going mechanistic-empirical pavement design effort. Unfortunately, the research team faced some major obstacles during construction and testing as described in the following paragraphs.

While the roadway was scheduled to finish construction in the summer of 2004, contractor issues and wet weather conditions prevented completion of the roadway before the end of the construction season. The research team was forced to remove the instrumentation already installed in the subgrade and repeat the effort in the summer of 2005.

Secondly, the construction of a nursing home was initiated in 2005 and the proposed access road to the nursing home was designed to intersect the frontage road in test Section 8, which would have compromised the integrity of the test data. No longer would a vehicle be forced to travel from one end of the test area to the other end (all test sections receiving the same traffic load without a change in the traffic pattern). The nursing home was scheduled to open March 1, 2006. As a result, the type, frequency, and duration of the test traffic had to be adjusted. AHTD agreed to delay the opening of the frontage road to keep the nursing home construction traffic off of the test sections and allow the research team to collect controlled data before they were forced to permit access in March of 2006. Therefore, the data collection phase was accelerated and the ability to collect the data necessary to make test section comparisons and calibrate the finite element model was limited.

Finally, while the initial goal was to test the pavement over a wide range of temperature and moisture conditions, the weather was uncharacteristically dry during the field test, and the subgrade remained relatively stable. During testing, asphalt temperatures varied from approximately -1.1 to 51.7 ^{0}C (30 to 125 ^{0}F) while subgrade moisture contents varied from 17% to 20%. This moisture content range was almost equal to the range of optimum moisture contents. Due to the dry conditions and limited testing time, the tensile strength of the geosynthetic materials was not mobilized and the conventional benefits of these materials played no role in the stability of the flexible pavement frontage road in Arkansas.

While the desired testing conditions were not achieved, this document outlines the extensive work regarding the design and construction of the test sections, the programming, acquisition, and management of the data, and the empirical and mechanistic analysis of the results. More specifically, the following list summarizes the major accomplishments provided by the body of work described in this document.

1. A full-scale, instrumented roadway reinforced with multiple geosynthetics was constructed over a three month period in 2005. Prior to construction, an instrumentation plan detailing the selection, layout, calibration, and installation of all gages was developed. A total of 129 sensors were installed, requiring approximately 5,000 m (16,400 ft) of sensor cable and 370 m (1210 ft) of protective conduit.
2. A preliminary pilot scale study was performed to assess the data acquisition methodology and to establish pertinent timing parameters. Subsequently, extensive programming was developed to seamlessly acquire and monitor continuous streams of structural data from each axle and test section independently using section-specific trigger sensors, and to perform preliminary data calculations to soften the post-processing effort. Note that the research team was able to incorporate an independent trigger for all 16 structural test sections using only three DAQ cards (a significant cost savings to the project). The system was

properly implemented into the field to resolve any filtering needs and modify the timing parameters for the full-scale loading conditions (as necessary).

3. Over 2,000 passes of a loaded, single axle dump truck, over 500 FWD drops, and all corresponding environmental and site evaluation data were collected during a six month time interval (over 800 files of data were generated). Data was formatted, filtered, and consolidated before it was analyzed. Relative damage predictions were made for fatigue cracking and permanent deformation using Miner's concept coupled with transfer functions developed by the Asphalt Institute.
4. A non-linear finite element model that applied a dynamic load to a geosynthetic-reinforced pavement system was developed to contribute to the on-going mechanistic-empirical design effort, and more than 250 simulations were performed. Based on an extensive literature review and knowledge of material behavior, constitutive material models were selected to simulate behaviors such as non-linearity and stress dependency. The majority of the inputs were determined by laboratory testing.

The study was inconclusive for the reasons already discussed. Ideally, a study of this magnitude requires a longer life span. Data should be collected over a number of years to properly calibrate the model and assess geosynthetic performance over a variety of conditions. Even though the traffic pattern within the test sections has changed due to the construction of the nursing home access road and data has not been collected for the past year, continued monitoring of these test sections would be invaluable. The University of Arkansas has proposed a three year extension of this project to collect additional FWD, vehicle, and site evaluation data over time.

11.2 Conclusions

1. The data acquisition methodology was successfully employed during the full scale field test. Gages responses were independently recorded for each vehicle axle and

each test section to soften the post processing effort, which was especially important for the amount of data collected during a project of this size.

2. The potential benefits of the geosynthetic materials were not realized in this study due to the dry conditions. The subgrade moisture content varied minimally from the optimum conditions and the subgrade resilient modulus values varied from 56.5 MPa - 90.2 MPa (8.2-13.1 ksi) throughout the test. Modulus values of this magnitude (under the stress conditions encountered) are relatively high for a fat clay material (CH) and would have decreased significantly under wet conditions. Due to the dry, stable conditions, the tensile strength in the geosynthetics (as measured by the data acquisition system) was not mobilized during the test, which was validated by the model. Additionally, there was no visual evidence of layer intrusion at the subgrade-base course interface after a crude forensic examination.
2. Some rutting and minimal to no fatigue cracking was observed and also validated by the model. Typical rut depths equal to 3.25 mm - 6.25 mm (0.13-0.25 in) compared favorably with the values calculated using the Asphalt Institute transfer functions.
3. While a finite element analysis model was developed for this project and the material properties, constitutive models, and simplifying assumptions were carefully selected and in line with previously performed numerical studies, the model was "calibrated" under very limited environmental/testing conditions. Without additional data, this model should not be used to perform a parametric analysis or develop design curves.
4. The measured stress and strain responses (from FWD and traffic loads) compared reasonably well with the calculated values (FEA model), but the *measured* variability was significantly higher. In comparison to the earth pressure cells, the asphalt strain and surface deflection data were also more variable (especially at high temperatures).
5. Generally, deflections were under predicted by the finite element model while stresses and strains were over predicted. While the FWD test was developed to simulate traffic loads, traffic responses were higher in all cases and the calculated

versus measured values were also in better agreement during the traffic loads. The calibration factors varied from 0.60 – 0.76 under traffic loads and from 0.28 – 0.60 under FWD loads for the pressure and strain responses (a perfect match would result in a value equal to 1.0). Additionally, the difference between the FWD and traffic calibration factors increased with depth (a 27% increase from the asphalt strain response, a 76% increase from the crushed stone pressure response, and a 143% increase from the compacted subgrade pressure response). Based on engineering judgment. A ratio of the measured to the calculated values in the range of 0.80 - 0.85 would be reasonable and on the order of the precision and/or accuracy of the study. This range is approximately halfway between the calculated ratios of 0.60-0.76 and a perfect correlation of 1.0.

6. A meaningful assessment and comparison of the test sections was not possible due to the dry conditions and the expedited test interval. Continued monitoring of the frontage road (qualitative and quantitative) would provide valuable long term performance information.

11.3 Recommendations for Future Research

1. Continue long term monitoring of the test sections (over a variety of seasonal conditions) and work towards the development of design charts and procedures for low volume flexible pavements reinforced with geosynthetics.
2. Investigate the reason for the differences observed between FWD and traffic load responses.
3. Compare and contrast the benefits of subgrade stabilization using geosynthetics versus other chemical treatments (such as lime or fly ash) in a full scale field test.
4. Since mechanistic-empirical design procedures are rapidly becoming the new state of practice in pavement design, more work is needed to investigate the procedures necessary to calibrate and handle non-linear finite element models that incorporate geosynthetics.

12. REFERENCES

Asphalt Institute (AI), 1982, "Research and Development of The Asphalt Institutes Thickness Design Manual (MS-1)" 9th Edition, Research Report 82-2, Asphalt Institute.

Alexander, D. R., and Barker, W. R., 1994, "Backcalculation of Material Properties Based on Non-Linear Material Behavior" Proceedings of the 4th International Conference on the Bearing Capacity of Roads and Airfields, Vol. 1, Minneapolis, MN, USA., pp. 47-59.

Al-Khoury, R. Scarpas, A., Kasbergen, C., and Blaauwendraad, J., 2001, " Spectral element technique for efficient parameter identification of layered media. Part I. Forward Calculation" International Journal of Solids and Structures, Vol 38, pp. 1605-1623.

Al-Qadi, I. L. and Appea, A. K, 2003, "Eight-Year Field Performance of A Secondary Road Incorporating Geosynthetics at the Subgrade-Base Interface" Transportation Research Board-82nd Annual Meeting, January 12-16, Washington, D.C.

Al-Qadi, I. L. and Bhutta, S. A., 1999, "In Situ Measurements of Secondary Road Flexible Pavement Response to Vehicular Loading" Transportation Research Record 1652, TRB, National Research Council, Washington, D. C., pp. 206-216.

Al-Qadi, I. L., Brandon, T. L., Smith, T. E., and Lacina, B. A., 1996, " How do Geosynthetics Improve Pavement's Performance" Proceedings of Material Engineering Conference, San Diego, California, ASCE, pp. 606-616.

Al-Qadi, I. L., Brandon, T. L., Valentine, R. J., Lacina, B. A., and Smith, T. E., 1994, "Laboratory Evaluation of Geosynthetic-Reinforced Pavement Sections" Transportation Research Record 1439, TRB, National Research Council, Washington, D. C., pp. 25-31.

Al-Qadi, I. L., Hughes, J. J., 2000, "Field Evaluation of Geocell Use in Flexible Pavements" Transportation Research Record 1709, TRB, National Research Council, Washington, D. C., pp. 26-35.

Appea, A. K., Al-Qadi, I. L., 2000, "Assessment of Falling Weight Deflectometer Data for Stabilized Flexible Pavements" Transportation Research Record 1709, TRB, National Research Council, Washington, D. C., pp. 19-25.

[10] Austin, D. N., Coleman, D. M., 1993, "A Field Evaluation of Geosynthetic-Reinforced Haul Roads Over Soft Foundation Soils" Geosynthetics 93', Vancouver, Canada, pp. 65-80.

Baker, H. B., Buth, M. R., and Van Deusen, D. A., 1994, "Load Response Instrumentation Installation and Testing Procedures" Final Report Submitted to Minnesota Department of Transportation, No. MN/PR-94/01.

Barden, L., and Proctor, D. C., 1970, "The Drained Strength of Granular Material" Canadian Geotechnical Journal, Vol. 8, pp. 372-383.

Barksdale, R. D., Brown, S. F., and Chan, F., 1989, "Potential Benefits of Geosynthetics in Flexible Pavement Systems" National Cooperative Highway Research Program Report No. 315, Transportation Research Board, National Research Council, Washington, DC, pp. 1-53.

Bell, D. A., 1984, "Fundamentals of Electric Circuits", Third Edition, Reston Publishing Company, Inc., Reston, Virginia, USA.

Bhutta, S. A, 1998, "Mechanistic-Empirical Pavement Design Procedure For Geosynthetically Stabilized Flexible Pavements" PhD Dissertation, Virginia Polytechnic Institute and State University.

Bodhinayake, B. C., and Hadi, M., 2003, "A Design Chart for the Design of Flexible Pavements Based on Finite Elements", Proceedings, Invited Speakers & Workshops 21st ARRB and 11th REAAA Conference, May 18-23, Cairns, Queensland, Australia.

Bolton, M. D., 1986, "The Strength and Dilatancy of Sands" Geotechnique, Vol. 36, No. 1, pp. 65-78.

Bowles, J. E., 1996, *Foundation Analysis and Design,* 5th Edition, McGraw-Hill.

Boyce, J. R., 1980, "A non-linear model for the elastic behavior of granular materials under repeated loading" Proceedings International Symposium Soils Under Cyclic and Transient Loading, Swansea, pp. 285-294.

Brandon, T. L., Al-Qadi, I. L., Lacina, B. A., and Bhutta, S. A., 1996, "Construction and Instrumentation of Geosynthetically Stabilized Secondary Road Test Sections" Transportation Research Record 1534, TRB, National Research Council, Washington, D. C., pp. 50-57.

Brinkgreve, R. B. J., Al-Khoury, R., Bakker, K. J., Bonnier, P.G., Brand, P. J. W., Broere, W., Burd, H. J., Soltys, G., Vermeer. P. A., and Den Haag, .DOC, 2002, "PLAXIS 2D – Version 8" User Manual, A.A. Balkema Publishers, Netherlands.

Brown, S. F., 1977, "State-of-the-Art Report on Field Instrumentation for Pavement Experiments" Transportation Research Record 640, TRB, National Research Council, Washington, D. C., pp. 13-28.

Cancelli, P., Recalcati, P., and Shin, E., 2000, "Inchon International Airport: Subgrade Reinforcement With Geogrids" Tenax Corporation, Technical Document TDS005, Baltimore, Maryland, USA.

Carpenter, S., 2005, "Fatigue Performance of IDOT Mixtures; IHR-R39 Project-Extended Life of HMA Pavements" Report Prepared for the Illinois Cooperative Highway and Transportation Research Program, June 20, 2005.

Carroll, R. G., Walls, J. C., and Haas, R., 1987, "Granular Base Reinforcement of Flexible Pavements Using Geogrids" Geosynthetics '87, Volume 1, pp. 46-57.

Chazallon, C., 2000, "An Elastoplastic Model With Kinematic Hardening for Unbound Aggregates in Roads" Proceedings of the Fifth International Symposium on Unbound Aggregates in Roads, UNBAR5, Nottingham, UK, pp. 265-270.

Collin, J. G., Kinney, T. C., and Fu, X., 1996, "Full Scale Highway Load Test of Flexible Pavement Systems with Geogrid Reinforced Base Courses" Geosynthetics International, Volume 3, Number 4, pp. 537-549.

Cho, Y., McCullough, B. F., and Weissmann, J., 1996, "Considerations on Finite element Method Application in Pavement Structural Analysis" Transportation Research Record 1539, TRB, National Research Council, Washington, D. C., PP.96-101.

Construction Technology Laboratories, Inc. (CTL), 2004, Manufacturer Literature, 5400 Old Orchard Road, Skokie, Illinois, USA.

Craus, J., Yuce, R., and Monismith, C. L., 1984, "Fatigue Behavior of Thin Asphalt Concrete Layers in Flexible Pavement Structures" Proceedings, Association of Asphalt Paving Association Technologists, Vol. 53, pp. 559-582.

"Decagon Application Note", Decagon Devices, Inc., Pullman, WA, http://www.ech2o.com/downloads.html, (13 May 2004).

Decagon Instruction Manual, 2002, "ECH$_2$O Dielectric Aquameter User's Manual For Models EC-20 and EC-10 (Version 1.4)", Decagon Devices, Inc. Pullman, WA, USA.

Dewar, S., 1962, "The Oldest Roads in Britain" The Countryman, Vol. 59, No. 3, pp. 547-555.

Dondi, G., 1994, "Three-Dimensional Finite Element Analysis of a Reinforced Paved Road" Fifth International Conference on Geotextiles, Geomembranes and Related Products, Singapore, 5-9 September, pp. 95-100.

Duncan, J. M., and Chang, C. Y., 1970, "Nonlinear Analysis of Stress and Strain in Soils" Journal of the Soil Mechanics and Foundations Division; Proceedings of the American Society of Civil Engineers, Vol. 96, pp. 1629-1653.

Dunnicliff, J., 1988, "Geotechnical Instrumentation for Monitoring Field Performance", John Wiley & Sons, Inc.

Fannin, R. J., Sigurdsson, O., 1996, "Field Observations on Stabilization of Unpaved Roads with Geosynthetics" Journal of Geotechnical Engineering, July, pp. 544-553.

Fetten, C. P., Humphrey D. N., 1998, "Instrumentation and Performance of Geosynthetic beneath Flexible Pavements in Winterport and Frankfort, Maine" Technical Report ME 97-14 Submitted to Maine DOT, December 1998, pp. 1-137.

Federal Highway Administration (FHWA), 1990, "Highway Statistics".

Federal Highway Administration (FHWA), 2001, "Highway Statistics".

Garg, N., Thompson, M. R., and Ramirez, F. M., 2000, "Unbound Granular Base Modeling-Effects on Conventional Flexible Pavement Critical Response" Proceedings of the Fifth International Symposium on Unbound Aggregates in Roads, UNBAR5, Nottingham, UK, pp. 271-277.

Geokon Instruction Manual; Model 3500 Earth Pressure Cells, 2003, Geokon, Inc. Lebanon, New Hampshire, USA.

Geokon Instruction Manual; Model 3400 Semiconductor Piezometers, 2003, Geokon, Inc. Lebanon, New Hampshire, USA.

George, K. P., and Shah, N. S., 1974, "Dilatancy of Granular Media in Triaxial Shear" Transportation Research Record 497, TRB, National Research Council, Washington, D. C., PP.88-95.

Gonzalez, C. R., 1994, "Geogrid Design Criteria for Flexible Pavements and Light Aircraft" Final Report GL-94, Submitted to U.S. Army Corps of Engineers and USDOT and Federal Aviation Administration, Interagency agreement No. DTFAA1-89-02029.

Hall, K. D., and Elliott, R. P., 1992, "ROADHOG-A Flexible Pavement Overlay Design Procedure" Transportation Research Record 1374, TRB, National Research Council, Washington, D. C., PP. 9-18.

Hall, K. D., and Elliott, R. P., 2000, "An Improved Structural Material Model for Unbound Granular Bases" Proceedings of the Fifth International Symposium on Unbound Aggregates in Roads, UNBAR5, Nottingham, UK, pp. 353-358.

Halliday, A. R., and Potter, J. F., 1984, "The Performance of a Flexible Pavement Constructed on a Strong Fabric" Transportation and Road Research Laboratory, Report 1123.

Helwany, S., Dyer, J., Leidy, J., 1998, "Finite element Analyses of Flexible Pavements" Journal of Transportation Engineering, Vol. 124, No. 5, pp. 491-499.

Hornych, P., Kazai, A., and Quibel, A., 2000, "Modeling a Full Scale Experiment of Two Flexible Pavement Structures With Unbound Granular Bases" Proceedings of the Fifth International Symposium on Unbound Aggregates in Roads, UNBAR5, Nottingham, UK, pp. 359-367.

Hossain, M., Zaniewski, J., and Rajan, S., 1994, "Back Calculation of Pavement Layer Moduli Using a Nonlinear Optimization Technique" Proceedings of the 4th International Conference on the Bearing Capacity of Roads and Airfields, Vol. 1, Minneapolis, MN, USA., pp. 61-76.

Huang, Y. H., 1993, "Pavement Analysis and Design" Prentice-Hall Inc, New Jersey.

ILLI-PAVE, 1990, "ILLI-PAVE PC Version User's Manual" Deliverable from NCHRP 1-26; Calibrated Mechanistic Structural Analysis Procedures for Pavements, pp. 26.

Kallstenius, T., and Bergau, W., 1956, "Investigation of Soil Pressure Measuring by Means of Cells" Proceedings of Royal Swedish Geotechnical Institute, No. 12.

Kaswell, E. R., 1963, "Handbook of Industrial Textiles" Industrial Fabrics Division, West Point Pepperell, New York.

Kim, Y. R., Hibbs, B. O., Lee, Y., 1995, "Temperature Correction of Deflections and Backcalculated Asphalt Concrete Moduli" Transportation Research Record 1473, TRB, National Research Council, Washington, D. C., PP. 55-62.

Kinney, T. C., Stone, D. K., and Schuler, J., 1998, "Using Geogrids for Base Reinforcement as Measured by Falling Weight Deflectometer in Full-Scale Laboratory Study" Transportation Research Record 1611, TRB, National Research Council, Washington, D. C., PP. 70-77.

Koerner, R. M., 1984, "Construction and Geotechnical Methods in Foundation Engineering" McGraw-Hill, New York.

Koerner, R. M., 1986, "Designing With Geosynthetics" Prentice-Hall Inc., New Jersey.

Koerner, R. M., 1998, "Designing With Geosynthetics" Prentice-Hall Inc., Fourth Edition, New Jersey.

Li, N., Haas, R., and Kennepohl, G., 1992, "Geosynthetics in Asphalt Pavements: Structural, Materials, Design, and Performance Considerations" Proceedings of 37th Annual Conference of the Canadian Technical Asphalt Association, Victoria, British Columbia, Canada, pp. 224-242.

Ling, H. I., Liu, K., 2003, "Finite Element Studies of Asphalt Concrete Pavement Reinforced with Geogrid" Journal of Engineering Mechanics-ASCE, Vol. 129, No. 7, pp. 801-811.

Loulizi, A., Al-Qadi, I. L., Lahouar, S., and Freeman, T. E., 2001, Data Collection and Management of Instrumented Smart Road Flexible Pavement Sections" Transportation Research Record 1769, TRB, National Research Council, Washington, D. C., PP. 142-151.

Loulizi, A., Al-Qadi, I. L., Lahouar, S., and Freeman, T. E., 2002, "Measurement of Vertical Compressive Stress Pulse in Flexible Pavements; Representation for Dynamic Loading Tests" Transportation Research Record 1816, TRB, National Research Council, Washington, D. C., PP. 125-136.

Lytton, R. L., 1989, "Backcalculation of Pavement Layer Properties", Nondestructive Testing of Pavements and Backcalculation of Moduli, ASTM STP 1026, American Society of Testing and Materials, Philadelphia, PA, pp. 7-38.

Mery, J., 1995, "Field Studies on the Mechanical Behavior of Geosynthetic-Reinforced Unpaved Roads" Sixth International Conference on Low Volume Roads, Vol. 2, pp. 234-239.

Miura, N., Sakai, A., Taesiri, Y., Yamanouchi, T., and Yasuhara, K. 1990, "Polymer Grid Reinforced Pavement on Soft Clay Grounds" Geotextiles and Geomembranes, Volume 9, Number 1, pp. 99-123.

NCHRP 1-26, 1990, "NCHRP 1-26: Calibrated Mechanistic Structural Analysis Procedures for Pavements" Final Report Prepared for the National Cooperative Highway Research Program.

Newby, J. E., 1982, "Southern Pacific Transportation Co. Utilization of Geotextiles in Railroad Subgrade Stabilization" Second International Conference on Geotextiles, Las Vegas, U.S.A. Vol. 2, pp. 467-472.

Nishizawa, T., Himeno, K., Maruyama, T., and Saika, Y., 1994, "Comparison of Static and Dynamic FEM Analyses in Connection with Backcalculation of Pavement Layer Moduli Based on FWD Deflection Data" Proceedings of the 4th International

Conference on the Bearing Capacity of Airfields and Roads, Minneapolis, MN, USA, Vol. 1, pp. 215-227.

"Omega Product Selection Guide; Technical Reference Section", Omega Engineering, Inc., Stamford, Connecticut, http://www.omega.com/temperature/Z/zsection.asp (15 Jan 2004).

Park, H. M., Kim, Y. R., and Park, S., 2002, "Temperature Correction of Multiload-Level Falling Weight Deflectometer Deflections" Transportation Research Record 1806, TRB, National Research Council, Washington, D. C., pp. 3-8.

Parker, F. Jr., 1991, "Estimation of Paving Materials Design Moduli from Falling Weight Deflectometer Measurements" Transportation Research Record 1293, TRB, National Research Council, Washington, D. C., pp. 42-51.

Paulsen, W. C., 1971, "Finite Element Stress Analysis" Reprinted from *Machine Design* September 30, October 14, and October 28, United States Military Academy, West Point, New York, pp. 46-52, 146-150, 90-94.

Perkins, S. W., 1999, "Geosynthetic Reinforcement of Flexible Pavements: Laboratory Based Pavement Test Sections" Final Report to Montana Department of Transportation, Report No. FHWA/MT-99-001/8138.

Perkins, S.W. and Ismeik, M., 1997, "A Synthesis and Evaluation of Geosynthetic-Reinforced Base Layers in Flexible Pavements: Parts I and II" Geosynthetics International, Vol. 4, No. 6, pp. 549-604 and pp. 605-621.

Perkins, S. W., Wang, Y., Edens, M. Q., and Fragaszy, R. J., 2000, "Prediction of Permanent Deformation in the Unbound Aggregate and Subgrade Soils of a Paved Roadway" Proceedings of the Fifth International Symposium on Unbound Aggregates in Roads, UNBAR5, Nottingham, UK, pp. 377-384.

Qiu, Y., Dennis, N. D., and Elliott, R. P., 2000, "Design Criteria for Permanent Deformation of Subgrade Soils in Flexible Pavements for Low Volume Roads" Soils and Foundations, Vol. 40, No. 1, pp. 1-10.

Ramalho-Ortigao, J. A., Palmeira, E. M., 1982, " Geotextile Performance at an Access Road on Soft Ground Near Rio de Janeiro" Second International Conference on Geotextiles, Vol. II, Las Vegas, USA, pp. 353-358.

[80] Rollings, M. P., Rollings, R. S. Jr., 1996, "Geotechnical Materials in Construction" McGraw-Hill, New York.

Rowe, P. W., 1962, "The Stress-Dilatancy Relation for Static Equilibrium of an Assembly of Particles in Contact" Proceedings Royal Society A., No. 269, pp. 500-527.

Santoni, R. L., Smith, C. J., Tingle, J. S., and Webster, S. L., 2001, "Expedient Road Construction Over Soft Soils" Final Report ERDC/GSL TR-01-7, Prepared for U.S. Army Corps of Engineers by U.S. Army Engineer Research and Development Center.

Sargand, S., 1994, "Development of an Instrumentation Plan for the Ohio SPS Test Pavement (DEL-23-17.48)" Final Report for the Ohio Department of Transportation and Federal Highway Administration, Job No. 14573(0).

Sebaaly, P., Tabatabaee, N., and Scullion, T., 1989, "Instrumentation for Flexible Pavements" FHWA Report, Publication No. FHWA-RD-89-084.

"Smart Road Pavement Research Site", Virginia Tech University, Blacksburg, VA, http://www.cee.vt.edu/program_areas/tise/smart/index.html (12 Jan. 2004).

Sprague, C. J., Cicoff, G. A., 1993, "A Study of the Cost-Effectiveness of Using Geotextiles in Permanent Road Structures" Geosynthetics '93, Vancouver, Canada, pp. 49-63.

Suits, D., and Koerner, R., 2001, "Site Evaluation/Performance of Separation Geotextiles" Geosynthetics Conference 2001.

Tabatabaee, N. Sebaaly, P., 1990, "State-of-the-Art Pavement Instrumentation" Transportation Research Record 1260, TRB, National Research Council, Washington, D. C., pp. 246-255.

Thompson, M. R., 1994, "ILLI-PAVE Based Thickness Design Concepts and Practices for Surface Treatment Pavements" Proceedings of the 4th International Conference on the Bearing Capacity of Airfields and Roads, Minneapolis, MN, USA, Vol. 1, pp. 507-526.

Thompson, M. R., and Bejarano M. O., 1997, "Subgrade Criteria for Airport Flexible Pavement Design" Aircraft/Pavement Technology In the Midst of Change, ASCE, Seattle, WA, Aug 17-20, pp 18-32.

Thompson, M. R., and Nauman, D., 1993, "Rutting Rate Analyses of the AASHO Road Test Flexible Pavements" Transportation Research Record 1384, TRB, National Research Council, Washington, D. C., pp. 36-48.

Timm, D. H., Priest, A. L., and McEwen, T., 2004, "Design and Instrumentation of the Structural Pavement Experiment at the NCAT Test Track", Final Report, National Center for Asphalt Technology, pp. 100.

Edil, T. B., Benson, C. H., Sazzad Bin-Shafique, M., Tanyu, B. F., Kim, W., Senol, A., 2002, "Field Evaluation of Construction Alternatives for Roadways over Soft Subgrade" Transportation Research Record 1786, TRB, National Research Council, Washington, D. C., pp. 36-48.

Tutumluer, E., Little, D. N., and Kim, S., 2003, "Validated Model for Predicting Field Performance of Aggregate Base Courses" Transportation Research Record 1837, TRB, National Research Council, Washington, D. C., pp. 41-49.

Valentine, R. J., Brandon, T. L., Al-Qadi, I. L., and van't Hoog, L.,1993, "Laboratory Performance of Geosynthetic Reinforced Pavement Sections" Proceedings of 38th Annual Conference of the Canadian Technical Asphalt Association, Polyscience Publications, Inc., pp. 111-122.

Van Gurp, C., van Leest, A., 2002, "Thin Asphalt Pavements on Soft Soil" International Conference on Asphalt Pavements, pp 1-18.

Van Santvoort, G. (Translator), 1995, "Geosynthetics in Civil Engineering" A.A. Balkema/Rotterdam/Brookfield, Printed in the Netherlands.

Warren, K., Howard, I.L., Brooks, J. (2006) "Use of Digital Photography to Analyze Foil Strain Gages on Geosynthetics" Geo Congress '06, February 26 – March 1, Atlanta, GA, 2006.

Warren, K., Brooks, J., Howard, I.L. (2006) "Foil Strain Gage Attachment Techniques for Geotextile and Geogrid" Geo Congress '06, February 26 – March 1, Atlanta, GA, 2006.

Wathugala, G. W., Huang, B., and Pal, S., 1996, "Numerical Simulation of Geosynthetic-Reinforced Flexible Pavements" Transportation Research Record 1534, TRB, National Research Council, Washington, D. C., pp. 58-65.

Welcher, R. M., 2004, "Effect of Fines on the Shear Strength of Unbound Aggregate Base Course" Master's Thesis, University of Arkansas.

Yarger, T. L., Harrison, F. E. Jr., Mayberry, E. W., 1991, "Geogrid Reinforcement and Stabilization of a Highway Subgrade" Geosynthetics '91, Atlanta, GA, pp. 673-689.

Zarhampour, H., Elsander, J., Kolisoja, P., Nesslauer, S., and Lechner, B., 2002, "Modeling of Flexible Pavement Reinforced by Steel Net", Final Report REFLEX T7:02, Swedish National Road and Transport Research Institute, Contract No. BRPR-CT98-0816.